Aerosols and the Imaging Atmospheric Cherenkov Technique

fr Michael Connolly MSc BPh BTh

School of Physics

National University of Ireland, Galway

This dissertation is submitted for the degree of

Doctor of Philosophy

2017

I would like to dedicate this thesis to many of my brother catholic priests around the world who strive to be a light for the people who seek the Light.

For the creation waits with eager longing for the revealing of the children of God.

Romans 8:19

Declaration

I hereby declare that except where specific reference is made to the work of others, the contents of this dissertation are original and have not been submitted in whole or in part for consideration for any other degree or qualification in this, or any other University. This dissertation is the result of my own work and includes nothing which is the outcome of work done in collaboration, except where specifically indicated in the text. This dissertation contains less than 85,000 words including appendices, bibliography, footnotes, tables and equations and has less than 150 figures.

fr Michael Connolly MSc BPh BTh

2017

Acknowledgements

This thesis would have been all but impossible without the help of many people; I gratefully acknowledge their support and generosity.

Dr Mark Lang and Dr Gary Gillanders, along with the staff and students of the centre for astronomy, N.U.I. Galway, have allowed me to re-enter the world of physics again, after a very long sojourn. Firstly a Masters was completed with the Whipple 10 metre, then this work. Both I managed to complete in my spare time in about 9 years. Much patience was required by all involved, particularly with the tortuous novitiate in technical writing I had to undergo. I am thankful too for patience shown during my periods of 'disappearance', while I attended to more important priestly and pastoral matters. The research herein is interdisciplinary in nature, and would not have been possible without the help of C-CAPS, and in particular Dr Jana Preißler, to whom I am gratefully indebted. I also wish to acknowledge support received from the Science foundation of Ireland.

Dr Josh Reynolds had the vision to go for a ceilometer upgrade from the original model, which made the aerosol analysis herein possible. I pay special tribute to Dr Gernot Maier, DESY, Zeuthen, for his support and encouragement given to me. From time spent in the DESY facility, to the expensive MODTRAN upgrade, and ample computer time to produce so many simulations, I hope you will receive some benefit from it. Dr Henrike Fleischhack too was very helpful, and spent long hours with fortran formatting (that gratefully I did not have to figure out) and got me on the road to atmospheric simulations. It has certainly been an honour to be a part of the VERITAS collaboration, working with so many capable and

friendly people on an exciting project; I have learnt much more than physics from you.
I wish to pay tribute to the late bishop of Galway, +James McLoughlin, who sent me to Rome to study at the Gregorian University. The Jesuits there again taught me how to critique, study and explore in the search for truth. It was the love for truth that led me to VERITAS; I did not know what it was but I liked the name. Fr Martin Glynn was very enthusiastic and supportive that I continue and complete my studies, despite my heavy workload. I wish to thank him and my brother priests who stepped in and covered for my absence while spending considerable time in Arizona.
I wish to thank my family finally; it is so important to be grounded when so much research time is spent 'way out there'. I have especially enjoyed seeing my nephews and niece slowly grow up before my eyes. They have helped me realise what a responsibility we adults have to them, *a duty to future generations (pope Francis)*. Scientific research is at its most dignified when it serves the common good and looks towards the future with an attitude of stewardship.
There is a spiritual side to this thesis not immediately evident, a labour of love to re-connect with an earlier love in my life (physics) and bring it into relationship with the deeper love in my life, Christ and his body, the church. I am still trying to figure out why I spent so much time and effort joyfully doing this work, usually alone at home after a long days work in parish and hospital ministry. Some things are still mystery, some things just cant be explained by data and theory. Maybe living with the the tension between the physical and the spiritual, allowing both to be just what they are and come together in me, will be my real achievement.

Abstract

The ability to extract energetic γ-rays from the overwhelming high energy cosmic ray background has opened up a new window of observation on the non-thermal universe. By utilising an atmospheric technique VERITAS, an array of four imagining atmospheric Cherenkov telescopes, detects astrophysical gamma radiation in the energy range 85 GeV to >30 TeV. As the atmosphere is an integral part of the detector understanding the effects of aerosols is important.

This thesis reports on a novel aerosol extinction estimation technique that utilises an optimised and repurposed ceilometer. Taking advantage of water vapour absorption correction for the 905-910 nm laser and optimised ceilometer data quality cuts an independent measurement is provided for aerosol extinction profile up to 5 km above ground level. The inherent uncertainties are as low as $\pm$ $\sim$5-7%, with a high duty cycle $>$ 95% for dusk to dawn operation in the absence of clouds. From close to 6 years of ceilometer data (December 2011 to June 2017) aerosol optical depth is now known to seasonally increase more than 4-fold regularly from mid-winter to mid-summer, with a corresponding increase in overall atmospheric aerosol extinction $\sim$7-8%. During rare episodes of heavy aerosol loading atmospheric aerosol extinction increases by more than 15%.

A historical flaring episode, during a period of elevated aerosol loading, of the blazar Mrk 421 in April 2013 was analysed with new elevated aerosol extinction instrument response functions. For the elevated aerosol extinction analysis the following result was obtained; $I = 6.8\pm0.6\times10^{-10}$ cm^{-2}s^{-1}TeV^{-1}, $\Gamma = -1.75\pm0.06$, $E_o = 1.45\pm0.14$, $\chi^2/NDF = 42.86/31$. This result lies within experimental accuracies for the result obtained with the

normal aerosol extinction analysis. However, it is noted that below 237 GeV the elevated aerosol analysis shows a marked decline in significance σ. The spectral plot deviates slightly from a power-law with exponential cutoff below 237 GeV, but the differences are small.

An in depth examination of systematic uncertainty in reconstructed energy arising from elevated aerosol loading has yielded a year-on-year value of $\sim$5%, while the Mrk 421 April 2013 flaring episode yielded an uncertainty in reconstructed energy of $\sim$6-7%. This analysis was not carried out for the next source examined, PKS 1441 +25.

A soft VHE γ-ray source from April 2015 was analysed, PKS 1441 +25, whose data set was partially taken during elevated aerosol loading. For the elevated extinction analysis the following result was obtained; $I = 8.9\times10^{-12}\pm1.3\times10^{-12}$ cm^{-2}s^{-1}TeV^{-1} , $\Gamma = -5.81\pm0.57$, $\chi^2/NDF = 4.98/3$. This result also lies within experimental accuracies for the result obtained with the normal aerosol extinction analysis.

In conclusion, the aerosol extinction correction applied to the Mrk 421 and PKS 1441 +25 data sets do not benefit noticeably from the elevated aerosol correction developed in this thesis, implying that VERITAS data taken during periods of elevated aerosol loading is not in need of re-analysis.

Contents

List of Figures

List of Tables

Chapter 1

Introduction

1.1 An atmospheric technique for detection of very high energy γ-rays

Studying the violent non-thermal universe requires scientific instruments capable of detecting and measuring relativistic particles and highly-energetic photons. Very high energy (VHE) γ-rays (100 GeV < E_γ < 50 TeV), being immune to galactic and inter-galactic magnetic field deflection, are valuable messengers that carry much information regarding their environment of origin [Lorenz and Wagner, 2012]. The flux of VHE γ-rays is very low. Thus, their detection requires long exposures from small detector-size space-borne experiments [Li et al., 2016], unless another method allowing a larger detection area is possible. The interaction of energetic particles and photons of extra-terrestrial origin with a planetary atmosphere offers the opportunity of large detection areas from ground-based instrumentation [Krennrich, 2009]. The energetic particle's interactions with the atmosphere produce one type of shower cascade, the energetic photons produce another. For this method of ground based detection of atmospheric shower cascades to work, an in-depth understanding of the resulting interaction products arising from both types of cascade is needed [Heck et al., 1998, Singh et al., 2011]. Additionally, the resulting cascade interaction products (in

particular lower energy photons in the blue / UV band) must travel to detector level. Therefore, a sound understanding of the atmosphere's transmission properties is also essential [McClatchey et al., 1972]. However, the atmosphere is not composed of gaseous molecules alone. Particles of small dimensions called aerosols, in solid and liquid form, are almost always present close to the planetary surface [Wenny et al., 1998, Dubovik et al., 2002]. The molecular density profile of the atmosphere above a particular geographical position is shown to be quite stable. Seasonal variations in atmospheric density are the principal cause of varying refractive index when the hydrological cycle (atmospheric water in gaseous, liquid (droplet) and solid (ice crystal) form) is not considered [McClatchey et al., 1972]. This however is not the case with aerosols.

The aerosol layers high temporal variability necessitates constant ground-based or space-borne monitoring. Ground-based monitoring can be achieved by passive instruments such as sun photometers [Holben et al., 1998, Holben et al., 2001], which offer an aerosol optical depth (the total extinction for a column of air due to aerosols) that is time resolved to several hours while there is sufficient sunlight. They are robust and inexpensive instruments. A preferred method for ground-based aerosol profiling relies on light detection and ranging. Here laser pulses are emitted into the atmosphere and backscattered from aerosols into a receiver [Ansmann et al., 1990, Welton et al., 2001, Flentje et al., 2010]. This method allows good spatial and temporal resolution of aerosol concentrations, termed aerosol loading. A particular type of laser backscattering instrument for cloud-base detection and ranging, ceilometers, are made use of in this thesis. Space-borne instruments are not used [Winker et al., 2003], because aerosols inhabit the lower boundary layer of the atmosphere and hence the furthest distance from space-borne detectors.

Having a reliable aerosol profile and a representative molecular atmospheric profile for a particular observatory site allows accurate radiative transfer simulations to be produced. With these atmospheric parameters the simulation of cosmic ray and VHE γ-ray atmospheric cascades, often called extensive air showers, is possible. CORSIKA [Heck, 2005], a Monte

Carlo extensive air shower simulation package, has been in continual development for a quarter of a century, making it the best means to test a VHE γ-ray telescope's performance against Monte Carlo simulations. This proves crucial for the production of instrument response function simulations for γ-ray telescopes.

1.1.1 Previous studies of the impact of aerosols on γ-ray astronomy

Research into the impact of the atmosphere, and more specifically the aerosol component of the atmosphere, on extensive air showers has been undertaken by a number of experiments in VHE γ-ray astronomy. The basic theory of atmospheric modeling was outlined by Bernlöhr [2000], where the use of a well-tested radiative transfer code with broad-application aerosol typologies allowed a basic methodology to be applied to all telescope sites.

The research closest in approach to the work in this thesis is Nolan et al. [2010], where a low-power ceilometer was used to estimate the aerosol loadings on various nights of γ-ray telescope operation. Their method did not give an absolute value for aerosol extinction, but relied on a comparison of the mean of the distribution for the reconstructed depths of shower maximum for cosmic rays and γ-rays, both real and simulated, under the application of different atmospheric models. The best match between real and simulated telecope data was deemed the $defacto$ working atmosphere.

Other work similar to Nolan et al. [2010] is found, for example, in Dorner et al. [2009], which uses optical photometry to estimate the total atmospheric optical depth to correct for the impact of Saharan desert dust layers carried to site by air mass movements. A 532 nm laser and telescope receiver (a custom-made lidar system), examined in Fruck et al. [2014], allows backscattering from up to 20 km elevation to be recorded. Lastly, a method using atmospheric transparency to blue / UV light based on cosmic ray background telescope triggering found in Hahn and De los Reyes [2015], and Hahn et al. [2014], allows a reliable method of data-quality monitoring to be achieved using data from γ-ray telescopes alone.

1.1.2 Personal contributions to the VERITAS experiment

Outside of the research in this thesis, a number of other contributions were made by me during my tenure as a PhD student with the VERITAS Collaboration, with collaboration membership from 2010 to present. I completed a MSc with VERITAS prior to beginning this work, analysing archival data from the Whipple 10 m telescope and publishing a masters thesis in 2010.

A total of over four months were spent at the VERITAS experiment site, Fred Lawrence Whipple Observatory, Arizona, where five separate observing runs, ranging from 2-3 weeks in duration, were carried out. The duties included telescope start-up / shut-down, nightly source-observing rota, data taking, high sky-background-noise observations, calibrations, troubleshooting, atmospheric monitoring, electronic-log and technical wikipage update and blazar monitoring among others. Of particular importance were multiwavelength campaigns with other experiments who observed particular sources simultaneously with VERITAS in the radio, infrared, optical, UV, *x*-ray and high energy *x*-ray band.

I am also a signed co-author on over 50 published papers by the VERITAS Collaboration, listed in Section B.1.1, where data taken during the five observing runs mentioned was included in many of the papers. The authorship process involves an active sign-up, with careful reading and comments on papers signed, among other suggestions.

The hardware components of atmospheric monitoring have been led by Dr Josh Reynolds, Cork Institute of Technology, Ireland, to whom I am indebted. These instruments included a ceilometer and three infrared radiometers. I have taken the lead on the analysis of atmospheric data, as described in this thesis. Preliminary analysis on aerosol optical depth approximation (pre-correction), not presented in this thesis, has been used as part of the data quality monitoring program from 2013 to present. All work with ceilometer analysis presented herein was developed by me alone from the ground up. A total of $>$ 25,000 lines of original code has been tested and implemented for analysis and plotting algorithms for ceilometer, radiometers, telescope triggering and the associated simulations outlined in this

thesis. All the analysis was carried out in Octave/Matlab, C / C++ and the data analysis framework ROOT.

Lastly I was, on two occasions, invited to give a presentation on atmospheric monitoring for the VERITAS Collaboration at AtmoHEAD, Atmospheric High Energy Astroparticle Detectors. The first in 2013 in Paris, and also 2015 in Padua (which I had to decline).

1.1.3 Thesis outline

This thesis is inter-disciplinary in its approach; it seeks to benefit from expertise from the atmospheric physics community and apply it to astroparticle physics research. In Chapter 2, the relevant theory will be presented for cosmic ray interactions with the atmosphere and the atmosphere's relevant transmission properties. As extensive use will be made of a tried and trusted extensive air shower simulation code, an in-depth understanding of particle interactions and decays will not be required. Emphasis will be placed on understanding the atmosphere's transmission properties, both molecular and particulate. In Chapter 3, the atmospheric monitoring equipment in use before the introduction of a ceilometer at the observatory site will be described. A new data set will be added to the telescope analysis chain pertaining to atmospheric water vapour, while use of regional aerosol studies will quantify some necessary optical properties relating to local aerosol typologies. Finally, the radiative transfer code for atmospheric transmissions, which has been extensively tested for over 40 years, will be introduced. In Chapter 4 the ceilometer will be examined along with lidar theory and mie scattering, the light scattering model for particles with a size approximately equal to the wavelength of light scattered. The ceilometer's characteristics will be examined in detail in order to optimise its data stream for a new purpose, aerosol profiling and monitoring. Novel quality cuts, which set acceptable limits on certain parameters outside which ceilometer data is rejected, are developed and implemented. Water vapour extinction correction, necessary for the particular ceilometer used, will be estimated and applied to ceilometer data. Finally, aerosol extinction profiles will be estimated, including stringent

error estimation. Particular ceilometer data sets from pertinent dates will be examined in detail. In Chapter 5 extensive air shower simulations will be presented, with the express aim of understanding the effects of varying aerosol loading, water vapour, progenitor particle type, progenitor energy and progenitor source elevation on cosmic ray and γ-ray air shower simulations. These simulations will guide the production of telescope instrument response functions for both normal and elevated aerosol profiles. In Chapter 6, these telescope instrument response functions will be used to analyse some telescope data obtained from extragalactic VHE γ-ray sources during know periods of elevated aerosol loading. This analysis is carried out in the hope of determining if aerosol extinction correction is a useful tool for the current generation of γ-ray telescope.

Finally, a note on the thesis presented itself. Due to the complexity required, mentioned above, to perform atmospheric monitoring and correction for the Cherenkov Imaging technique, detailed cross-referencing has been employed across this thesis to assist the reader. These cross-references appear in "()" brackets. Studying this work in a modern PDF viewer allows the reader to left-click the mouse at a reference and be brought directly to the reference in question. Left-clicking [> toolbar > Go > Back] brings the reader back to the initial jump-off point.

Chapter 2

γ-ray atmospheric interactions

2.1 A brief history of extra-terrestrial particle research

Very High Energy (VHE) (100 GeV $\leq E_\gamma \leq$ 50 TeV) γ-ray astronomy, forming an integral part of high energy astrophysics, is a relatively recent field of research that helps probe the non-thermal universe. Violent regions of the cosmos emit relativistic atomic nuclei or highly energetic photons. Cosmic rays consist principally of protons and to a lesser extent charged nuclei up to Iron in the periodic table, while VHE γ-rays are believed to emanate from the same non-thermal regions. The instruments required for their detection may be ground based or space borne. The Earth's atmosphere shields the planet surface from all but the most energetic cosmic rays and VHE photons (more commonly referred to as VHE γ-rays). Ground based detection is achieved by the ability of cosmic rays and γ-rays of sufficient energy to interact with the atmosphere and produce light signals detectable at ground level. If the energy of the energetic photons is sufficiently high, they produce electromagnetic showers in the atmosphere while the charged nuclei of sufficient energy produce hadronic particle showers. γ-rays are of particular interest in high energy astrophysics, as they are unaffected by inter-stellar and inter-galactic magnetic fields. This allows their putative source location

to be estimated with some accuracy.

The first attempt to overcome the atmosphere's absorptive effects when detecting cosmic rays were with high altitude balloons that searched for cosmic ray abundance and constitution. In 1911-1912, a series of ballon flights by Victor Hess brought Wulf electrometers more than 5 km above ground level (a.g.l.). Averaging over the electrometers at this height a roughly fourfold increase in ionisation was found compared to ground level [Hess, 1912]. In order to rule out the Sun as the radiation's source, a balloon flight was made during a near total eclipse [Hess, 1936]. Cosmic ray research stagnated for many years, due to the lack of reliable detection methods. It required the promise of ground-based detection of cosmic rays, with large detector areas, to stimulate development in this nascent field of research. As the flux of VHE γ-rays and highly energised nuclei is very low ($\sim 10^{-3}\mathrm{m}^{-2}\mathrm{s}^{-1}$ at 1 TeV [Swordy et al., 2002]), large detection area is essential.

As this thesis seeks to determine the impact of certain atmospheric conditions on the detection and calorimetry of VHE γ-rays, this brief introduction now branches to examine the development of instruments capable of the detection and measurement of such γ-rays.

Historically, the development of ground-based γ-ray astronomy is closely linked to the study of hadronic cosmic rays and hadronic air showers. The idea of searching for astrophysical γ-rays and their point of origin, at modest energies of $\sim$100 MeV, was first proposed in 1958 [Morrison, 1958]. The prediction of VHE γ-rays from known objects such as the Crab nebula, which would initiate air showers that would be observable by particle array detectors at high altitudes, was made in 1959 [Cocconi, 1959].

It has been known since the 1950s that highly-energetic particles and photons would initiate nuclear reactions with atmospheric molecules. The resulting particle/photon cascades generate, among other constituents, electromagnetic radiation in the ultraviolet (UV) to blue-visible part of the spectrum, named Cherenkov radiation [Galbraith and Jelley, 1953]. Cherenkov light, with a wavelength of 300-600 nm, is caused by a charged particle traveling faster than the speed of light in the medium (air in this case). The Superluminal

charged particles in the shower cascade sends a light pool, which lasts for the order of several nanoseconds and is tightly bound about the shower axis, towards the Earth's surface. Such a light pool could in practice be detected by photomultiplier tubes (PMTs) and background suppression. In 1968 a γ-ray telescope design based on the Davies and Cotton solar collector [Cotton and Davies, 1961], was placed on Mount Hopkins, Arizona ($31^\circ\ 40^{'}\ 52^{''}$ N $110^\circ\ 52^{'}\ 42^{''}$ W, 2606 m above sea level (a.s.l.)). With this new telescope design and the use of a single photomultiplier tube at the solar collector focus, a borderline detection of 3 standard deviations (3σ) was obtained when the telescope was pointed at the Crab Nebula [Fazio et al., 1972]. This nascent field of energetic γ-ray observation, despite early optimism, remained in a state of near stagnation for approximately two more decades until the introduction of a 2-dimensional 39 PMT camera, in place of a single PMT [Kildea et al., 2007]. The Cherenkov light from electromagnetic and hadronic showers, usually referred to as shower images when they are focused onto a camera plane, could now be converted into a charge reading for each PMT and stored digitally for later analysis. The possibility of discrimination between energetic γ-rays and charged nuclei by discriminating between the image produced by each ensued. The development of the 39 PMT camera permitted pixelisation and moment fitting of the shower images, guided by the results of Monte Carlo simulations [Weekes and Turver, 1977]. This allowed the γ-ray signal to be separated from the overwhelming hadronic cosmic ray background [Hillas, 1985], due to the differences between electromagnetic and hadronic showers. This method, known as the Cherenkov imaging technique, is in continual development and refinement up to the present day. The combination of light collector and pixellated camera at the focal plane is called an Imaging Atmospheric Cherenkov Telescope (IACT). Charged cosmic rays have their path deflected by interstellar and intergalactic magnetic fields, nullifying attempts to ascertain their point of origin. Therefore the principle initiators of air showers, overwhelmingly protons, are not of particular interest in this thesis as their source location is undeterminable for all but the highest energy particles. Cosmic rays will however be of some interest in due course, as

they are the principal events recorded by the telescope and provide useful information pertaining to telescope operating efficiency.

The breakthrough in ground-based VHE γ-ray astronomy using the above mentioned technique came in 1989 with the detection of a 9σ signal from the Crab Nebula [Weekes et al., 1989]. The 1990s saw the detection of the first extragalactic VHE γ-ray sources by the Whipple Collaboration, the name given to the institutions and personel that together collectively ran the Whipple 10 m telescope. This campaign started with nearby blazars (a particular type of Active Galactic Nuclei) Mrk 421 [Punch et al., 1992], and Mrk 501 [Quinn et al., 1996]. A new programme of putative source detection was undertaken, with the aim of producing a sizable VHE γ-ray source catalogue. Despite the Whipple 10 m telescope being the world's most sensitive telescope of its kind from 1989 to about 2000, the relative scarcity of bright TeV γ-ray sources (fewer that 10 were identified prior to 2000) highlighted the need for improved instrumentation. In 2007 the then new generation of Imaging Atmospheric Cherenkov Telescope for the northern hemisphere saw first light in Arizona; the 4-telescope stereoscopic VERITAS array (Very Energetic Radiation Imaging Atmospheric Telescope). It is operated by an international Collaboration led by the Smithsonian Astrophysical Observatory and is one of 3 principal ground-based γ-ray IACTs worldwide, the others being H.E.S.S. in Namibia [Abdalla et al., 2017], and MAGIC in the Canary Islands [Aleksić et al., 2016].

The VERITAS array, the successor to the Whipple 10 m telescope, consists of four 12 m diameter IACTs situated at ($31^\circ\ 40^{'}\ 30.21^{''}$ N $-110^\circ\ 57^{'}\ 7.77^{''}$ W; altitude 1268 m a.s.l.), with a typical distance between reflectors of $\sim$100 m. The telescope lower and upper sensitivity limits are from 85 GeV to $>$ 30 TeV, with an energy resolution of $\sim$20% at 1 TeV [Park et al., 2016]. The peak effective area is greater than 10^5 m^2, advantageous owing to the very low flux of VHE photons reaching the upper atmosphere. The angular resolution is 0.1° at 1 TeV, 0.14° at 200 GeV (68% containment radius) while the source location accuracy is $\sim$50 arcseconds. The observation time per year is $\sim$750 hours non-moonlight,

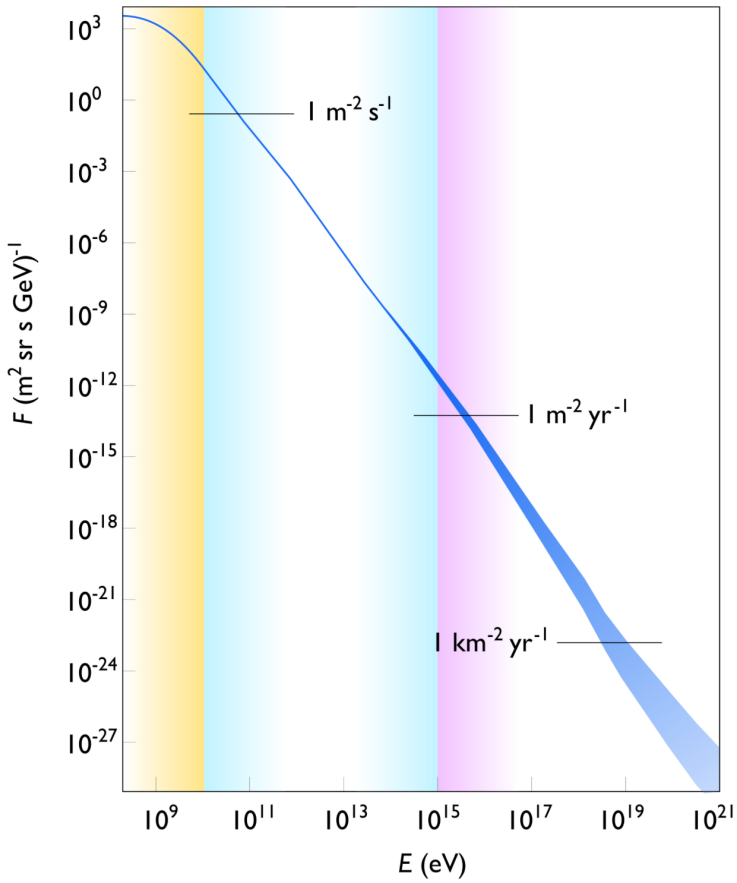

Fig. 2.1 Plot of cosmic ray flux with principal particle origins colour coded. The yellow energy band is of solar system origin, the blue band is of galactic origin, while the purple is of extra-galactic origin. Taken from Swordy et al. [2002].

$\sim$200 hours moonlight, typically 70-100 hours total per month over 10 months. A PMT upgrade in 2012 gave a 50% increase in photon detection efficiency, and a 30% reduction in triggering threshold [Kieda et al., 2013].

Figure 2.1 displays the flux of cosmic ray particles as a function of their energy. At the highest energies cosmic rays of $\sim 10^{19}$ eV may have a flux of 1 nucleus km^{-2} yr^{-1} [Swordy et al., 2002]. Thus the Auger observatory, which searches for these extremely high energy particles, has an effective collection area of 3000 km^2 [Abraham et al., 2009]. In comparison VERITAS has a collection area of 0.1 km^2, a difference of more than four orders of magnitude.

2.2 Extensive Air Showers (EAS)

The Cherenkov imaging technique is based on the ability to detect, qualify (distinguish between hadronic and electromagnetic showers) and quantify (perform calorimetry) the Cherenkov air shower images. The resulting particle cascades are called Extensive Air Showers (EAS). An in-depth understanding of the EAS caused by both γ-ray primaries and hadronic primaries is required to facilitate γ/hadron seperation techniques. After an introduction to air shower physics in this chapter, all future reference to and study of EAS will be made in relation to the dedicated and extensively tested EAS simulation package, CORSIKA (COsmic Ray SImulation for KAskade) [Klages et al., 1997], examined in detail in Chapter 5. Note that interaction heights will be given in atmospheric depth units, g cm^{-2}.

2.2.1 The progenitors of extensive air showers

Cosmic rays arriving at Earth are mostly protons accelerated at sites principally, it is believed, within our galaxy. As they are mostly charged particles, they are deflected by inter galactic, galactic, solar and terrestrial magnetic fields. Consequently for hadrons, source location is only determinable with accuracy for $E > 10^{19}$ eV [Aab et al., 2016], where E is the energy of the particle. For Extremely High Energy ($E \sim 10^{19}$ eV) γ-rays, it is believed that their interactions with the cosmic microwave background radiation limits their horizon to tens or hundreds of Mpc [De Angelis et al., 2013]. Figure 2.2 gives the Spectral Energy Distribution for a large number of cosmic ray nuclei, showing the abundance of H^+ to be about an order of magnitude greater than that of He^{++}, with the overall relative abundance of H to He in the current universe epoch being about three to one. The following discussion on VHE photon and hadron interactions with the atmosphere, outlined in Sections 2.2.2 and 2.2.3, may be referenced in greater detail in Rao and Sreekantan [1998], Grieder [2010] and Longair [2011].

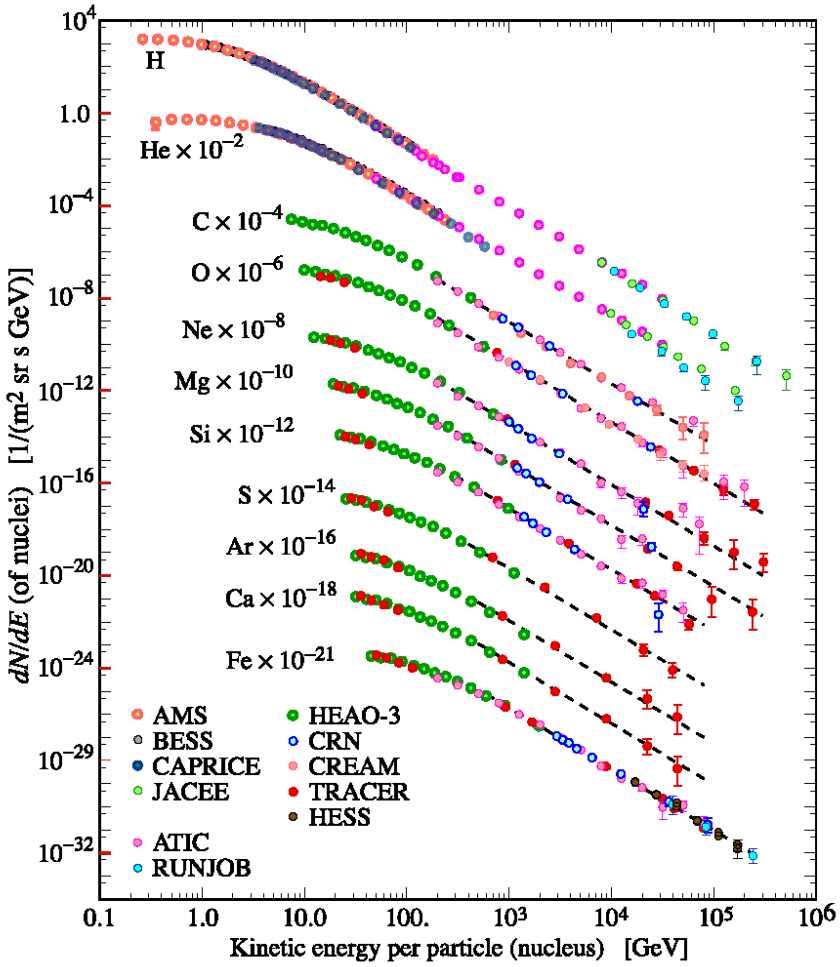

Fig. 2.2 A plot of the relative abundances of cosmic ray nuclei and their energy distributions as gathered by the listed experiments. Taken from Beringer et al. [2012].

The energy spectrum of primary nuclei from ∼1 GeV to ∼100 TeV is given by

$$I(E) \approx 1.8 \times 10^4 (E/1\ \text{GeV})^{-2.7} \frac{\text{nucleons}}{\text{m}^2\ \text{s sr GeV}} \tag{2.1}$$

where the differential spectral index $\equiv 1 + \Gamma = -1.7$.

The spectrum of VHE γ-rays typically follows a power law. The spectral index (Γ) may range from hard ($\Gamma \sim 1.5$) to soft ($\Gamma > 5$) where Γ is defined by

$$\frac{dN}{dE} \propto E^{-\Gamma} \tag{2.2}$$

where N is the number of γ-rays used to make the spectrum. See Figure 2.3 for an example of a VHE γ-ray emitter that will be examined in Chapter 6 of this thesis, Mrk 421. The VHE γ-ray spectral energy distribution needs to be corrected for pair production with the extragalactic background light, the average photon density in the universe from all infrared to ultraviolet light emitters from all epochs [Dwek and Krennrich, 2013].

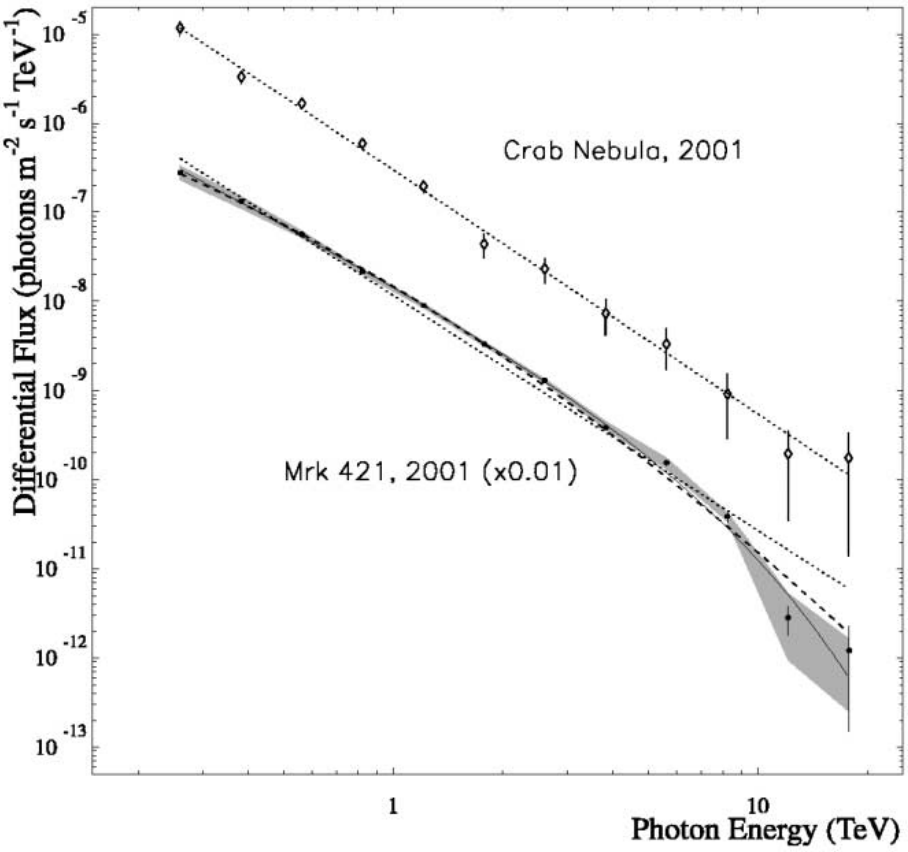

Fig. 2.3 A spectrum of an extragalactic blazar, Mrk 421 (filled circles), and the Crab Nebula (diamonds) for a data set taken from [Krennrich et al., 2001]. The dotted lines correspond to power-law fits, the dashed line (Mrk 421) corresponds to a parabolic fit, and the solid line is the result from a fit with an exponential cutoff. Note that the Mrk 421 spectrum has been offset by a factor of 0.01 in flux for clearer presentation, and errors shown include only statistical uncertainty. The shaded area shows the systematic uncertainties except for the 20% uncertainty in absolute energy.

2.2.2 Energetic γ-ray atmospheric interactions

Electromagnetic showers, of primary interest in VHE γ-ray astronomy, are produced by energetic photons and leptonic particles (electrons / positrons). These progenitors interact primarily by way of the electromagnetic force. Above several MeV, beyond the region of Compton scattering and the photoelectric effect, photons interact with matter primarily by pair production. This section will focus on electron / positron pair production, though proton / antiproton or muon / antimuon pair production are also possible. Pair production occurs when photons of sufficient energy convert into an electron-positron pair, conserving momentum by interacting with a nucleus or perhaps electron. The threshold energy for pair production, an elastic process, is the rest mass of the electron and positron combined, that is 1.02 MeV.

$$\gamma \rightarrow e^{+} + e^{-} \tag{2.3}$$

The surplus energy of the incident photon is imparted equally to both electron and positron, which explains why electromagnetic showers may be very extensive in longitudinal propagation. The progenitor VHE γ-ray that produce them often exceeds the threshold energy for pair production by 6-7 orders of magnitude.

VHE γ-rays produce positrons and electrons by pair production in the atmosphere over a distance of $\frac{9}{7}X_0$, where X_0 is the radiation length and is $\sim 36.5\ \mathrm{g\,cm^{-2}}$ in air. The radiation length is defined as the length over which a positron or electron travels before it has just $\frac{1}{e}$ of its energy remaining due to bremsstrahlung and is also $\frac{7}{9}$ of the mean free path for pair production by a high-energy photon [Völk and Bernlöhr, 2009].

The positrons and electrons produced undergo more bremsstrahlung over the next radiation length, with new lower energy γ-rays that generate new positron / electron pairs of lower energy again, and so on. This continues until the energy of the final generation of electrons and positrons drops below the threshold energy for bremsstrahlung. Thereafter ionization losses dominate, causing rapid energy loss of the particle cascade. The result of these processes is an electromagnetic air shower that exists for $\sim 10^{-4}$ s.

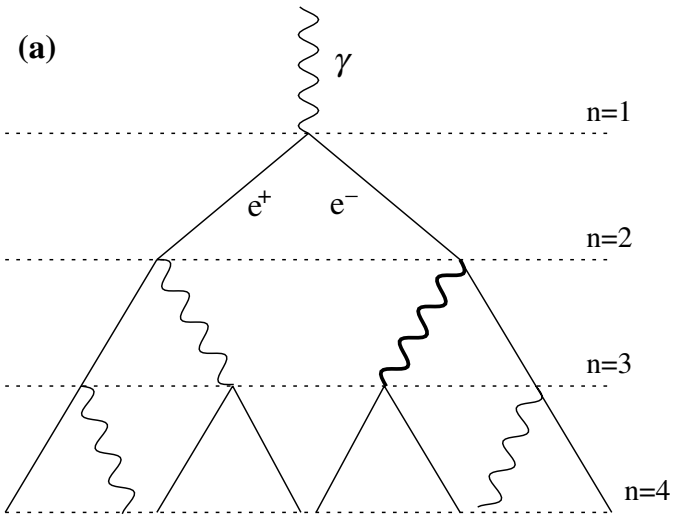

Fig. 2.4 Electromagnetic cascade where the radiation lengths X_0 are represented by the dashed horizontal lines. Taken from Matthews [2005].

Figure 2.4 shows the radiation lengths as horizontal dashed lines for the interactions in an electromagnetic shower. Note that the physical distance travelled by the particles and photons varies about the radiation length, due to the probabilistic nature of the interactions. The length of the shower cascade before it reaches maximum intensity, often referred to as the shower depth (X_{sd}), scales with X_0. The shower depth is determined by estimating when the bremsstrahlung and ionisation rates are equal, at the 'critical' energy E_c [Rossi and Greisen, 1941]

$$X_{sd} \approx X_0 \, ln\frac{E_0}{E_c} \tag{2.4}$$

where E_0 is the initial energy of the progenitor γ-ray. For electromagnetic air showers E_c has a value of $\sim$85 MeV [Matthews, 2005]. The shower depth increases logarithmically with the energy of the progenitor γ-ray. For a primary γ-rays of 20 GeV to 20 TeV, X_{sd} occurs at an atmospheric depth from 250 to 450 g cm^{-2} which is from 12 km to 7 km a.s.l. [Völk and Bernlöhr, 2009]. The lateral spread of the shower is mainly due to the multiple scattering of the electrons, which may be estimated by approximating the Moliére radius [Capdevielle and Gawin, 1982].

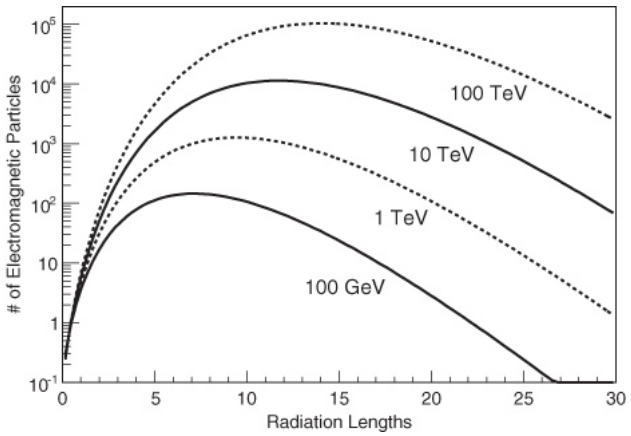

Fig. 2.5 The longitudinal development of an extensive air shower for several different primary γ-ray energies. The x-axis is the atmospheric depth expressed as the number of radiation lengths X_0. Taken from Aharonian et al. [2008].

Figure 2.5 shows the longitudinal development for electromagnetic air showers of various energies, with corresponding radiation lengths. The shower depth X_{sd} increases with increasing energy, as seen by where the individual plots reach maximum number of electromagnetic particles.

Figure 2.6a shows particle tracks due to a 1 TeV γ-ray, where red tracks are for bremsstrahlung γ-rays and $e^{\pm}$s. Though the particle track distribution may not seen dissimilar to the particle track distribution for hadronic showers, discussed next, it is the impact the particle track distribution has on the production of Cherenkov light that is of interest.

2.2.3 Energetic hadronic atmospheric interactions and decays

The overwhelming complexity of energetic hadronic interactions with the atmosphere means only a most brief introduction here follows. The principal propose of this sub-section is to highlight the very different nature of hadronic air showers as compared to electromagnetic air showers, thereby showing how γ/hadron seperation is possible with the Cherenkov imaging technique.

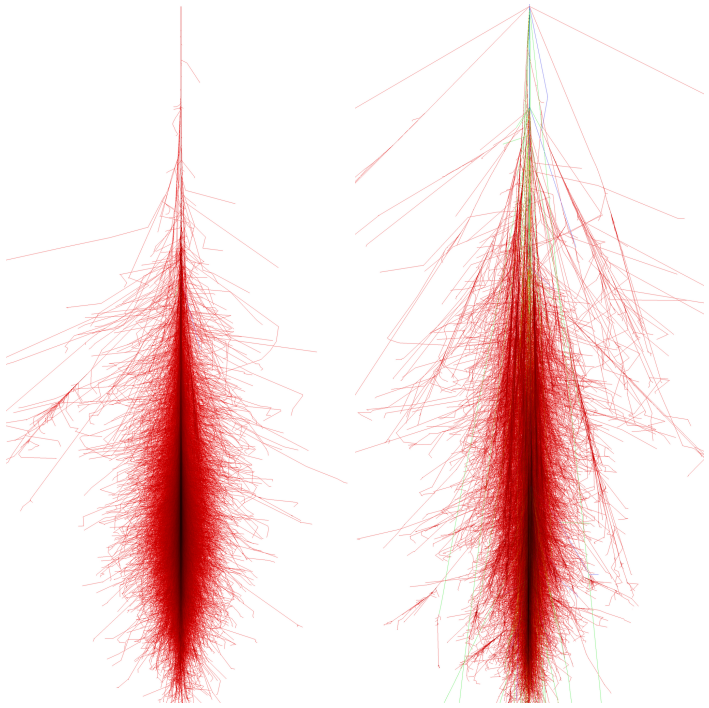

(a) Particle tracks of 1 TeV γ-ray (b) Particle tracks of 1 TeV p^+

Fig. 2.6 Particle tracks arising from an electromagnetic air shower (left), and a hadronic air shower (right). Red tracks represents electrons and positrons, other colours are for elementary particles [1].

Figure 2.7 gives a representation of the varied interactions and decays that are possible in hadronic shower cascades, now briefly outlined.

Hadrons include sub-categories of baryons and mesons, which can take part in strong force interactions. Baryons are particles, such as nucleons (protons, neutrons) or hyperons (with differing categories of quark combination than nucleons), that have a mass greater than or equal the mass of a proton. They are made of 3 quarks. Mesons are particles with a mass between that of an electron and a proton. They transmit the strong force that binds nucleons together in the atomic nucleus. Mesons, an example of which are pions, are made of 1 quark and 1 anti-quark.

After the progenitor hadron, an energetic cosmic-origin nucleus, has collided with an air

[1] https://www.ikp.kit.edu/corsika/

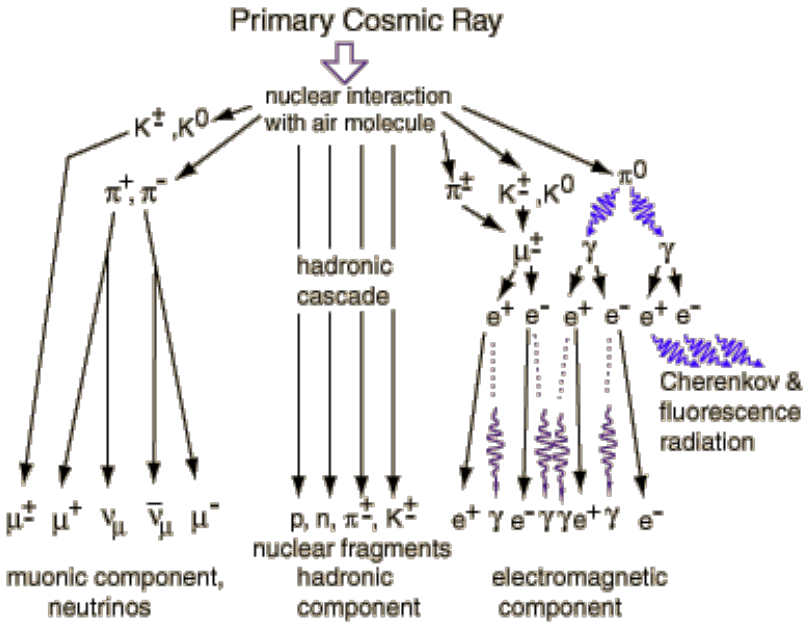

Fig. 2.7 The array of possible hadronic, muonic and electromagnetic air shower cascades from relativistic progenitor hadrons. Note that Cherenkov radiation is also produced by muons and the hadronic cascades, not shown in the diagram [2].

molecule, most probably one nucleus of either N_2 or O_2, the main constituents of the first interaction are pions (π). Pions are the lightest hadrons, as they are composed of the lightest quarks (up / down quarks). They are, like most hadrons, unstable, with the charged pions ($\pi^{\pm}$) decaying with a mean lifetime of 2.6×10^{-8} s, and the neutral pion (π^{o}) decaying with a much shorter lifetime of 8.4×10^{-17} s. Their interaction cross sections are effectively zero due to their lifetimes, meaning that only the decay particles are accounted for in EAS simulations. Additionally, kaons (κ) and baryons may be created. Kaons, like pions, are not stable, thus they will decay into other constituent particles, comprising short-lived fundamental particles, dominantly π^{o} or $\pi^{\pm}$.

$$\kappa^{\pm} \rightarrow \pi^{\pm} + \pi^{0} \tag{2.5}$$

[2] http://hyperphysics.phy-astr.gsu.edu/hbase/astro/cosmic.html

Neutral pions decay into two γ-rays

$$\pi^0 \rightarrow \gamma + \gamma \tag{2.6}$$

The charged pions, $\pi^{\pm}$, most often decay into muons and neutrinos along the channel

$$\pi^{\pm} \rightarrow \mu^{\pm} + \nu \tag{2.7}$$

Charged pions may also produce an electron, positron and two neutrinos or anti-neutrinos (ν or $\bar{\nu}$) via the pion-muon-electron decay. This leads to secondary electromagnetic air showers, with an ongoing hadronic core and penetrating muon component.
Muons, $\mu^{\pm}$, belong to the same class of particles as electrons (Leptons). They have the same charge as electrons, but a much greater mass and have a mean lifetime of 2.2 x 10^{-6} s. Being leptons they are thought to be elementary (non-composite) particles. The principal decay mode for muons, the Michel decay [Michel, 1950], is as follows

$$\mu^+ \rightarrow e^+ + \bar{\nu}_e + \nu_\mu \tag{2.8}$$

$$\mu^- \rightarrow e^- + \nu_e + \bar{\nu_\mu} \tag{2.9}$$

where ν_e and $\bar{\nu}_e$ are electron neutrinos and electron antineutrinos, while ν_μ and $\bar{\nu_\mu}$ are muon neutrinos and muon antineutrinos respectively. An understanding of muon production in cosmic ray initiated air showers is important, for muons produce Cherenkov light pools that form shower images on the VERITAS camera. These muon shower images may appear as a ring on the camera plane when the first interaction height is sufficiently far from the camera. If the first muon interaction height is not sufficiently far from the camera, the shower image may be difficult to distinguish from VHE γ-ray shower images. Yet it is possible that muon shower images be rejected, due to the very localised nature of muon production. More de-

tails follow in Chapter 3.

Figure 2.6b shows particle tracks initiated by a 1 TeV proton. The red tracks are for bremsstrahlung γ-rays and $e^{\pm}$ only, green are for muons. There is a great diversity in hadronic air shower morphology owing to the large variety of possible particle decay channels.

2.2.4 Cherenkov light

Cherenkov light is electromagnetic radiation with a continuous spectrum that is emitted when a charged particle travels through a dielectric medium at a speed greater than the phase velocity of light in that medium. The phase velocity, v_p, is given in terms of the frequency ω and period T of the light as $v_p = \frac{c}{\omega T}$, where c is the speed of light in a vacuum.

It is instructive to examine the case of a subluminal and superluminal charged particle as they travel through a dielectric medium, such as air. For a subluminal charged particle, the molecules of the medium have a dipole induced momentarily that aligns the molecules about the velocity vector of the charged particle. The net charge about the charged particle trajectory is, up to a short time after the charged particle passes, non-zero but symmetrical, see Figure 2.8.

For an electron induced disturbance the net positive charge induced is greater closer to the electron trajectory, but can thereafter relax back to equilibrium due to the symmetrical dipole induced charge distribution. This may be likened to the absence of a shockwave, as the speed of the charged particle is not too great.

However, if the speed of the charged particle is superluminal (faster than the phase velocity of the medium) the net charge about the charged particle trajectory is, up to a short time after the charged particle passes, both non-zero and asymmetrical, see Figure 2.9. The dipole relaxation is now unable to happen quickly enough due to the build up of shockwave like front. As the superluminal charged particle passes, the induced dipoles relax near instantaneously. The result is a coherent shockwave of light emitted when the energy built up in

the local dielectric medium is released. The medium then returns to zero net charge and equilibrium.

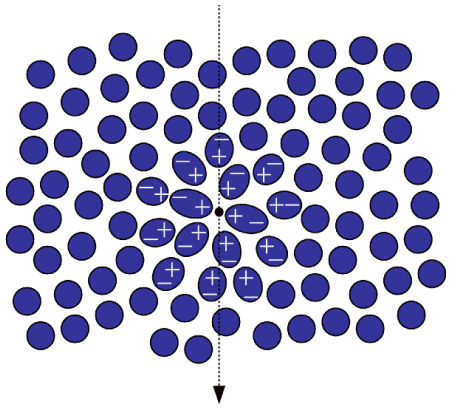

Fig. 2.8 An illustration of the subluminal disturbance (induced dipoles) caused by the passing of the charged particle through the dielectric medium[3].

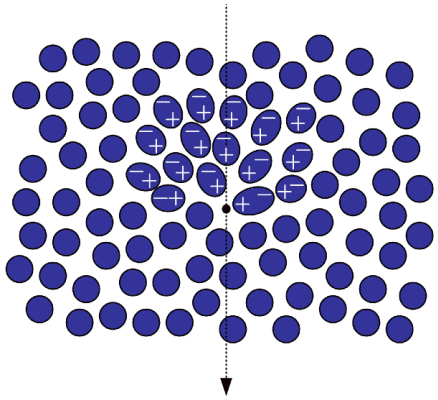

Fig. 2.9 An illustration of the superluminal disturbance caused by the passing of the charged particle through the dielectric medium[4].

In Figure 2.10 the charged particle, represented by a red arrow, travels through the dielectric medium with speed v_p such that $\frac{c}{n} < v_p < c$, where c is speed of light in vacuum, and n is the refractive index of the medium. The ratio between the speed of the charged

[3]http://mxp.physics.umn.edu/s04/projects/s04cherenkov/theory.html
[4]http://mxp.physics.umn.edu/s04/projects/s04cherenkov/theory.html

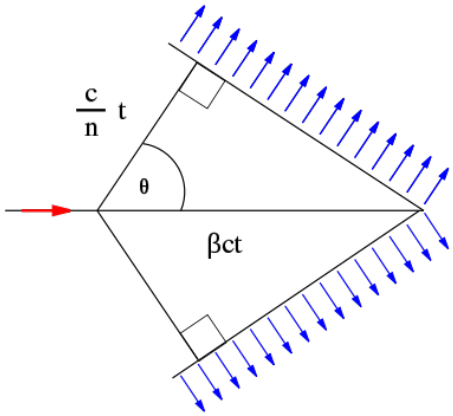

Fig. 2.10 An illustration of the emission angle of Cherenkov photons from a charged particle in a non-dispersion medium. The blue arrows represent the Cherenkov photons emitted [5].

particle and the speed of light in a vacuum is given as $\beta = \frac{v_p}{c}$. The emitted light waves, represented by blue arrows, travel at a speed $v_{\text{em}} = \frac{c}{n}$. From trigonometry it can be deduced that the angle θ is

$$\cos\theta = \frac{1}{n\beta} \tag{2.10}$$

The above theory is deduced for a non-dispersive medium, that is, one whose index of refraction n is not a function of energy. In reality, n_λ will be wavelength dependent. When the particle velocity drops below the local speed of light in the dielectric medium, Cherenkov photons are no longer emitted. At that particle velocity (β_{min}), the Cherenkov light cone disappears

$$\beta_{min} = \frac{1}{n_\lambda} \tag{2.11}$$

This can be translated into an energy threshold, E_{th}, for production of Cherenkov light by the particle

$$E_{th} = \frac{m_o\, c^2}{\sqrt{1-\beta_{min}^2}} = \frac{m_o\, c^2}{\sqrt{1-n_\lambda^{-2}}} \tag{2.12}$$

where m_o is the particle rest mass.

[5] https://en.wikipedia.org/wiki/Cherenkov-radiation

The Frank–Tamm formula [Frank and Tamm, 1937], governs the Cherenkov emission at a given frequency as a charged particle moves through a medium at velocity v_p. The energy dE emitted per unit length travelled by the particle per unit of frequency $d\omega$ is

$$\frac{dE}{dx\,d\omega} = \frac{q^2}{4\pi}\mu_\omega\omega\left(1 - \frac{c^2}{v_p^2 n_\omega^2}\right) \tag{2.13}$$

provided that $\beta = \frac{v_p}{c} > \frac{1}{n_\omega}$. Here μ_ω and n_ω are the permeability and index of refraction (dispersive) of the medium at fequency ω Hz, q is the electric charge of the particle, v_p is the speed of the particle.

Cherenkov radiation is a continuous emission and does not have spectral peaks, as is found for fluorescence or emission spectra. The relative intensity of one frequency is approximately proportional to the frequency. That is, higher frequencies are more intense in Cherenkov radiation.

The total amount of energy radiated per unit length is important to quantify, as it is proportional to the Cherenkov light arriving at the VERITAS telescope from an EAS. This is derived by the Frank-Tamm formula, where the integral is over the frequencies ω for which the particle's speed v_p is greater than the speed of light in the medium. This integral is convergent (finite) because at high frequencies the refractive index becomes less than unity and for extremely high frequencies it becomes unity

$$\frac{dE}{dx} = \frac{q^2}{4\pi}\int_{v_\mathrm{p} > \frac{c}{n\omega}} \mu_\omega\omega\left(1 - \frac{c^2}{v_\mathrm{p}^2 n_\omega^2}\right) d\omega \tag{2.14}$$

The number of Cherenkov photons emitted by a charged particle [Frank and Tamm, 1937], per unit path length and per unit energy (or wavelength λ) interval of the photons is equal to

$$\frac{dN^2}{dx\,d\lambda} = \frac{2\pi\varepsilon}{\lambda^2}\left(1 - \frac{1}{\beta^2 n_\lambda^2}\right) \tag{2.15}$$

where ε is the fine structure constant = $\frac{e^2}{\hbar c} = \frac{1}{137}$ and n_λ is the refractive index as a function of wavelength.

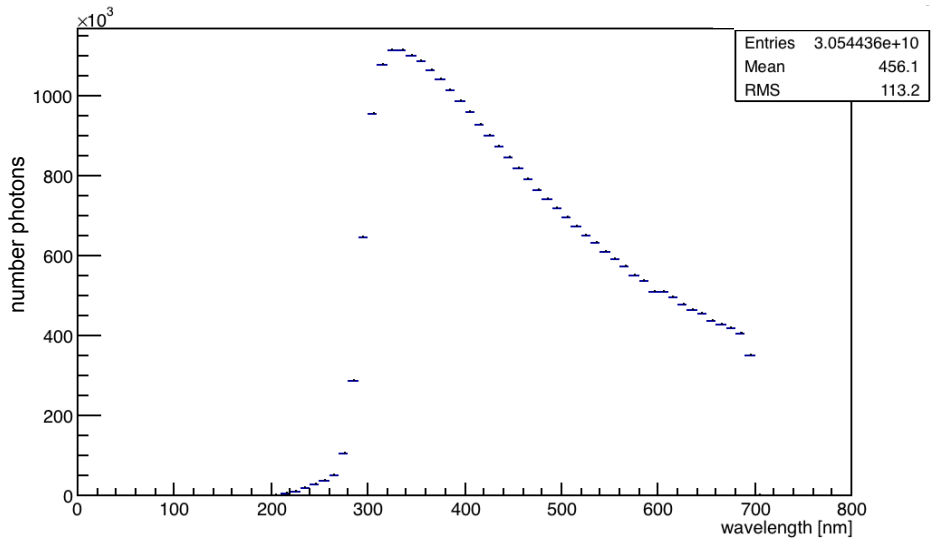

Fig. 2.11 A 1D histogram of the wavelength of Cherenkov photons from 1000 simulated 1 TeV γ-ray showers from zenith during normal atmospheric conditions at the VERITAS site. The peak λ = 330 nm, while the mean λ = 456 nm. The wavelength binning is 10 nm.

For the particular case of an electron moving along a track of length l within a spectral region bounded by wavelengths λ_1 and λ_2, the total number of Cherenkov photons, N, produced is

$$N = 2\,\pi\,\varepsilon\,l\left(\frac{1}{\lambda_2}-\frac{1}{\lambda_1}\right)\left(1-\frac{1}{\beta^2\,n_\lambda^2}\right) \tag{2.16}$$

The greater part of Cherenkov photons are emitted in the ultraviolet range, because $\frac{dN^2}{dx\,d\lambda} \propto \frac{1}{\lambda^2}$, and the spectrum has a peak at around 330 nm before O_3 extinction. However, due to the sharp O_3 cut-off, the average wavelength is ∼450 nm, as can be seen in a simulation of 1000 × 1 TeV γ-rays in Figure 2.11. From Equation 2.16, it can be seen that the more energetic the electron or positron, the more photons are produced. Similarly an increase in the refractive index will likewise produce more Cherenkov photons.

The Cherenkov yield from both electromagnetic and hadronic showers will be examined in greater detail in Chapter 5.

2.3 An introduction to Earths atmosphere

An atmosphere is a layer of gases surrounding a planet (or another body of sufficient mass to prevent gases from escaping to space), that is held in place by gravity. For smaller planetary bodies a strong magnetic field called a magnetosphere will also aid atmosphere retention. This is because charged solar particles, from solar winds and coronal mass ejections principally, can impart sufficient kinetic energy for the individual atmospheric molecules to escape a smaller planet's gravity [Axford, 1962, Russell, 2000]. The Earth's magnetosphere will also place a lower limit on the energy of charged particles that arrive at the upper atmosphere.

At any place within its defined outer limits an atmosphere will exert a pressure. The atmospheric pressure is the force per unit area that is applied perpendicularly to a surface by the surrounding gas. It is determined by a planet's mass in combination with the total mass of the perpendicular column of gas. This pressure determines the density of molecules per unit volume at a given point, which affects the refractive index n_λ of the atmosphere at that point and also the radiation length X_0 and hence shower depth X_{sd} achievable for that columnar air volume (derived by Equation 2.4).

By volume, dry air contains 78.09% nitrogen, 20.95% oxygen, 0.93% argon, 0.04% carbon dioxide, and small amounts of other gases. Air also contains a variable amount of water vapour, on average around 1% at sea level, and 0.4% over the entire atmosphere [Ramanathan et al., 2001]. The atmosphere of Earth has a mass of about 5.15×10^{18} kg, three quarters of which is within $\sim$11 km of its surface.

Figure 2.12 shows a photograph of a section of Earth's atmosphere taken from the International Space Station, where its thickness can be referenced against the radius of Earth. The density of air at sea level is $\sim$1.2 kg m^{-3}. This density of air molecules shields living organisms from many harmful radiation bands of the electromagnetic spectrum in addition to dangerous cosmic rays below $\sim 10^{15}$ eV.

Fig. 2.12 A photograph of a section of Earths atmosphere taken from a low Earth orbit ∼250 km a.s.l. Taking 100 km as the atmosphere's outer limit, this equates to ∼1.5% of Earth's radius [6].

Figure 2.13 shows an illustration of Earth's transparency windows for various electromagnetic bands. This thesis will focus on the transmission properties of electromagnetic radiation through Earth's atmosphere, namely in the UV / optical / IR bands, by means of radiative transfer simulation code. It will examine each of the principal components, absorption, emission, and scattering processes, in varying detail. As this thesis is principally concerned with elastic processes, suitable approximations allow simplified atmospheric transmittance calculations to suffice. Transmittance will thus be governed by the Beer-Lambert law, which was developed in the 18^{th} century [Bouguer, 1729, Klett et al., 1760]. It states that the transmittance, T, of a material sample is related to its optical depth, τ, and to its absorbance, A, by

$$T = \frac{\Phi_e^t}{\Phi_e^i} = e^{-\tau} = 10^{-A} \tag{2.17}$$

[6] https://www.grc.nasa.gov/www/k-12/airplane/atmosphere.html

where Φ_e^t is the radiant flux transmitted by that material sample and Φ_e^i is the radiant flux received by that material sample.

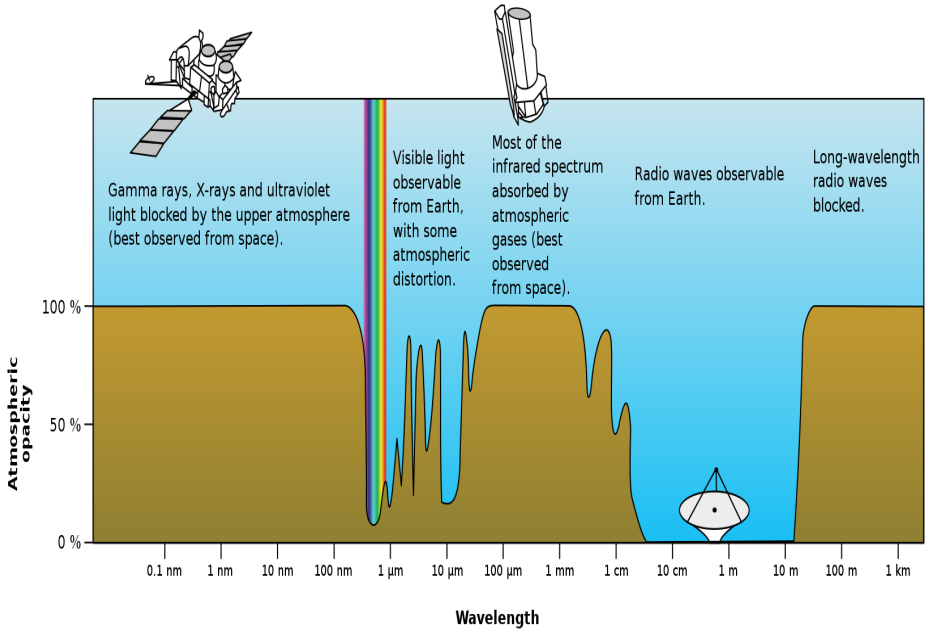

Fig. 2.13 A graphic of the atmospheric opacity of Earth's atmosphere, showing transmission windows for the visible and radio parts of the electromagnetic spectrum. [7].

2.3.1 Light scattering

The interaction of photons with matter may be thought of as scattering of light through varying angles and intensities. For this section, the ideal case of elastic scattering alone will be examined, with no change in polarisation and no line absorption. As the photons encounter the matter particles, the oscillating electric fields of the photons induce an oscillating dipole-moment in the electron lobes (the probability space inhabited by the electrons) as illustrated in Figure 2.14. These oscillating induced dipoles themselves re-radiate electromagnetic radiation elastically, which then induce more oscillating dipole-moments in further electron lobes of the next incident particles, and so on the wave propagation continues. Elastic refers to stringent conservation of energy being observed, which implies that the oscillating dipole-

[7] http://gisgeography.com/atmospheric-window/

induction and subsequent re-radiation is of the same frequency as the initial incident photon. This idealised example outlined holds for only certain cases. To better understand the wider situations encountered in light scattering, an estimation of the effective cross section of the scattering particle must be determined.

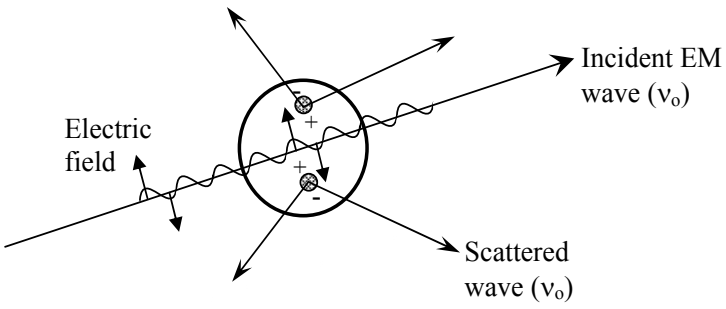

Fig. 2.14 A graphic of the induced dipole moment in a particle from an incident electromagnetic wave. The dipole oscillates at the same frequency as the photon in elastic scattering. Taken from Hahn [2006].

The size of a scattering particle, more accurately referred to as a size parameter, x, is expressed by the ratio

$$x = \frac{2\pi r}{\lambda} \tag{2.18}$$

where r is its characteristic length (or radius if the particle is quasi-circular) and λ is the wavelength of the incident light. The size parameter provides a way to determine which type of scattering will dominate for a particular situation. Objects with $x \gg 1$ scatter light according to their geometric shape, that is reflection off of their incident surface. This is often called non-selective scattering, as it is wavelength independent. At $x \cong 1$, Mie scattering dominates, where interference effects develop through phase variations over the object's surface. Rayleigh scattering applies to the case when the scattering particle is very small, that is $x \ll 1$, with a particle size $< \frac{1}{10}$ the wavelength. In this case, the whole surface re-radiates with the same phase. Both Mie and Rayleigh scattering will be discussed in the next sections.

For the work presented in this thesis, the following scattering mechanisms are applied to

atmospheric simulations at VERITAS as follows;

- in cases where $x \ll 1$, such as molecular scattering, Rayleigh scattering is employed by radiative transfer code to model Cherenkov transmittance through air molecules.

- in cases where $x \cong 1$, such as the presence of desert dusts, Mie scattering is employed by radiative transfer code. Additionally, use is made of the Beer-Lambert approximation where $\tau \ll 1$, namely $T \approx 1 - A$ (introduced in Equation 4.8), to model the transmittance of Cherenkov light through the atmosphere. This is possible due to single scattering alone being estimated for aerosol scattering [Eck et al., 1999].

- in cases where $x \gg 1$, such as water droplets due to clouds, no scattering modelling is applied as telescope data taken during these episodes will be rejected. This is because the high scattering cross section of such water droplets greatly increases atmospheric extinction in comparison to aerosol dust particles or air molecules. Secondly, highly volatile cloud morphology makes extinction profile modelling very difficult if not impossible to achieve.

As the Cherenkov imaging technique is an atmospheric technique that observes the Cherenkov photons that result from EAS, it requires not only an in-depth understanding of the interactions of cosmic rays and VHE γ-rays with the atmosphere, but also an in-depth understanding of the transmission of the resulting UV and optical photons that are detected by VERITAS. As the atmosphere is a multivariate environment, its principal components are described in turn, the molecular, particulate and water vapour. This is so that the transmission properties of electromagnetic radiation, and more specifically Cherenkov radiation, may be better understood.

2.4 The molecular atmosphere and Rayleigh scattering

Rayleigh scattering, named after Lord Rayleigh, formally John William Strutt, is the elastic scattering of electromagnetic radiation by particles much smaller than the wavelength of the radiation. Rayleigh scattering is a parametric process, implying there can be no net transfer of energy, momentum, or angular momentum between the optical field and the physical system.

2.4.1 A brief historical perspective

Lord Rayleigh's original paper [Rayleigh, 1871] was intended to show that the blue sky could be explained as scattering of light by small particles. The development of his scattering theory in this paper was done entirely on the basis of elastic-solid theory of the luminiferous ether [Thomson, 1888]. In a later paper [Rayleigh, 1881], Rayleigh re-derived the same results from the electromagnetic theory. It was not until almost 30 years after the original 1871 paper [Rayleigh, 1899], that Rayleigh concluded that the molecules of air alone would suffice to explain the blue sky, as well as the refractivity of air.

2.4.2 Details of molecular scattering

The Rayleigh scattering cross-section per molecule, $\sigma_{s_{(\lambda)}}$, [Bucholtz, 1995], which takes account of molecular anisotropy and is a function of wavelength is

$$\sigma_{s_{(\lambda)}} = \frac{24\pi^3}{\lambda^4 N_s^2} \frac{\left(n_s^2-1\right)^2}{\left(n_s^2+2\right)^2} \left(\frac{6+3\rho_n}{6-7\rho_n}\right) \tag{2.19}$$

where 'standard' air is assumed, defined as dry air with 0.03% CO_2 per volume at pressure 1013 mb and temperature 15 °C [Penndorf, 1957]. The terms of Equation 2.19 are as follows; λ is the wavelength (in cm), n_s is the refractive index for standard air, N_s is the molecular number density (2.54743×10^{19} cm^{-3}) and ρ_n accounts for the anisotropy of the

air molecule, which is a function of wavelength.

The amount of incident light travelling through a volume of standard air that will be scattered is readily calculated with the above information. It may be referred to as molecular extinction, α_{mol}, and is simply the number of particles per unit volume, N_s, times the Rayleigh scattering cross-section per molecule, $\sigma_{s_{(\lambda)}}$. As the molecular number density will be a function of pressure, which is a function of height, z, the molecular extinction $\alpha_{mol_{(\lambda,z)}}$ may be written as

$$\alpha_{mol_{(\lambda,z)}} = N_{(\lambda,z)}\, \sigma_{s_{(\lambda)}} \tag{2.20}$$

and the total molecular optical depth between heights z_1 and z_2, is defined as

$$\tau_{mol_{(\lambda,z)}} = \int_{z_1}^{z_2} \alpha_{mol_{(\lambda,z)}} dz \tag{2.21}$$

Nitrogen has a Rayleigh cross-section of 5.1×10^{-27} cm^2 at a wavelength of 532 nm (green light). This means that with $\sim 2 \times 10^{19}$ molecules cm^{-3}, about one part in 10^5 of the light will be scattered for every metre of travel. The strong wavelength dependence of the scattering ($\sim \lambda^{-4}$) means that shorter (blue) wavelengths are scattered more strongly than longer (red) wavelengths.

The angular distribution of the scattered light for an angle θ [Chandrasekhar, 1960], which again takes account of molecular anisotropy is described by the Rayleigh phase function

$$P_{ray\,\theta} = \frac{3}{4\left(1+2\gamma_\theta\right)} \left((1+3\gamma_\theta) + (1-\gamma_\theta) cos^2\,\theta \right) \tag{2.22}$$

where γ_θ is defined as

$$\gamma_\theta = \frac{\rho_n}{2-\rho_n} \tag{2.23}$$

The charge distribution anisotropy, accounted for by ρ_n, within the electron probability space has considerable impart on the scattering phase function. This is simplified by air being composed principally of two diatomic molecules. As the molecular number density

for Earths atmosphere is so large, all Rayleigh scattering will be multiple scattering and will therefore greatly impact on $P_{ray\,\theta}$, even over very short distances.

2.4.3 Refractive index

The refractive index, n, is critical to Cherenkov light production. There is an apparent change in the speed of light passing through a medium of differing refractive index, given by $v = \frac{c}{n}$.

The refractive index n [Feynman et al., 1965] is

$$n = 1 + \frac{N q_e^2}{2\,\varepsilon_0 m(\omega_0^2 - \omega^2)} \tag{2.24}$$

Where N is the number of charged electrons per unit volume, ε_0 is the absolute permittivity and ω is the frequency of light and ω_0 the natural oscillation frequency. The index of refraction is seen to be frequency dependent, which is called dispersive (as displayed in Figure 2.15). For simple structure gases, of less that 3 to 4 constituent atoms, ω_0 is close to ultraviolet; therefore, ω_0^2 dominates making the refractive index nearly constant from near-UV and longer wavelengths thereafter. As ω increases past the near UV n becomes more dispersive. As $\omega \rightarrow \omega_0$, the refractive index greatly increases.

To finalise the refractive index expression, two further additions will be required. Firstly, there needs to be a damping term for the induced oscillations. Secondly, a number of differing oscillators need to be accounted for (as air is made of various gases with their unique response to oscillating electric fields). The final equation for refractive index is now

$$n = 1 + \frac{q_e^2}{2\varepsilon_0\, m} \sum_k \frac{N_k}{\omega_k^2 - \omega^2 + i\gamma_k\omega} \tag{2.25}$$

where k represents the individual molecular / atomic oscillators, ω_k is the natural frequency with damping and γ_k is the damping factor. The introduction of damping into the refractive index formula makes n a complex number; thus the correct way to refer to refractive index

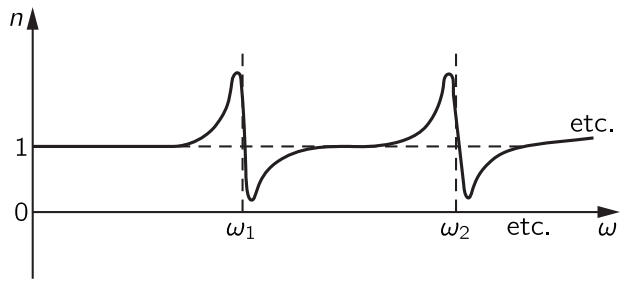

Fig. 2.15 A plot showing the refractive index n as a function of frequency ω. Damping has been incorporated. Taken from Feynman et al. [1965].

is

$$n = n_{real} - i n_{comp} \tag{2.26}$$

where n_{real}, representing the elastic component, and n_{comp}, representing the attenuation component, are both positive integers. For visible light and radio-waves in our atmosphere, $n_{comp} \ll 1$.

2.5 The particulate component of the atmosphere and Mie scattering

Aerosols are small particles held in suspension in air by Brownian-motion driven buoyancy [Friedlander and Wang, 1966] and thermal and convective mixing processes. They originate from a great variety of sources, for example wildfires, volcanoes, exposed soils and desert sands, breaking waves, natural biological activity, agricultural burning, cement production, and wood/dung/fossil-fuel combustion, among other lesser sources [Chin et al., 2007]. The particles typically having the largest direct environmental impact, by means of local radiative forcing, cloud condensation and pollution factors among others, are sub visible. Radiative forcing refers to the ability of aerosols or gasses to impact on the energy balance of a local air parcel. Aerosol particles are an important part of climatology models. They range in size from 10^2 nm to 10^4 nm and typically remain in suspension from days to more

than a week. Some anthropogenic aerosols, in particular from poorly combusted hydrocarbons called black or brown carbon, are highly light absorbing and may be a considerable component of localised radiative forcing [Andreae and Gelencsér, 2006]. Often aerosols travel great distances, crossing continents at times, before returning to the Earth's surface via gravitational settling or washout by rain. As such, they can affect regions thousands of kilometres from their sources, as witnessed in Western Europe where Sirocco winds bring brown Saharan sands to north Atlantic coasts.

Aerosol particles, in particular those of naturally occurring mineral and organic constituency, reflect sunlight, cooling local ground areas. Carbonaceous particulates often absorb sunlight efficiently, warming and stabilizing the ambient atmosphere as they re-radiate the solar energy absorbed. Aerosols are essential participants in the formation of cloud droplets and ice crystals, functioning as the collectors of water vapour molecules. They are hypothesised to increase the lifetime of clouds where they are found in high concentrations at cloud-formation heights. This is because increased concentrations of smaller droplets lead to decreased drizzle production and reduced precipitation efficiency. In significant near surface concentrations aerosols may be pollutants, reducing visibility and raising health risks for those exposed. In short, they are small particles that have a big impact on our environment. This work focuses its interests on aerosols that frequent the Southwestern United States, and their effects on optical transmittance of the atmosphere.

The Sonoran desert is the most biologically diverse desert on Earth, due to heavy rains for two months of the year which may total up to 350 mm precipitation. The desert dust mix is therefore richer in organic particulates than other very arid regions such as Saharan and Mongolian deserts. There are therefore associated changes in aerosol optical properties and once an aerosol typology is determined, radiative transfer code will account for these transmission properties.

2.5.1 An introduction to Mie theory

The Mie solution to Maxwell's equations, Mie theory or the Lorenz–Mie solution [Mie, 1908], deals with light scattering by homogeneous spherical particles; by homogenous it is meant the sphere's constituent material is uniform and does not have net charge anisotropies. Additions are continually being added to the available Mie calculation codes that introduce spheroidal and other irregular shaped particles [Yang et al., 2007], but do not form part of this thesis. All electric fields and sources of electric fields are assumed to be proportional to the harmonic factor $e^{i\omega t}$, where $i = \sqrt{-1}$, ω is the angular frequency, and t is time.
Mie scattering is a calculation / approximation methodology and not a physical process *per se*. It is based on two principal approximations. First, on continuum electromagnetic theory where an infinite, homogenous elastic medium allows electromagnetic radiation to propagate unhindered and unaltered. Secondly, the homogenous sphere is illuminated by a plane wave infinite in lateral extent, meaning that edge diffraction patterns will not interfere with the scattering by the sphere. These approximations form a perfect wave propagation environment into which the homogenous sphere is now placed. The electric fields in the perfect propagation space are now modified by the sphere, and this modification is called electromagnetic scattering. The difference between the total electric field in the presence of the particle and the original electric field that existed before the particle was introduced can be thought of as the field scattered by the particle. Putting this into a mathematical expression, the resulting electric field is

$$E_{(r)} = Ei_{(r)} + Es_{(r)} \tag{2.27}$$

where $Ei_{(r)}$ is the incident electric field, r is the field vector $\vec{r}$, $Es_{(r)}$ is the scattered electric field. Note that the harmonic factor $e^{i\omega t}$ is omitted [Mishchenko and Travis, 2008]. Calculation of the scattered electric field, $Es_{(r)}$, is non-trivial. The size of the scattering particle is parameterised (as discussed in Equation 2.18), while the scattering phase function is derived

from a seminal study of the diffuse radiation in the Galaxy, called the Henyey-Greenstein phase function [Henyey and Greenstein, 1941].

For a better approximation to reality, a damping factor is included in Mie calculations. This is similar to the factor introduced in Equation 2.25. The index of refraction, m, of a sphere in Mie theory is given as;

$$m = n\big(1 - i\,k\big) \tag{2.28}$$

where the the real refractive index is n and the complex refractive index, nk, is the damping factor while k is called the index of attenuation.

Finally, it is safe to assume that all Mie scattering will be single scattering, due to the low particle density (and corresponding low total particle cross-section) in a volume of air. Aerosol number density is of the order of $\sim 10^1$ to $\sim 10^2$ cm^{-3}, with an average diameter (for desert dusts) of $\sim 10^2$ to $\sim 10^3$ nm.

2.6 The water component of the atmosphere and absorption

The hydrosphere, the water component of Earth, is composed of ice / permafrost (solid), water (liquid) and water vapour (gas). Water vapour is replenished in the atmosphere by either evapouration or sublimation and removed by precipitation arising from condensation onto cloud condensation nuclei. Unlike other forms of water, it is invisible or colourless to the visible region of the electromagnetic spectrum. However, water vapour has strong absorption bands, particularly in the infrared. This makes it a a potent greenhouse gas along with other gases such as carbon dioxide and methane. Water vapour is the most volatile component of the atmosphere, where H_2O concentrations may vary from $0.4-1.0\%$ of the total atmosphere (as related in Section 2.3).

At the same temperature, a column of dry air will be denser or heavier than a column of air containing any water vapour, as the molar masses of diatomic nitrogen and diatomic oxygen are greater than the molar mass of water. The density of dry air (relative humidity

$= 0\%$) referred to as $\rho_{0\%}$, at 20 °C and 1 atm pressure is 1.205 kg m^{-3}. Holding the same temperature and pressure, but varying the relative humidity we have; $\rho_{25\%} = 1.202$ kg m^{-3}, $\rho_{50\%} = 1.199$ kg m^{-3} and $\rho_{100\%} = 1.194$ kg m^{-3}. Water vapour will thus have a vertical profile that must be accounted for in radiative transfer calculations, should a wavelength in a water absorption band be present. Cherenkov radiation, a continuous emission from 300-700 nm (as seen in Figure 2.11) is not impacted on by water vapour absorption. However, atmospheric sensing equipment that operate in the infrared, both remote and *in situ*, will be [Bernath, 2002]. Considerable effort will be given to correcting for this absorption in Chapter 4. Figure 2.16 shows radiative transfer code simulations of the vertical atmospheric transmittance in the wavelength range 700-1020 nm. The code used (MODTRAN) is to be discussed in detail in Chapters 3, 4 and 5. The simulation is for a midlatitude summer atmosphere with normal loading aerosol extinction for the mid-Western United States. The most sensitive changes in transmission to water vapor content occur around 940 nm.

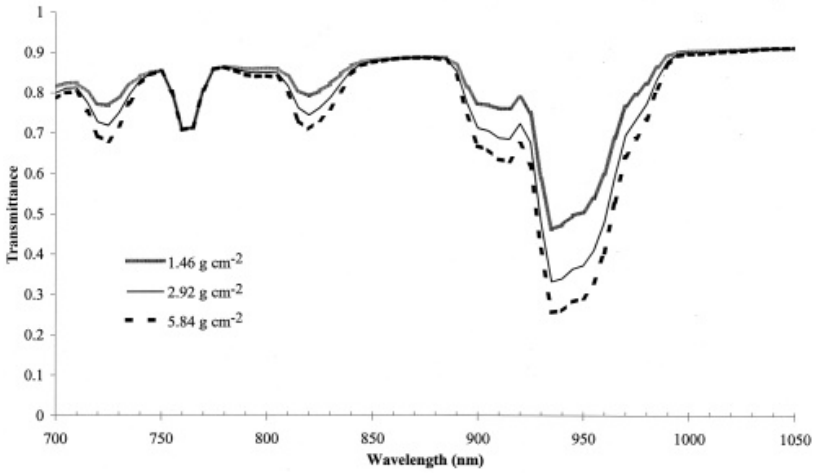

Fig. 2.16 A radiative transfer simulation for a midlatitude summer atmosphere of normal aerosol extinction for the mid-Western United States. Three separate water vapour concentrations are used, 14.6, 29.2 and 58.4 mm of precipitable water. Precipitable water refers to the total amount of water in a columnar volume of air, measured in mm at the base of the column or g cm^{-2} where 10 mm = 1.0 g cm^{-2}. Taken from Barducci et al. [2004].

2.7 Dynamical forces and changes in transmission properties

As well as being an environment with many constituent elements (molecular, particulate and hydrological), the atmosphere is highly dynamic. Massive amounts of solar energy heat the atmosphere and, along with planetary rotational energies and some lesser tidal effects from the Moon and Sun, cause global convective flows that move huge air parcels across continents. These air mass trajectories are modelled by the National Oceanic and Atmospheric Administration (NOAA) HYSPLIT model (he Hybrid Single Particle Lagrangian Integrated Trajectory Model). It computes air parcel trajectories and dispersion or deposition of atmospheric pollutants [Stein et al., 2015]. The principal causes of these air mass movements are now listed.

Firstly, latitudinal circulation is driven by the differences in solar radiation per unit area between the heat equator and the poles. The main convection cells produced, regions of differing air densities that seek equilibrium by air mass movement, are the Hadley cell and the polar vortex [Huang and McElroy, 2014].

Secondly, longitudinal circulation occurs due the differing thermal properties between sea and land. The ocean has a higher specific heat capacity and thermal conductivity than land, therefore it absorbs and releases more energy during the solar day. However, the sea temperature changes less than land. This brings the sea breeze and land breezes that operate diurnally. Longitudinal circulation consists of two cells, the Walker circulation and El Niño/Southern Oscillation [Xie, 1998].

It is noted that air mass trajectories may carry differing aerosol species with unique optical properties to the Southwestern United States, sometimes from distant continents. It is also be noted that a region specific moist air mass trajectory from the Gulf of Mexico reaches the Southwestern United States in July and August, bringing heavy downpours and prolonged cloudy periods.

2.8 The need for a study on aerosol extinction and VHE γ-ray detection

This chapter has looked at the properties of EAS and the constituent elements of the atmosphere that will impact on the production then propagation of the subsequent Cherenkov light through it. The following questions seem important to ask. What indications are there that the volatile aerosol extinction profile is impacting on the Cherenkov imaging technique? Can the extinction profile be estimated with sufficient accuracy with the current instrumentation on site? What systematic uncertainties will be most susceptible to varying aerosol loading?

For the first question, EAS simulations have been carried out with varying aerosol extinction to ascertain how the Cherenkov imaging technique will be affected. However, a reliable method of aerosol extinction profiling has not been implemented at VERITAS prior to this thesis, meaning the simulations can not be directly related to VERITAS data taken during episodic aerosol loading. For the second question, very expensive ($\sim 10^6$) Raman inelastic lidars [Ansmann et al., 1990], which operate lasers at 355nm and 532nm wavelength, can accurately determine the relevant atmospheric information by backscatter retrieval. However, VERITAS data taking will not be possible during its operation as the lidar lasers operates in the Cherenkov emission band. A remote sensing instrument with a laser wavelength outside the Cherenkov light band is ideally required. The qualifying and quantifying of the systematic uncertainties is also of considerable importance, presently introduced.

2.8.1 Assessing the atmospheric systematic uncertainties involved in VHE γ-ray detection

There will always be an inherent uncertainty present in real world measurements. These uncertainties are both statistical, deriving from normal fluctuations, and systematic, deriving from a bias in the instrumentation or experiment parameter space. The statistical uncertain-

ties normally follow a Gaussian distribution quite well (apart from counting experiments where a Poisson distribution is a better fit); more data readings will often reduce the mean uncertainty. The systematic uncertainties are more skewed, such that extra data readings will not reduce the mean uncertainty. Often they are modelled on Gaussian distributions too, though it is a poor approximation. Both uncertainties should be quoted separately.
For the work in this thesis, the systematic uncertainties involved in analysis of a VERITAS data set from 2013 will be calculated in Chapter 6 both for the official or standard aerosol loading estimate, and the updated measured aerosol loading estimate, soon to be introduced in Chapter 4.

2.9 Preparatory work for an aerosol loading analysis

Chapter 3 details the instrumentation initially used to monitor the atmosphere on site prior to this thesis. It will present data from these monitoring campaigns and also from regional studies by dedicated atmospheric physicists.

Chapter 3

The VERITAS experiment and atmospheric monitoring

3.1 The atmosphere at VERITAS

The Cherenkov imaging technique separates VHE γ-rays from the hadronic background and source localises, energy bins and plots spectra for analysis. It relies on the atmosphere as its main detection medium. Therefore, constant monitoring of the atmospheres relevant properties is essential. These relevant properties relate to the production of Cherenkov light, governed by the refractive index mainly, and the transmission of Cherenkov light to the telescopes, governed by Rayleigh and Mie scattering. This chapter outlines the atmospheric monitoring undertaken from when full VERITAS operations began in 2007 up to work presented in this thesis. It is not an exhaustive survey, but an overview aimed at explaining the motivating factors that led to this thesis. The principal concern, in the past as now at present, is passing cloud in the telescope field of view [Sobczyńska and Bednarek, 2014]. Only cloud-free skies are suitable for detailed science at VERITAS; partially cloudy skies offer opportunity to monitor highly variable VHE γ-ray sources for elevated activity. The impact of aerosols on the atmospheres optical transmittance for Cherenkov light was, in

general, poorly understood and seldom referred to until recently (Fruck and Gaug [2015], Daniel et al. [2015]). A dedicated weather station on site is used for safety reasons alone and its data do not enter the VERITAS analysis chain. For example, wind speed is monitored because the very large telescope mirror area may be caught like a sail with resulting damage to the telescope drives. Humidity is monitored to ensure that no electrical arcing happens at high voltages applied to the telescope cameras. Ambient air temperature on site is recorded also to ensure that the cooling systems for the power-hungry telescope electronics are not overloaded.

This thesis studies principally the particulate component of the atmosphere, however the molecular component is also addressed. The molecular atmosphere, 78% Nitrogen, 20% Oxygen and various other gases, has a constituent number density sixteen orders of magnitude greater than the particulate component. A 1 cm^3 volume of air may contain 10^{18} air molecules and only 10^2 aerosol particles; the particles are however of greater size and hence scattering cross section. The principal means of determining properties of the molecular atmosphere important for EAS development is by use of radiosonde data [Abreu et al., 2012]. As the molecular atmosphere at a site close to VERITAS has been studied previously with this data and been found to be quite stable [Daniel, 2008], a brief introduction alone is given to it. To detect passing cloud, three infrared radiometers are employed on site. One radiometer is fixed, pointing north at 15° from zenith, while the other two are attached to telescope optical support structures and monitor the area of sky that VERITAS observes at any given moment. Finally, the telescope triggering rate may be used for rudimentary atmospheric monitoring, for cloud detection and possibly for detection of aerosol layers. Each of these three instruments, radiosonde, radiometer and the VERITAS telescope, will now be examined in more detail.

The following should be noted to assist in reading this thesis. The preferred timestamp for all plots is Modified Julian Date (MJD), while at times the user-friendly (yyyy-mm-dd) timestamp may accompany MJD where helpful. Source elevation is stated in degrees

(°) from zenith, in keeping with the system that will be used in later chapters for EAS simulations. Further, the reader is assumed to be familiar with 2D histograms, which are extensively used in this work. All frequency sidebars represent counts per bin alone and are not weighted unless otherwise stated.

3.2 Tucson radiosonde data

A radiosonde transmits temperature, pressure and humidity readings from a weather balloon that is automated to ascend and descend 25-30 km over a fixed time. These profiles may then be used to produce useful data products such as atmospheric density (the amount of gas in a given volume) [Nee, 1964], among others. Nightly balloon launches from Tucson Airport, Arizona, were carried out from 1956 to June 4, 2007; since 2007 launches are from the University of Arizona campus in Tucson. Twice a day, at 00:00 hr and 12:00 hr UTC, radiosonde measurements are taken from this site (station number 72274) about 60 km north of VERITAS. These readings, taken close to the start and end of normal nightly telescope operations, allow construction of density height profiles of the atmosphere relevant to the VERITAS experiment. In particular, it allows the atmospheric density at height to be used to estimate the refractive index height profile. It is reasonable to ask if the Tucson data from 60 km distance is representative of the atmosphere at VERITAS. Interpolating radiosonde data between fixed stations separated by several hundred kilometres to a high degree of accuracy ($\sim$1-2%) has proven consistent over mid-latitude regions such as the VERITAS site. The Integrated Global Radiosonde Archive [Durre et al., 2006], consists of radiosonde and pilot balloon observations taken at over 1,500 globally distributed stations. The variables measured include pressure, temperature, geopotential height (the height a.s.l. of a particular atmospheric pressure), dew point depression (the difference between the air temperature and dew point temperature at a certain height), wind direction, and wind speed. These data sets are interpolated onto a global grid (co-ordinate) system meaning that most

places in the world may have access to site-specific radiosonde data to the high accuracies mentioned. As this dataset provides an accurate reference, it is safe to take the Tucson radiosonde data without correction for atmospheric density measurements at VERITAS in the absence of sizable discrepancies. Finally, a cross check is possible with the Global Land Data Assimilation System (GLDAS) [Rodell et al., 2004], which is an uncoupled land surface modeling system producing several models by integrating observation-based data. It runs globally at high resolution ($0.25^\circ \times 0.25^\circ$), with results in near–real time ($\sim$48 hours).

3.2.1 Atmospheric density and refractive index

Air density, or atmospheric density, is the mass of air per unit of volume it occupies, and it is expressed in kg m^{-3}. ρ_z (the atmospheric density at height z) is given by

$$\rho_z = \left(\frac{P_z}{R_d \cdot T}\right) \cdot \left(1 - \frac{0.378 \cdot P_v}{P_z}\right) \tag{3.1}$$

where P_z is the pressure in pascals at height z and R_d, the gas constant for dry air, is 287 J kg^{-1} K^{-1}. It is derived from the universal or ideal gas constant divided by the molecular weight of the gas in question. T the temperature in kelvin and P_v the pressure of water vapour in pascals.

The refractive index of air, n_{air}, the ratio of the speed of light in air, v, to the speed of light in a vacuum, c, is a complicated function of pressure, temperature, water vapour content and wavelength (as described in Section 2.4.3). It can however be approximated as being proportional to the air density [Bernlöhr, 2000, Berhlohr, 2008].

$$n_{air} = \frac{v}{c} \propto \rho_z \tag{3.2}$$

Thus, an accurate estimation of atmospheric density with height for a particular time (telescope operation) is essential. This is because the amount of Cherenkov light produced by electrons and positrons is a function of n_{air} (seen in Equation 2.16). It would be most ad-

vantageous to group a spread of differing density profiles into seasons; this would allow a small number of particular seasons to define the atmospheric density throughout the year. Analysis of radiosonde data over many years is required for this. It would also be advantageous to match the defined seasons, where possible, with standard atmospheric seasons that may be found in radiative transfer simulations of the atmosphere. This would allow gaps in radiosonde data (usually at heights above 25-30 km a.s.l.) to be replaced by these standard atmospheres.

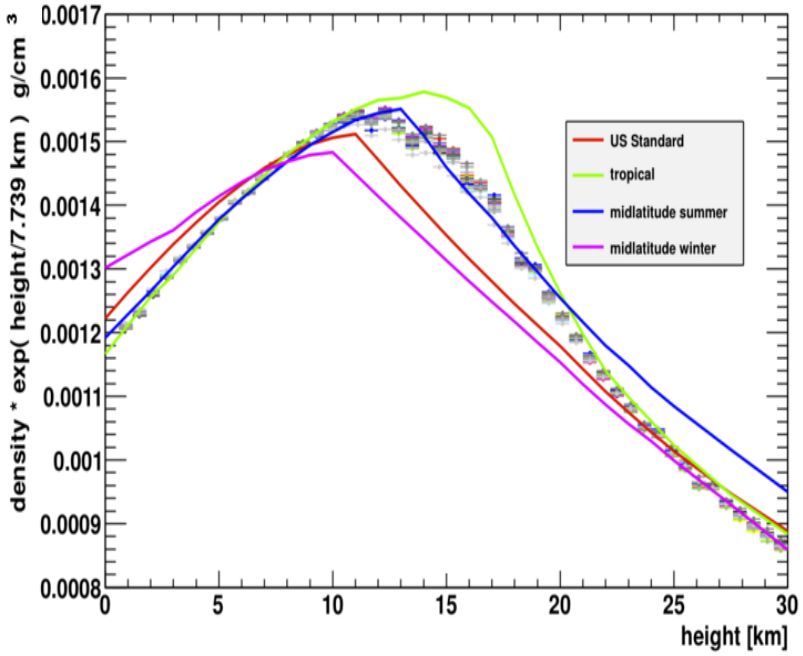

Fig. 3.1 A log-lin scatterplot of scaled atmospheric density (averaged yearly) as a function of height for Tucson radiosonde data from 1995-2010 (from Tucson airport site up to 2007). The lack of a closely matching atmospheric model below 25 km a.s.l. necessitates a user-defined atmosphere. Refer to Appendix A for details. (Private correspondance, G.Maier).

From ongoing examination of over 20 years of Tuscon radiosonde station 72274 archival data, it is noted that none of the available atmospheric models from MODTRAN [Berk et al., 1998], a radiative transfer code used by the astroparticle community and discussed in detail in Section 3.6, can be said to accurately reconstruct the density profile across the entire year [Daniel, 2008]. Figure 3.1 shows 15 years of Tucson radiosonde-derived data, where the

y-axis is log of density normalised and the x-axis for height a.s.l. The atmospheric scaling density factor used, $\frac{height a.s.l.}{7.739km}$, represents an upper limit for shower depth for the majority of γ-rays detected (defined in Equation 2.4), and equates to progenitor γ-ray energy of $\sim$5 TeV. In the region of greatest interest for the production of Cherenkov light (10 to 20 km a.s.l., the shower depth for most VHE γ-ray sources) the spread in atmospheric density readings is somewhat (poorly) approximated by the mid-latitude winter and the mid-latitude summer profiles found in MODTRAN. For better accuracy, a user-defined molecular profile is constructed for heights up to 25 km a.s.l., using the above-mentioned Tucson radiosonde density profiles. Above this height, the built-in MODTRAN models (mid-latitude winter and summer) are used. The procedure is explained in Appendix A.

VWinter start - MJD (yyyy-mm-dd)	*VSummer start - MJD (yyyy-mm-dd)*
54048 (2006-11-09)	54255 (2007-06-04)
54428 (2007-11-24)	54605 (2008-05-19)
54782 (2008-11-12)	54988 (2009-06-06)
55137 (2009-11-02)	55343 (2010-05-27)
55520 (2010-11-20)	55697 (2011-05-16)
55875 (2011-11-10)	56052 (2012-05-05)
56229 (2012-10-29)	56435 (2013-05-23)
56613 (2013-11-17)	56790 (2014-05-13)
56969 (2014-11-08)	57174 (2015-06-01)
57322 (2015-10-27)	57529 (2016-05-21)

Table 3.1 Dates for the start of the two VERITAS observing seasons, in MJD (yyyy-mm-dd) format. Seasonal changes in atmospheric density necessitate the use of two particular atmospheres, VSummer and VWinter, with corresponding changeover dates derived from radiosonde density profiles. Over the ten year period shown, the start dates for VWinter and VSummer vary by $\pm$2 weeks.

VERITAS has adopted a two-season approach, hereafter referred to as VERITAS winter

(VWinter) and VERITAS summer (VSummer), in line with MODTRAN standard atmospheric models. VWinter and VSummer are observing seasons, linked to atmospheric optical properties and not climatology. To estimate when season transition occurs, one firstly plots the average scaled density (seen in Figure 3.1) divided by average temperature for a particular height bin over a month, remembering that 'month' refers to observing months that are dictated by lunar phases, and are not calendar months. This plot is then examined as a function of the relative differences to VERITAS seasons, VSummer and VWinter atmospheres. When the plot trend is best defined by a different season that the previous months season, the transition point is taken as mid-way through that transitional observing month. The season changeover is better defined some years more than others, and is not an exact science. The density profile changeover date varies year on year and it presented in Table 3.1.

3.2.2 Precipitable Water Volume (PWV) measurements

During July and August each year, hereafter referred to as summer-downtime, strong airmass trajectories carry moisture-rich air over the VERITAS site from the Gulf of Mexico, necessitating the cessation of operations. Precipitable water volume (PWV), measured in mm or $\mathrm{g\,cm^{-2}}$ where 10 mm $\equiv$ 1 $\mathrm{g\,cm^{-2}}$, is a measure of all the water present in a column of air if it could be precipitated into a container of equal area to the air column cross-section. This derived estimate of total columnar water content can be seen in Figure 3.2, a 2D histogram plot of precipitable water volume from MJD 54710 (2008-09-01) to MJD 57569 (2016-06-30), where exceptionally high moisture content is present during summer-downtime (seen as sharply rising peaks of up to 50 mm). Note that the radiosonde data, taken every 12 hours, was subjected to an interpolation of 10 min steps to allow production of a lookup table for contemporaneous ceilometer data, to be discussed in Chapter 4. The resulting dataset plotted contains $> 5.5 \times 10^5$ timestamped PWV readings from this interpolation. The horizontal axis binning (time) is two weeks, while binning for the vertical

axis (PWV in mm) is 1 mm. The coloured sidebar (representing frequency per bin) shows a PWV fluctuation range principally from 2-12 mm for VWinter observing months (which are mid-way between the high PWV peaks).

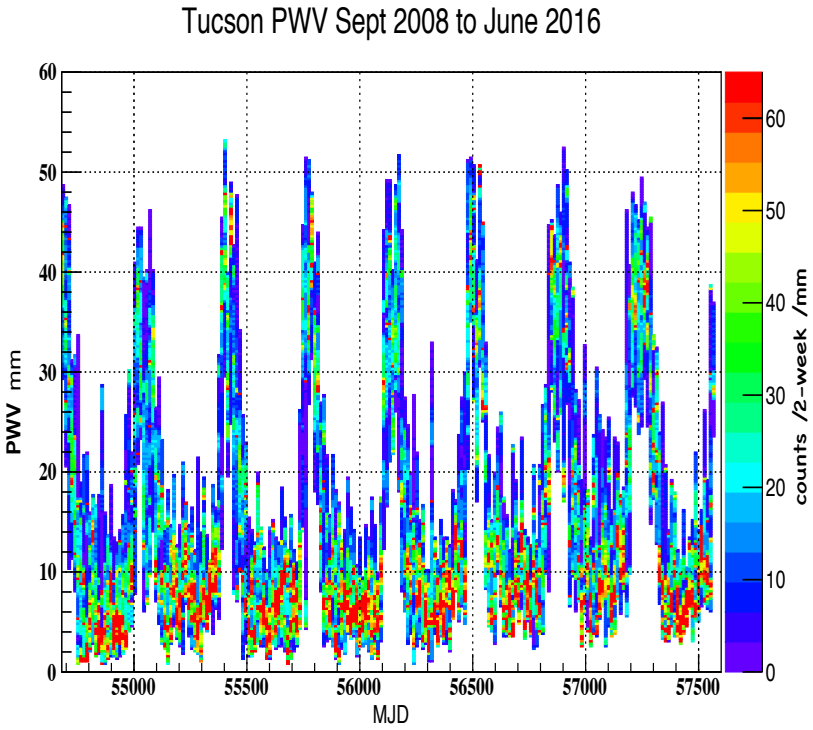

Fig. 3.2 A 2D histogram of precipitable water volume (PWV) in mm as measured at Tucson radiosonde station from MJD 54710 (2008-09-01) to MJD 57569 (2016-06-30) with 10 min interpolation between data points (usually 12 hours). The time binning of 2 weeks and PWV binning of 1 mm reveals seasonal fluctuations where peak PWV occurs in July-August. The mid-point between these peaks is mid-VWinter. The more stable PWV season is thus seen to be VWinter, where the frequency sidebar registers the most datasets per bin. Here the PWV is normally below 10 mm. Note that the PWV fluctuations outside of the summer-downtime moist air trajectories are on average an order of magnitude smaller than during summer-downtime months.

3.3 The infrared radiometers

VERITAS has employed the use of infrared radiometers since observations began with first light in 2007. The principal purpose of their use is to detect passing cloud that would adversely affect the Cherenkov light pool development [Aye et al., 2001]. Some studies have

postulated that radiometers may be able to detect the presence of aerosols in conjunction with satellite data [Chen et al., 2010].

There are three infrared radiometers currently in use at VERITAS; two Heitronics KT15.82D, sensitive from 800 to 1400 nm and sensing ranges from -100 or -50 °C to 100 °C and one Heitronics KT15.85 IIP, sensitive from 960 to 1150 nm and sensing range of -100 °C to 200 °C. The two telescope-mounted radiometers (one KT15.82D and one KT15.85 IIP) have K6 germanium lenses of 90 mm focal length with a 2.7° field of view that broadly matches the field of view of VERITAS. These are not used in this thesis due to elevation-correction complications. The third radiometer, a KT15.82D, is a static detector pointing north at 15° from zenith with a M6 germanium lens, 20 mm focal length and 6° field of view. All radiometers are set to have a 10-second averaging time giving a temperature resolution of 0.01 °C for the KT15.85 IIP and 1.0 °C for the KT15.82D.

3.3.1 The infrared radiometers as cloud monitors

Clouds, being formed mainly of water droplets, absorb and emit electromagnetic radiation as a blackbody. They will do so more efficiently than the surrounding air without clouds. Cloud-free air parcels may contain varying levels of water vapour, which will absorb and re-emit more radiation than drier air parcels. More infrared radiation will emanate from regions of the sky where clouds form, but the differences will vary with water vapour content. Additionally, the volatile morphology of clouds means that the infrared radiation received will fluctuate wildly, whereas clear skies (cloud-free) will have much more stable radiometrics. However, the infrared radiation entering the radiometers is subject itself to water vapour extinction. Thus, a method must be found to correct for or perhaps nullify this loss. Absolute calibration of radiometers (allowing accurate and stable radiometrics by accounting for atmospheric absorption / extinction in addition to the instrument's response function) lies outside the scope of this thesis. A simple method that can be utilised to classify if the field of view of the radiometer is free of cloud is as follows. For this, a basic elevation correction

has been carried out on the radiometer data, along with ambient temperature correction. A time window over which the sky temperature may be averaged must be selected and it's Root Mean Square (RMS) value calculated. This time window has been set to 10 min. The absolute value of the RMS sky temperature divided by sky average temperature in this 10 min window will give a value proportional to the variability in infrared radiation received from the field of view. This value may be referred to as the Clear Skies Ratio (CSR) and gives an upper limit where cloud is most unlikely to be present. This is because the greater the amount of cloud in the field of view, the greater will be the amount of infrared radiation re-radiated back to the radiometers, while cloud morphology means the re-radiated infrared will be highly variable. The Clear Skies Ratio may be used as a means of selecting the best atmospheric quality data for the VERITAS experiment, which requires cloud-free skies, at least for the telescope field of view.

An upper limit for CSR needs to be estimated. This can be accomplished with ease with the aid of a ceilometer. Due to the introduction of cloud base height detection and ranging up to a height of 15 km above ground level (a.g.l.) between 2011 and 2016 at VERITAS, it is known that there is approximately 25% cloud cover. That is, $\sim \frac{1}{4}$ of all ceilometer backscattering data outside of summer-downtime times has detected and ranged cloud base height. Knowing that 75% of radiometer data will be cloud free up to 15 km a.g.l. at least, a 1D histogram of CSR estimates will help fix the ratio upper limits for clear skies. The resulting histogram of CSR estimate will peak quickly very close to 1.0, and thereafter slowly diminish in frequency for increasing CSR estimates as cloud effects increase. For clear skies, the CSR has been set to the following value (an upper limit) after 8 years of data (2008-2016) were analysed

$$CSR \;=\; abs\Big(\frac{skyT_{RMS}}{skyT_{avg}}\Big) \;\leq\; 1.025 \tag{3.3}$$

where $skyT_{RMS}$ and $skyT_{avg}$ are the RMS and average values of sky temperature and *abs* refers to the absolute value. The time averaging window, 10 minutes, gives a total of 60 radiometer sky temperature estimates to work with. A 10 min window was chosen over

30 minutes, to better monitor cloud variability. See Figure 3.4 for a 2D plot of $skyT_{avg}$, ambient temperature and camera elevation correction corrected, over the same 8 year period as Figure 3.2, but with a data cut of CSR $\leq$1.04 used.

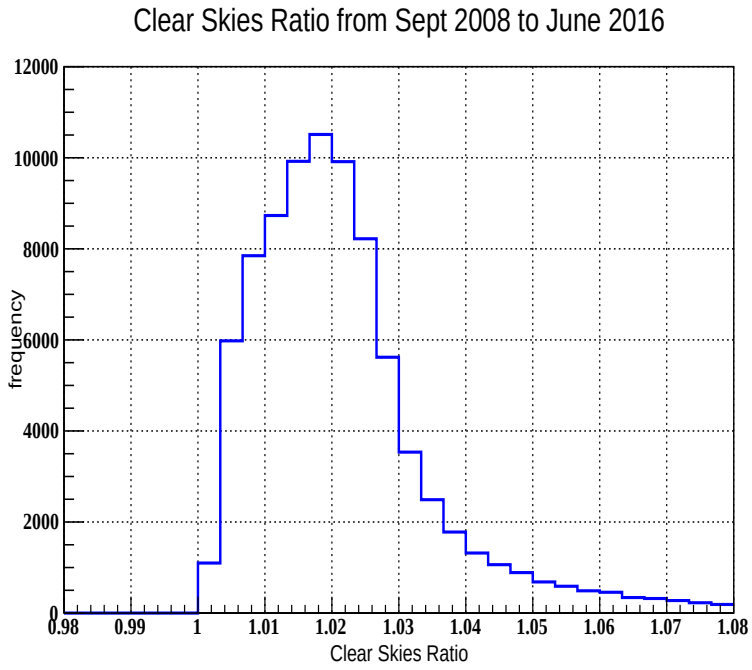

Fig. 3.3 A 1D histogram showing the CSR estimate, corrected for ambient temperature and 15° from zenith, during eight years of operation at VERITAS. The data were recorded from a Heitronics KT15.82D radiometer with a field of view of 6° and sky temperature averaged over a 10 min period. Binning is of 3.3×10^{-3}.

This slightly larger CSR limit is allowed to examine the contribution of slight cloud cover to the sky temperature estimate. Remembering that cloud will have a more variable sky temperature signature that clear-skies, it is reasonable to expect the frequency sidebars to register lower binning for cloud contanimated sky temperature readings than for cloud-free estimates. An increase of CSR from 1.025 to 1.04 brings an increase of up to 10 °C in sky temperature during mid-VWinter (the mid-points between summer-shutdown, the blank spaces in Figure 3.4), along with low frequency binning. This data is not seen when the CSR is set to $\leq$1.025.

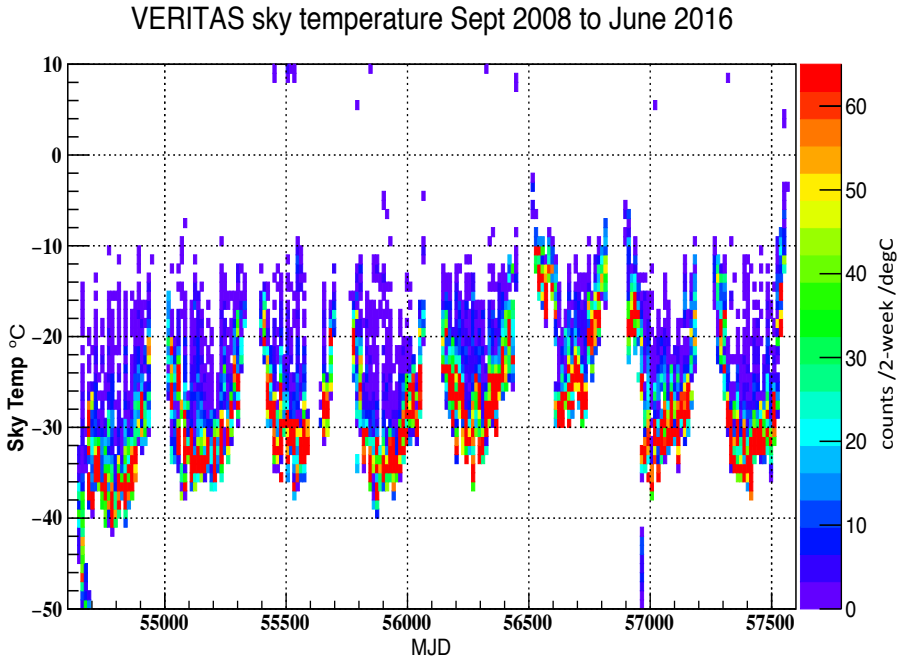

Fig. 3.4 A 2D histogram showing the sky temperature, corrected for ambient temperature and 15° from zenith, during eight years of operation at VERITAS. The data were recorded from MJD 54710 (2008-09-01) to MJD 57569 (2016-06-30) and were derived from a Heitronics KT15.82D radiometer with a field of view of 6° and sky temperature averaged over a 10 min period. Binning is of two weeks (x-axis) and 1 °C (y-axis) respectively. A data-cutoff of CSR $\leq$ 1.04 has been used.

The following caveats are noted with regard to cloud-free sky estimation. The fixed radiometer used to estimate the CSR ratio, a KT15.82D, has a temperature resolution of only $\pm$ 1 °C (as related in Section 3.3). As the (roughly) average $skyT_{avg}$ estimate year on year is -30 °C (seen in Figure 3.4), this represents a possible uncertainty in CSR of $\pm 3\%$. It was thus deemed wise not to set the CSR upper limit more stringently than 1.025. Further, it is noted that cloud base above a height of 15 km a.g.l. would not be visible to the ceilometer, so its effect on the CSR can not be determined. However, shower maximum for

EAS rarely exceeds this height so this cloud, if present, will not affect the Cherenkov light yield at telescope.

3.3.2 Investigating if radiometers can monitor aerosols

Radiation is continuously being emitted from surfaces and being absorbed, transmitted, and reflected. The atmosphere may be considered as a continuous series of thin layers, varying in molecular density up to the top of the atmosphere and with a near constant aerosol density up to the top of the boundary layer. The boundary layer is the height limit a.g.l. below which most of the aerosols are kept. The aerosols are trapped below this layer by a temperature inversion in the lower atmosphere that normally resides from 2-5 km a.g.l. Some surfaces emit or absorb electromagnetic radiation better than others. This is measured by a bodies emissivity, which is determined by intrinsic material properties. To quantify, emissivity is a ratio of how well a surface performs as an emitter of infrared radiation in comparison to a blackbody. According to the Stefan-Boltzmann Law, the emissive power of a blackbody is

$$E_{black\ body} = \sigma\, T^4 \tag{3.4}$$

while the emissive power of a real body is;

$$E_{real\ body} = \varepsilon\, \sigma\, T^4 \tag{3.5}$$

where σ is the Stefan-Boltzmann constant and ε is the emissivity of the surface while the surface temperature T is measured in kelvin. When many different surfaces are part of the environment, all must have their contribution added. Thus the total emissive power radiated from all non blackbody surfaces (that is, layers of atmosphere up to top of atmosphere) is,

from largest contributor to smallest contributor;

$$\Sigma_{z=0}^{\infty} E_{total} = \varepsilon_{cloud}\sigma T^4_{(cloud,z)} + \varepsilon_{H_2O}\sigma T^4_{(H_2O,z)} + \varepsilon_{air}\sigma T^4_{(air,z)} + \varepsilon_{aer1}\sigma T^4_{(aer1,z)} + .. + \varepsilon_{aerN}\sigma T^4_{(aerN,z)} \tag{3.6}$$

Here *cloud* refers to water droplets while H_2O refers to water vapour. The distance from the emitting surface to the radiometer is denoted by z. There may be several aerosol species present at one time, $aer1$ to $aerN$, each with its own emissivity. An in-depth knowledge of local aerosol properties may allow all the individual aerosol emissivity components to be combined into an effective aerosol emissivity [Ackerman, 1997], but may be accounted for by selection of a particular aerosol typology in a radiative transfer code.

A further complication is that the use of the Stefan-Boltzmann Law does not account for the emitted radiation suffering attenuation on the way to the detector. Further, the detector needs to have a linear instrument response, or be correctable for non-linearity. For aerosol detection, an absolute calibration of the radiometer data is essential. This is because the aerosol emissivity over the chosen time-averaging window (30 minutes for aerosol detection instead of 10 minutes for cloud detection; more will be said of this in Chapter 4) will be near constant and very low in comparison to other contributors (as related in Equation 3.6). Any instability in instrument response will probably be greater than that of the aerosol emissivity component being measured. Accurate estimates of water vapour content at VERITAS is essential in order to correct for water vapour extinction loss. The calibration process is additionally complicated by a number of factors. Firstly, the large wavelength integration window width of 600 nm could allow large errors in atmospheric spectral calculations. There are several absorption bands in the range from 800 nm to 1400 nm that must be accounted for; this may be achieved by producing an effective water vapour extinction correction over the wavelength band in question. However, a moderate resolution atmospheric spectral analysis code is employed, details of which follow towards the end of this chapter, which means the approximations resulting from lower spectral resolution will

be compounded over such a large wavelength integration window. Secondly, the germanium radiometer lens has a temperature-dependent transparency; manufacturer tables may be used to correct for ambient temperature transmission fluctuations. Thirdly, the theoretical photon integration of the radiometer is from zero to infinity, or more concretely, from the camera lens to the top of the atmosphere. Infrared radiation from any source in this 120 km range will make up part of the final sky temperature estimate. Lastly, the emissivity of each reflecting and scattering surface must be known. In short, too many difficult-to-measure variables are required to estimate the radiative forcing in the infrared by aerosols using this method. Radiative forcing refers to the ability of particulate or gaseous components of the atmosphere to impact on the local energy balance of the atmosphere. The small contribution of aerosol emissivity to the total radiation detected by the radiometer will most probably be lost in the errors associated with detection.

3.3.3 Concluding remarks on radiometers

The average monthly sky temperatures during the VSummer months, defined in Table 3.1, is $\sim$8 $^{\circ}$C higher than the average sky temperature in VWinter months. Higher concentrations of aerosols are believed to be present, but their emissions cannot be separated easily from the higher concentrations of water vapour also present, verified by radiosonde data and seen in Figure 3.2. The radiometers may however prove of some use in low water vapour atmospheres, especially for examining archival data when other methods of aerosol monitoring were not available. Therefore, the infrared radiometers discussed will not form part of the research campaign to detect and quantify aerosols at VERITAS.

3.4 The VERITAS imaging atmospheric Cherenkov telescopes

The VERITAS array [Krennrich et al., 2004] consists of four identical IACTs, where the primary components for each telescope are: a 12 m diameter reflector with optical support structure and drive mechanisms, a 499 PMT camera with integrated charge pre-amplifier and programmable high voltage for each tube, a telescope triggering system with three integrated levels and finally a data acquisition and output file-build system. The four telescopes are controlled from a central building which houses an array-level triggering system and operator controls [LeBohec et al., 2006]. Each of these four principal system components are now described.

3.4.1 The optical support structure

The optical support structure refers to the mechanical structures that the VERITAS telescope is built around. Cherenkov light from an EAS travels through the atmosphere in a compact light pool, which may be likened to a slowly expanding circular slab of light about 1 m in thickness, with a total area on the ground of up to 10^5 m^2. The VERITAS array, consisting of 4 telescopes, must be spatially arranged so as to maximise the effective collection area for the EAS. The arrangement is important as it also aids in rejecting local muons, which may be indistinguishable from VHE γ-ray air showers (mentioned in Section 2.2.3). This is achieved by separating the telescopes by at least 100 m. The VERITAS array layout has undergone a number of additions and changes since 2005 when the first telescope became operational [Holder et al., 2006a]. A particular name is given to each telescope array version. Array version 1 (V1) was the first telescope employed on site. Array version 2, 3 and 4 (V2, V3 and V4) were the introduction of Telescopes 2, 3 and 4 to the VERITAS array. Array version 5 (V5) resulted from the moving of Telescope 1 to its current position; this was carried out to keep the minimum distance between telescopes to around 100 m. Finally

Fig. 3.5 Aerial photographs showing the relative position of the telescopes at VERITAS, with the move of Telescope 1 in 2009 shown in the bottom photograph. Taken from Holder et al. [2015].

the current Array version, V6, was initiated not by the moving of individual telescopes but by the introduction of upgraded cameras to all 4 telescopes. All data for this thesis uses only V6 array version. Figure 3.5 shows the telescope layouts before and after the moving of Telescope 1. The light pool from an EAS arrives at the four VERITAS telescopes where it is collected and focused. Only a small fraction ($\sim$0.4%, $\frac{4.4\times10^2}{10^5}$, *i.e.* total mirror area divided by total lightpool area) of the light pool will be incident on the mirrors; it may be less if the shower center is far from the array center. Each VERITAS telescope is designed around the Davies-Cotton solar collector [Davies and Cotton, 1957], where each collector has a collection area of $\sim$110 m^2 (or total mirror surface of $\sim 4.4 \times 10^2$). This type of reflector consists of a spherical optical support structure, with counter-weights, pedestal base and camera-box with supporting arms (Figure 3.6). The Davies-Cotton reflectors are not a single surface but tessellated (smaller identical sections laid out like tiles) and have 345

identical hexagonal mirror facets mounted on each optical support structure. Each facet has a surface area of 0.322 m^2 and is made of slumped, polished glass, which is aluminized and anodised at an on-site optical coating laboratory. To prevent degradation due to exposure to wind-blown sand from the Arizona desert, facets are periodically re-coated and replaced to maintain their peak reflectivity above $\sim$90% [Roache et al., 2008]. The collector radius of curvature r, is 12 m, upon which the many spherical mirror facets with a radius of curvature of $2r$, 24 m, are mounted. The Davies-Cotton light collector of VERITAS has an optical point spread function width of 0.05° [McCann et al., 2010]. Davies-Cotton reflectors offer many benefits over parabolic reflectors; all mirror facets are identical and therefore cheaper to manufacture, alignment of the mirrors is simple and importantly on-axis and off-axis aberrations are smaller than those inherent in parabolic reflectors. The main disadvantage of Davies-Cotton reflectors is that they are asynchronous. As the Davis-Cotton design is spherical, Cherenkov light will reach the outer regions of the reflecting surface and be reflected onto the camera plane before light reaching the center of the camera. This introduces a time-spread of $\sim$4-6 ns for the incoming Cherenkov shower.

3.4.2 The VERITAS 499 PMT cameras

The optical support structure of each telescope houses a camera box at the focal plane to protect the sensitive VERITAS camera from sun and wind-borne dust. Each camera has 499 PMTs, with a diameter of 25 mm, have an angular size of 0.15° each that taken together cover 3.5° of sky. The PMTs were upgraded in the summer of 2012 with Hamamatsu R.10560-100-20MOD, with the new PMTs having peak quantum efficiency of $\sim$35% at 350 nm, [Zitzer and Collaboration, 2012, Kieda et al., 2013]. As the circular cross-section of PMTs allows undesirable light loss between neighbouring tubes, hexagonal light-collecting cones are fitted to minimise this loss (seen in Figure 3.7). The PMTs are operated at a gain $\sim 2 \times 10^5$, at a typical voltage of $\sim$850-1000 VDC, so a photoelectron will generate approximately $2 \times 10^5 \times q_e$ (electron charge) or $\approx$ 0.03 pC of charge at the anode of the PMT.

Fig. 3.6 A photograph of VERITAS Telescope 1, post 2009 move, showing the electronics trailer and a side view of the optical support structure, with a camera box at the focal plane. The tessellated mirrors are visible edge on.

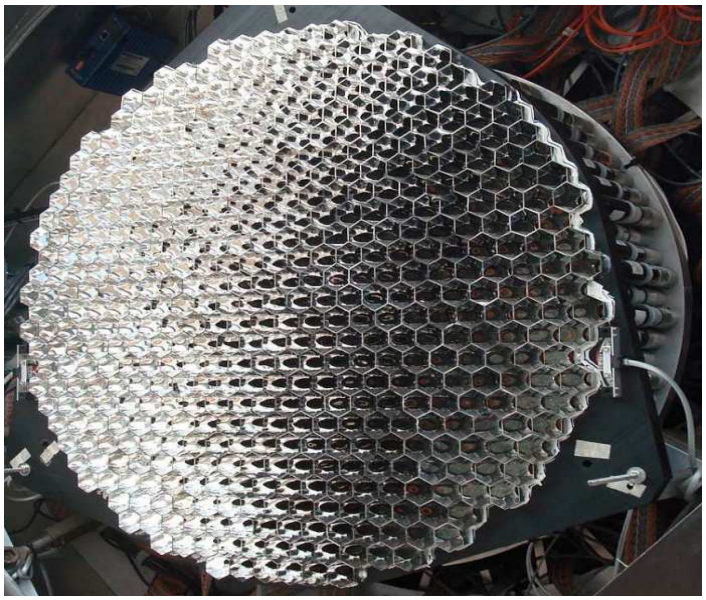

Fig. 3.7 A photograph of a VERITAS camera showing 499 light cones tightly packed, with a PMT at the center of each. Taken from Griffin [2011].

Preamplifiers are connected to the PMTs to provide an amplification factor of 6.6, necessary in minimizing the effects of ambient electronics noise as this charge travels ∼45 m through co-axial cable from each camera to an electronics shed besides each telescope.
Each PMT has a unique gain that must be adjusted accordingly. Flat fielding is achieved in part by individually varying the High Voltage supplied to each tube. The correct voltage required by each tube is determined by illuminating the camera of each telescope with a set of blue / UV LEDs, in sequential pattern flashing mode, that is passed through a diffuser. This happens while all the telescopes track a dark (low stellar light) patch of sky. This even illumination of varying light levels allows a quite consistent relative gain to be achieved for all PMTs, by relating the PMT integrated charge with the High Voltage (HV) setting for that PMT. This High Voltage setting is stored to file, where it is used by a programmable HV supply. Adjusting the HV for each PMT allows an initial flat-fielding to within 10-20% [Hanna et al., 2010], of true flat-fielding. From this preliminary flat-fielding a histogram of relative gains for all 499 PMTs is obtained for each camera. Afterwards, during data analysis, software level final flat-fielding is achievable by accounting for the individual relative gains, an example of which is seen in Figure 3.8.

3.4.3 Telescope triggering on three levels

The output from each of the PMTs, an integrated charge, arrives at the Flash Analogue to Digital Converter (FADC) running at 500 MHz for conversion of the pulse trace to digital form. The pulse trace refers to the integrated charge of the PMT as a function of time, where the time is measured in sample counts (1 sample count = 2 ns). Figure 3.9 displays the VERITAS data acquisition system in block diagram format. At its most basic, the data acquisition consists of real-time analogue to digital conversion, a trigger that prompts data output, then the creation of the final data file. The three trigger levels are now discussed.

1. The Level 1 or pixel level trigger, L1, is designed to trigger on the fast rising (∼4 ns) current pulses generated by the PMTs in response to a Cherenkov light front. It

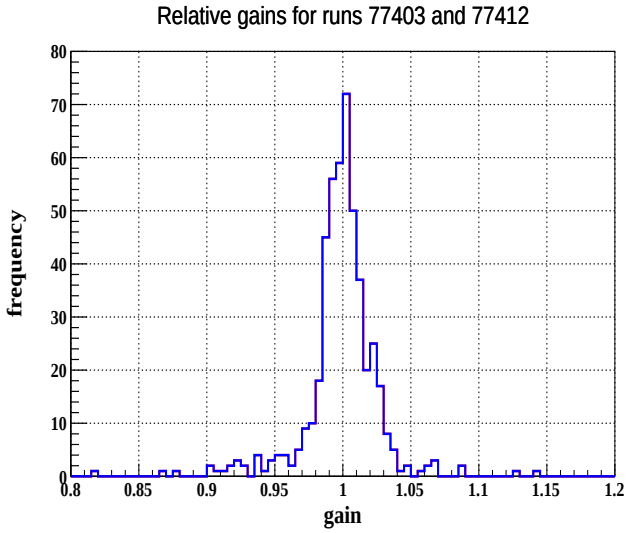

Fig. 3.8 A 1D histogram of the relative gains for the 499 PMTs of Telescope 1 for two separate data runs, the choice of which is explained in Section 3.4.5. As only one LED flasher run was taken for the night, the relative gains are identical for both data runs.

is desirable that the pixel level trigger not be strongly dependent on the amplitude of the PMT pulse. It is also desirable that the pixel level trigger rate not be strongly driven by the changing night sky background light in the blue / UV, (NSB_{uv}), such as stars in the PMT field of view. To facilitate this, a threshold discriminator operates with a simple programmable voltage limit, typically set to 45 mV. Secondly, a zero-crossing discriminator will fire at a pre-defined point of the input pulse. This is incorporated with the threshold discriminator to overcome timing jitter for varying amplitude pulses. Timing jitter could be caused by widely varying pulse amplitudes where the point at which a threshold is reached will vary in time with regard to pulse maximum. The combination of both, called a Constant Fraction Discriminator (CFD), will fire at a set fraction of maximum pulse amplitude. The voltage used to vary the threshold and hence the pixel level triggering is referred to as the CFD threshold.

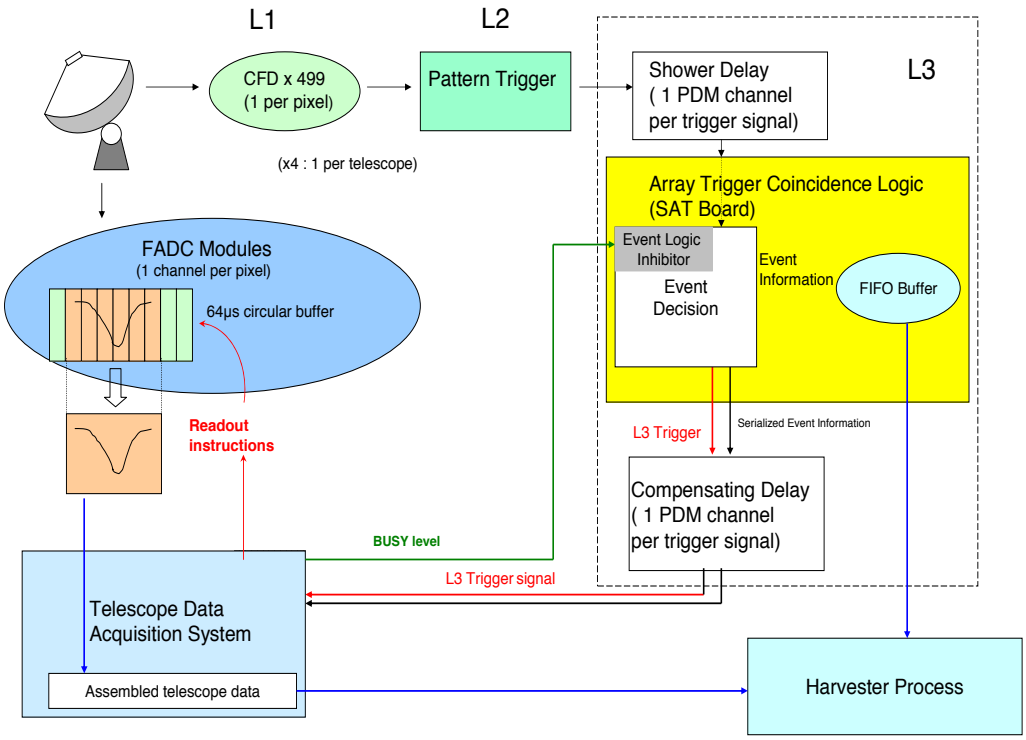

Fig. 3.9 A block diagram of the VERITAS data acquisition system. Taken from Weinstein [2008].

2. The Level 2 or pattern level trigger, L2, represents when a neighbouring group of PMTs (minimum of 3) achieves L1 trigger status within a particular time coincidence window. The arrival time of Cherenkov light from a EAS is not simultaneous in all PMTs. The Davis-Cotton light collector causes a time arrival difference at the camera of $\sim$5 ns between light reflecting off the edge and light reflecting off the center of the light collector. When this is coupled with the Cherenkov light pool arrival time spread, a time coincidence window of 5-7 ns is required. Further, as the co-axial cables which join the PMTs to the FADCs are not of equal length, and the overall transmission times for each will vary due to varying impedances, an individual timing coincidence window must also be determined for each co-axial cable. This co-axial travel coincidence window is in addition to the asynchronicity caused by the telescope design and light pool spread.

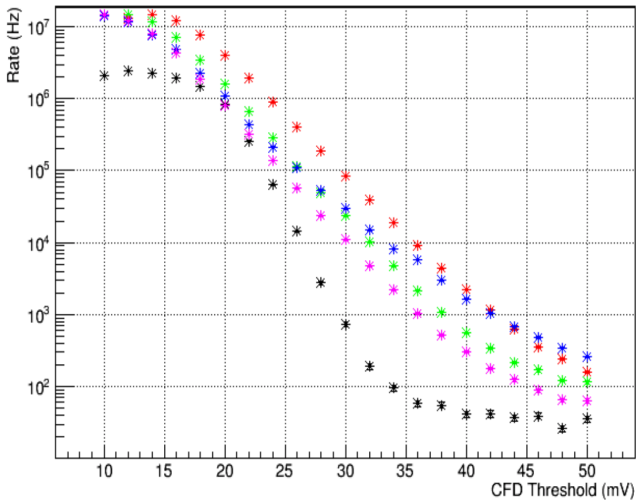

Fig. 3.10 A log-lin plot of a typical bias curve for L2/L3 triggering from Run 68163 (MJD 56404.33472, 2013/04/22 08:02 UTC). L2-T1 = red, L2-T2 = green, L2-T3 = blue, L2-T4 = pink, L3 = black. The *x*-axis shows the CFD voltage in mV, the *y*-axis shows the corresponding trigger rate in Hz. As the CFD threshold is lowered, the night sky background in the blue / UV begins to dominate L2 triggering, causing a corresponding rise in L3 triggering. The L3 rate becomes constant for CFD $\approx$ 35 mV.

3. VERITAS has a Level 3 or array level trigger, L3, corresponding to a light pool producing a pattern level trigger on at least two telescopes. The time coincidence window for this is set to 50 ns. The array level trigger also initiates event read-out. This involves the signalling of the individual telescope data acquisition systems to read their buffered PMT signals and to parse this with system-wide data to form the output file. It is this array level trigger that may possibly be used to some limited effect to detect the presence of elevated aerosols on site, as the array level rate is more stable than either pixel or pattern level triggers.

Figure 3.10 shows a plot of the pattern level and array level triggering as a function of CFD threshold (mV) for a particular run, selected as it is quasi-contemporaneous with data that will be analysed later in Chapter 6. The plot is referred to as a Bias Curve because it displays how increasing CFD threshold for the pixel level triggering impacts on or 'biases' the pattern level and array level triggering. Array level triggering becomes near-constant with voltage around CFD $\sim$35 mV.

3.4.4 The VERITAS data acquisition system

The PMT outputs are continuously digitised and buffered by a custom-built 500 mega-sample s^{-1} FADC system [Rebillot et al., 2003]. The PMT pulses are digitised with 8-bit resolution and stored in a circular RAM buffer 64 μs deep. When a readout (array level or L3) trigger is received, the buffering process halts, a busy signal is emitted, and a segment of each channel's buffer is read out. This segment is called the readout window. It contains the PMT traces of the event which generated the local pattern level trigger. The FADCs record the PMT pulses in digital counts with a sample width of 2 ns.

At the input to the FADC, a DC bias voltage called the pedestal is applied to the PMT signal to allow input values fluctuating near zero to be recorded. The pedestal voltage level is such that in the absence of a signal in a PMT, its FADC will record an input $\sim$15-19 digital counts. In the absence of a normal L3 trigger, the L3 system sends a pedestal trigger to all the telescopes at a rate of $\sim$1 Hz, allowing measurement of the pedestal. These recorded pedestal events are of importance in the VERITAS data analysis chain where the variance of the pedestal about its mean value, referred to as pedestal-variance (pedvar), is a measure of the NSB_{uv} and electronic noise in the camera.

In order to increase the dynamic range of the FADCs without saturation, each of the channels offers a reduced gain output. At the input point to the FADC, the PMT signal is split into three copies (as seen in Figure 3.11). One copy is delayed and reduced in gain by a factor of $\sim$6. The second is sent to a threshold discriminator to measure if the normal-gain PMT pulse is within the dynamic range of the 8-bit FADC. The third copy is sent directly into the digitiser. If the amplitude of the raw input pulse is beyond the range of the FADC, the delayed low-gain line is then fed into the digitiser, behind the raw copy. A flag is then set which modifies what part of the read-out window is available to read, called the lookback time. The modified lookback time of the FADC allows the low-gain pulse to be read rather than the high-gain version, which will have saturated the digitiser. This system results in a

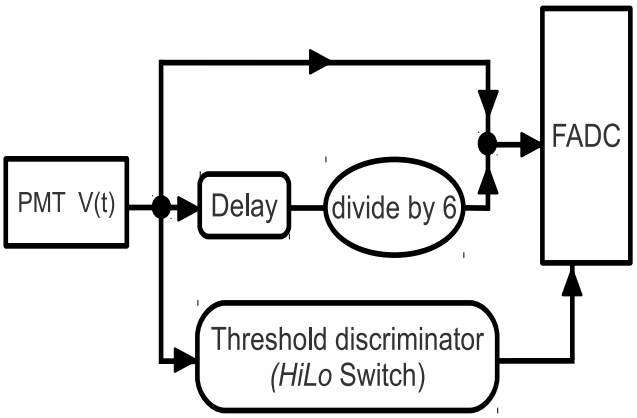

Fig. 3.11 An illustration of the High/Low gain discriminator of the FADC input.

dynamic range which is $\sim$6 times larger than a non-switched output.

At read-out time, the 499 buffered traces of each telescope from the FADC read-out windows are collected, together with the L1 trigger patterns and the Hi/Lo discriminator pattern for each. Finally, all the event information is sent from the L3 trigger (including pedestal trigger), along with the local GPS time stamp to an Event Builder program. The Event Builder makes the offline data stream by constructing each array level trigger as a particular event recording all system-wide information; it then parses the unified data streams to a Harvester. As the name implies, the data streams are gathered together, verified as complete (sanity checked) at the end of the data run and sent to local hard disk (where they reside temporarily as preliminary backup) before being archived in RAID storage (Redundant Array of Independent Disks) in an affiliate university.

3.4.5 The *Eventdisplay* analysis chain

A moderate VHE γ-ray emitter may only produce $\sim$3 detectable EAS from progenitor γ-rays min^{-1}; the Crab nebula may emit up to an order of magnitude more. When VERITAS is pointed at a weak VHE emitter, on array level trigger there is a 1 in $\sim 10^4$ chance that the event in question may be caused by a VHE γ-ray. Even when the VERITAS telescope is pointed at a powerful γ-ray emitter such as the Crab Nebula there is still only a 1 in $\sim 10^3$

chance a VHE γ-ray caused the trigger. From 2012 to 2017, the V6 VERITAS array reports an average array lever trigger rate of 400-500 Hz or 3×10^4 triggers min^{-1}. It is now necessary to move from "may be a γ-ray event" to "in all probability is a γ-ray event", by means of the analysis chain. The field of γ-ray astronomy came into being with the advent of effective γ/hadron separation algorithms, where 99.7% of hadrons are removed, along with $\sim$50% of γ-rays too [Krawczynski et al., 2006].

Eventdisplay, one of two analysis packages for VERITAS data, has been in continuous development since 2005 principally by Dr Gernot Maier of DESY, Zeuthen, Germany [Krawczynski et al., 2006]. As this thesis seeks to determine the impact of aerosol extinction on the Cherenkov imaging technique, some attention is given to the analysis steps thought be to most influenced by such extinction. To help highlight any differences due to aerosol extinction two separate data runs, 77403 (MJD 57134.20889, 2015/04/22 05:00:48 UTC), 28° from zenith, and 77412 (MJD 57134.50069, 2015/04/22 12:01:00 UTC), 27° from zenith, will be used to examine parts of the VERITAS analysis chain. These runs were chosen firstly because they will form part of the analysis of PKS1441 +25 in Chapter 6, secondly and more importantly because there were unusual aerosol conditions that varied from low to moderately high aerosol extinction over the course of the 7 hour period spanning these runs. This will be discussed in more detail in Chapter 4. The pedestals and pedvars are determined first along with a particular point of the PMT charge rise time, named t_{zero}.

Calculation of pedestals, pedvars and t_{zero}

To calculate the pedestals and pedvars use is made of the 1 Hz pedestal readouts. A 3-min averaging of each of the (499 x 4) PMT integrated charges from the 1 Hz readouts gives the pedestal in digital counts and its standard deviation, the pedvar, for each individual PMT. See Figure 3.12 for an example of pedestal estimation in T1 from the two data runs described in Section 3.4.5, 77403 and 77412.

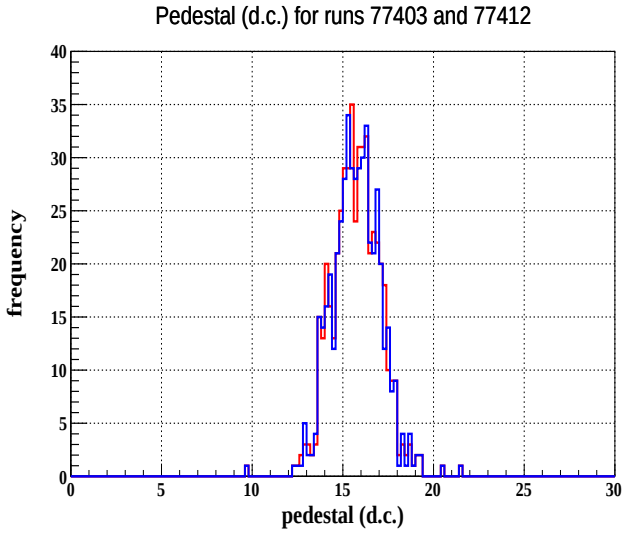

Fig. 3.12 The average of the pedestal readings in digital counts for each of the 499 PMTs of Telescope 1 for data runs 77403 (red) and 77412 (blue). The pedestal mean and RMS are statistically identical.

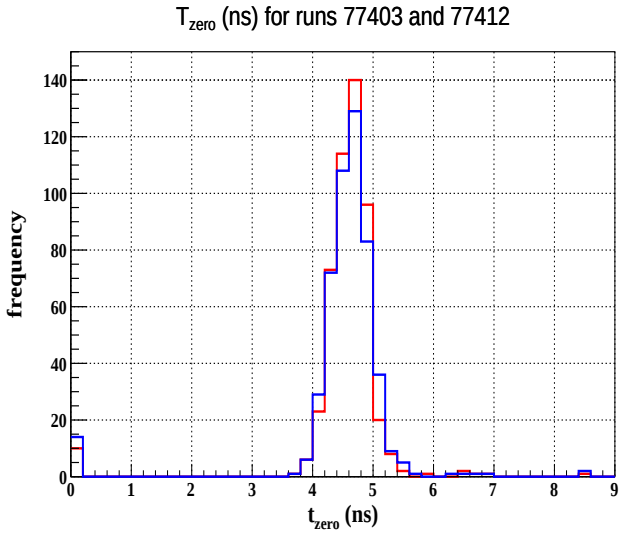

Fig. 3.13 The t_{zero} estimates for the 499 PMTs of telescope 1 for data runs 77403 (red) and 77412 (blue). The range in t_{zero} values are almost identical for both.

The averaging of the pedestal over many integration windows allows a baseline charge to be estimated for each PMT in the absence of any input. The total charge of a particular

PMT arising from an EAS may then be determined by subtracting the baseline charge. When the PMT charge has been digitised and is ready for signal processing, it is referred to as a channel.

t_{zero}, denotes where the negative PMT pulse reaches half of its amplitude. See Figure 3.14 for the plot of a PMT pulse with the t_{zero} estimation shown as a vertical black dotted line. The analysis in this thesis uses a 6-sample-width window, that is 6 x 2 ns sample width = 12 ns. See Figure 3.13 for an example of t_{zero} estimation in T1 from the same two data runs examined in Figure 3.12.

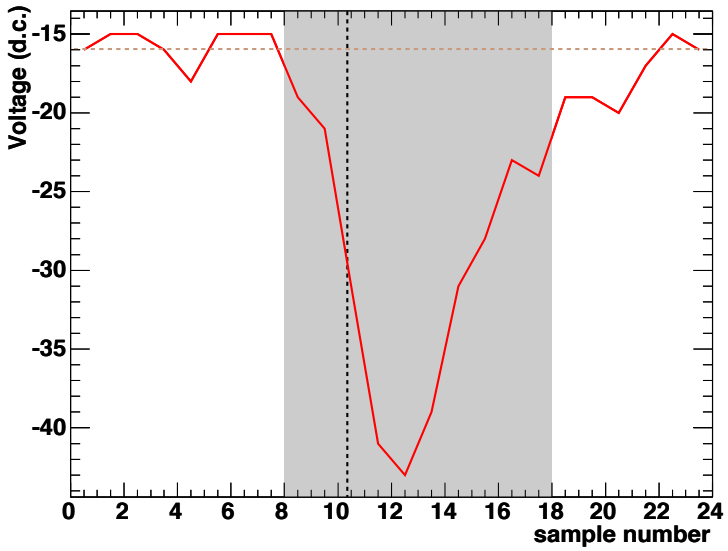

Fig. 3.14 A plot of a FADC trace showing the integrated charge at the base of a pre-upgrade PMT (outlined in Section 3.4.2) when a Cherenkov pulse is present. The black dashed vertical line marks t_{zero} and the red horizontal dashed line at -16 d.c. is fixed as zero charge (discussed in Section 3.4.4). The integration window is shaded and for this example is 10 samples or 20 ns. The upgraded PMTs have a narrower pulse width, allowing a smaller integration window. Taken from Holder [2005].

The integrated charge estimation in each PMT is accomplished by a double-pass method. The first pass is to determine if a pulse is present in the PMT tube (by a first order estimate of the charge present), and if so to estimate its t_{zero}. This is followed by a time-gradient correction. Time gradient refers to neighbouring PMTs having their t_{zero} shifted by such factors as longitudinal shower development of the EAS, the lateral distance of Cherenkov photons

from the shower core and telescope reflector asynchronicity (as explained in Section 3.4.1). With an individual t_{zero} for each PMT time gradient corrected, a second pass is carried out to integrate the PMT charges in all channels over its 6 sample window. Accurate PMT charge integration requires a set integration window, but not necessarily a set integration window start. The start time of the integration window depends on the timing gradient across the image.

Image cleaning of L3 triggered events

For an array level trigger event, once the integrated charge of a certain pixel in digital counts is calculated by means of the double pass and the pedestal value for the same integration window is subtracted, the relative gains may be used to calibrate the individual pixel charge. This is the final stage of flat-fielding and is achieved by artificially increasing / decreasing the integrated charge estimation by an amount proportional to the relative gain for that particular pixel. The next stage of the analysis, critical for the Cherenkov technique, is to find the image the EAS light pool makes on the camera planes and parameterise it.
Quality cuts are now applied to the pixellated images on the camera plane as a form of image cleaning. Adjoining pixels on a particular camera will show an ellipsoidal or more irregular cluster of elevated integrated charge if a VHE γ-ray or cosmic ray initiated EAS respectively has been detected. This ellipsoid cluster, hereafter referred to as a shower image, is divided into an inner region, called the signal, and an outer region, called the boundary. Firstly, the pixel with the maximum integrated charge is found. If it is estimated to have an integrated charge above a set threshold, called the signal threshold (set to pedestal $+ 5 \times$ pedvar d.c., for a standard analysis), and if the four adjacent pixels are above the signal threshold, the shower image qualifies for parameterisation. Next the boundary threshold is set (pedestal $+ 2.5 \times$ pedvar d.c., for a standard analysis) and all pixels which pass this threshold and surround the signal pixels define the outer limits of the shower image. Moment fitting of these signal and boundary pixels, which are weighted according to the integrated

charge, allows the semi-major and semi-minor axis of the ellipse-like image to be determined, among other parameters.

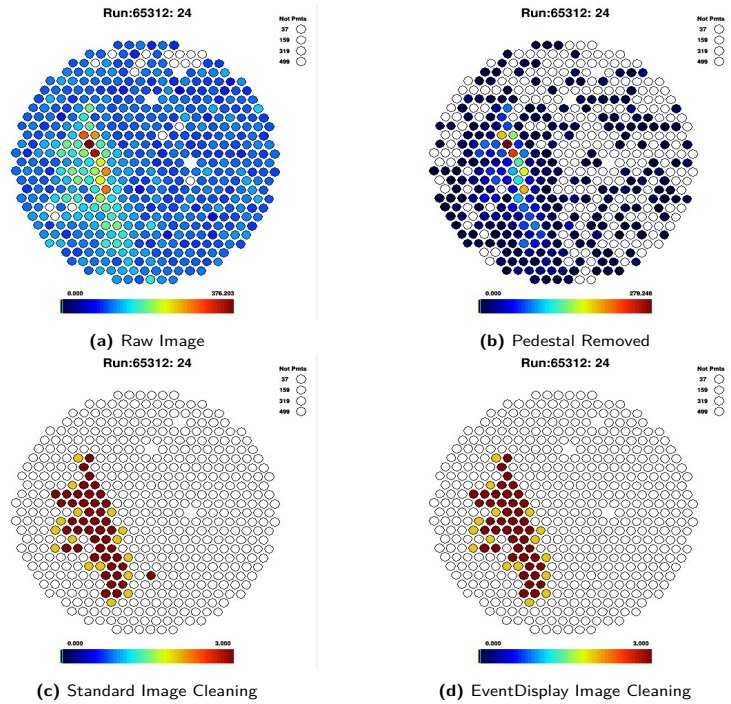

(a) Raw Image **(b)** Pedestal Removed

(c) Standard Image Cleaning **(d)** EventDisplay Image Cleaning

Fig. 3.15 An example of a VHE γ-ray shower image; (left-top) is the raw image, (right-top) has the pedestal subtracted, (left-bottom) is the standard cleaned image, (right-bottom) is the *Eventdisplay* cleaned image. The *Eventdisplay* cleaning removes pixel outliers. The colour bar represents integrated charge in d.c., while the picture and boundary pixels are represented by brown and yellow respectively. Taken from Bird [2015].

All other pixels are set to zero, see Figure 3.15 for an example. It is noted that different astrophysical sources have their own set of quality cuts to optimise γ/hadron rejection; in this thesis two sets of cuts are used, standard and soft, which are to be used in Chapter 6.

Parameterisation of shower image

Image parameterization is carried out on the cleaned images, by moment fitting. Moment fitting of shower images on the camera plane, defined first by Hillas [Hillas, 1985], allows the camera image to be described by a small number of defined parameters. The following are the main Hillas parameters, displayed in Figure 3.16:

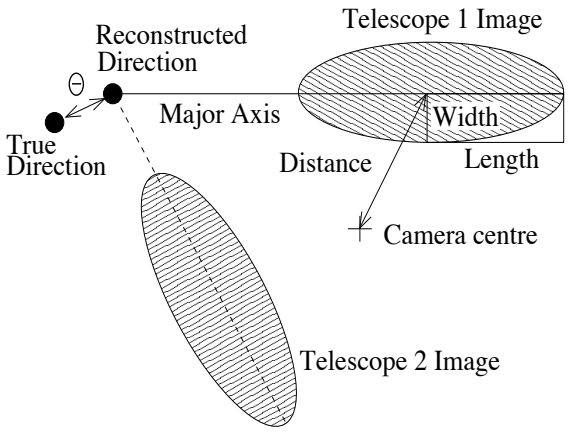

Fig. 3.16 Diagram showing the main parameters used to discriminate between γ-ray and hadronic progenitor EAS. Note that Width and Length are used to calculate Mean Scaled Width and Mean Scaled Length, explained in this section. θ is used more commonly than α for checking if a γ-ray is from the putative source location. Taken from **?**.

- Size: total integrated charge of all the pixels in the fitted ellipse (shaded area) of Figure 3.16. The energy of the progenitor γ-ray is proportional to the size of the shower which is related to the total charge measured in the PMTs.

- Distance: angular distance between the center of the camera and the center of the fitted image centroid.

- Width: angular length of the semi-minor axis of the fitted ellipse.

- Length: angular length of the semi-major axis of the fitted ellipse.

- Theta (θ): angle between the fitted major axis and the source direction. The greater the angle measurement the less likely a γ-ray is from the putative source location.

Note that all parameters bar size are measured in degrees ($^\circ$).

It is crucial to correlate the parameters of the ellipse/ellipsoid on the camera plane, with the impact parameter of the shower on the ground. The shower impact parameter, D, is the distance of the shower core from a telescope and accounts for the reduction in image size

for showers which arrive further away from telescope. D can be used to define a scaler that corrects for the shower image reduction. The Width and Length parameters are not used in their raw form.

With multiple telescope data, the mean scale width ($MSCW$) and mean scale length ($MSCL$) can be estimated by averaging over all telescopes that have an image

$$MSCW = \frac{1}{n}\left(\sum_{i}^{n}\frac{width_i - \hat{w}(S,D)}{\sigma_{width,MC}(S,D)}\right) \tag{3.7}$$

$$MSCL = \frac{1}{n}\left(\sum_{i}^{n}\frac{length_i - \hat{l}(S,D)}{\sigma_{length,MC}(S,D)}\right) \tag{3.8}$$

where S is the image size (the total integrated charge of all PMTs in the image) and D is the impact parameter, $width_i$ is the measured width of the image, $\hat{w}(S,D)$ is the mean or median of the image width of the simulated images (both likewise for length l), n is the number of telescopes that have an image and $\sigma_{width,MC}(S,D)$ and $\sigma_{length,MC}(S,D)$ are the errors on the values from the Monte Carlo simulations. An example of $MSCW$ derived from data and Monte Carlo simulations is seen in Figure 3.17. Monte Carlo simulations allow lookup tables to be derived for $MSCW$ and $MSCL$ limits.

Image containment, radial acceptance and source location

An image containment of $\geq$ 80% is additionally required, meaning that less that 20% of integrated charge may be found in the outermost pixels or outside of camera. This is referred to as the Loss cut and is readily estimated from the moment-fitted ellipsoid on the camera plane.

The camera angular acceptance or radial acceptance refers to the relative γ-ray rate decrease for increasing angular distance from camera center. This is caused mainly by some fraction of the image falling outside of the camera, and a correction table is again derived from Monte Carlo simulations.

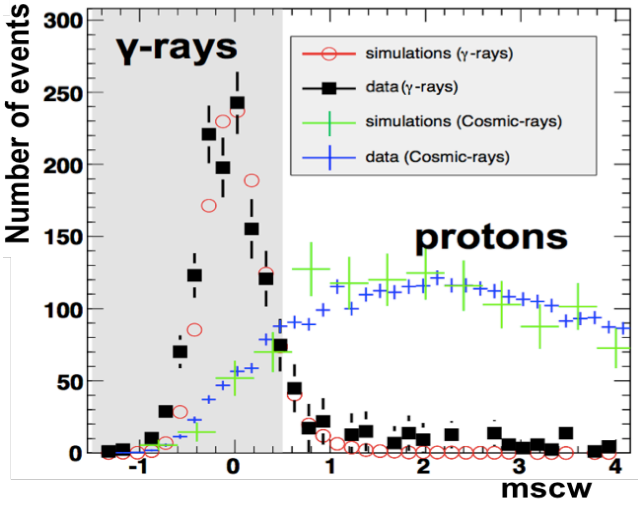

Fig. 3.17 An example of *MSCW* estimation from Monte Carlo and real data for VHE γ-ray showers and cosmic ray showers. Taken from Maier [2008].

Applying cuts for γ/hadron discrimination

The cuts used in the standard analysis are listed in Table 3.2. The minimum size cut for the standard analysis is 100 digital counts (d.c). The core distance is the distance between the telescope and the shower core on the ground, while the fiducial cut is how far from the camera centre an image centroid is allowed. The minimum number of tubes to parameterise an image is 5 while N_{tel} is the minimum number of telescopes with an image required for analysis. Hadron rejection may now be carried out by applying *MSCW*, *MSCL* and θ^2 cuts. θ is the angle between the reconstructed shower direction and the centre of the camera, as seen in Figure 3.16. Smaller θ^2 values are more likely to be initiated by γ-rays from the putative source location [Daniel, 2007].

Background γ-ray rejection

The γ/hadron seperation technique removes practically all (99.7%) hadronic showers, however $\sim$50% of VHE γ-rays are also rejected by this filter. Of the 0.3% cosmic rays that pass the γ/hadron cuts, many will appear indistinguishable from γ-ray events and be close enough to the putative source location as to form a background signal that will augment

Cut	*Value*
Loss	$< 20\%$
Size	> 100 d.c.
N_{tel}	≥ 2
θ^2	$< 0.008^{\circ 2}$
$\min_{Tubes}$	5
MSCW	$-1.2^{\circ} <$ MSCW $< 0.5^{\circ}$
MSCL	$-1.2^{\circ} <$ MSCL $< 0.7^{\circ}$
Core distance	< 250 m
Fiducial cut	$< 2^{\circ}$

Table 3.2 The cut set for the standard analysis of VERITAS.

the γ-ray count [**?**]. γ-ray background estimations is carried out by two principal methods, which are illustrated in Figure 3.18. The principal observing mode for VERITAS is 0.5° wobble, where the putative source location is offset from the center of camera by 0.5° either north, south, east or west. This small offset allows the source location and sufficient background regions of similar sample size to have their γ-ray count estimated at the same time [Daniel, 2007]. In the ring background method, the background is estimated for each bin of the skymap by using an annulus (ring) region around the bin. Since the ring crosses different regions of the camera, the background values for each point must be weighted by an angular acceptance value. In addition, stars brighter than magnitude 6, are excluded from the background region. In the reflected region background model, the background is estimated using several background regions at the same angular distance from, and of the same size, as the test region. This method has several advantages; there is no need for angular acceptance corrections and the number of background regions may be varied and positioned individually if required. Once the γ-ray count for each background region is estimated the average is found, called OFF source normalisation. The γ-ray count from the putative source location is called the ON counts, measured in photons min^{-1} from the ON test region, while OFF source counts from all OFF test regions divided by the number of OFF test regions gives the normalisation factor. The total γ-ray flux is estimated by the VERITAS analysis chain and

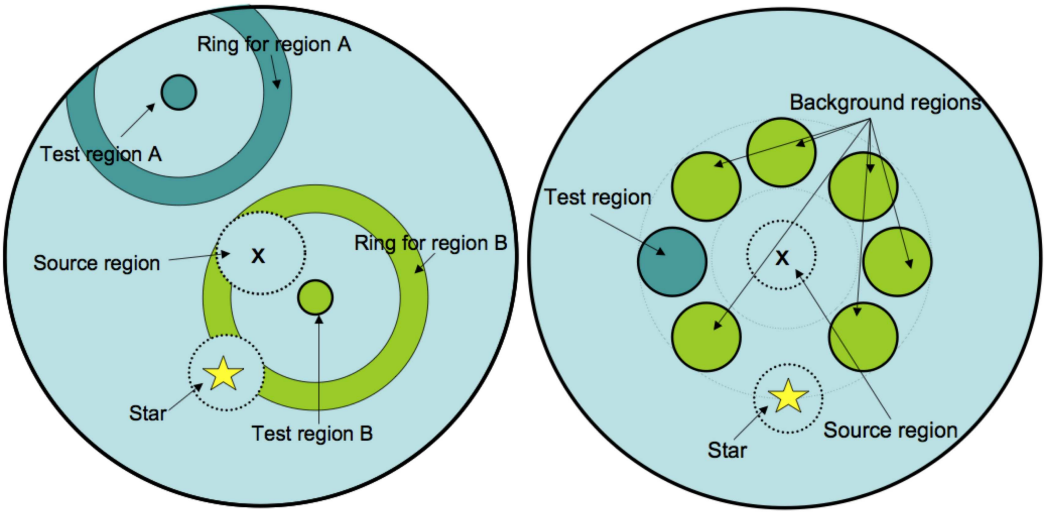

(a) Background estimation by ring method (b) Background estimation by reflected region method

Fig. 3.18 The two favoured methods of γ-ray background estimation for VERITAS. Taken from Guenette [2010].

the significance of detection, if any, is estimated from Li and Ma [1983] using the ON and OFF counts with the normalisation factor applied.

3.4.6 γ-ray energy estimation

A progenitor particle of a particular energy will produce an air shower whose development is a function of many parameters. Monte Carlo simulations are needed to relate particle energy with image size, S, and impact parameter, D, taking various factors like the NSB_{uv} (spurious blue / UV light), telescope elevation and the stereoscopic telescope combination (4 or 3 working telescopes) into account. From this calorimetric information, γ-ray flux and spectral energy distributions may be deduced, again with the aid of Monte Carlo simulations. As these estimations form a major part of this thesis, they will be dealt with in detail in Chapters 5 and 6.

3.4.7 The Cherenkov Telescope as atmospheric monitor

As aerosols are nearly always present in air parcels and their impact on the Cherenkov technique is still open to debate, methods of quantifying them are important. A seasonal decrease in run-by-run averaged L3 triggering rate at VERITAS, which can be seen in Figure 3.19, remained largely unexplained prior to this thesis. This figure shows four years (September 2012 to June 2016) of average L3 trigger rate for data runs $< 10^{\circ}$ from zenith plotted against time (MJD). Seasonal trends are visible, with the lowest triggering at end of the observing year (prior to summer-shutdown) with some evidence for lower L3 trigger rates at the beginning of the observing year too. As a small fraction of these triggers (0.1% to 0.01%) will possibly be γ-rays the L3 trigger rate decline, until better understood, raises concerns. The main concern is, does a drop of $\sim$25% in L3 trigger rate mean that $\sim$25% of potential γ-rays will be lost to detection? It had also been an open question at the outset of this thesis if this seasonal effect may have some bearing on γ-ray EAS calorimetry, whereby a spectral index of a particular source could be altered during periods of lower-than-expected triggering rate. Further, it was also an open question if the cause of lowering L3 rate could also change the effectiveness of γ/hadron separation algorithms, allowing more hadronic EAS to enter the analysis chain. These were and are very important questions that must be addressed.

A method to quantify decreased atmospheric transmission utilising an IACT triggering rate has been implemented with the H.E.S.S. telescope [Hahn et al., 2014]. This method relies on a relative calibration of telescope throughput, which is a global measure of the H.E.S.S. array level trigger rate efficiency. An IACT with higher throughput would have a higher array level trigger rate in a given atmosphere observing a particular astrophysical source location than an identical IACT with a lower throughput observing the same source location at the same time. With the relative calibration of each telescope used to normalise the throughput, any changes in array level triggering rate could not be ascribed to the telescope but other factors, namely atmospheric conditions. The end product of Hahn et al. [2014] is called

the Cherenkov Transparency Coefficient, which has vales from 0.0 (maximum extinction) to 1.0 (no extinction) at Cherenkov wavelengths.

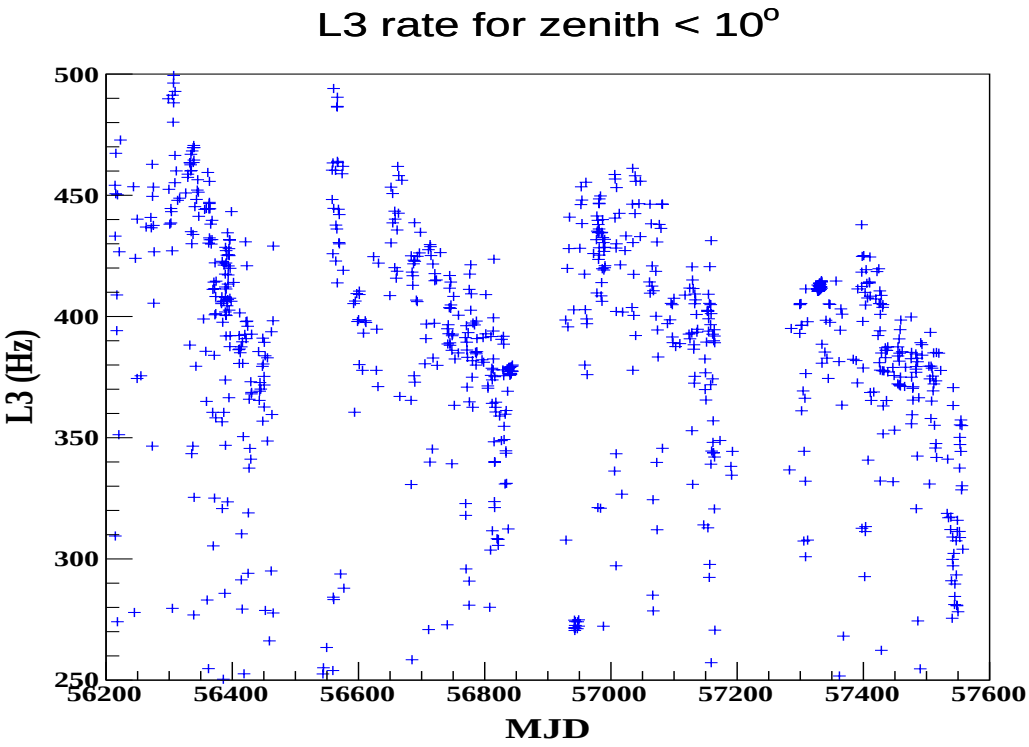

Fig. 3.19 A binned scatterplot, binning of two weeks and 5 Hz respectively, showing the averaged L3 trigger rate for data runs $\leq 10^{\circ}$ from zenith, from the 2012-2016 operation of the current VERITAS telescope configuration, V6. The plot comprises of $\sim$900 data runs. There is a clear downward trend in L3 trigger rate as summer-shutdown approaches. Additionally, there is a year on year reduction of unknown origin in peak L3 trigger rate.

Considerable time and effort was invested into implementing the Cherenkov Transparency Coefficient with VERITAS. The attempts were finally abandoned due to unexplained lowering of the VERITAS array level trigger rate on a regular basis. More will be said in Chapter 5. It is still possible to investigate if atmospheric conditions, such as increased aerosol extinction, can be seen in L3 trigger rates. This proposal is built on two premises examined now. Firstly, that protons constitute by far the bulk of progenitors of EASs in the energy range of Cherenkov telescopes and that they have no preferential arrival direction on Earth. Secondly, that the telescope triggering may be kept stable by holding to

strict operating conditions, outlined below.

The Cherenkov light yield from cosmic ray induced EAS must also be constant for stable atmospheric conditions. Heavier nuclei will produce more secondary particles which will result in larger EAS and greater Cherenkov light pools. Proton cosmic ray abundance is one order of magnitude greater than for He^{++} (as displayed in Figure 2.2). Additionally, the cosmic ray flux must be isotropic to avoid biasing in L3 trigger rates. This implies the cosmic ray induced trigger rate must be azimuthally independent for a given source elevation. This assumption has validity as cosmic rays, being charged particles, are deflected by galactic and inter-galactic magnetic fields before reaching the Earth. Their arrival direction is thus assumed to be largely isotropic, however the local geomagnetic field will have some effect on TeV shower development. Further, there is a well known anti-correlation between solar activity and cosmic rays arriving in Earth's atmosphere [Lockwood, 2002]. Only lower energy cosmic rays will succumb to deflection is this weak oscillating solar magnetic field of eleven-year periodicity. The energy of these charged nuclei falls below the detection threshold of IACT arrays, as will be seen in Chapter 5. Thus stated, our assumptions of isotropicity and proton relative abundance for cosmic rays seem valid.

An enumerated list of conditions relating to telescope response now follows. It must be met to minimise L3 triggering variability over a set time window.

1. Telescope array configuration: reducing the number of telescopes from four to three will reduce the L3 trigger rate, as the telescope multiplicity (set to 2) has fewer possibilities of being met with one less telescope. Four-telescope data only are thus used.

2. Non-operational PMTs: the full-component of 499 PMTs per camera are rarely all operational at the same time. Setting a maximum number of 10 dead PMTs per camera, representing 2% of total, should offset pixel level trigger rate drop.

3. Data acquisition dead time: should the buffering of data in the live stream from the telescopes fail to be processed in time by the Event Builder and parsed to the Har-

vester, the data acquisition will hang until the queue is flushed. This can increase dead time and reduce overall telescope throughput. Dead time should be kept to 10-14% maximum.

4. Telescope field of view: ideally the same sky patch should be used to minimise the effects of NSB_{uv} on triggering. Differing star fields can cause variation in pixel level trigger rate, when for example the light from bright stars falls on the intersection of three PMTs. Smaller zenith angle data runs are preferred, as the Cherenkov light yield from EAS drops sharply for increased source zenith angle. Additionally, there should be little or no moonlight present.

5. Molecular atmosphere: keeping to a particular molecular season, (VSummer or VWinter), and avoiding the changeover period where the molecular extinction may vary unpredictably, allows a constant molecular extinction to be assumed.

6. Cloud-free conditions: the CSR should fall below the threshold of 1.025 for all data runs.

Other factors are less critical: Mirror reflectivity; there is some evidence for telescope-wide mirror degradation over time (related in Figure 3.20), but over the course of weeks it can be taken as negligible. This is thanks to a dedicated mirror cleaning and re-coating regime Archambault et al. [2013], which sees a large percentage of mirror facets being replaced on all four telescopes over an observing season. PMT gain: the relative gain estimation of all PMTs means there is a nightly calibration that should keep the PMT gains stable over periods of several weeks. This is because all 499×4 PMTs will degrade at varying rates, which can be accounted for with software-level flatfielding. Telescope throughput: there is not presently a working estimate for relative telescope throughput applicable to atmospheric monitoring. It may however be assumed a constant over a time window of 6-8 weeks, thanks to a technique of using muon-ring air showers to monitor telescope throughput [Humensky, 2005].

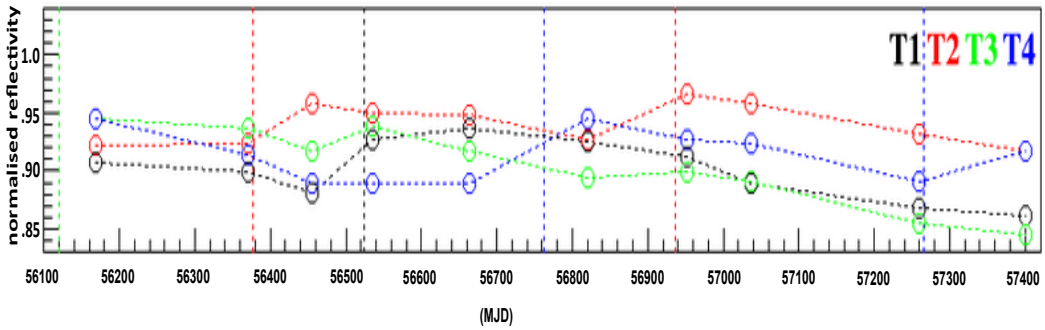

Fig. 3.20 A plot showing the mirror efficiency averaged for each of the 4 VERITAS telescopes from September 2012 to January 2016. The mirror efficiency is estimated in a lab, where mirrors are compared to newly coated mirrors [Roache et al., 2008]. A gradual degradation is evident over a number of years, but this is negligible over shorter timeframes of several weeks.

With this list of conditions fulfilled, any variability in L3 trigger rate should not be attributable to the telescope instrument response, but to aerosol atmospheric conditions alone.

3.4.8 The L3 trigger rate change displayed

Applying the criteria set out in Section 3.4.7 the following data sets were chosen, with the following information for each run to note

1. Run 67146 (Mrk 421) from MJD 56358.31458 (2013/03/07 07:33), which had an unexplained high L2 triggering on all telescopes.

2. Run 67286 (H1424 +428) from MJD 56363.41319 (2013/03/12 09:55), which had a number of recoated mirror facets fitted on T3 days before the run.

3. Run 67959 (Mrk 421) from MJD 56394.22292 (2013/04/12 05:21), which had the T4-L2 rate reduced from 3.5 kHz to 2 kHz, possibly due to bright pixels suppression (PMTs with high anode current have their HV turned off to prevent damage). Also to note, the following work was carried in the previous month. All 4 telscope mirrors washed and 94 recoated mirror facets fitted on T2.

4. Run 68251 (H 1424+428) from MJD 56414.28056 (2013/05/02 06:44), which had T2-L2 and T3-L2 rate slightly lower than other runs, with a high anode current in T4. Also, all 4 telescope mirrors washed the previous week.

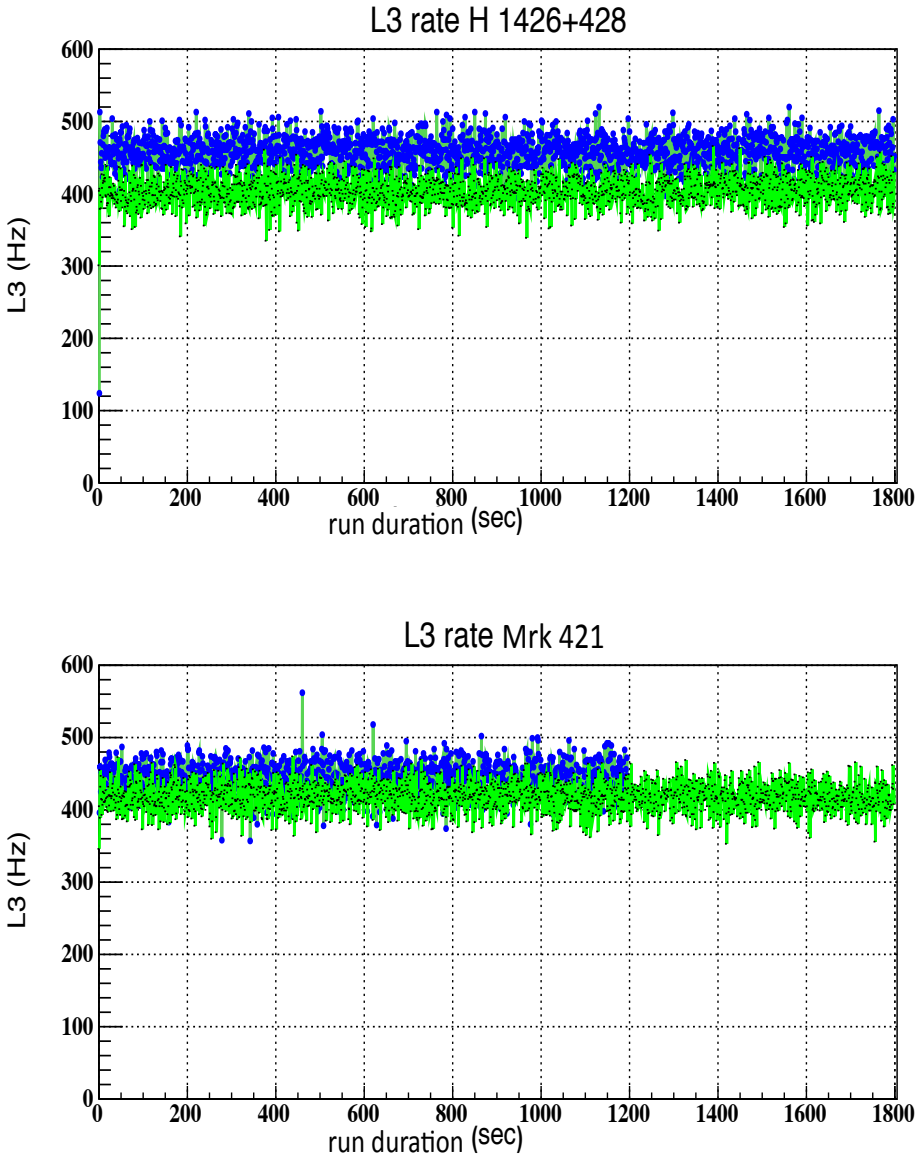

Fig. 3.21 A plot showing the L3 trigger rate (not averaged) for four individual low zenith data runs. (*top*) H 1424+428 with wobble offset of 0.5° west; run 67286 in blue and run 68251 in green. (*bottom*) Mrk421 with wobble offset of 0.5° south, with run 67146 in blue and run 67959 in green. There was a L3 rate drop of >15% between the H1426 +428 data runs. Note that the Mrk421 data run 67146 (blue) is only 20 min long; all other runs are 30 min duration.

These runs include observations of two extragalactic sources that rise high in elevation for VERITAS, Mrk421 (runs 67146 and 67959) and H 1424 +428 (runs 67286 and 68251). Both sets were at $\sim 20^{\circ}$ from zenith and wobble offset of 0.5° south and west respectively. No elevation correction is applied to the L3 trigger rate as all data sets are in the same elevation bin.

Referring to the enumerated data runs, mirror washing will increase the L3 rate, but as this happened later in the season when L3 rates are naturally lower it will serve only to minimise L3 rate drop. Run 67146 did not have an unusually high L3 trigger rate, despite elevated L2 rates. Run 67959 did not have excessive PMTs turned off / dead. In short, all the requirements of Section 3.4.7 were adhered to.

The raw triggering rates as a function of run time elapsed are plotted in Figure 3.21. Unlike data shown in Figure 3.19, the L3 trigger rate data are not averaged. This is to highlight the natural variations found in this complicated telescope variable. It was data such as shown in Figure 3.21 and many other examples besides that prompted this thesis.

It must be noted that another atmospheric component exists that could possibly cause the drop in L3 trigger rate. Sky temperature measured by a infrared radiometer (Figure 3.4) shows an increase at roughly the same time as the drop in L3 trigger rate is observed. The contemporaneous data from Figures 3.4 and 3.19 (within a 10 min time bin) are scatter plotted in Figure 3.22. Though there is no clear relationship between water vapour and L3 triggering, some possibility of anti-correlation needs to be examined in this thesis. Extensive simulation sets of EAS in varying water vapour conditions will be presented in Chapter 5, together with analysis.

As this thesis is inter-disciplinary, it now turns to regional aerosol studies to see what insight dedicated atmospheric experts, familiar with the Southwestern United States, may offer.

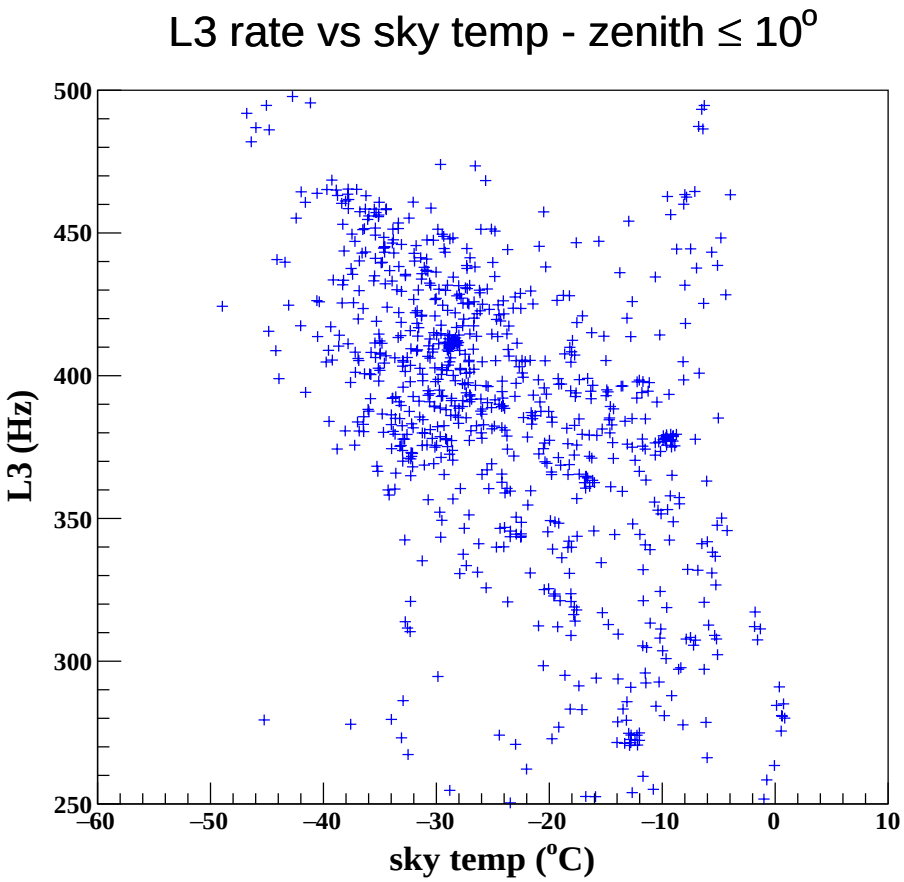

Fig. 3.22 A scatter plot of the same L3 array trigger rate dataset as Figure 3.19 with contemporaneous sky temperature estimate, taken from the dataset presented in Figure 3.4. Though there is some apparent structure to the plot with increased sky temperature corresponding often to lowering L3 triggering, no conclusions may be drawn, nor possible connection be ruled out without further investigation.

3.5 Regional aerosol studies for the South Western United States

Situated in the Coronado National Forest, at the foothills of the Santa Rita mountains, the Fred Lawrence Whipple Observatory site has been in existence for almost half a century as an astrophysical complex. The original Cherenkov imaging telescope, the 10 m Whipple telescope, was situated 1 km higher than the VERITAS array at an elevation of 2.3 km a.s.l.

[Holder et al., 2006b]. Being a foothill site, as distinct from a plateau, introduces difficult-to-model turbulence and mixing scenarios which will be detailed in the next chapter. VERITAS is only operational for about ten months per year. Moist air mass trajectories from the Gulf of Mexico well up and cross the Southwestern United States typically during July and August, causing a monsoon-like season where the Sonoran desert may receive up to 350 mm of rain in the form of heavy downpours and thunderstorms.

Fig. 3.23 A photo of the VERITAS array showing the large expanse of desert valley lower in altitude in the distance. The haze, visible in the distance, is due in large part to desert aerosols and had been quantified by a single extinction profile up to this thesis. Taken from Holder [2015].

As has been seen the amount of water in the atmosphere can increase by up to 500% over the average water vapour content found in the atmosphere during VWinter months (Figure 3.2). This moist air mass has aided the Sonoran desert in becoming the most biologically diverse desert on Earth, with many unique flora and fauna species. This fact is of some consequence to this thesis, as the particulate mix is not pure desert dust, as can be found in Saharan, Arabian gulf or North-East Asian regions. The Southwestern United States particulate mix has a higher percentage of organics and anthropogenic material which alters its overall optical properties accordingly. As can be seen in Figure 3.23, where the VERITAS array is in the foreground, the background expanse of desert displays some haze. The principal cause of this is believed to be desert aerosols. The work in this thesis aims to monitor

aerosol profiles from ground to heights of 5 km a.g.l. and quantify the aerosol extinction accordingly.

3.5.1 Regional aerosol study of southern Arizona

As stated by Sorooshian et al. [2011], dust strongly influences the atmosphere of the Tucson region between March and July. This is due to dry and hot weather and air-mass movements. Dust deposits, similar to the Sirocco dust episodes in Europe, are seen often during these times. At times it has necessitated the cleaning of the telescope mirrors. Trend analyses between 1988 and 2009 indicate increases in fine-soil aerosols during the spring (March-May) measured at select monitoring sites, which can be explained by population growth and land-use changes according to Sorooshian et al. [2011].

The most common air-mass trajectory (all altitudes, year on year) comes from the Pacific region. HYSPLIT from NOAA (the National Oceanic and Atmospheric Administration) is the preferred model for atmospheric trajectory and dispersion calculations [Stein et al., 2015]. Nearby dust-rich areas in the Southwestern parts of the United States and in Baja California have their aerosols transported overland and reach VERITAS and further inland. The important question to ask now is, can the optical properties of this dust mix be quantified and used in aerosol extinction correction? Firstly, in preparation for atmospheric aerosol extinction simulations that are an essential component of this thesis, an aerosol model is required. MODTRAN [Berk et al., 1998], discussed in more detail in the following section, is a radiative transfer code that offers a number of such models. Secondly, a value for a particular optical property of aerosols called the lidar ratio will be sought. This is the ratio between light scattering off aerosol particles over all solid angles to the scattering back along the direction of the light source. It is largely independent of aerosol loadings, however it is subject to seasonal variations, in addition to being height dependent [De Tomasi et al., 2006]. For a european research campaign from 2000 to 2002 it was found that the lidar ratio below 2 km a.g.l. varied differently than from 2-5 km a.g.l. The changes relating to Desert

dusts are dealt with in [Mona et al., 2012]. Discussion on modelling aerosol loading and the subsequent aerosol extinction profiles now follows.

3.6 MODTRAN simulations of atmospheric transmittance

This thesis relies heavily upon MODTRAN [Berk et al., 1989, Berk et al., 1998], a tried and trusted radiative transfer code which is in continuous development for over 40 years. MODTRAN is the U.S. Air Force standard moderate spectral resolution radiative transport modeling code. It caters for wavelengths extending from the ultraviolet to the visible and into the thermal infrared (200 nm to 10^7 nm). This thesis used two principal spectral bands, 205-700 nm for Cherenkov light (to be introduced in Chapter 5) and 900-920 nm for remote sensing instrumentation (to be introduced in Chapter 4). The spectroscopy of MODTRAN 5.2 is based on HITRAN2008 line compilation [Rothman et al., 1992]. The notable improvements to MODTRAN 5.2 compared to MODTRAN 4 include increasing the resolution of its spectral calculations to 0.1 cm^{-1} and increased speed and accuracy of multiple scattering calculations. Further, it models boundary layer aerosols whose extinction coefficient obeys the Angström law and can modify the extinction of a model aerosol with an Angström-law perturbation. The Angström law relates the aerosol optical properties and size distribution to optical response as a function of wavelength, where the Angström coefficient, $\dot{A}$, is

$$\frac{\tau_{\lambda_1}}{\tau_{\lambda_2}} = \left(\frac{\lambda_1}{\lambda_2}\right)^{-\dot{A}} \tag{3.9}$$

where τ is the aerosol optical depth, the sum of the aerosol extinction over the depth of atmosphere in question. It will be described in more detail in Chapter 4. λ_1 and λ_2 are the two wavelengths being compared.

A recent study [Wiegner and Gasteiger, 2015] has shown that a spectral resolution of 0.2 cm^{-1} is sufficient for effective water vapour extinction estimates. MODTRAN 4 would not

have been capable of this with it's spectral resolution of 1.0 cm^{-1}.

A radiative transfer package such as MODTRAN is useful for a number of reasons. For the molecular atmosphere, MODTRAN offers a number of standard atmospheric models which are ready to use. If the standard models do not sufficiently match the atmosphere in question, a user-defined atmosphere may be included up to a certain height a.s.l., after which MODTRAN will provide the atmospheric data from one of its particular models. This is done for VERITAS, as described in Section 3.2.1, using radiosonde data from Tucson to provide atmospheric density profiles up to 25 km a.s.l. after which the mid-latitude models are used. For the aerosol component of the atmosphere, a number of aerosol types are provided by MODTRAN. By means of regional studies such as found in Section 3.5.1, which explains the mineralogy and other properties of aerosols, an aerosol model of MODTRAN may be selected that best represents those found regionally. Further, high spectral resolution tables (from HITRAN) for molecular absorption lines, in particular H_2O and O_3, are referenced by MODTRAN and their contribution is added to the overall transmittance profile. This greatly reduces the computation time required for generation of moderate resolution transmittance profiles in comparison to deriving these profiles by raw computation alone.

3.6.1 The effects of changing molecular atmosphere on transmittance

The VERITAS molecular profiles are derived from radiosonde atmospheric sounding, as previously outlined in Section 3.2.1, where VSummer and VWinter seasons alone describe the atmosphere on site from September to June. This thesis employs user-defined molecular profiles ATM61 and ATM62, which are the VSummer and VWinter VERITAS molecular profiles respectively. They are an improvement on the previous molecular profiles, the ATM21 and ATM22 atmospheres, used to produce the original VERITAS Instrument Response Function (IRF) simulations for VERITAS data analysis. These IRFs will be examined in detail in Chapter 5. ATM61 and ATM62 produce a smoother plot of atmospheric density profile as a function of height thanks to interpolating of the radiosonde readings.

There is little difference, $\sim$3% in Cherenkov yield, between EAS simulations produced by both sets of profiles. The differences arise due to differing versions of MODTRAN being used for their production. Hence ATM61 and ATM62 are chosen as the new official collaboration-wide molecular profiles. More detail about this decision to change molecular profile is provided in Appendix A, along with information about the radiosonde soundings, differing atmospheric profiles and MODTRAN simulation setup.

As new aerosol extinction profiles are to be soon introduced, the following atmospheres have been produced whose molecular components are identical to ATM61 and ATM62, but with normal and twice normal water vapour content. ATM31, which corresponds to VWinter atmosphere with normal water vapour content (*1). ATM32, VSummer atmosphere with normal water vapour content (*1). ATM33, VWinter with twice normal water vapour (*2) and ATM34, VSummer with twice normal water vapour (*2). VWinter *1 $= 0.875$ g cm^{-2} and VSummer *1 $= 1.95$ g cm^{-2}, meaning that VSummer molecular atmospheres can hold up to twice the amount of water than VWinter. These atmospheric profiles give atmospheric density (g cm^{-3}), atmospheric depth (g cm^{-2}) and refractive index $(n-1)$ as a function of height. They have been specially produced to test their corresponding Desert Dust aerosol profiles, detailed in the next section, and also examine water vapour extinction at Cherenkov wavelengths (which is detailed in Appendix A).

3.6.2 The effects of changing particulate atmosphere on transmittance

The aerosol models used in MODTRAN are principally from [Shettle and Fenn, 1979, Shettle, 1984] and were constructed to represent the basic aerosol types on a regional basis: urban, rural, desert, maritime and tropospheric. Though a coarse typology, this method has stood the test of time, as the model allows fine tuning to be made by adjustment of the Angström coefficient. The models of Shettle and Fenn are built upon fundamental components, which are all water soluble; dust like, organics, soot, sea salt and water. In these aerosol models, the amount of water present is usually expressed as relative humidity (and

not PWV), which is the amount of water vapour present as a percentage of the amount of water needed for saturation at the same temperature. MODTRAN quantifies the changes in the aerosol particle's size and refractive index for varying levels of relative humidity, as high relative humidity means a higher likelihood of water vapour condensing onto the aerosol particles. From these fundamental components an average aerosol typology for each region is constructed. Shettle and Fenn [1979] call such aerosol typologies 'internally-mixed'. The concept of internal mixing refers to the highly dynamic turbulence in the atmosphere's boundary layer that causes constant mixing of the aerosol species until the component distribution is homogenous. For an internally-mixed air parcel, the optical properties of the individual aerosol components on the microscopic scale are subsumed into a global set of optical properties on the macroscopic scale. In short, a highly complex mix of differing particles with differing optical properties is replaced by one standard optical response. This dispenses the need for users to reference complex tables of aerosol species optical properties. The urban aerosol model, for example, has a component that is rural (dust, organics, water but no salt), and is weighted (by volume) with additional species representing anthropogenic aerosol sources. The Desert Dust model is simpler, consisting of dust and a smaller percentage of organics per volume than the rural model. The majority of aerosol species are therefore internally-mixed aerosol particles and are hygroscopic. This hygroscopicity is incorporated in such a way that when used in MODTRAN, the aerosol model (if correctly chosen) gives an accurate representation of the real aerosols optical properties under normal conditions.

The aerosol model chosen in this thesis is Desert Dust, deemed to be a good match for VERITAS aerosols for the following reasons. The aerosols are replenished by the year on year prevalent air mass trajectory over Southern California and Baja California. The resulting aerosol mix is very similar to the mix in the Desert Dust aerosol model found in MODTRAN [Shettle, 1984]. VERITAS is in the Sonoran desert, meaning that local dusts, the principal component of low-altitude aerosols, will be better modeled. The research into

desert dust properties from Shettle [1984] was carried out almost 40 years ago, principally in the Southwestern United States. It did not have access to data from more arid desert regions such as the Sahara or Gobi desert, which have a lower organics content. The next closest models on offer in MODTRAN, Rural Mix with 23 km visibility or Tropospheric model with 50 km Visibility, has a higher organics component than would be expected in a desert, even the Sonoran desert. Here Visibility is defined as the greatest distance at which a black object of suitable dimensions (to be easily visible in optimum viewing conditions), situated near the ground, can be seen and recognized when observed against a bright background. Visibility (by this definition) is more commonly referred to as the Meteorological Optical Range as reported in weather forecasts. The Tropospheric model, with a 50 km visibility, has been the working aerosol model used in VERITAS simulations prior to this thesis. Though it is of a differing aerosol constituent mix than the Desert dust model, it appears to work well for the VERITAS experiment. This is because comparative studies of particular astrophysical sources, undertaken by VERITAS, H.E.S.S. and MAGIC contemporaneously, have yielded consistent results over several years of data taking. More will be said in a comparative study between the Tropospheric and Desert Dust aerosol models in Section 5.2.6. The Tropospheric model is however limited to just one aerosol extinction profile, whereas the Desert Dust model can have a continuum. For this thesis the Tropospheric model with 50 km visibility is referred to as the official extinction profile, though 'official' does not imply best as no aerosol studies have been conducted at VERITAS before this thesis.

3.6.3 Producing atmospheric simulations

MODTRAN is programmed by means of so-called "input cards", a legacy from its development in the early days of computing. Input Card 1A of the radiative transfer code allows the relative humidity to be adjusted by varying the precipitable water vapour while Card 2 allows the aerosol content per unit volume, called aerosol loading, to be adjusted by use of Wind Speed Selector (WSS), where WSS10, a typical mid VWinter aerosol estimate for

VERITAS, has a lower aerosol loading than WSS16, a typical mid VSummer (elevated) aerosol estimate. WSS does not refer to the actual wind speed, which is nearly always measured at ground level, but refers to the forced mixing of the boundary layer due to a combination of wind, convective forces and the diurnal day / night change in boundary-layer height. The units of WSS are $\mathrm{m\,s^{-1}}$, where an increase in WSS brings a corresponding increase to the mean aerosol diameter and size distribution (when homogenous mixing is assumed). Figure 3.24 shows a plot of WSS10 (normal aerosol loading), and WSS16 (elevated aerosol loading), for a VWinter molecular atmosphere at VERITAS with normal water vapour. Note that the reduction in transmittance between both plots is due to aerosols alone, as the molecular atmosphere remains constant. Another plot, Figure 3.25, for WSS16 VSummer atmosphere with normal, *1, and twice normal, *2, water vapour content is shown. There is no appreciable difference in transmittance between then when the water vapour content alone is increased. If the atmosphere is participatory in the cause of L3 trigger rate drop (referred to in Section 3.4.8), these plots point possibly to aerosols being responsable (in part at least), and not water vapour. This will be examined in detail in Chapter 5.

It is noted that the molecular atmospheres mentioned above in Section 3.6.1, ATM31 to ATM34, have 11 aerosol extinction sets each. These extinction profiles correspond to WSS04 up to WSS24 in steps of WSS02; that is WSS04, WSS06,..,WSS22, WSS24. This fine gradient in aerosol extinction allows one to better test the effects of changing aerosol extinction on Cherenkov transmission. ATM61 and ATM62 have only one extinction profile, the 50 km Tropospheric extinction, which is close in extinction to WSS10. The first requirement for representative atmospheric aerosol simulations at VERITAS, a good aerosol model, has been met. Next a working estimate for the lidar ratio is required.

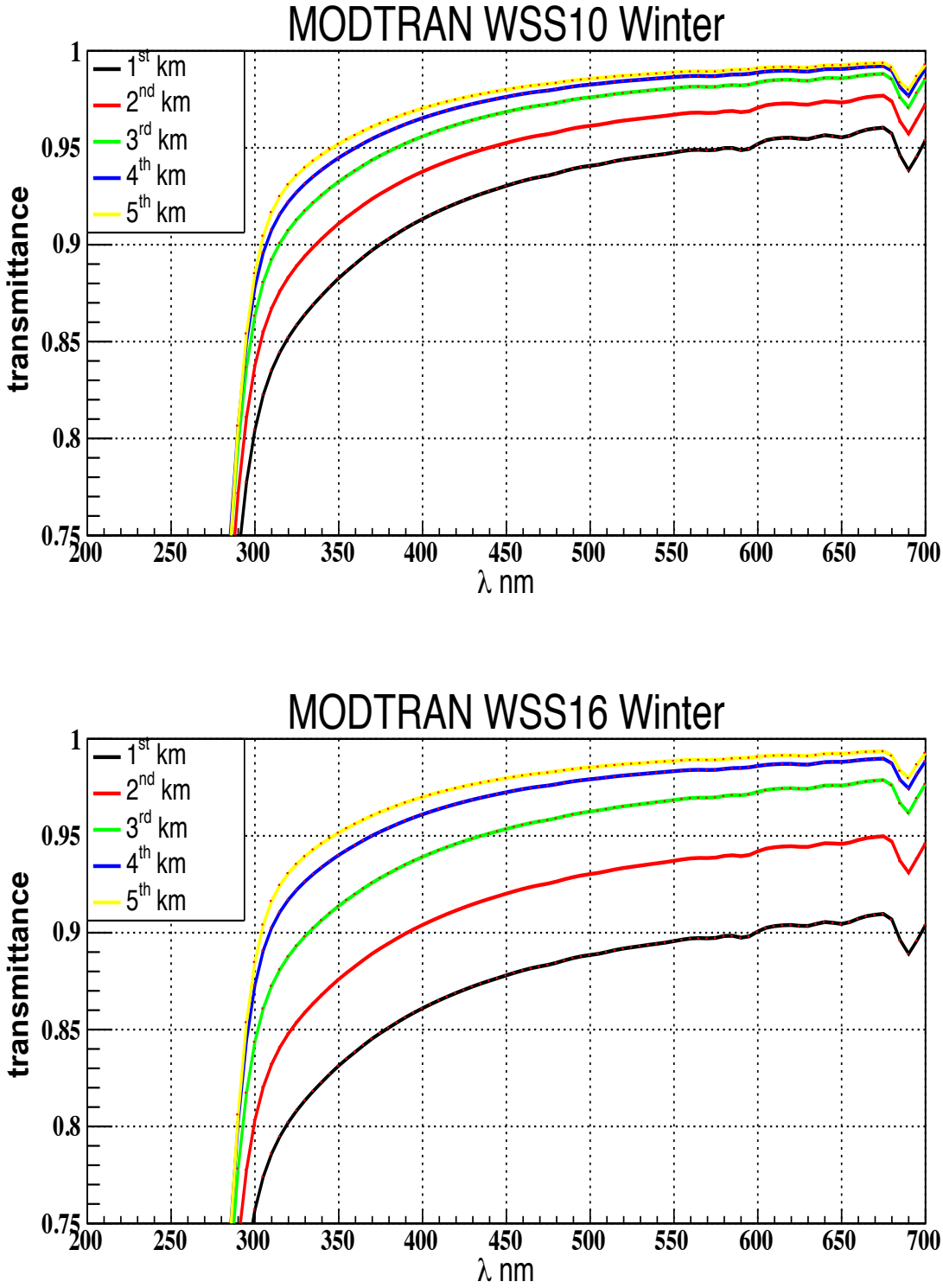

Fig. 3.24 A plot of the atmospheric transmittance derived from a VWinter atmosphere at VERITAS with normal water vapour (*1) and aerosol extinction WSS10 (top), and WSS16 (bottom). The boundary layer was set to 3 km, instead of the default 2 km, as this is more representative of the atmosphere at VERITAS and is to be explained in the next chapter. Above this boundary layer low aerosol loadings persist.

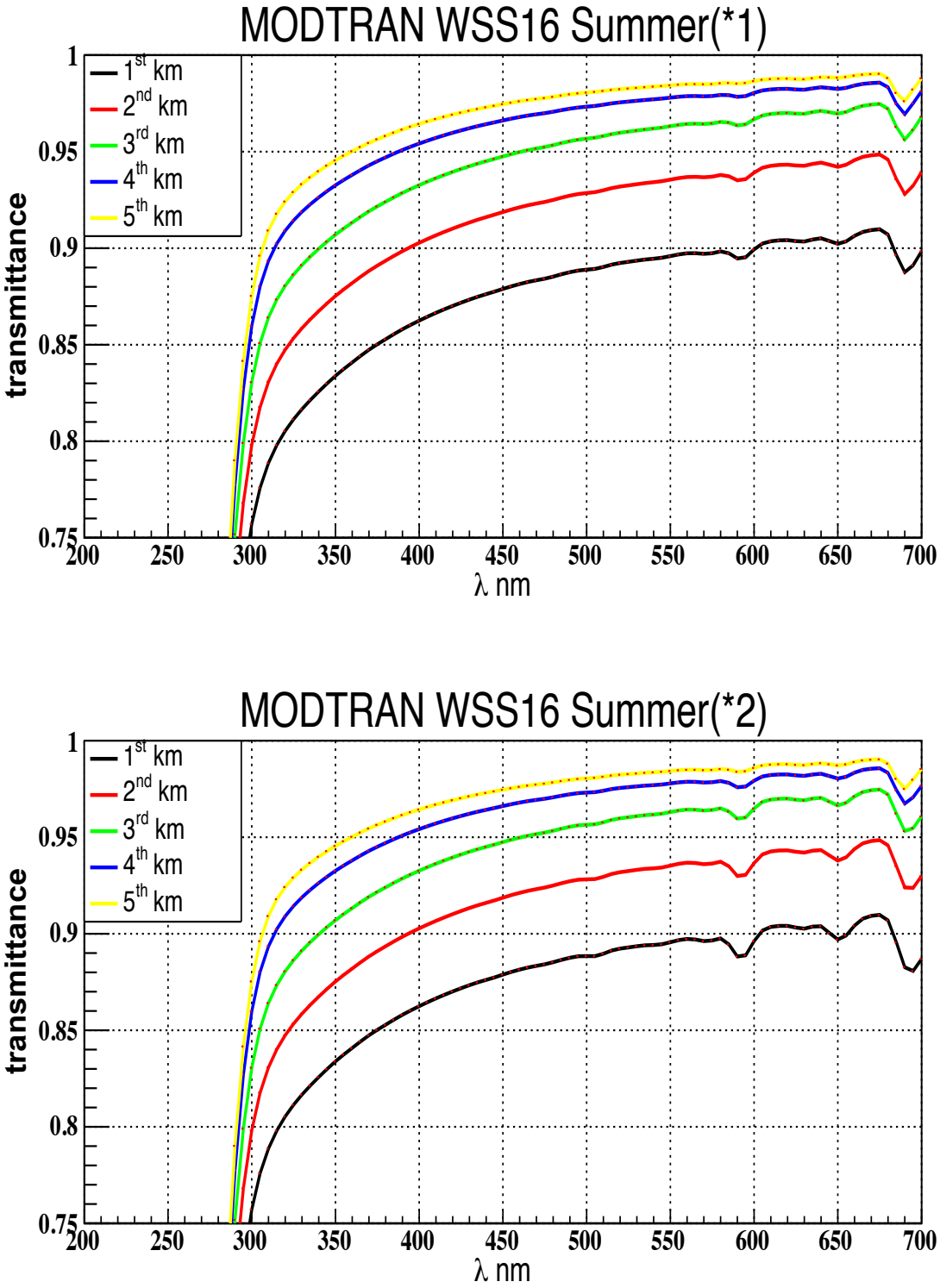

Fig. 3.25 A plot of the atmospheric transmittance for WSS16 VSummer atmosphere with normal (*1) (top), and twice normal (*2) (bottom), water vapour content. There is no appreciable difference in transmittance seen, seemingly ruling our water as the culprit in decreased transmittance during VSummer months.

3.7 Quantify aerosol optical properties with region-based studies

A key optical property needed for aerosol research is the ratio of scattering to backscattering or lidar ratio. A study by Burton et al. [2012] gives values of lidar ratio for various aerosol mixes. Being derived from a regional study in California, it drew data from slightly further north than the path of the prevailing trajectories that transport aerosols to VERITAS. The lidar ratio value thus has an unavoidably large uncertainty. This uncertainty would at first appear to limit the usefulness of the derived lidar ratio. However a Monte Carlo error estimation developed for turbulent environments and detailed in Chapter 4, shows that even a large lidar ratio uncertainty produces a low overall error in aerosol extinction estimation. The reason for this is that the uncertainty in aerosol extinction is derived from the product of the lidar ratio, which has a gaussian distribution uncertainty of $\pm 25\%$, and the backscatter from the lidar, with an uncertainty of $\pm \mathrm{BS}_{err}\%$. For the sample set in question, a lower estimate in lidar ratio multiplied by a higher estimate in backscattering (or visa versa) will keep the estimated aerosol extinction close to the median value, meaning that the Monte Carlo uncertainty estimate will be low (in the absence of particulate density anisotropies). The work in this thesis has assumed a constant lidar ratio with height up to 5 km a.g.l., which is an acceptable approximation when the total aerosol optical depth is of interest. More will be said of this in the next chapter. The obvious way to verify this would be to make a lidar ratio measurement at VERITAS using a Raman lidar [Muller et al., 2007], which lies outside the scope of this thesis. The Burton et al. [2012] derived value of lidar ratio for a Dusty Mix is 40 ± 10, which gives an uncertainty of $\pm 25\%$. This figure for lidar ratio is derived from data plotted in Figure 3.26, where the spread in values for lidar ratio is seen. The backscatter color ratio is defined as the ratio of aerosol backscattering, β, for two wavelengths, represented as $\beta^{532nm} \ / \ \beta^{1064nm}$, where β^{532nm} is the backscattering at 532 nm, β^{1064nm} the backscattering for 1064 nm. The aerosol backscatter coefficient at 532 nm

is a direct measurement made with the high spectral resolution lidar technique, while the backscatter coefficient at 1064 nm depends on a retrieval that uses an assumed lidar ratio; the systematic error in β^{1064nm} is $\leq 15\%$. There are indications that the central value for lidar ratio may vary seasonally from $38-42 \pm 10$, caused largely by changes in aerosol size distribution over the months [Sorooshian et al., 2011]. These small monthly variations are incorporated into this thesis.

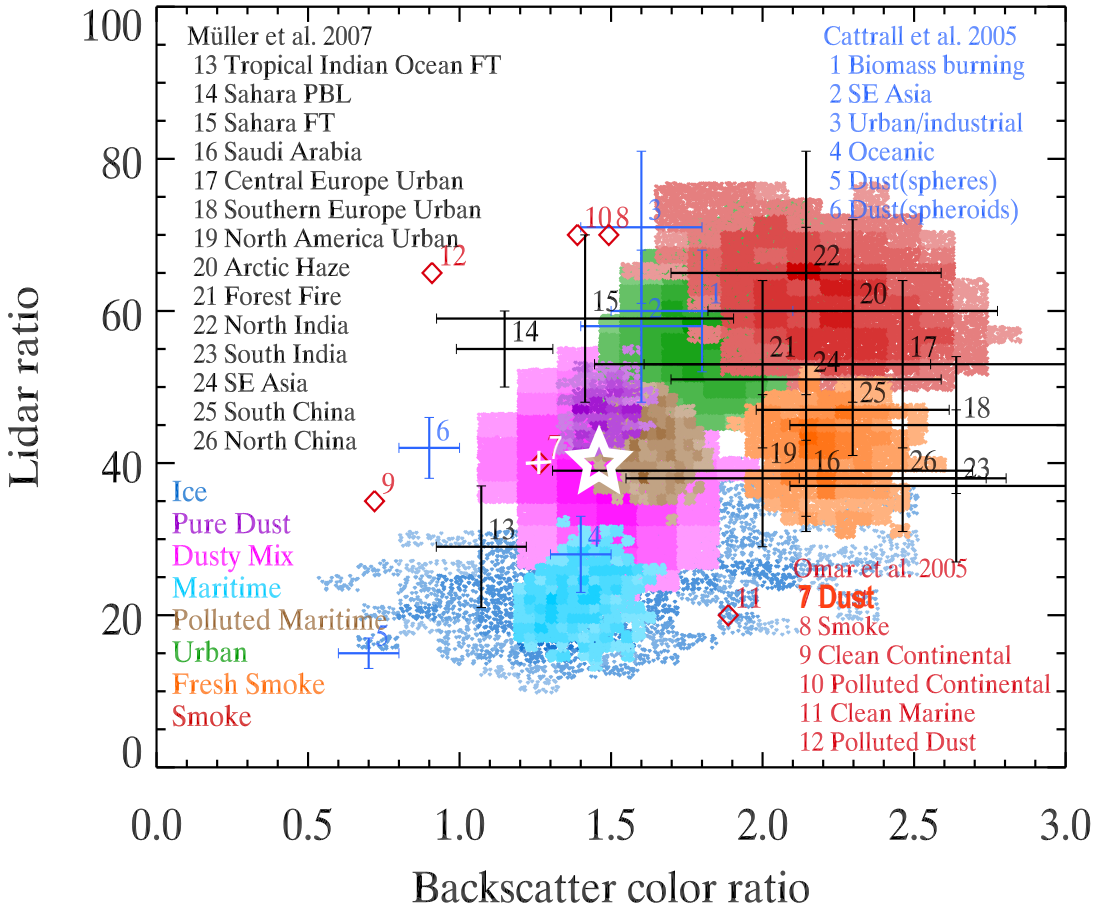

Fig. 3.26 A plot from Burton et al. [2012] showing the spread of values for the lidar ratio for various aerosol mixes. The Dusty Mix is chosen for VERITAS, coloured in pink, as it was derived from nearby California. The white star marks the central lidar ratio value used for this work. The white cross marked "7" is the lidar ratio for Dusts from a satellite-borne campaign Omar et al. [2009].

Figure 3.26 displays a white star which is centered on the lidar ratio used in this thesis. Note that a satellite-borne campaign [Omar et al., 2009] marked with a white + and num-

bered 7, has as its lidar ratio for Dusts a value very close to that chosen in this thesis. Pure desert dust, coloured purple, found in the deserts of the Atacama, Persian Gulf and Saharan, have a lidar ratio of 50-55 $\pm$5; the lower uncertainties are due to the low or near absence of organic and anthropogenic particulates in the aerosol mix.

3.8 The need for a method to quantify aerosol extinction

Ongoing monitoring of the atmosphere at VERITAS for the presence of clouds with three dedicated infrared cameras has successfully selected best clear sky conditions for observations, but the radiometers may not reliably be used for aerosol detection, as outlined in Section 3.3.2. The L3 trigger rate of the VERITAS telescope can monitor clouds in the field of view, and perhaps register the presence of elevated aerosols on site. However, aerosol detection based on L3 trigger rate will prove unreliable in the absence of either very stable telescope throughput or reliable correction of telescope throughput variability. Regional studies point to the presence of dusts and aerosols, but lack the necessary precision needed for atmospheric transmittance profiling.

In summary, an independent instrument capable of profiling aerosol loadings at VERITAS is required. The introduction of a cloud detecting and ranging remote sensing instrument opens the possibility of accurately detecting, ranging and quantify the presence of aerosols at VERITAS.

Chapter 4

Ceilometer application at VERITAS

4.1 Remote sensing of aerosols

Remote sensing is by far the most common method for aerosol profiling and temporal monitoring of columnar aerosol load. Atmospheric aerosol loading is suspensions of solids and / or liquid particles in the atmosphere. Large swaths of the Earth's atmosphere may be measured for aerosol content by satellite sensing in the infrared [Ackerman, 1997]. However, ground-based instrumentation offers the best spatial resolution for site-specific demands common to astrophysical observatories. Indeed satellite retrieval programmes require constant calibration of their data by ground-based instruments unless a coarse categorisation alone is required [Sorek-Hamer et al., 2013]. One of the most common methods of ground-based aerosol retrieval uses sun photometers such as the AERONET network [Li et al., 2014]. The best spatial and temporal resolution is provided by instruments with their own light source and have retrieval systems tuned into the expected return, to cut out as much background noise as possible. All subsequent attention will now be directed towards lidar technology, with particular detail being given to a class of lidar called ceilometers. Ceilometers are single-wavelength elastic-backscattering lidars of low power and high pulse frequency, used to detect and range cloud base layers.

Fig. 4.1 A photograph showing the positioning of the ceilometer at FLWO. It sits ∼3 metres above the base of Telescope 2 seen in the background, and ∼1-3 metres below Telescopes 1, 3 and 4. (Picture: J. Reynolds)

4.2 Ceilometers as distinct from lidars

The history and development of elastic lidars as high-resolution atmospheric-monitoring instruments has been documented extensively [Kovalev and Eichinger, 2004, McCormick, 2005, Weitkamp, 2006]. The advent of this application occurred soon after the invention of the laser [Goyer, 1963]. Originally powerful lasers were exclusively used in elastic atmospheric backscattering retrieval campaigns, which offered narrow spectral widths ($<$ 0.01 nm), wavelength tunability, high peak energies ($>$ 1.0 J) very short pulse width ($<$ 10 ns), in addition to very narrow beam divergences ($<$ 0.5 mrad). These powerful light pulse generators are usually Q-switched ruby or Nd:YAG lasers (Neodymium-doped Yttrium Aluminium garnet, where Nd is $Y^3Al^5O^{12}$, a crystal lasing medium for solid-state lasers). Today they are being superseded in many cases by much smaller ceilometers with μJ InGaAs (Indium Gallium Arsenide) diode lasers with pulse rates in the low kilohertz region [Tsaknakis et al., 2011]. These high switching rates allow for greater rejection of background noise and hence greater Signal to Noise Ratio (SNR), with the added value of eye-safe operation (Class 1M for a Vaisala CL51) and lower production and running costs, but at the expense of power and, hence, detection range.

4.2.1 The lidar equation and atmospheric transmission

As ceilometers are a sub-class of lidars, the same basic physics hold for both. The elastic backscattered signal retrieved from the emitted pulses is governed by the lidar ratio equation, presented here in simplified form [Münkel et al., 2007]:

$$P_{(z,\lambda)} = \left(\frac{c}{2z^2}\right)\left(P_o\, A\, \eta\, O_{(z)}\, \Delta t\right)\left(\beta_{(z,\lambda)}\, \tau^2_{(z,\lambda)}\right) \tag{4.1}$$

where c is the speed of light, Δt is the laser pulse duration, P_0 is the average laser power during the pulse, A is the area of the receiver optics and η is its overall efficiency (optical and electronic). $O_{(z)}$ is the range-dependent overlap integral between the transmitted beam

and the field-of-view of the receiver (complete overlap at $O_{(z)} = 1$). $\beta_{(z,\lambda)}$ is the backscatter coefficient (units of m^{-1}), $\tau_{(z,\lambda)}$ is the optical depth of the atmosphere between the lidar and the scattering volume, λ is the wavelength of the emitted laser pulse, and z is the distance between the lidar and the scattering volume. Optical Depth (dimensionless) is defined as the natural log of the ratio of the light energy falling on a body or a surface to that transmitted through it (the Transmittance, T)

$$\tau_{(z,\lambda)} = -lnT \tag{4.2}$$

In addition to $\beta_{(z,\lambda)}$ the extinction coefficient, $\alpha_{(z,\lambda)}$ (units of m^{-1}) and their ratio $S_{(z,\lambda)}$, the lidar ratio, are important. In an elastic scattering medium, $\alpha_{(z,\lambda)}$ is a measure of the scattering in all directions while $\beta_{(z,\lambda)}$ is the scattering directed back to emitter source. As the atmosphere is gaseous with particles in suspension, it is neccessary to break up the components of the lidar equation accordingly. Normally a simplified atmospheric scenario is introduced, where the change in aerosol optical properties due to water vapour condensation onto the aerosol particles is ignored. Hygroscopicity is accounted for in this study thanks to MODTRAN's ability to model this added complexity. The constituent components of the backscatter coefficient are

$$\beta_{(z,\lambda)} = \beta_{mol(z,\lambda)} + \beta_{par(z,\lambda)} + \beta_{hygro(z,\lambda,H_2O)} \tag{4.3}$$

The subscript *mol* represents the molecular scattering component, the subscript *par* the particulate (aerosol) component while *hygro* denotes the change in the optical properties of the aerosol species in varying water vapour due to the aerosols hygroscopic properties.
The extinction coefficient, $\alpha_{(z,\lambda)}$, is related to optical depth $\tau_{(z,\lambda)}$ by

$$\tau_{(z,\lambda)} = \int_0^z \alpha_{(z,\lambda)} dz \tag{4.4}$$

where

$$\alpha_{(z,\lambda)} = \alpha_{mol(z,\lambda)} + \alpha_{par(z,\lambda)} + \alpha_{H_2O(z,\lambda)} \tag{4.5}$$

Here the gaseous H_2O, water vapour, adds to the overall molecular extinction as a constituent gas, but its volatility gives it a unique status. It is not independent of the overall molecular optical scattering response but is treated separately due to its high temporal variability. The relevance of water vapour (measurements of which for VERITAS are given in Section 3.2, derived from nearby radiosonde data) in the backscattering and extinction components of the lidar equation are non negligible at the wavelengths of the Vaisala CL51 used in this study, namely 905-910 nm, λ_{CL51}. The Vaisala CL51 laser has a wide spectrum, whose peak emission wavelength will change with temperature and also over time. This will be discussed in Section 4.3.

Acknowledging that the atmosphere has both elastic and inelastic scattering, is is necessary to define the total optical depth

$$\tau_{total} = \tau_{scat} + \tau_{abs} = \left(\tau_{mol} + \tau_{par}\right) + \left(\tau_{H_2O} + \tau_{carbon} + \tau_{O_3} + ...\right) \tag{4.6}$$

where subscript *scat* denotes elastic scattering, and *abs* denotes absorbance or damping, which can have many constituent components. This thesis will deal with elastic scattering, with correction for water vapour (inelastic) extinction, while MODTRAN is able to account for Ozone, O_3 extinction. However, the optical response of air parcels with carbonaceous aerosols is not catered for.

The lidar ratio for elastic backscattering, $S_{par(z,\lambda)}$, is defined as

$$S_{par(z,\lambda)} = \frac{\alpha_{par(z,\lambda)}}{\beta_{par(z,\lambda)}} \tag{4.7}$$

A working value for $S_{par(z,\lambda)}$ has been derived for VERITAS in normal atmospheric conditions from regional studies as detailed in Section 3.7.

The theory of the Beer-Lambert-Bouguer law (Section 2.3 and Equation 4.8) relates the at-

tenuation of light to the properties of the material through which the light is traveling. It can be approximated by a simple relationship when the incident light has a wavelength in an atmospheric transmission window, that is when the light experiences little or no scattering by the molecular atmosphere. This is the case for various wavelengths in the IR, including λ_{CL51}

$$T = \frac{I}{I_O} = e^{-\tau_{(z,\lambda)}} \tag{4.8}$$

where I is the radiant flux transmitted by the air parcel and I_O is the radiant flux received by the air parcel and $\tau_{(z,\lambda)}$ is the optical depth. This relationship of transmitted to received flux is shown in Figure 4.2, where $\tau_{(z,\lambda)} = \alpha_{(z,\lambda)} \times z$, assuming a homogenous extinction coefficient through z.

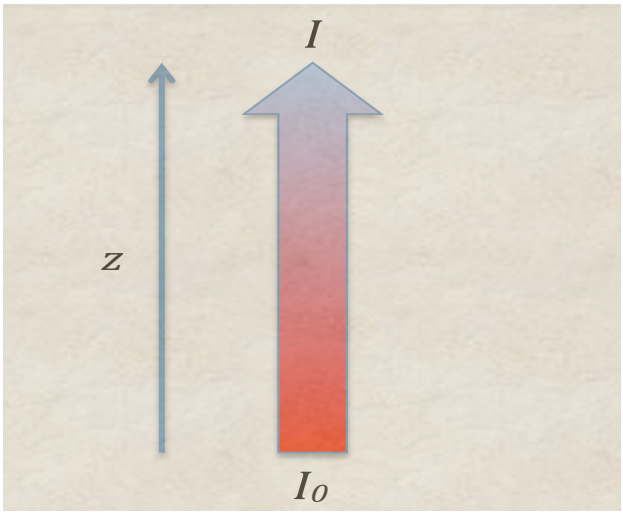

Fig. 4.2 A simple plot to demonstrate the Beer-Lambert-Bouguer law for light passing through a section of atmosphere with aerosol loading; the shaded area (aerosols) is characterised by $\alpha_{(z,\lambda)}$, the extinction coefficient.

In cases where $\tau \ll 1$ (*i.e.*, a transparent medium or atmospheric transmission window), the transmittance T can be approximated by

$$T = e^{-\tau_{(z,\lambda)}} \approx 1 - \tau_{(z,\lambda)} = 1 - (\alpha_{(z,\lambda)} \times z) \tag{4.9}$$

This only holds when atmospheric optical conditions relate to transmission windows, such

as those present at λ_{CL51}. Any transmission losses are due to the total elastic scattering in the medium alone. In this case $\alpha_{(z,\lambda)}$ is estimated from all its constituent components (listed in Equation 4.5), gaseous, particulate and water vapour, the last of which must be removed by correction methods soon introduced.

4.2.2 Mie scattering examples

Mie theory simulations are now presented in Figures 4.3, 4.4 and 4.5 derived from MiePlot, Laven [2003], a Mie scattering algorithm that aids in displaying the scattering of light from aerosol particles. The logarithmic polar scales refer to scattering intensity, while the values for peak backscattering intensity, at 0°, are found in Table 4.1. The incident light is from the right at 0°.

For these plots to be representative of VERITAS conditions, the coated sphere option (water vapour condensed onto spheres) was chosen above pure Mie scattering for spheres. For simplicity, no spheroidal or asymmetrical particles are incorporated. The index of refraction, m, of a sphere in Mie theory (introduced in Section 2.5.1) is given as

$$m = n\big(1 - i\,k\big) \tag{4.10}$$

where the the real refractive index is n and the complex refractive index, nk, is the damping factor while k is called the index of attenuation. Note that the sign of the imaginary part of the index of refraction is negative, meaning that large values of k point to inelastic scattering. The values for the real and complex refractive index of the aerosols simulated are reported from an African research campaign [Di Biagio et al., 2014]. The African desert mineralogy matches closely the Sonoran desert, and are applied to MiePlot simulations for VERITAS. The refractive index values used for the spherical mineral particle are n = 1.5, k = 0.05 for desert dusts and n = 1.9, k = 0.7 for spherical carbonaceous particles. The absorption, nk, according to Di Biagio et al. [2014], arises mainly from carbon but also from clays, less so

from pure minerals which make up the bulk of desert dusts. The Mie scattering simulations are carried out for separate wavelengths, the infrared (specifically the ceilometer's wavelength called λ_{CL51}) and the blue / UV (specifically the atmospheric Cherenkov wavelength band).

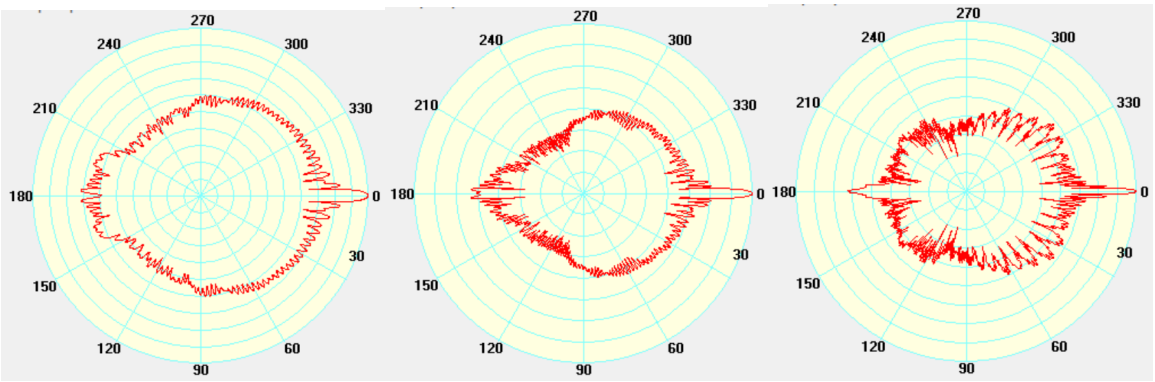

(a) (10+0) μm, scale x0.150 (b) (10+2.5) μm, scale x0.402 (c) (10+10) μm, scale x2.457

Fig. 4.3 MiePlot scattering of non-polarised 910 nm monochromatic point source of 100 W m^{-2} placed 100 m from spherical mineral particle with diameter ϕ_{par} = 10 μm and real refractive index, n, =1.5, while k = 0.05. The scattering intensity is plotted on a logarithmic polar scale (with scaling factor shown), while the incident light is from the right at 0°. The 0, 2.5 and 10 represents the increase in particle diameter in μm due to H_2O condensation. Refer to Table 4.1 for the normalisation giving rise to the scale factor.

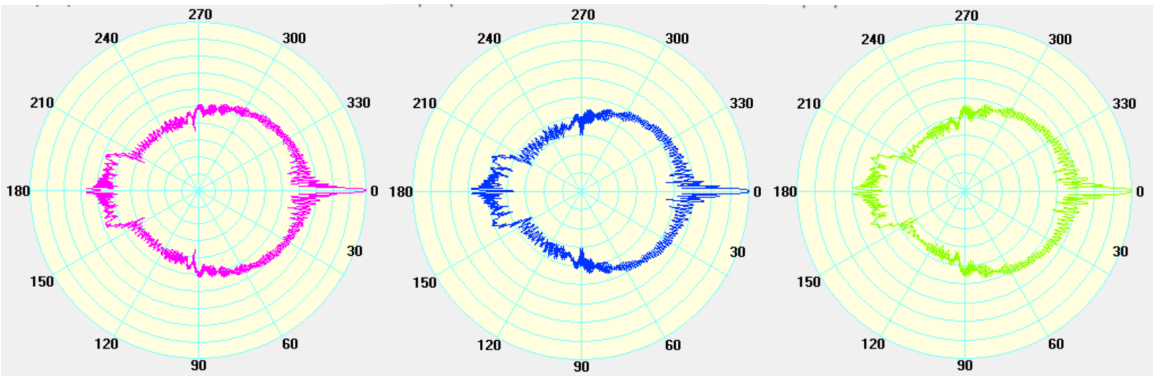

(a) 350 mn, scale x1.000 (b) 450 mn, scale x0.579 (c) 550 mn, scale x0.387

Fig. 4.4 MiePlot scattering of same point source as Figure 4.3, but with wavelength of 350 nm, 450 nm and 550 nm. The mineral particle diameter ϕ_{par} = 10 μm, but with no water coating.

A mean aerosol diameter of ϕ_{par} = 10 μm, $\sim 10 \times \lambda_{CL51}$, is chosen because this is one of the most prevalent values for aerosol diameter in the Sonoran region [Csavina et al., 2011]. Figure 4.3 shows scattering at λ_{CL51} while Figure 4.4 shows scattering for Cherenkov wave-

λ *(nm)*	$\phi_{par}(\mu\text{m})$	BS_{peak} (W m^{-2})	*ratio* BS_{peak}
350	10.0	8.75x10^{-9}	1.000
350	12.5	2.10x10^{-8}	2.400
350	20.0	1.37x10^{-7}	15.657
450	10.0	5.07x10^{-9}	0.579
450	12.5	1.24x10^{-8}	1.417
450	20.0	8.32x10^{-8}	9.509
550	10.0	3.39x10^{-9}	0.387
550	12.5	8.38x10^{-9}	0.958
550	20.0	5.62x10^{-8}	6.423
910	10.0	1.31x10^{-9}	0.150
910	12.5	3.52x10^{-9}	0.402
910	20.0	2.15x10^{-8}	2.457
350	10.0	8.61x10^{-9}	0.984
450	10.0	5.27x10^{-9}	0.602
550	10.0	3.56x10^{-9}	0.407

Table 4.1 Backscattering from Mie theory simulations for various aerosol sizes and λ_{CL51}/Cherenkov wavelengths. For the upper part of the table, the light source and refractive index values are as for Figure 4.3. The lower part of table is for spherical carbonaceous particle, with refractive index values n = 1.9, k = 0.7, whose Mie scattering is plotted in Figure 4.5. The *ratio* BS_{peak} column is the peak backscattering from a particle of diameter ϕ_{par} and wavelength λ divided by peak backscattering from a particle of diameter ϕ_{par} = 10 μm and wavelength λ = 350 nm. Results derived from MiePlot.

lengths (with just three representative wavelengths examined; 350, 450 and 550 nm respectively). MODTRAN is able to account for differences in scattering arising from differing wavelengths once the correct aerosol model is chosen, due to Angstrom coefficients (discussed in Section 3.6.2) being known for the particular aerosol typology. It can be seen in Figures 4.3, 4.4 and 4.5 that backscattering is confined to a narrow solid angle, while the scattering in all other directions, extinction or $\alpha_{par(z,\lambda)}$, is much more irregular over a given solid angle. It would be very difficult to place a detector, an avalanche photodiode for exam-

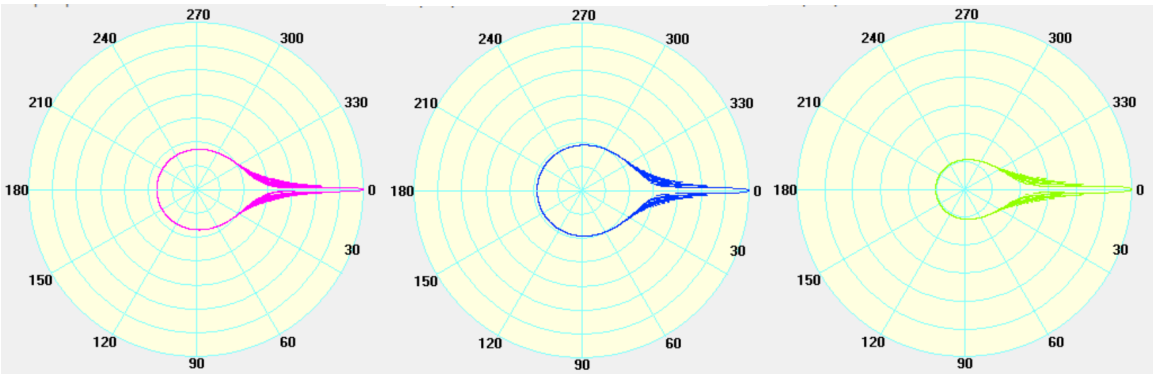

(a) 350 mn, scale x0.984 (b) 450 mn, scale x0.602 (c) 550 mn, scale x0.407

Fig. 4.5 MiePlot scattering from spherical carbonaceous particle ϕ_{par} = 10 μm with no water coating. The real refractive index, n, = 1.9, index of attenuation, k, = 0.7, are taken from Di Biagio et al. [2014]. All plot parameters as for Figures 4.3 and 4.4.

ple, at a fixed scattering angle (20° for example), and determine the overall extinction from this reading alone. This is why the estimation of $\beta_{par(z,\lambda)}$ is nearly always more accurate than estimations of $\alpha_{par(z,\lambda)}$ by scattered light retrieval methods, and will be used in this thesis.

Table 4.1 shows a number of peak-backscattering estimates from Mie simulations, for varying wavelength, particle diameter, hygroscopicity and refractive index. An increase in particle diameter (due to water vapour condensation) by a factor of 2 increases backscattering by a factor of 15-20. It is beyond the scope of this thesis to determine what degree of water vapour condensation actually occurs at VERITAS. These simulations seek to show the effects could be non-negligible in field backscatter retrieval campaigns. Interestingly and of some concern, carbonaceous particles of similar size to mineral particles have an almost identical backscatter signature, see Figure 4.5. However the inelastic nature of carbonaceous aerosol extinction, more properly referred to as attenuation or damping, lowers the lidar ratio drastically. It must be recalled that this thesis deals with single-wavelength elastic scattering. When inelastic interactions between photons and the absorbing/scattering surfaces occur, a large and difficult-to-determine percent of the incident light is re-radiated at a differing wavelength, usually in the infrared. A smaller percentage of the scattering

light will be at the same wavelength as the incident light, hence the lidar ratio is reduced often by an order of magnitude. Carbonaceous particles are on average much larger than mineral aerosols due to their semi-hollow internal structure. Being much less dense than mineral aerosols, the atmosphere can keep soot particles, often referred to as black or brown carbon (as introduced in Section 2.5), up to $\phi_{par} = 100\ \mu$m in suspension for considerable times.

4.2.3 Solving the lidar equation to determine $\alpha_{par(z,\lambda)}$

It is necessary to derive the particulate extinction coefficient, $\alpha_{par(z,\lambda)}$, or at least the particulate backscatter coefficient, $\beta_{par(z,\lambda)}$, from the lidar equation. Having the particulate extinction and the molecular extinction allows calculation of the total transmittance of the atmosphere.

A constant lidar ratio with height can not be assumed always, further it must be noted that the lidar ratio, $S_{par(z,\lambda)}$ (Equation 4.7), holds only for purely elastic scattering at a single wavelength. For this thesis, it is assumed that $S_{par(z,\lambda)}$ is invariant over five vertical height bins of 1 km each (5 km in total) and that all atmospheric scattering at λ_{CL51} is elastic, in the absence of water vapour extinction (which can be corrected for). Mention was made in Section 3.5.1 that the lidar ratio is in fact height dependent; however the first 2 km a.g.l. are where the greatest concentration of particulate matter is found, making the largest contribution to the aerosol optical depth. For simplicity therefore the 5 km a.g.l. can be assumed to have a constant lidar ratio.

The derivation of $\alpha_{par(z,\lambda)}$ suffers from an inherent problem with all backscattering lidars, namely the unknown (or approximate in our case) lidar ratio $S_{par(z,\lambda)}$. This is because the retrieval of $\alpha_{par(z,\lambda)}$ is strongly influenced by the accuracy of the estimated lidar ratio [Wiegner et al., 2014]. The accuracy of the retrieval of $\beta_{par(z,\lambda)}$ is normally less sensitive to lidar ratio error, in particular at wavelengths in the near infrared.

Normally for $\beta_{par(z,\lambda)}$ retrieval methods, a backscattering measurement is needed from an

aerosol-free region of the atmosphere to serve as a reference. The calibration of lidar signals by such means is not an issue for powerful laser systems, but could cause intractable problems in the case of ceilometers. The reason for this is the low pulse energy of the laser resulting in a low SNR from layers above the free troposphere where aerosol-free conditions are expected. This can be mitigated to some degree if night-time measurements alone are needed.

In the case of elastic backscattering lidars, $\beta_{par(z,\lambda)}$ is normally derived by the methods outlined in Klett [1981]. An earlier general description of the concept can be found in Fernald et al. [1972]. In these methods $\alpha_{par(z,\lambda)}$ is expressed in terms of an optical depth $\tau_{par(z,\lambda)}$, from which a linear differential equation for $\tau^2_{par(z,\lambda)}$ is obtained. The solution requires both an estimate of the lidar ratio $S_{par(z,\lambda)}$ and assumptions on its stability over the height of the air parcel in question. The instrument's characteristics, such as aperture size, optical and signal processing efficiency, laser power among others, are described by the lidar constant. This lidar constant C_l is normally substituted by a boundary value derived from Rayleigh calibration, a backscatter signal from the aerosol-free upper troposphere. For the Vaisala CL51 Rayleigh calibration will require up to several hours of cloud-free backscattering data from heights $>$ 10 km above ground level (a.g.l.) to ensure a sufficient SNR from purely molecular backscattering. If this is possible the aerosol backscatter coefficient is zeroed, $\beta_{par(z,\lambda)}(z_{ref}) = 0$, enabling calibration of the ceilometer return signals.

4.2.4 A new proposal for determining $\alpha_{par(z,\lambda)}$

This thesis proposes a new method for determining the particulate extinction coefficient, $\alpha_{par(z,\lambda)}$, that does not rely on Rayleigh calibration, avoiding the associated problems with low SNR. The backscattering data from the Vaisala CL51 up to 5 km a.g.l. are used with the regional values of lidar ratio (40$\pm$10, as described in Section 3.7) to approximate $\alpha_{par(z,\lambda)}$ (by means of the lidar ratio, Equation 4.7). Next the molecular extinction, $\alpha_{mol(z,\lambda)}$, is calculated from molecular extinction tables derived from user-defined radiative transfer sim-

ulations (detailed in Section 3.6.1), again up to 5 km a.g.l. All of these components have their associated errors calculated. Next, an estimate of the combined transmittance profile of the atmosphere (molecular and particulate) with errors, up to 5 km a.g.l. is calculated by the Beers-Lambert approximation (using Equation 4.9). This estimate is then matched with a particular simulated atmospheric transmittance profile from a large set of pre-generated transmittance profile simulations. This method may be thought of as comparing derived atmospheric transmittance profiles with simulated atmospheric transmittance profiles until a best match is found by least-squares. The best-match simulated transmittance profile then becomes the *de facto* working atmosphere for the skies above the VERITAS telescope. It is now necessary to examine the ceilometer's characteristics in detail before this proposal may be implemented.

4.3 Vaisala CL51 characteristics

Vaisala manufacture approximately 90% of the ceilometers currently in operation in Europe. Introduced in 2010, the CL51 model was originally designed to detect up to three cloud layers, up to a range of 13 km a.g.l. It also offers boundary-layer height detection up to 4 km a.g.l. thanks to its increased optical aperture and a more powerful laser compared with previous models. The CL51 contains a Class 1M InGaAs laser diode with a nominal wavelength of $\sim$905-910 nm. The pulse duration is 110 ns with a pulse repetition rate of 6.5 kHz and pulse power of 3 μJ. Importantly, the instrument is not temperature regulated, but has a heater attached to the laser heatsink for cold temperature operation. The laser wavelength drifts with changes in ambient temperature at a rate of 0.25 nm K^{-1}. A laboratory measurement by Vaisala of the CL51 deployed at the VERITAS site gave a peak wavelength of 907 nm at 25 °C. This value will change over the lifetime of the instrument. The laser pulse has a FWHM of 4-5 nm.

A CL51 ceilometer has been deployed at the VERITAS site since December 2011. It has

been in near-continuous operation since, apart from annual shutdowns during the Arizona rainy season of July and August. It gives real-time cloud layer detection using the proprietary CLview software from Vaisala. This is used by the VERITAS observing crew in optimising astronomical observing strategies. The summed attenuated backscatter up to 15 km a.g.l. (broadly representative of aerosol optical depth) and the lowest cloud base heights are timestamped and recorded in the VERITAS astronomical data stream. Offline analysis is made possible by the output binary files being converted to ASCII format. These files contain the attenuated backscatter in 10 m and 6 s bins in addition to the cloud layers detected, internal temperature, ambient light at 905 nm, laser output power and window transparency, among others.

4.3.1 Attenuated backscatter as end-user data

The end user data for all Vaisala ceilometers is attenuated backscatter alone. At its most basic, the attenuated backscatter is the range and overlap-corrected return laser pulses at 10 m resolution where various factors such as varying window transparency (impacting on laser output power) are accounted for. A sample rate of 15 MHz is required to achieve a range resolution of 10 m, where the first observation reported at 10 m is the backscattered signal for 5 to 15 m from the ceilometer. The Vaisala CL51 operates in 2-second time blocks. The first 1.6 s sees laser pulses emitted with a frequency of 6.5 kHz, this is followed by 0.4 s of no laser output to perform the cloud-base detection algorithm. Afterwards the next set of laser pulses are emitted for 1.6 s and so on. Samples collected during the 2-second intervals are averaged over a user-defined interval to create the reported height-resolved backscatter signal, which in this thesis is 6 s.

According to Münkel et al. [2007] during all cases with range values z above $\approx$ 30-100 m (ovelap range) and visibility (defined in Section 3.5.1) at ground level $>$ 10 km, one calculates $\tau^2_{par(z,\lambda)}$, the loss in transmittance resulting from travel to and return from the backscattering volume, to be greater than 0.83. This is close enough to 1, according to

Münkel et al. [2007], to take the attenuated backscatter, $\beta'_{par(z,\lambda)}$, as a measure for backscatter coefficient $\beta_{par(z,\lambda)}$. Further assumptions of a constant $S_{par(z,\lambda)}$ with height imply that attenuated backscatter would correlate with the range-resolved aerosol loadings, solid or liquid. Thus cloud height detection and indeed boundary-layer height detection are both, in differing degrees, independent of instrument calibration. This is not the case however with atmospheric transmittance profiling. The attenuated backscatter is derivable from Equation 4.1, and described in Rogers et al. [2011]

$$\beta'_{par(z,\lambda)} = \frac{P_{(z)}\, z^2}{C_l} = \beta_{par(z,\lambda)}\, e^{\left(-2\int_0^z \alpha_{(z',\lambda)} dz'\right)} \tag{4.11}$$

The lidar constant, C_l, is defined as the product of the instrument's parameters that impact on backscatter retrieval efficiency

$$C_l \propto A\ \eta\ O_{(z)} \tag{4.12}$$

where A (the area of receiver optics), η (the overall ceilometer efficiency, optical and electronic) and $O_{(z)}$ (the overlap function) are from Equation 4.1. From this relationship the following is noted; A is always constant, η will change with time and $O_{(z)}$ may vary slightly with temperature but is assumed constant in the operational mode used in this thesis, namely within set instrument temperature limits of 23-43°C.

The ceilometer has no way of determining the relative humidity at height during data taking, nor the microphysical properties of the aerosol species, implying that the internal construction of the attenuated backscatter is most probably assuming a transmission window under nominal conditions (transmittance $\sim$1.0), that is only slightly height dependent. Thus the attenuated backscatter produced by the ceilometer must be seen as subject to three principal causes of variability in cloud-free and soot-free conditions; the contemporaneous water vapour profile, the aerosol species and the instrument characteristics C_l. Water-vapour extinction must be corrected for, aerosol species must be identified for their optical properties

and C_l must be estimated, or at least held with a narrow range of values. A novel methodology is introduced below that holds the value of C_l towards its lower limits. All three factors are extensively addressed in the following sections.

Finally, $\beta'_{par(z,\lambda)}$ may be more correctly written as $\beta'_{par(z,\lambda,H_2O)}$, as the hygroscopic properties are accounted for. The associated lidar ratio and extinction coefficient are likewise changed to $S_{par(z,\lambda,H_2O)}$ and $\alpha_{par(z,\lambda,H_2O)}$ respectively.

4.3.2 Backscattering from cloud at VERITAS

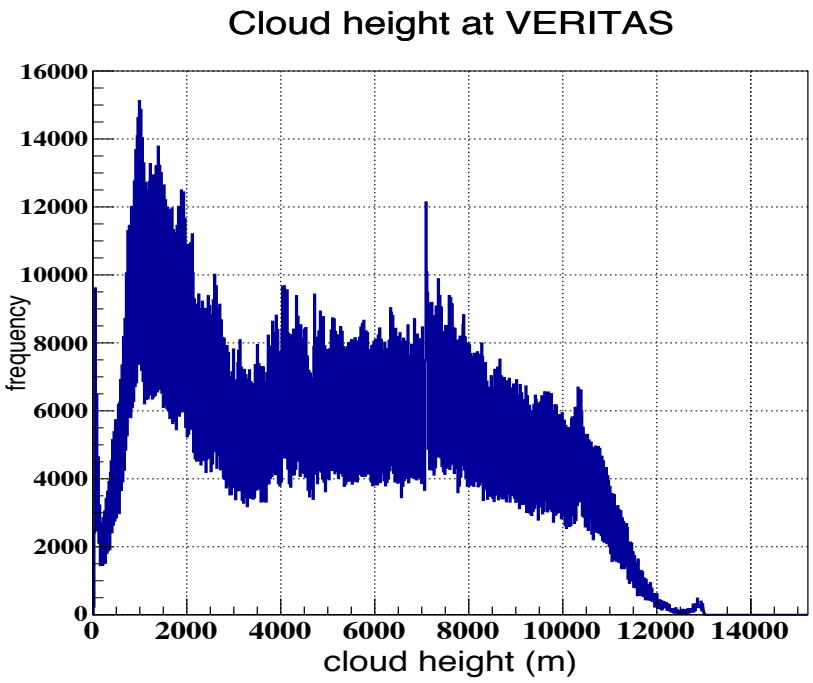

Fig. 4.6 A 1D histogram (containing $\geq 4.5 \times 10^6$ data points) of 1^{st} cloud height detection at the VERITAS site during five years of operation of the CL51 ceilometer. Height binning is 15 m, chosen to highlight the volatile nature of cloud-base height. The most common cloud base heights are below 2 km, while the average is 5.2 km. Note that the spike in cloud-base detection at 7.2 km is due to firmware injection of noise into the return signal for background analysis, as is done for the CL31 at this same height [Kotthaus et al., 2016].

Before beginning the next section on detecting, ranging and quantifying aerosol loadings, discussion turns to the principal operational mode for all ceilometers, cloud-base height detection and ranging. This does not require any form of calibration (as seen in Section 4.3.1);

furthermore, the backscattering returns are so large that long time averaging windows are not required. On completion of its fifth observing-year of operation at VERITAS, from mid-December 2011 to late-June 2016, the ceilometer produced $\geq 1.8 \times 10^7$ backscatter reports at 6 s intervals and found a total of $\sim$25% cloud-base detections for 24-hour operation over all operational months (which exclude summer-shutdown). This means that at zenith, where the ceilometer points, $\frac{1}{4}$ of all backscattering returns detected the presence of water droplets at various heights.

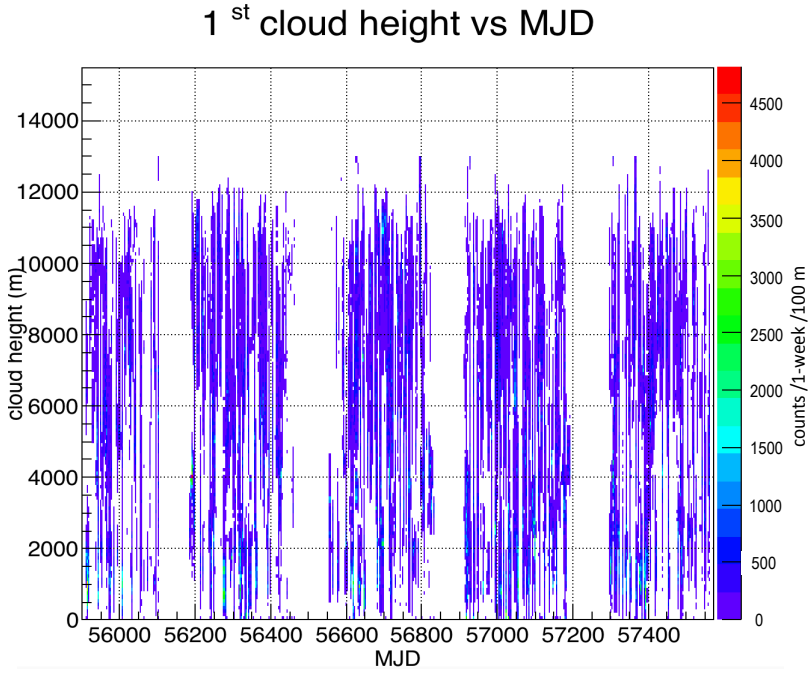

Fig. 4.7 A 2D histogram of timestamped cloud-height detection at the VERITAS site, using the same dataset as Figure 4.6. Histogram binning of 1 week (x-axis) and 100 m (y-axis) respectively.

During twilight and nighttime only, broadly from 19:00 to 07:30 local time, the ceilometer found a total of $\sim$28% cloud base detections. Figure 4.6 shows a 1D histogram for the height (total of 1000 bins, binning of 15 m) at which first cloud base was detected, remembering that the CL51 can detect up to three cloud layers (if lower clouds are not too opaque for the laser to pass through and return). This very narrow height binning was chosen to show the highly erratic nature of cloud base formation as a function of height at VERITAS.

The plot appears unusually wide for a histogram because neighboring height bins on the x-axis, separated by only 15 m, may have very differing numbers of cloud-bases detected for those height bins. Between 3-7 km a.g.l., where the average frequency of cloud-base formation is constant (but having a high standard deviation), the difference in frequency of cloud-base detections for neighbouring height bins may be up to 100%. From this plot, containing $\geq 4.5 \times 10^6$ data points, it can be seen that there are cloud-bases detected at 1 km a.g.l. approximately twice as often as cloud-bases are detected from 2-10 km a.g.l. The cloud base detections from 0-200 m a.g.l. may be possibly a mixture of rolling fog and heavy dew, being driven up the foothills of the Santa Rita mountains by wind. The erratic nature of cloud-base formation is better demonstrated by Figure 4.7, a 2D histogram of the same data set as Figure 4.6, but with cloud-base height binning of 100 m (y-axis) and time binning of 1 week (x-axis) (giving a total of 150 vertical x 250 horizontal bins). This binning is chosen to detect seasonal trends of high / low cloud base formation. There is no discernable pattern to cloud base height formation at VERITAS for the extensive dataset examined.

4.4 A methodology for quantifying aerosols

A working approximation of $\alpha_{par(z,\lambda,H_2O)}$ may be derived as follows. An estimate of $S_{par(z,\lambda,H_2O)}$ from regional aerosol studies together with the aerosol loading measurable by attenuated backscattering allows an uncorrected estimate of the aerosol extinction profile

$$\alpha_{par(z,\lambda,H_2O)} \approx S_{par(z,\lambda,H_2O)} \times \beta'_{par(z,\lambda,H_2O)} \tag{4.13}$$

where the addition of the "$\approx$" sign relates to the attenuated backscatter being taken as a working estimate of the true backscatter coefficient ($\beta_{par(z,\lambda,H_2O)}$), when certain conditions hold. These are discussed below. Additionally, radiosonde data needs to approximate the molecular atmosphere accurately and give good Percipitable Water Volume (PWV) esti-

mates for the VERITAS site. This allows for water vapour extinction correction of the attenuated backscatter and the additional subtraction of molecular backscatter, $\beta_{mol(z,\lambda)}$, from the ceilometer-derived attenuated backscatter, discussed below. Finally, the Beers-Lambert approximation needs to hold. Any uncertainty in $\beta'_{par(z,\lambda,H_2O)}$ will give a large uncertainty in $\alpha_{par(z,\lambda,H_2O)}$ (by a factor of $S_{par(z,\lambda,H_2O)}$), therefore software-level processing of attenuated backscatter is of considerable importance.

4.4.1 Processing attenuated backscatter data

The spatial 10 m resolution attenuated backscatter readings are averaged in 1 km intervals, as this is the required transmittance profile binning for γ-ray studies, which is the overlying motivation behind development of this technique. The averaged attenuated backscatter in each 1 km interval is then averaged over a 30 min time interval which could contain up to 300 time samples; refer to Figure 4.8 for the actual number of samples in 1D histogram format. A time averaging of 30 min is selected as it allows good statistics but does not smooth out aerosol variability excessively. Instrument stability can be further increased by removing poor data; this is achieved by introducing data cuts (*i.e.*, removing data that falls outside set limits) on the following parameters;

1. The ambient background light measured around 905 nm, NSB_{ir}, during the night time must be reasonably low, as the relatively broad laser spectrum hampers attempts at filtering. A threshold of 20 mV in the output from the infrared photodiode which measures the background light has been selected, based on an examination of the full data presented next (Section 4.4.3).

2. The internal ceilometer temperature must be below 43°C. There is a small temperature dependence in the average attenuated backscatter which is linear in the range 23-43°C. A correction of 0.3×10^{-5} sr^{-1} m^{-1} K^{-1} is applied. Above 43°C the relationship becomes nonlinear and the data block is rejected.

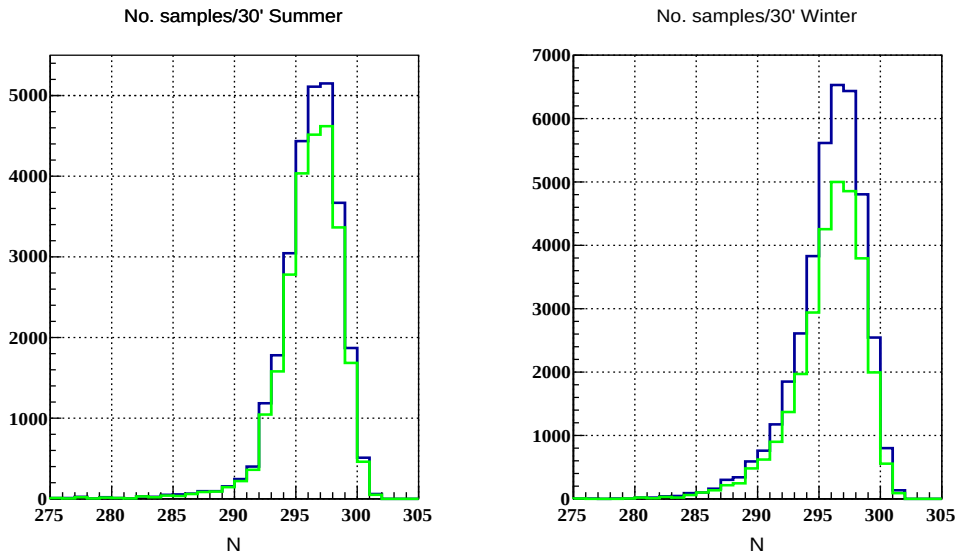

Fig. 4.8 Two 1D histograms of N, the number of data samples per 30 min bin after instrument-temperature and NSB_{ir} cuts (blue) and instrument-temperature, NSB_{ir} and cloud cuts (green). A slight timing jitter allows at times $>$ 300 6 s samples per 30 min, at other times a 6 s reporting is dropped, causing the total available data volume to drop by $\sim$1.5% overall. January and February are chosen to represent VWinter, left plot, while May and June represent VSummer, right plot. Data is from 2012-2016 inclusive.

3. All data with cloud detected below 5 km by the ceilometer is rejected. Useful information may still be obtained when higher cloud is present. This is determined after quality cuts are applied and the data is analysed.

4. The data must be free of faint passing clouds below 6 km. Faint clouds may be present which are not detected by the on-board ceilometer software. They may be identified by looking at the km^{-1} binned distribution of attenuated backscatters over the 30-min data blocks. Blocks with broad distributions (standard deviation > 40% of the mean) and skewed distribution (absolute skewness $>$ 2.5) are rejected. The backscattering from water droplets is two to three orders of magnitude greater than that for fine desert dust.

5. The data should, if possible, be free of carbonaceous particles such as soot. High backscattering with greater temporal variability than normal flags a dataset that re-

quires user examination for selection / rejection decision.

6. The water vapour variability measured at Tucson must not be excessive. In volatile water scenarios it is not reasonable to use 60 km distance measurements to represent the situation at VERITAS. Current upper limits are set to 50% change in 24 hours which is 0.34% change in 10 min.

7. There must be no significant data loss; the threshold is set at one min continuous loss or three min of total loss during the 30-min data block. Data loss may refer to data dropped by the ceilometer and data removed from analysis by the cuts listed.

4.4.2 The advantage of quality cuts for data rejection

The seven quality checks just outlined may remove up to 5% (depending on temporal-overlapping) of cloud-free night-time data, but are capable of altering the accuracy of a larger percentage of 30-min data sets. Of particular concern are undetected clouds, due to the magnitude of their backscattering. A precise estimate of the data lost to analysis from internal ceilometer temperature, NSB_{ir}, cloud (faint passing cloud and detected cloud) or instrument-data-dropping individually is very difficult to estimate, due to possible contemporaneity.

As the ceilometer analysis code herein described reads in attenuated backscatter data, it continually counts the quality cuts made for all the listed quality limits. Should the total cut count reach the maximum limit (set in Section 4.4.1, no. 7) before 30 min of data has been read in, the analysis code resets its counters and starts over again. This sliding time window is used to reduce as far as possible the data lost to analysis.

Large absolute skewness or an increase in standard deviation (Section 4.4.1, no. 4), probably indicates faint passing clouds in data. Should this happen, the compromised data samples are removed from the total N and a new number of samples for the 30 min bin, N', is determined. The statistical analysis is carried out again with the re-cut data set unless $N' <$

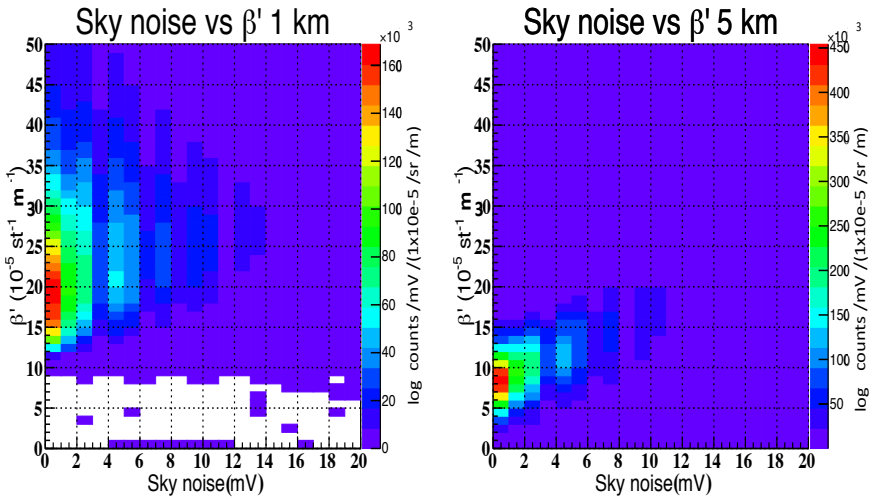

Fig. 4.9 Two 2D histograms of the arithmetic mean of attenuated backscatter for the 1^{st} km a.g.l. (left) and the 5^{th} km a.g.l. (right) as a function of NSB_{ir} at the VERITAS site. This plot contains $> 1.8 \times 10^7$ data samples, without any time averaging, taken from December 2011 to June 2016.

80% N, in which case the dataset is rejected. This limit prevents the backscattering error estimation becoming too large.

It is acknowledged that the "cuts" method outlined currently is not widely used in ceilometer attenuated backscattering analysis. It is chosen for this thesis as it affords flexibility in dealing with episodic poor data (faint clouds, high NSB_{ir}) and poor instrument systematics (high operating temperature) by not allowing total cuts to exceed a set limit. At current settings, the data rejection limit for high operating temperature is more stringent than rejection based on mean operating temperature.

4.4.3 The influence of sky background noise in the infrared

Elevated NSB_{ir} during ceilometer data taking was originally thought to affect the return signal by adding a pedestal to attenuated backscatter. The Vaisala CL51 has a dedicated IR photodiode that independently records the ambient light background in the ceilometer field of view, with an output in mV that forms part of the final data output file. Refer to Figure 4.9 where spatial arithmetic mean of attenuated backscatter (not time averaged) as

a function of NSB_{ir} for 24 hr operation over five osserving years of operation (2011-2016) are plotted in a 2D histogram format. The binning is 1 mV (x-axis) and 1×10^{-5} sr^{-1} m^{-1} (y-axis). The backscattering at 5 km a.g.l., at first inspection, appeared to rise with increase in NSB_{ir} from 0-12 mV. This could however be explained by the diurnal rise and fall of boundary-layer height caused by the Sun heating the atmosphere. To further investigate, all data were divided into monthly datasets and the mean backscattering from 1 km to 5 km then calculated for all data samples where $NSB_{ir} \leq 5$ mV. The mean backscattering was also calculated for all data where $NSB_{ir} \leq 7$ mV, ≤ 10 mV, ≤ 15 mV and ≤ 20 mV respectively. As the NSB_{ir} acceptance threshold increases, the number of data samples admitted into the averaging also increases. Should NSB_{ir} add a pedestal to the attenuated backscattering, a rise in average backscattering should be witnessed as NSB_{ir} increases. Refer to Table 4.2 for a sample of the data analysed, where the standard error in mean of the datasets (containing $\sim$2-3.5$\times 10^5$ samples) is always kept below 0.5% of the arithmetic mean of backscattering. The hypothesised pedestal, if it exists, is not seen below $NSB_{ir} \leq 20$ mV and height ≤ 5 km a.g.l. Thus the NSB_{ir} threshold is set to 20 mV for this thesis.

Month	*Year*	*Sky noise* (mV)	*no. data samples*	$\bar{\beta}'1km$ (a.u.)	$\bar{\beta}'5km$ (a.u.)
Jan	2012	5	314214	20.42	07.37
Jan	2012	20	350526	20.43	07.63
May	2012	5	236420	35.14	09.74
May	2012	20	355807	34.20	11.00
Feb	2013	5	284193	24.80	08.46
Feb	2013	20	306640	24.71	08.60
Jun	2013	5	205798	50.03	12.34
Jun	2013	20	338195	47.74	14.17

Table 4.2 A small sample of the NSB_{ir} analysis carried out for NSB_{ir} threshold of 5 mV and 20 mV, for 1 km a.g.l. and 5 km a.g.l. from December 2011 to June 2016, 24 hr operation. The column *no. data samples* shows the increase of data samples to the analysis by the increase of NSB_{ir} threshold; for January 2012 the increase $\sim$12%, for May 2012 the increase $\sim$50%, due to the shorter nights in summer. The standard error in mean, $std\ err = \frac{\sigma}{\sqrt{N}}$, is effectively $\sim$0% due to the very large data sample used.

4.5 Water vapour extinction for the ceilometer

The continuous operation of the ceilometer is ideally suited to VHE γ-ray astronomy, as the Cherenkov and ceilometer wavelengths do not overlap. A 532 nm lidar would ideally suit aerosol profiling, but would necessitate turning the telescopes PMTs off during lidar readings. Were the ceilometer wavelength to be at 1064 nm, as for Jenoptik CH15k [Milroy et al., 2011], the transmission window would allow the Beers-Lambert approximation to hold with the added benefit of no water vapour extinction. We now examine water vapour extinction at the Vaisala wavelengths of 905-910 nm, λ_{CL51}, with the help of MODTRAN.
For accurate water vapour extinction correction, two possible approaches are possible. In one approach, atmospheric transmittance profiles are calculated in real time for one particular atmosphere and laser wavelength (atmospheric season, water vapour content, aerosol loading). In the other approach, a set of atmospheric transmittance profiles with stepped values of laser wavelength, water vapour content and aerosol loading, for both atmospheric seasons, must be pre-generated. These may be referenced during ceilometer algorithm operation. To reduce processor time, the latter approach has been adopted. MODTRAN employs the use of HITRAN transmittance tables (introduced in Section 3.6) for spectral regions that require high-resolution line spectroscopy. From these, a moderate resolution (0.1 cm^{-1}) atmospheric transmittance simulation is produced for a particular atmospheric season (VSummer or VWinter), with a particular wavelength band and height profile. These are 900-920 nm and 1-5 km respectively and are plotted in Figure 4.10. A total transmittance for 0-5 km a.g.l. was chosen for plotting to spread out the transmittance profiles, making differences in extinction due to water vapour content more obvious. Additionally, an aerosol-free scenario has been chosen to avoid complexities caused by hygroscopicity. As λ_{CL51} can vary from ceilometer to ceilometer, the peak emission wavelength in this thesis is given a lower and higher value, λ_{lo} and λ_{hi}. This allows the results of the ceilometer algorithm to be applicable for many different Vaisala CL51 ceilometers.
It can be seen that a partial transmittance window exists from 901-907 nm, beyond which

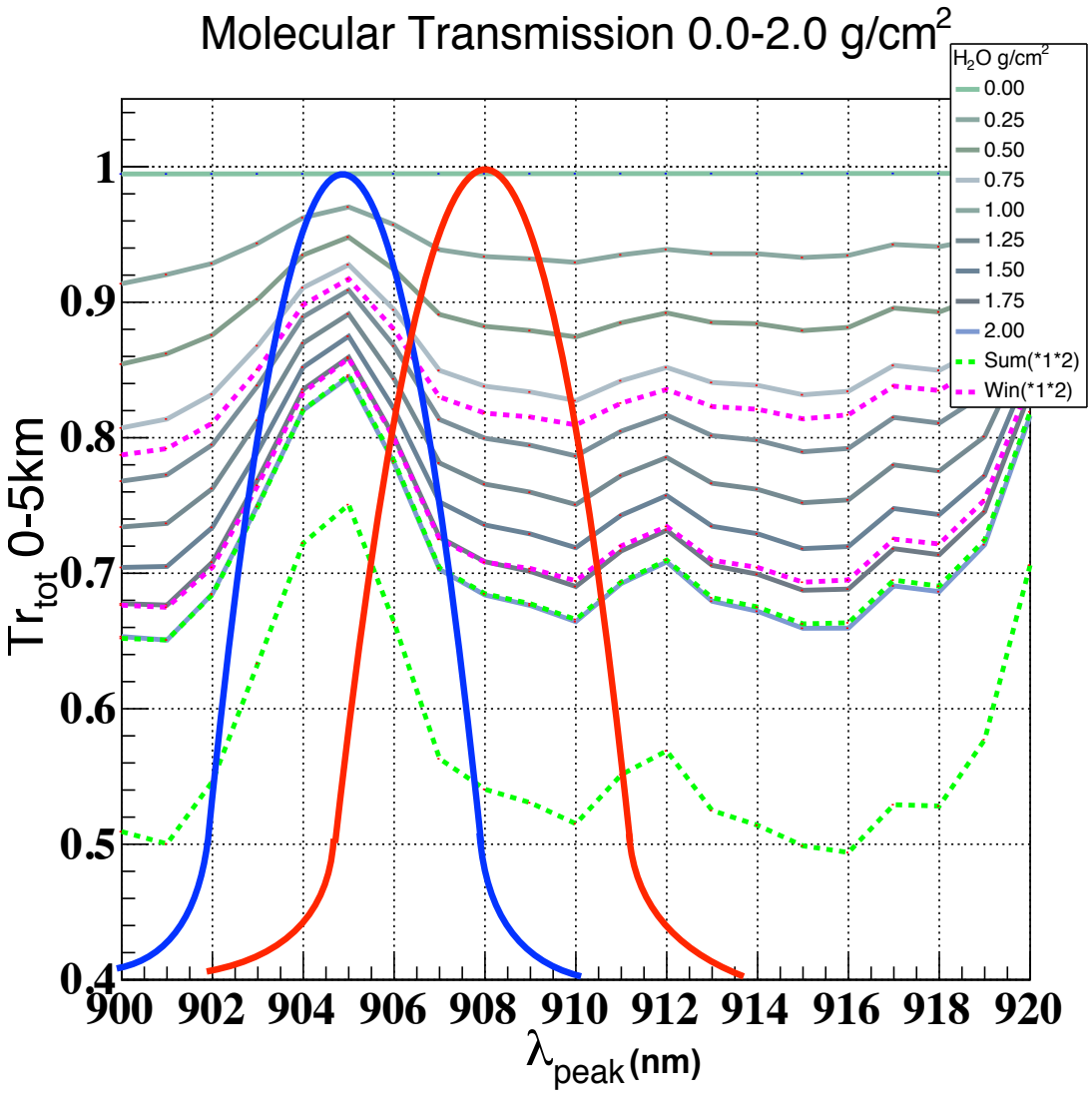

Fig. 4.10 MODTRAN 5.2 estimation of transmittance probabilities from 0-5 km a.g.l. at VERITAS for Vaisala CL51 wavelengths. Greyscale lines are PWV 0.0-2.0 g cm^{-2}, green lines are VSummer atmosphere for *1 and *2 water vapour, purple lines are VWinter atmosphere for *1 and *2 water vapour. Increasing water vapour leads to decreasing transmittance probability. Note that the blue curve is a CL51 laser spectrum approximation of λ_{lo}, the red is a spectrum approximation of λ_{hi}, FWHM = 4.5 nm; they are added only to show the superposition of the CL51 laser spectrum on the transmittance spectrum.

the transmittance is quite constant over Vaisala CL51 wavelengths. The magenta lines represent transmittance for normal (*1) and twice normal (*2) water vapour content for VWinter atmospheres (according to MODTRAN) while the green lines are transmittance for normal (*1) and twice normal (*2) water vapour content for VSummer atmosphere (discussed in Section 3.2.1). The grey lines of varying shades represent from 0.0 to 2.0 $\mathrm{g\,cm^{-2}}$ (0 to 20 mm) in VSummer. Refer to Appendix A for more information on the extinction profiles produced for this thesis. Of note is the higher expected water vapour present in VSummer; the normal expected VSummer water vapour is twice the expected VWinter level, independent of the monsoon rains, that cause summer-shutdown. Note additionally that for PWV = 0.0 $\mathrm{g\,cm^{-2}}$ the total transmittance from 0-5 km a.g.l. $> 99.7\%$, demonstrating why λ_{CL51} was chosen by Vaisala. The broad FWHM of the laser complicates calculation of water-vapour extinction, but must now be accounted for.

4.5.1 Spectral broadening of CL51 laser

According to the Angstrom approximation for wavelength dependence of aerosol extinction [Ångström, 1961], differences in backscatter coefficient, $\beta_{(x,\lambda)}$, can be neglected over the FWHM of the ceilometer. This however is not the case with molecular extinction. The unknown peak emission wavelength of the CL51, λ_{CL51}, the change in this wavelength with temperature and the unusually wide FWHM must be incorporated into this analysis. At the time of manufacture, a factory measurement was made on the Vaisala instrument currently at VERITAS. Peak emission wavelength was 907 nm. However this peak emission is purported to change with time and requires, ideally, measurement at least once per year [Okayasu and Fukuda, 1992]. Two separate representative peak emission wavelengths are chosen for MODTRAN transmittance profiling, λ_{lo} and λ_{hi}, which are lower and higher estimates of λ_{CL51}. This allows the CL51 ceilometer's instrument response to be better understood over many operating wavelengths. For this thesis they are given values of 905 nm and 908 nm respectively, with an assumed Gaussian FWHM of 4.5 nm. Choosing λ_{lo} at

905 nm allows analysis of the laser response to water vapour extinction in the partial transmission window from 901-907 nm. The values for λ_{lo} and λ_{hi} are corrected for increases in ceilometer internal temperature. This is done in steps of 1 nm for every 4 °C change in temperature. This rather large wavelength binning of 1 nm, in comparison to molecular absorption bands which are a small fraction of 1 nm, is made possible due to MODTRAN's ability to estimate the total effective transmittance profile over the wavelength bin in question, namely 1 nm. Recall that MODTRAN is a moderate resolution radiative transfer code, that relies on vast arrays of data tables from high resolution radiative transfer simulations, derived from HITRAN2008 (introduced in Section 3.6). This means that MODTRAN's transmittance profiles are in reality effective transmittance profiles over the wavelength bin in question. This wavelength binning of 1 nm is found to be adequate for effective water vapour extinction (ext_{H_2O}) calculation, in that shorter wavelength binning of 0.25 nm does not alter the overall transmittance values noticeably. The analysis developed for this thesis takes the output of MODTRAN and again creates an effective transmittance for the CL51 laser using the methodology now described. This 1 nm binning has proven most useful, for the number of atmospheric simulations needed is substantially reduced.

The molecular extinction at peak emission is calculated and given a weight of 1. Next the transmittance at x^i ($= \lambda_{peak} \pm i$ nm, i being an integer) is calculated and weighted according to the assumed Gaussian profile of the ceilometer laser

$$\omega^i = N\, e^{\left(-\frac{(x^i-\lambda_{peak})^2}{2\sigma^2}\right)} \tag{4.14}$$

where N = the peak power (set to 1) and x^i, λ_{peak} are integers and ω^i is the assigned weight at $\lambda_{peak} \pm i$ nm. Additionally, σ is the Gaussian standard deviation, related to FWHM by $FWHM = 2\sqrt{2\,ln\,2}\sigma$. This calculation is carried out n times until $\omega^i \ll 1$, where n is set to 20 for this analysis. Then combining the calculations one arrives at an effective

transmittance value

$$Tr^{eff} = \frac{\sum_{i=1}^{n} \omega^i Tr^i}{\sum_{i=1}^{n} \omega^i} \tag{4.15}$$

From Tr^{eff}, the total effective molecular transmittance, the total effective molecular extinction can now be estimated easily, thanks to the λ_{CL51} atmospheric transmission window. This transmission window implies that the total water vapour extinction, ext_{H_2O}, dominates overall atmospheric extinction in aerosol-free conditions. Thus

$$ext_{H_2O} \approx 1 - Tr^{eff} \tag{4.16}$$

The total effective molecular extinction, ext_{H_2O}, will serve as the basis for water-vapour extinction correction for the Vaisala CL51 laser.

4.5.2 Estimating effective water vapour extinction for the CL51

Effective water vapour extinction, ext_{H_2O}, defined as the overall extinction from gaseous water which the CL51's laser pulses undergoes as it transmits from and returns to the ceilometer, needs to be estimated. The process to estimate ext_{H_2O} is as follows. A large set of aerosol-free simulations of VSummer and VWinter atmospheres, with Precipitable Water Volume (PWV), ranging from 0.0 to 2.0 $\mathrm{g\,cm^{-2}}$ (which may also be measured as 0.0 to 20 mm depth of liquid water) in steps of 0.25 $\mathrm{g\,cm^{-2}}$, has been produced for 0-6 km a.g.l. (to allow some extrapolation beyond 5 km) and from 900-920 nm in steps of 1 nm as mentioned. This simulation set is called the CL51-PWV simset. The correct atmospheric simulation must be chosen from the CL51-PWV simset, that is correct VERITAS season and PWV bin. To explain the selection of PWV bin in more clarity; should the measured PWV in a particular VERITAS season fall between 0.375 $\mathrm{g\,cm^{-2}}$ and 0.625 $\mathrm{g\,cm^{-2}}$, for example, the appropriate VERITAS season extinction files for 0.50 $\mathrm{g\,cm^{-2}}$ are used, and so on. This binning acknowledges the impossibility of exactly measuring the PWV in the absence of co-located instrumentation, while further reducing the number of simulations required for

transmittance profile matching. It would be mathematically trivial to reduce the binning of PWV estimate from 0.25 g cm^{-2} to 0.1 g cm^{-2} for the Tucson radiosonde (as outlined in Section 3.2.2). However the high variability of PWV measurements over short time and distance intervals would nullify its validity. The total number of aerosol-free simulations required is 2 (VSummer and VWinter) * 9 (PWV bins) = 18.

This simulation set caters for nearly all ceilometer operating conditions encountered at VERITAS in the absence of aerosols. A further set of VSummer and VWinter simulations, identical to the CL51-PWV simset but with no water vapour present (dry air), are also produced. To determine the water-vapour transmittance profile for a particular atmosphere, one selects the correct VERITAS season and the correct PWV from the CL51-PWV simset and correct VERITAS season for the dry air simulation set. Subtracting a particular PWV instance of the dry-air simset from the corresponding PWV instance of the CL51-PWV simset, leaves the water-vapour transmittance profile alone. An estimate for ext_{H_2O} at the particular PWV estimate chosen now becomes possible by accounting for the temperature and FWHM of the laser (as outlined in Section 4.5.1). The molecular extinction profile of dry air is so small at λ_{CL51} it can in fact be neglected. Additionally, a study of VERITAS season transitions at λ_{CL51} shows a $\leq$1% difference between VWinter and VSummer extinction profiles from 0-6 km a.g.l. for a given PWV bin (detailed in Appendix A). This is to be expected as the differences in transmittance for molecular atmospheres are very small at λ_{CL51}.

With this outlined methodology, PWV binning of 0.25 g cm^{-2} and 2 molecular seasons, molecular profiling will have a stepped transmittance profile as the analysis code jumps from one binned simulation set to another. The steps chosen however are fine enough to offset any serious over / under estimation of transmittance profiling for the ceilometer. Figure 4.11 shows a plot of ceilometer transmittance for the 1^{st} km a.g.l. as a function of PWV for the December 2011 to June 2016 quality cut data set, amounting to $\sim 2.6 \times 10^4$ 30-min transmittance profiles from 0-5 km a.g.l. Both λ_{lo} (left) and λ_{hi} (right) are plotted. The

steps in transmittance estimates, due to moving from one bin value to another, is visible when viewing the upper transmittance values of the each plot.

It is important to remember that the laser peak emission wavelength is continually changing. As the permitted operating range is from 23-43 °C (detailed in Section 4.4.1), this gives 5 possible wavelengths (905-909 nm for λ_{lo}, 908-912 nm for λ_{hi}).

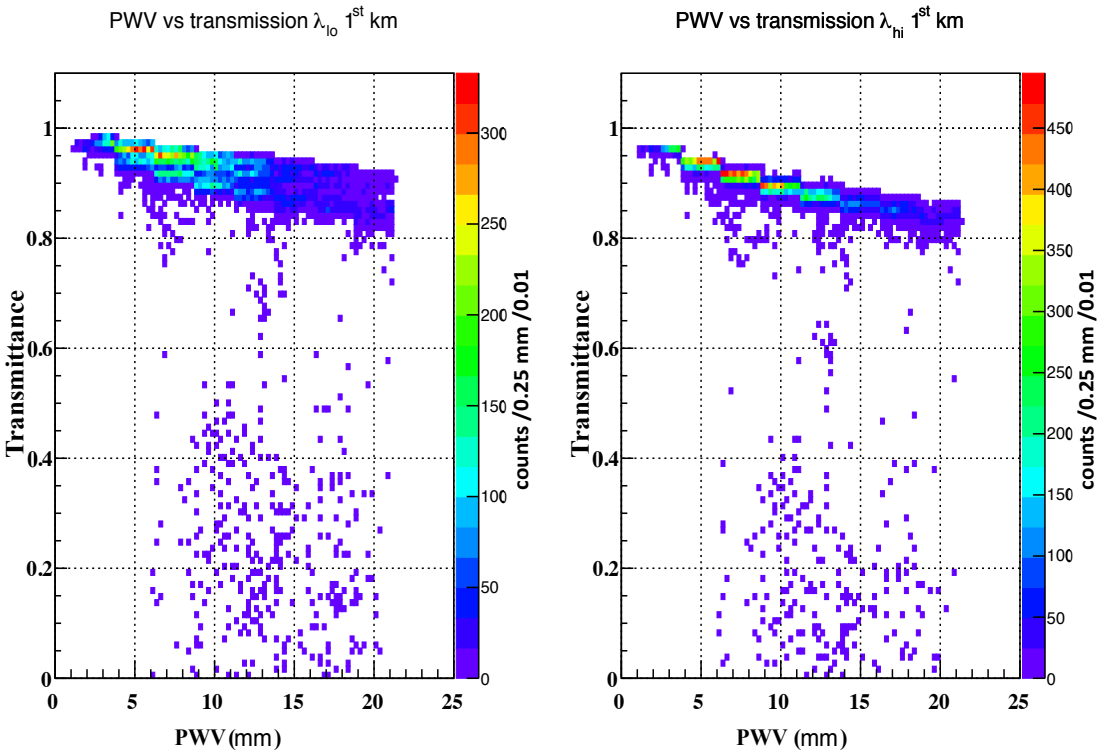

Fig. 4.11 MODTRAN estimation of transmittance probabilities from 1 km a.g.l. at the VERITAS for λ_{lo} (left) and λ_{hi} (right) for varying PWV in mm. Note the greater variability in transmittance at λ_{lo} wavelengths than λ_{hi}, due to the partial atmospheric transmission window. The plot contains data from December 2011 to June 2016, with $\sim 2.6 \times 10^4$ quality cut 30-min data blocks in total. The step in molecular transmittance for moving from one PWV bin to another is less than the spread in transmittance, particularly for λ_{lo}. Binning of 0.25 mm and 0.01.

This means there are 10 possible transmittance values for each PWV bin (5×2 (VWinter and VSummer)) for λ_{lo} and λ_{hi} in Figure 4.11. Additionally, the particulate transmittance makes up part of the total transmittance estimate. The particulate transmittance is not stepped but forms a continuum. These factors, changing peak laser wavelength and varying

particulate transmittance explain why the plot has a wide set of overall transmittance values for particular PWV values.

Starting with λ_{lo} (left), the peak emission of the laser is on the trailing edge of a partial atmospheric transmission window (as seen in Figure 4.10, blue lined spectrum). Thus small changes in peak wavelength emission can have large changes in transmittance. This explains the wide spread in transmittance estimates for various PWV bins. The laser peak emission wavelength is continually changing due to changes in instrument temperature, which is accounted for in the analysis. For λ_{hi} (Figure 4.10, red lined spectrum) the situation is less variable. The peak emission of the laser is in a region of more or less stable transmittance with wavelength changes; in fact transmittance is relatively stable from 907 nm $\leq \lambda \leq$ 918 nm for a particular PWV bin. However for λ_{hi}, a change in PWV bin registers a larger change in transmittance than for λ_{lo} for a particular wavelength. This is seen by a wider distribution in ceilometer transmittance profiles from 907 nm $\leq \lambda \leq$ 918 nm. In short, for λ_{lo} a small change in wavelength can register a large change in transmittance, while for λ_{hi} a small change in water vapour can register a larger change in transmittance.

From the spectral broadening analysis and application of the Beers-Lambert approximation (seen in Equations 4.15 and 4.16), recalling that the water vapour component dominates extinction at λ_{CL51}, the calculation of ext_{H_2O} proceeds as follows.

λ_{lo} or λ_{hi} is selected, then the peak laser wavelength emission for each is adjusted by finding the average laser heatsink temperature over the 30 min bin in question and correcting accordingly. The atmosphere is selected, VSummer or VWinter, then the PWV table is consulted to find the PWV bin for the 30 min data bin in question (from the interpolation lookup table plotted in Figure 3.2). The PWV bin above and below the chosen PWV estimate is noted for subsequent error estimations. During times of increased water vapour change the actual PWV reading on site may be above or below the reference-table estimate. Next the molecular transmittance is estimated from 900 nm to 920 nm in steps of 1 nm by referring to the correct simulation set among the 18 CL51-PWV simsets mentioned. The same is

done for the dry air simulation set. These profiles are subtracted, km per km, nm per nm, and weighted accordingly as per Equation 4.14. From these data the effective water vapour transmittance, $Tr^{eff}_{H_2O}$, is calculated, then the effective water vapour extinction, ext_{H_2O}, is estimated according to Equation 4.16. The above process is carried out a total of six times, (2 (λ_{lo} and λ_{hi}) $\times$ 3 (PWV bins)).

As an accurate estimate of PWV is important, the PWV readings from Tucson radiosonde station are examined next.

4.5.3 Change in precipitable water

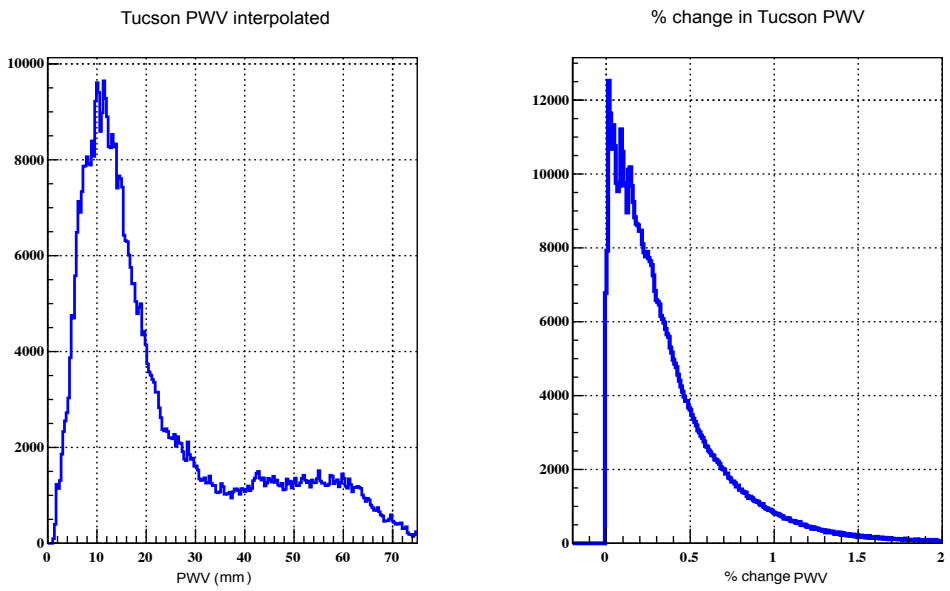

Fig. 4.12 Two 1D histograms showing the PWV distribution over an 8 year time scale, September 2008 to June 2016 (as also plotted in Figure 3.2) (left) and the absolute % change in PWV for adjoining 10 min interpolated readings (right). Note that 10 mm $\equiv$ 1.0 g cm^{-2}, a simple conversion factor.

It is important to ask when are the PWV estimates not representative of conditions at VERITAS? The PWV lookup table, containing $\sim 5.5 \times 10^5$ timestamped PWV readings of 10 min steps, is presented in 1D histogram format in Figure 4.12. From the right plot, it can be seen that on average the PWV changes quite slowly. A $\pm$50% change in one day, high

but not unusual by hydrological cycle standards, would register as $\sim\pm 0.33\%$ on this plot. This is currently taken as an upper limit for variability in the absence of co-located PWV measurements. An uncertainty of ± 1 PWV bin (± 0.25 g cm^{-2}) is included in total error estimates. This means the $+$error will include the transmittance estimate for PWV (bin $+$ 1) while the $-$error will include the transmittance estimate for PWV (bin $-$ 1). It is noted that, with the exception of the monsoon-like moist-air trajectories (discussed in Section 3.2.2), the PWV follows a quasi-Gaussian distribution with year-on-year mean of 12-14 mm or 1.2-1.4 g cm^{-2}, as can be seen in Figure 4.12, left plot.

4.6 Quantifying statistical uncertainties in backscattering retrieval

This study relies upon a Monte Carlo error estimation ideally suited to backscattering measurements, outlined in Pornsawad et al. [2012]. It allows dynamic aerosol morphologies caused by turbulent mixing to be modelled, and avoids an excessive uncertainty due to stacking of successive uncertainties. Only the statistical uncertainty coming from the laser's backscatter return is considered presently. Due to quality cuts for ceilometer data (outlined in detail in Section 4.4.1), and in the absence of information on the Angström coefficient, the systematic errors are taken to be almost negligible for this analysis. Large variations in Angström coefficient, briefly introduced in Section modtranIntro, could increase the systematic uncertainty to appreciable levels, as the wavelength gap between λ_{CL51} and Cherenkov radiation is quite large.

This Monte Carlo method is based on a random extraction of ceilometer return signals, each reading considered a sample element of a 2D Gaussian probability distribution. These backscatter returns are analysed as follows. If we indicate with $\overline{\alpha}_{aerosol}$ the average aerosol extinction obtained from a ceilometer with a standard error profile err and α^{j}_{extr} the aerosol extinction obtained from the j^{th} extracted signal of total number of extracted signals N_{extr},

the standard error of the aerosol extinction is

$$err_{\alpha_{aerosol}} = \sqrt{\frac{1}{(N_{extr}-1)} \sum_{j=1}^{N_{extr}} \left(\alpha^{j}_{extr} - \overline{\alpha}_{aerosol}\right)^2} \tag{4.17}$$

N_{extr} is the number of extracted data samples and N_{total} the total number of data samples, where $\frac{N_{extr}}{N_{total}} = 0.15$, or a sample equivalent to 15% of total data. The aerosol extinction $\overline{\alpha}_{aerosol}$ is calculated by Equation 4.13, which means that the uncertainty in lidar ratio as well as the uncertainty in attenuated backscatter are included in this Monte Carlo calculation.
To quantify, there are on average 300 ceilometer reportings per 30 min dataset. The height resolution is 10 m, so there will always be 100 height reportings per km for every ceilometer reporting.

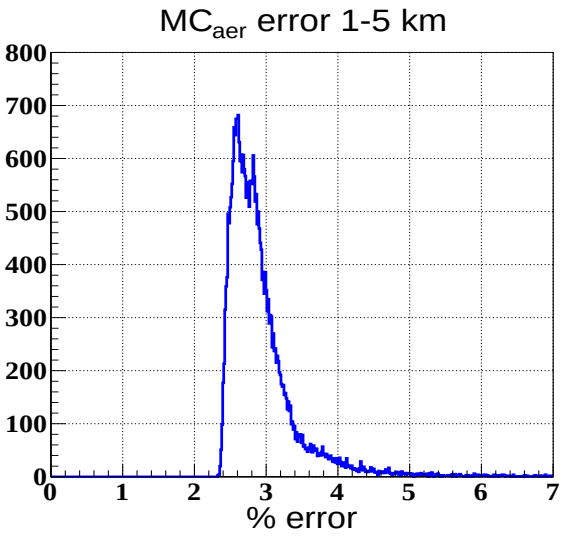

Fig. 4.13 1D histogram of Monte Carlo error estimation for the first 5 km a.g.l. at VERITAS. A total of 5.5 years data, yielding $\sim 3.1 \times 10^4$ quality cut aerosol profiles, has been used to produce this plot. The quality cuts, in particular the removal of any data with water droplets (Section 4.4.1, no. 3,4) reduce the Monte Carlo error estimate. Passing cloud, or other high-backscattering aerosols, could increase the error estimate by an order of magnitude, as is seen in Table 4.3.

The attenuated backscattering is profiled per km up to 5 km a.g.l. For every 1 km profile over 30 min there will be on average 300×100 or 3×10^4 data samples km^{-1}. Thus N_{extr}

$\sim 4.5 \times 10^3$ samples km^{-1}. Thus j counts from 1-4500 random ceilometer reporting's km^{-1}. Figure 4.13 shows a 1D histogram of the total error estimates, MC_{aer}, for 1-5 km a.g.l. Note that this is for the backscattering and lidar ratio alone and does not include any uncertainty arising from water vapour correction. Should an anomalous backscattering air parcel be present, the Monte Carlo error will register a large uncertainty, as is seen in Table 4.3. In the absence of such anomalies, the uncertainty is $\sim$3%.

$$MC_{aer} = \sum_{i=1}^{5} err_{\alpha_{aerosol}}^{i-km} \tag{4.18}$$

Height a.g.l.	$\tilde{\beta}'_{par}$	$\pm$% *error*
MJD 57889.27210		
1000	56.4	0.39
2000	34.8	0.78
3000	14.8	0.84
4000	11.1	0.69
5000	10.0	0.69
MJD 57889.29294		
1000	58.7	0.41
2000	37.4	24.78
3000	15.2	0.82
4000	11.2	0.68
5000	10.0	0.66

Table 4.3 Two side-by-side data sets from 16th May 2017 (separated by 30 min), the later one with an anomalous backscattering air parcel between 1-2 km a.g.l. that causes the error estimation to increase from $<$1% to $\sim$25%. The nature of the scattering morphology is unknown, and is one of only several that passed the faint passing cloud quality cuts. $\tilde{\beta}'_{par}$ represents the arithmetic mean of backscattering over the 30 min^{-1} / km^{-1} data block and will be introduced in more detail below.

4.7 A final corrected value for aerosol backscattering

For an initial ceilometer pulse power $P_{z=0}$ at λ_{CL51} and $\bar{P}_z$ being the range-corrected pulse power at height z, the total transmittance from ground to height z being the product of the individual transmittances for each 1 km bin, denoted $Tr_{tot_{(z)}}$, it would then follow that

$$\bar{P}_z \;=\; P_{z=0} \;\times\; Tr_{tot_{(z)}} \tag{4.19}$$

where in the absence of aerosol extinction

$$Tr_{tot_{(z)}} \;\approx\; Tr^{1}_{H_2O(z)} \;\times \ldots \times Tr^{n}_{H_2O(z)} \;;\; (n \leq 5) \tag{4.20}$$

where n is the number of height bins a.g.l. It is to be noted that the total transmittance, $Tr_{tot_{(z)}}$, is to be more accurately referred to as the total effective transmittance $Tr^{eff}_{tot_{(z)}}$, due to quantifying the effects of water vapour extinction and spectral broadening of the ceilometer laser. As the Mie backscattered light will in turn be attenuated by the same amount on its way back to the ceilometer's optics, the attenuated backscatter can be corrected by

$$\left\{ \left(Tr^{eff}_{tot_{(z)}} \right)^2 \right\}^{-1} \tag{4.21}$$

This allows us to account for the effects of water vapour extinction at CL51 wavelengths. It can be seen from Figure 4.10 that in the absence of water vapour, $P_{z=0} \approx \bar{P}_z$, however for a VSummer atmosphere with twice normal water vapour or *2 (not common during telescope operations but measured on several occasions) the ceilometer return may be reduced to almost $\frac{1}{4}$ of the PWV ≈ 0.0 g cm^{-2} atmosphere at a height of 6 km a.g.l.

As the estimate of particulate extinction relies on accurate backscatter retrieval, the effective water vapour extinction correction is applied to the attenuated backscatter, after additional sources of backscattering into the ceilometer optics are accounted for.

4.7.1 Molecular backscatter

As the ceilometer attenuated backscatter is the only means of height and temporal resolution for aerosols currently available at VERITAS, it is important that any molecular component of the total backscatter be removed. Backscattering from water vapour is negligible due to the absorption lines at ceilometer wavelengths. The retrieval of the molecular extinction was described and modeled by Elterman [1968] with later additions by Teillet [1990]. A more straightforward method exists for $\beta_{mol(z,\lambda)}$ estimation.

The molecular lidar ratio follows from Rayleigh scattering theory. It is a known constant

$$S_{mol} = \frac{\alpha_{mol(z,\lambda)}}{\beta_{mol(z,\lambda)}} = \frac{8\pi}{3}\text{sr} \tag{4.22}$$

MODTRAN allows the simulation of purely molecular atmospheres, having a value for $\alpha_{mol(z,\lambda)}$ the value for $\beta_{mol(z,\lambda)}$ is readily calculated from Equation 4.22

$$\beta_{mol(z,\lambda)} = \frac{3}{8\pi}\,\alpha_{mol(z,\lambda)}\,10^{-5}\,\text{m}^{-1}\,\text{sr}^{-1} \tag{4.23}$$

4.7.2 A corrected attenuated backscatter

As the particulate extinction profile alone is of interest, any additional sources of backscatter need to be accounted for. From Equation 4.3 it is seen that the molecular atmosphere backscatters light, therefore the need to subtract $\beta_{mol(z,\lambda)}$ from the total attenuated backscatter arises. The value of $\beta_{mol(z,\lambda)}$ is estimated from radiosonde data and not the ceilometer, therefore atmospheric extinction is applied to the return flight of the laser photons alone. The measured value of $\beta'_{par(z,\lambda,H_2O)}$ is measured by laser light traveling to and from the scattering medium, therefore the travel to and return from extinction must be corrected for. Thus, the most accurate estimate of $\beta'_{par(z,\lambda,H_2O)}$ available from the outlined method, named the water vapour extinction and molecular backscatter corrected ceilometer attenuated backscatter or more simply corrected attenuated backscatter, $\beta^{corr}_{par(z,\lambda,H_2O)}$, is given by

$$\beta^{corr}_{par(z,\lambda,H_2O)} = \frac{\beta'_{par(z,\lambda,H_2O)}}{(Tr^{eff}_{tot_{(z)}})^2} - \left(\beta_{mol(z,\lambda)}\,(Tr^{eff}_{tot_{(z)}})\right) \tag{4.24}$$

where $\beta'_{par(z,\lambda,H_2O)}$ is the attenuated backscatter, while $Tr^{eff}_{tot_{(z)}}$ is from Equation 4.20. With this valuable corrected data product the possibility of accurately determining the aerosol loading at VERITAS becomes possible.

4.7.3 The full analysis chain for aerosol load estimation

Bringing Sections 4.4.1 to 4.7.2 together into a step by step methodology, the process proceeds as follows;

- Height and time averaging, 1 km and 30 min, of attenuated backscatter data is time-stamped and written to file, cutting out poor quality data before averaging takes place (Section 4.4.1).
- VERITAS season and PWV bins are selected (Section 4.5.3).
- The effective water-vapour extinction is calculated for 1-5 km a.g.l. (Section 4.5.2).
- The height and time averaged attenuated backscatter is corrected for water-vapour extinction, the molecular backscatter is subtracted and the results, $\beta^{corr}_{par(z,\lambda,H_2O)}$, are written to file (Section 4.7.2).
- The Monte Carlo error estimation is carried out for λ_{lo} and λ_{hi} (Section 4.6). Uncertainties arising from correction for water-vapour extinction (Section 4.5.3) are added to overall errors.
- The estimate for corrected ceilometer attenuated backscatter, $\beta^{corr}_{par(z,\lambda,H_2O)}$, is compared to estimates from pre-generated aerosol simulations at VERITAS. The correct

VERITAS season and PWV bins are selected for CL51-PWV simsets and new simsets that contain aerosol extinction, named CL51-PWV-aer. There are 18 unique molecular atmospheres (as mentioned in Section 4.5.2), but now an additional 11 particulate extinction profiles are added for each of these 18 (WSS04-WSS24 in steps of WSS02). The total number of unique simulated atmospheres with aerosols (CL51-PWV-aer simsets) to select from is therefore 198. By subtracting (one of 11 of) the CL51-PWV-aer simsets from the corresponding CL51-PWV simsets, the transmittance profile for that particular aerosol load (WSS**) is estimated. When the aerosol loading is varied from WSS04 to WSS24 in steps of WSS02 (*i.e.* WSS04, WSS06,..., WSS**), the resulting aerosol extinction profiles may be compared to the derived profile for the corrected ceilometer attenuated backscatter, $\beta^{corr}_{par(z,\lambda,H_2O)}$, by least squares. Refer to Table 4.4 for an example from data soon to be analysed. This gives the WSS** value that best matches the $\beta^{corr}_{par(z,\lambda,H_2O)}$ measured. The total corrected attenuated backscatter from 0-5 km a.g.l. was used for the least squares comparison and not a km by km comparison.

- The upper Monte Carlo aerosol uncertainty (Section 4.6) and the upper PWV bin values used for water vapour correction (Section 4.5.3), are used to calculate the upper uncertainty in aerosol load estimate, likewise for the lower Monte Carlo aerosol uncertainty.

- Finally, coarse aerosol binning is introduced. The estimated aerosol load is set to "normal" if extinction $\leq$ WSS14, or to "elevated" if extinction $\geq$ WSS16. These threshold values will be discussed in Chapter 5. Care needs to be taken if the errors estimated are large.

The application of the outlined aerosol extinction estimation for three particular time windows of interest now follows. The first is from the 1^{st}, 7^{th} and the 30^{th} May 2013, chosen as it includes normal, elevated and highly elevated boundary-layer aerosol loadings in the

WSS	AOD-1km	AOD-2km	AOD-3km	AOD-4km	AOD-5km	AOD-1-5km
–	0.014	0.014	0.017	0.007	0.005	0.056
04	0.009	0.005	0.002	0.001	0.0009	0.019
06	0.010	0.006	0.003	0.001	0.0009	0.021
08	0.011	0.006	0.003	0.001	0.0009	0.022
10	0.012	0.007	0.003	0.001	0.0009	0.024
12	0.017	0.009	0.003	0.001	0.0009	0.032
14	0.024	0.012	0.004	0.001	0.0008	0.041
16	0.032	0.016	0.004	0.002	0.0008	0.055
18	0.045	0.022	0.005	0.002	0.0007	0.075
20	0.063	0.030	0.007	0.002	0.0007	0.103
22	0.094	0.045	0.009	0.002	0.0007	0.152
24	0.131	0.063	0.013	0.002	0.0007	0.208

Table 4.4 Aerosol optical depth analysis taken with data soon presented in Table 4.7, where the estimated AOD, presented on the top line, is compared to values derived from MODTRAN for Desert Dust aerosol extinction WSS04-WSS24. The MODTRAN derived AOD varies slightly with water vapour content; the values shown were from VWinter atmosphere with PWV bin = 10 g cm^{-2}.

space of one month. Also included is the 13^{th} April 2013, when an exceptional Mrk 421 VHE γ-ray flare was recorded during elevated aerosol loading. Finally the 22^{nd} April 2015 is examined, because from the 21-28 April 2015 the high redshift blazar PKS1441 +25 flared in the VHE range during varying aerosol loadings on site.

4.8 Selection and testing of particular ceilometer data sets at VERITAS

Three ceilometer data sets are chosen to test the ceilometer aerosol analysis algorithm. Data from May 2013 are firstly chosen, as in the space of one month normal, elevated and highly elevated aerosols were present; refer to Table 4.5 and Figure 4.14. The data in Table 4.5 are from (*top*) MJD 56419.27097 (2013/05/07 at 06:30:12 UTC), (*middle*) 56413.27301 (2013/05/01 at 06:33:08 UTC) and (*bottom*) 56442.35119 (2013/05/30 at 08:25:43 UTC).

The remaining two data sets, the 13^{th} April 2013 and 22^{nd} April 2015, need to be examined as the astrophysical data from these dates will be analysed in Chpater 6.

4.8.1 Examining May 2013 data

Before water vapour correction and transmittance profiling may be attempted, the attenuated backscatter data is subjected to a normal statistical analysis, post cuts. The total possible number of data samples in a 30-min average, N, is $\sim$300, but may be lower (as described in Section 4.4.1). N is not allowed to decrease by more than 10% of maximum (meaning $N \geq$270 for analysis to proceed). This preliminary analysis first produces arithmetic mean, $\bar{\beta}'_{par}$, standard deviation, STD, standard error in mean, *std err*, and *skewness*, in 5 separate height bins of 1 km thickness from ground level at VERITAS to 5 km a.g.l. From Table 4.5 it is seen that the *std err*, defined as $\frac{\text{STD}}{\sqrt{N}}$, is low. Even though the SNR drops to $\sim$3 at 5 km height, $\bar{\beta}'_{par}$ still has a low *std err* in the absence of anomalous backscattering air parcels, thanks to the 30 min time averaging and 1 km height averaging. The SNR is continuously calculated according to Heese et al. [2010] in 1 km bins up to 5 km a.g.l. and 30 min averaging by

$$SNR = \frac{\beta'_{par(z,\lambda,H_2O)}}{\sqrt{\beta'_{par(z,\lambda,H_2O)} + 2\,\beta'_{par(10-15km,\lambda,H_2O)}}} \tag{4.25}$$

where $\beta'_{par(10-15km,\lambda,H_2O)}$ is the average attenuated backscatter from 10-15 km a.g.l. and $\beta'_{par(z,\lambda,H_2O)}$ is the average attenuated backscatter for the height bin, z, in question. The SNR does not form part of the final aerosol analysis but serves as a data-quality indicator for data from 4-5 km a.g.l. Times of exceptionally low aerosol loading may bring the SNR from these heights below 1.0. The relative humidity ($RH_{mid-point}$) is also tabulated. The mid-point refers to the interpolated relative humidity value for 0.5, 1.5, ... , 5.5 km a.g.l. directly from Tucson radiosonde readings. This $RH_{mid-point}$ data point can flag backscatter data that may be subject to excessive water vapour extinction and cause erroneous transmit-

Height a.g.l.	$\bar{\beta}'_{par}$	*STD*	*std err*	*skew*	*SNR*	RH_{mid-pt}
metres	$\frac{\times 10^{-5}}{\text{sr m}}$	$\frac{\times 10^{-5}}{\text{sr m}}$	$\frac{\times 10^{-5}}{\text{sr m}}$	–	–	% saturation
WSS12 - MJD 56419.27097 (2013/05/07 06:30:12 UTC)						
1000	21.8	0.71	0.042	0.5	4.7	42.0
2000	15.4	1.71	0.100	-0.3	4.0	34.5
3000	14.3	2.97	0.175	0.1	3.9	41.1
4000	9.9	2.25	0.132	0.6	3.2	6.4
5000	7.5	2.25	0.132	-0.3	2.9	22.4
WSS16 - MJD 56413.27301 (2013/05/01 at 06:33:08 UTC)						
1000	46.0	3.11	0.181	1.0	6.9	16.9
2000	31.2	1.45	0.084	0.1	5.7	11.7
3000	22.7	2.67	0.155	0.1	4.9	15.7
4000	11.1	1.93	0.112	-0.1	3.6	24.9
5000	8.3	2.19	0.127	-0.2	3.2	3.8
WSS18 - MJD 56442.35119 (2013/05/30 at 08:25:43 UTC)						
1000	90.4	2.33	0.135	0.2	9.6	41.5
2000	29.7	1.81	0.105	0.0	5.6	30.5
3000	15.2	2.69	0.156	0.0	4.1	19.8
4000	9.6	2.62	0.153	0.0	3.4	22.7
5000	7.1	2.12	0.123	0.1	3.0	17.0

Table 4.5 The table displays mean attenuated backscatter ($\bar{\beta}'_{par}$), it's standard deviation (STD), standard error in mean (std err), skewness, SNR and relative humidity mid-point value (RH_{mid-pt}), for 1 to 5 km a.g.l. for the three days in May 2013.

tance estimates.

From this primary analysis of attenuated backscattering data the following information may be elicited. Firstly, the data cuts optimise data quality allowing a low standard error in mean to be obtained without an excessive loss of data. This enables even low SNR backscatter from 5 km a.g.l. to enter the transmittance calculation chain without fear of large Monte Carlo errors being passed through. Secondly, though the RH_{mid-pt} profiles from the 1^{st} and 30^{th} May 2013 are quite similar, the attenuated backscatter as seen varies greatly.

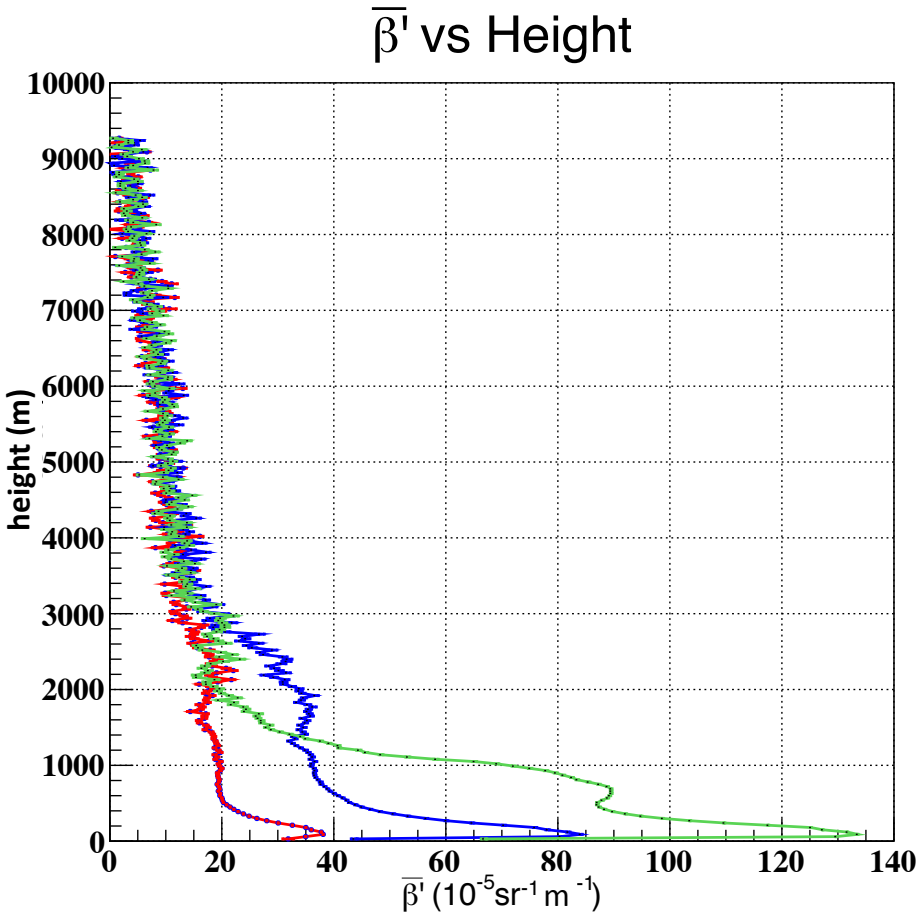

Fig. 4.14 The data tabulated in Table 4.5 of attenuated backscatter as a function of height; red plot (low aerosol) for MJD 56419.27097 (2013/05/07 at 06:30:12 UTC), blue plot (elevated aerosol) for MJD 56413.27301 (2013/05/01 at 06:33:08 UTC) and green plot (very elevated aerosol) for MJD 56442.35119 (2013/05/30 at 08:25:43 UTC) with a height binning of 30 m and identical 30-min time averaging.

Though there is a seasonal correlation between rises in water vapour and average backscattering, it is weak and is probably coincidental (as previously discussed in Section 3.4.8). This question will be addressed in Chapter 5. Thirdly, from column *std err* in Table 4.5, it is seen that high aerosol loadings have higher standard errors in mean in the first km a.g.l. than low aerosol loadings. This may be due to the increased mixing and turbulence of the atmosphere in the lower boundary layer. Highly-turbulent air parcels will pick up large-size aerosol particles; turbulence may cause the aerosol particles to mix in-homogeneously according to the aerosol diameter, with larger particles frequenting the lower regions of the

height bin. A more reliable explanation will require additional data, such as the aerosol size distribution.

A plot with greater spatial resolution of attenuated backscatering with height (Figure 4.14) shows the upper limits where the majority of attenuated backscatterings are recorded. The negative gradient is visible on the 1^{st} and the 7^{th} May beginning at height $\sim$2 km and ending at height $\sim$3 km. However the 30^{th} May (green) shows a more acute negative gradient at $\sim$1 km. Note that a 30 m height binning is chosen to maximise plot detail; a 10 m height binning would have large errors, while a 50 m binning could lower errors but offer less aerosol height profile detail. A height binning $>$ 50 m would cause spatial detail to be lost.

4.8.2 BL View - an independent analysis of CL51 data

At VERITAS, there is no other instrument (such as a lidar or another ceilometer) which may be used to independently corroborate the ceilometer analysis outlined in this thesis. However, Vaisala has produced a proprietary boundary-layer detection software package named BL View [Münkel and Roininen, 2010]. This package takes the binary format files of attenuated backscattering from the CL51 and produces plots of attenuated backscatter as a function of time, plotting the output in 24-hour blocks. It uses a negative-gradient algorithm to detect the changes in aerosol loading that indicate the top of the planetary boundary layer. This technique finds the greatest drop in backscattering over a set height window, the highest negative gradient, and selects this to be the top of the boundary layer. Where a threshold negative gradient is detected, an empty black square is placed at that height; the next time bin is analysed and another black box is plotted if a threshold negative gradient is found. These black boxes will, in principle, outline the boundary layer. To reduce sensitivity to sky noise and atmospheric changes, height and time averaging are applied of 320 m and 30 min respectively. The 3 days from May 2013 which have been examined in part so far, 2013/05/01, 2013/05/07 and 2013/05/30, are presented in the screen output formalised by BL View. See Figures 4.15, 4.16 and 4.17. The 30-min averaging window used for the

analysis in Section 4.8.1 are shown by red dashed lines.

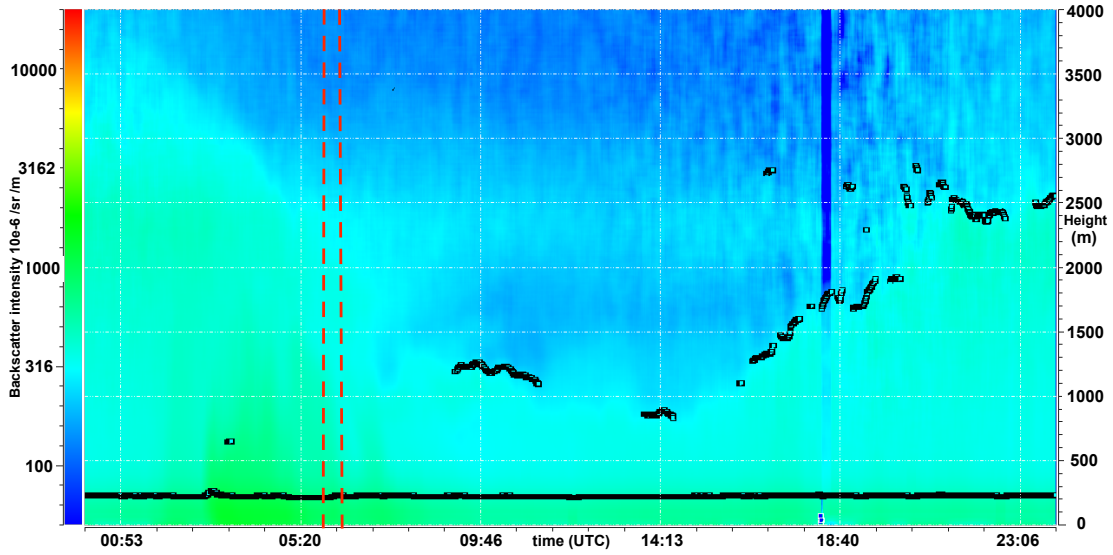

Fig. 4.15 BL View from May 1st 2013, with the red dashed lines showing the approximate 30-min of atmosphere (up to 4 km) analysed by the new technique presented in Section 4.8.1.

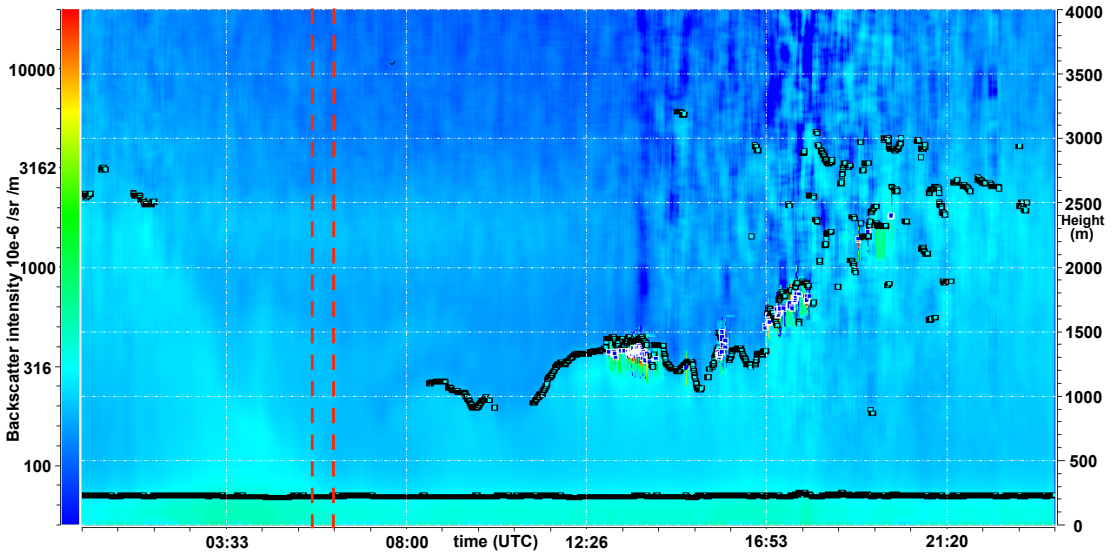

Fig. 4.16 BL View May 7th 2013, red dashed lines represent approximate start and end of the 30-min analysis presented in Section 4.8.1.

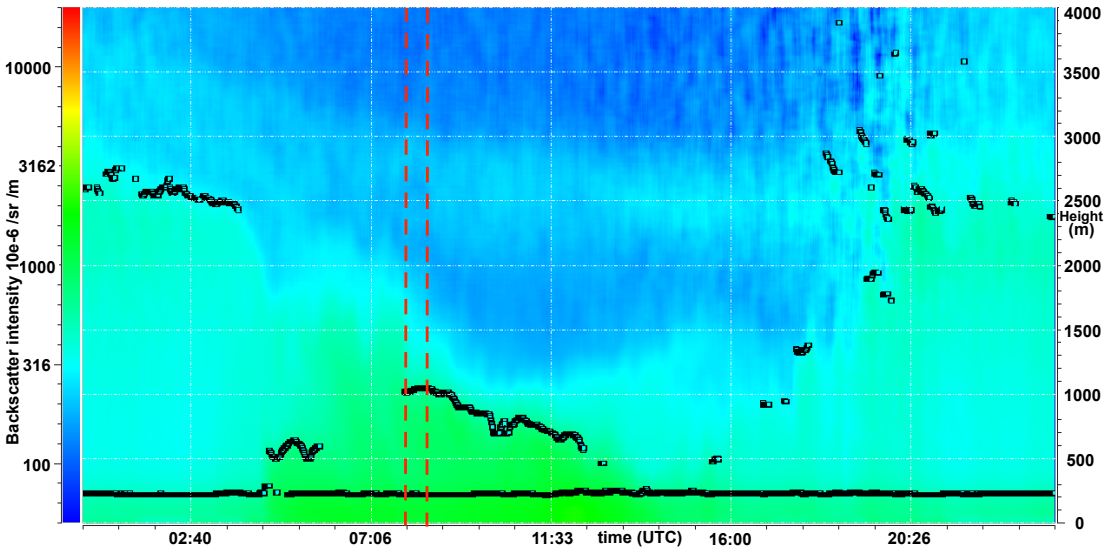

Fig. 4.17 BL View May 30^{th} 2013, red dashed lines represent approximate start and end of the 30-min analysis presented in Section 4.8.1.

The BL View negative gradient algorithm did not register a well defined boundary layer for the datasets of the 1^{st} and the 7^{th} May 2013, despite a small negative gradient being visible from 2 to 3 km a.g.l. (a poorly befined boundary layer is seen in Figure 4.14 between 2-3 km a.g.l.). BL View detected higher aerosol loading on the 1^{st} May compared to the 7^{th}, displayed with the aid of the colour bar on the left-hand y-axis (backscattering intensity). The example from the 30^{th} May is more definitive; BL View detects a boundary layer at 1 km a.g.l., with heavy aerosol loading below this layer, while above the layer the aerosol loading drops quite suddenly. This is what is seen in Figure 4.14. In summary, the independent analysis BL View is useful for cross-checking if the aerosol analysis presented in Table 4.5 is implementing basic height and time averaging of aerosol profiles correctly.

4.8.3 Applying corrections to May 2013 data

From this data (listed in Table 4.5) and the CL51-PWV simset (introduced in Section 4.5.2) the ceilometer transmittance profiles are easily calculated for both λ_{lo} and λ_{hi} (described in Section 4.4). However, these transmittance profiles may be of little use for the effective

water vapour extinction, ext_{H_2O}, has not been applied. Table 4.6 displays ceilometer data from the same three seperate days. Firstly, the 7^{th} May representing a low aerosol loading (*top*), where the PWV_{lowAer} = 1.25 g cm^{-2}. Secondly, the 1^{st} May which represents an elevated aerosol loading (*middle*), where the $\text{PWV}_{elevAer}$ = 0.69 g cm^{-2}. Thirdly, the 30^{th} May which represents an unusually high aerosol loading (*bottom*), where the $\text{PWV}_{HighAer}$ = 1.77 g cm^{-2}. The attenuated backscattering data from these three episodes have already been tabulated above (Table 4.5), but new data columns are now presented. $\beta^{corr}_{par_{lo}}$ and $\beta^{corr}_{par_{hi}}$ are the corrected attenuated backscatter for both wavelengths. Tr_{lo} and Tr_{hi} represent the total transmittance, particulate and molecular, for both wavelengths. Finally, ext_{H_2O-lo} and ext_{H_2O-hi} are the effective water vapour extinction estimates for the two wavelengths. The impact of effective water-vapour extinction correction on averaged attenuated backscatter and on total transmittance is examined. Of interest is the slight change in $\beta^{corr}_{par_{lo}}$ to $\beta^{corr}_{par_{hi}}$, the corrected attenuated backscatter for λ_{lo} and λ_{hi}, with the large difference in Tr_{lo} to Tr_{hi}, the total transmittance in the particular height bin for λ_{lo} and λ_{hi}. This is due to λ_{hi} being outside of the partial transmission window of 901-907 nm (discussed in Section 4.5). Small changes in peak laser emission around λ_{lo} may produce considerably higher variations in transmittance estimates than for λ_{hi}. Of more importance is the differences seen in effective water vapour extinction for λ_{lo}, ext_{H_2O-lo} and effective water vapour extinction for λ_{hi}, ext_{H_2O-hi} for the three days in question. For the 7^{th} May and the 1^{st} May, the values for ext_{H_2O-lo} are very similar, not so for ext_{H_2O-hi}. This is because the transmittance values for λ_{lo} for various values of PWV lie closer together than for λ_{hi} (seen in Figure 4.10). This means that an increase in water vapour will effect ext_{H_2O-lo} less that ext_{H_2O-hi}. This is seen in Table 4.6, where the value of PWV on 7^{th} May are almost twice that of the 1^{st} May. Examining some data from these two days, ext_{H_2O-lo} at 1^{st} km changes from 0.034 to 0.031, $\sim$9% change, while ext_{H_2O-hi} at 1^{st} km changes from 0.078 to 0.054, $\sim$31%. The effects of varying effective water vapour extinction produce less variability between λ_{lo} and λ_{hi} when the attenuated backscattering alone is being corrected and not the total transmittance.

$Height$	$\bar{\beta}'_{par}$	$\beta^{corr}_{par_{lo}}$	$\beta^{corr}_{par_{hi}}$	Tr_{lo}	err_{lo}	Tr_{hi}	err_{hi}	ext_{H_2O-lo}	ext_{H_2O-hi}
metres	$\frac{\times 10^{-5}}{\text{sr m}}$	$\frac{\times 10^{-5}}{\text{sr m}}$	$\frac{\times 10^{-5}}{\text{sr m}}$	0-1	$\pm\%$	0-1	$\pm\%$	–	–
WSS12 - MJD 56419.27097 (2013/05/07 06:30:12 UTC)									
1000	21.9	23.4	25.7	0.957	1.60	0.911	1.03	0.034	0.078
2000	15.4	17.4	20.6	0.966	1.38	0.930	0.88	0.027	0.062
3000	14.3	16.8	21.0	0.974	1.07	0.946	1.07	0.019	0.045
4000	9.9	11.9	15.3	0.983	0.78	0.965	0.53	0.012	0.029
5000	7.5	9.1	12.1	0.989	0.45	0.989	0.27	0.007	0.016
WSS16 - MJD 56413.27301 (2013/05/01 at 06:33:08 UTC)									
1000	46.0	49.0	51.4	0.949	1.67	0.925	0.73	0.031	0.054
2000	31.2	34.9	38.0	0.961	1.45	0.942	0.53	0.024	0.042
3000	22.7	26.2	29.3	0.972	1.06	0.958	0.70	0.017	0.030
4000	11.1	13.2	15.0	0.983	0.70	0.975	0.28	0.011	0.019
5000	8.3	10.0	11.4	0.990	0.47	0.985	0.23	0.006	0.010
WSS18 - MJD 56442.35119 (2013/05/30 at 08:25:43 UTC)									
1000	90.4	108.2	111.9	0.912	3.07	0.897	1.58	0.086	0.101
2000	29.7	41.1	43.5	0.929	2.55	0.918	1.36	0.069	0.081
3000	15.2	23.3	25.1	0.947	2.33	0.940	1.39	0.051	0.059
4000	9.6	15.8	17.1	0.966	1.68	0.961	1.04	0.034	0.038
5000	7.1	12.2	13.3	0.980	1.26	0.978	0.87	0.019	0.022

Table 4.6 The data from Table 4.5 with water-vapour extinction correction applied. Attenuated backscattering pre and post correction shown, total effective water-vapour extinction and total transmittance values (for corrected data only). All calculations are for both λ_{lo} and λ_{hi}. Note that errors are $\pm$ err_{lo} and err_{hi}.

This is why the methodology for determining the aerosol load of the atmosphere uses the particulate component alone and not the total transmittance (as outlined in Section 4.7.3). Table 4.6 lists the corrected attenuated backscatter data for May 2013 while Figure 4.18 plots the λ_{hi} estimate alone, but without associated errors that have been calculated in this instance for total transmittance alone. Note that solid lines represent averaged attenuated backscatter while dashed lines are for corrected attenuated backscatter. The 7^{th} May data (blue) have had their attenuated backscatter increased by $\sim$18% for a PWV_{LowAer} of 1.252 g cm^{-2}, which represents 60% of the normal PWV for a VSummer atmosphere according to MODTRAN molecular profiles.

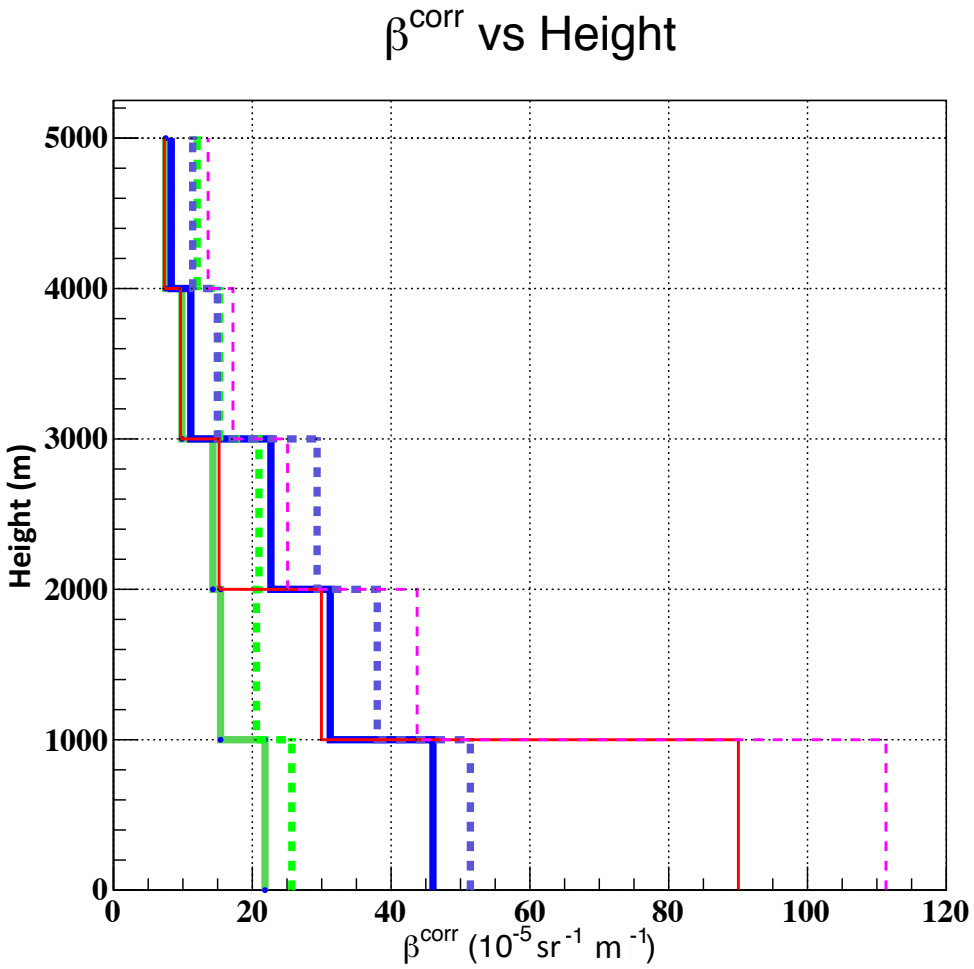

Fig. 4.18 The data from Table 4.6, λ_{hi}, plotted as follows; $\bar{\beta}'_{par}$ (solid-line, table column 2) and $\beta^{corr}_{par_{hi}}$ (dashed-line, table column 4) from the days MJD 56413 (2013/05/01) (*blue*), MJD 56419 (2013/05/07) (*green*) and MJD 56442 (2013/05/30) (*pink*), as per Tables 4.5 and 4.6. All data are from 0-5 km a.g.l.

The 1^{st} May data (green) have had their attenuated backscatter increased by $\sim$12% for a $\text{PWV}_{HighAer}$ of 0.694 g cm^{-2}, which represents 32% of the normal PWV for a VSummer atmosphere. The 3^{rd} dataset, plotted in pink, is from the 30^{th} May where their attenuated backscatter increased by $>$ 23% for the 1^{st} km a.g.l. This was for a $\text{PWV}_{veryHighAer}$ = 1.772 g cm^{-2}, which represents $\sim$100% (normal) PWV for a VSummer atmosphere according to MODTRAN's modelling of the VERITAS site.

4.8.4 Examining 13^{th} April 2013 data

A well known extra-galactic VHE γ-ray emitter,Mrk 421 [Balokovic et al., 2016], reached a high elevated state on the 13^{th} April 2013. It was also a day of elevated aerosol loading, which was not taken into account in the blazar analysis as no working measurement for aerosol profiling had been developed to that point. As there were intermittent clouds below 7 km it was only possible to obtain aerosol profiles for the following 30-min windows, ending on MJD 56395.14453 (2013/04/13 03:28:00), MJD 56395.19412 (2013/04/13 04:39:32) and MJD 56395.29876 (2013/04/13 07:10:13). The later set ending on MJD 56395.29876 is chosen for examination, as a full 30 min VERITAS data run from this window will be included in Chapter 6. The aerosol extinction was estimated to be WSS16, which was consistent with two other aerosol profiles measured on the same day but not presented here.

$Height$	$\bar{\beta}'_{par}$	$\beta^{corr}_{par_{lo}}$	$\beta^{corr}_{par_{hi}}$	Tr_{lo}	err_{lo}	Tr_{hi}	err_{hi}	ext_{H_2O-lo}	ext_{H_2O-hi}
metres	$\frac{\times 10^{-5}}{\text{sr m}}$	$\frac{\times 10^{-5}}{\text{sr m}}$	$\frac{\times 10^{-5}}{\text{sr m}}$	0-1	$\pm\%$	0-1	$\pm\%$	–	–
WSS16 - MJD 56395.29876 (2013/04/13 07:10:13 UTC)									
1000	27.5	30.8	32.9	0.945	1.98	0.914	1.39	0.056	0.086
2000	27.5	33.4	37.2	0.963	1.65	0.941	1.23	0.038	0.059
3000	30.9	39.3	45.0	0.977	1.55	0.963	1.28	0.024	0.037
4000	14.3	18.7	21.8	0.985	1.14	0.977	0.95	0.015	0.023
5000	12.4	16.6	19.5	0.991	1.05	0.986	0.92	0.010	0.015

Table 4.7 April 2013 data. All columns are as per Table 4.6. Of note is the higher boundary layer than found in May 2013. PWV estimate of 1.134 g cm^{-2}

4.8.5 Examining April 2015 data

In April 2015 a distant extra-galactic object became active in the VHE $\gamma - ray$ band; for 7 continuous days VERITAS observed PKS 1441 +25 at less than 30° from zenith [Abeysekara et al., 2015]. During this time there was some unusual variability in the boundary-layer aerosols, especially noted on 22^{nd} April. Table 4.8 displays data from the beginning of

observations on this day, MJD 57134.20889 (2015/04/22 05:00:48 UTC), top section, and from halfway through the night's observations, 57134.50069 (2015/04/22 12:01:00 UTC), bottom section. The variability on the 22^{nd} April is unusual in its rate of change over 7 hrs.

Height	$\bar{\beta}'_{par}$	$\beta^{corr}_{par_{lo}}$	$\beta^{corr}_{par_{hi}}$	Tr_{lo}	err_{lo}	Tr_{hi}	err_{hi}	ext_{H_2O-lo}	ext_{H_2O-hi}
metres	$\frac{\times 10^{-5}}{\text{sr m}}$	$\frac{\times 10^{-5}}{\text{sr m}}$	$\frac{\times 10^{-5}}{\text{sr m}}$	0-1	$\pm\%$	0-1	$\pm\%$	–	–
WSS16 - MJD 57134.20889 (2015/04/22 05:00:48 UTC)									
1000	51.4	57.1	58.2	0.947	1.91	0.939	0.95	0.052	0.060
2000	37.7	45.0	46.3	0.964	1.55	0.960	0.88	0.035	0.040
3000	21.3	26.6	27.5	0.978	1.44	0.975	1.03	0.021	0.024
4000	13.0	16.6	17.3	0.986	1.02	0.985	0.76	0.013	0.015
5000	13.1	17.0	17.7	0.991	0.92	0.991	0.75	0.009	0.009
WSS12 - MJD 57134.50069 (2015/04/22 12:01:00 UTC)									
1000	19.5	21.1	22.0	0.963	1.20	0.941	0.77	0.037	0.059
2000	12.5	14.3	15.4	0.975	0.80	0.961	0.53	0.025	0.039
3000	16.8	19.7	21.6	0.985	0.51	0.976	0.32	0.015	0.024
4000	10.7	12.7	14.1	0.991	0.31	0.985	0.19	0.010	0.015
5000	09.7	11.7	13.0	0.994	0.19	0.991	0.11	0.006	0.009

Table 4.8 The following data are taken from the April 2015. The PWV was quite low and constant at H_2O = 0.738 g cm^{-2}. All columns are as per Table 4.6. Of note is the rapid drop in boundary layer aerosols, more than what would be expected by a drop in boundary layer height, which tends to increase the aerosol concentrations into a lower total height. The cause is unknown.

At 03:30:00 UTC, $\bar{\beta}'_{par} = 30 \times 10^{-5}\text{sr}^{-1}\text{m}^{-1}$, at 05:30:48 UTC, $\bar{\beta}'_{par} = 42 \times 10^{-5}\text{sr}^{-1}\text{m}^{-1}$, for the 1^{st} km a.g.l. The *std err* was very low for 05:00:48 UTC, much lower than for the two adjoining data sets. The observed aerosol profile is therefore not caused by turbulent mixing; its exact nature can not be determined with the limited data available. This quick change in aerosol loading provided an opportunity to test if VERITAS data may be adversely impacted on by changes in aerosol extinction over short periods. The plots were presented in Chapter 3 (Figures 3.12 and 3.13) and show the pedestals and t_{zero} estimates for all 499 PMTs of T1 from both times on the night of 22^{nd} April. The aerosol loading profiles present during the two data runs are plotted in Figure 4.20. They plots for pedestals

and t_{zero} estimates are unaffected by the change in aerosol extinction. The data quality monitoring team of VERITAS passed the two data sets (77403 and 77412) as science quality, the highest quality classification. Additional information on the aerosol loading for the night in question is available from BL View, Figure 4.19. Firstly, the normal diurnal lowering / rising of aerosol height profiles is seen.

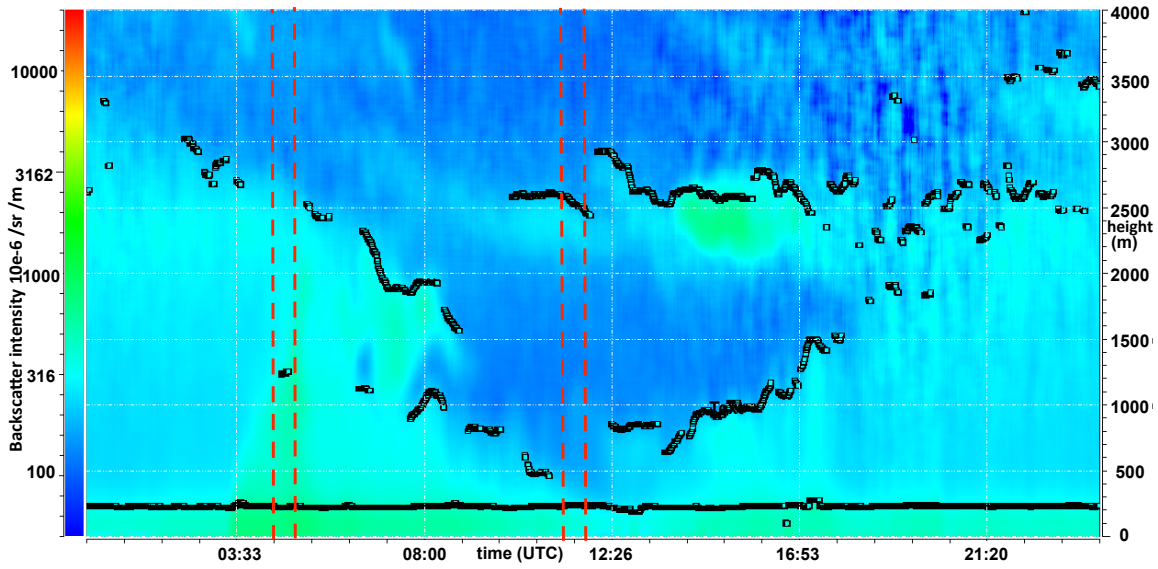

Fig. 4.19 BL View April 22nd 2015, red dashed lines represent approximate start and end of the 30 min analysis runs plotted in Figure 4.20; left set of dashed lines for WSS16 aerosol loading, right set for WSS14 aerosol loading.

For the earlier ceilometer data run, elevated aerosol loading is seen principally below 1.2 km a.g.l. where the BL View negative gradient algorithm has put a boundary layer marker. However, aerosol particles are still present in elevated quantities up to ∼2.5 km. The later ceilometer run reveals a low aerosol loading, with a boundary layer detected at 2.5 km a.g.l., caused by an (unidentified) passing air parcel with increased backscattering. Its effects are seen in Table 4.8, where the attenuated backscatter from 2.0-2.5 km increases, before the decrease (negative gradient) is detected by BL View. There is therefore good corroboration between the basic aerosol analysis algorithm in this thesis and BL View.

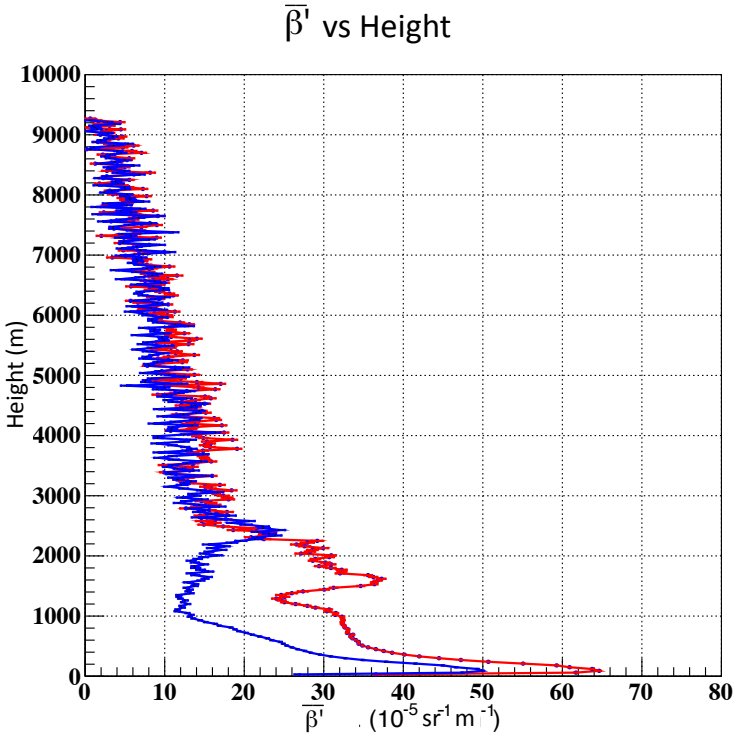

Fig. 4.20 The data tabulated in Table 4.8, red (elevated aerosol) for MJD 57134.20889 (05:00:48 UTC) and blue (normal aerosol) for MJD 57134.50069 (12:01:00 UTC), with a height binning of 30 m and identical 30 min time averaging, with error bars. The aerosol layer appears to increase in height during the night.

4.9 Results from 5.5 years of ceilometer operation

Running 5.5 years of ceilometer data, from December 2011 to June 2017, through the technique outlined in section 4.7.3 will display the overall aerosol trends at the VERITAS site during that period. Refer to Figure 4.21 for $> 2.2\times10^8$ ceilometer reportings that produced $\sim3.15\times10^4$ aerosol profiles, where just $\sim3.08\times10^4$ aerosol profiles have been plotted, due to cloud detections from 5-7 km a.g.l. for 0.07×10^4 profiles. When cloud is detected between 5-7 k.m. a.g.l. the algorithm does not calculate the WSS selector, as the accuracy of the aerosol extinction estimation can not be immediately verified. Such data will need more careful examination before it's corrected attenuated backscatter estimate, $\beta^{corr}_{par(z,\lambda,H_2O)}$, is deemed accurate. The 1D histogram shows the overall aerosol extinction binned in WSS

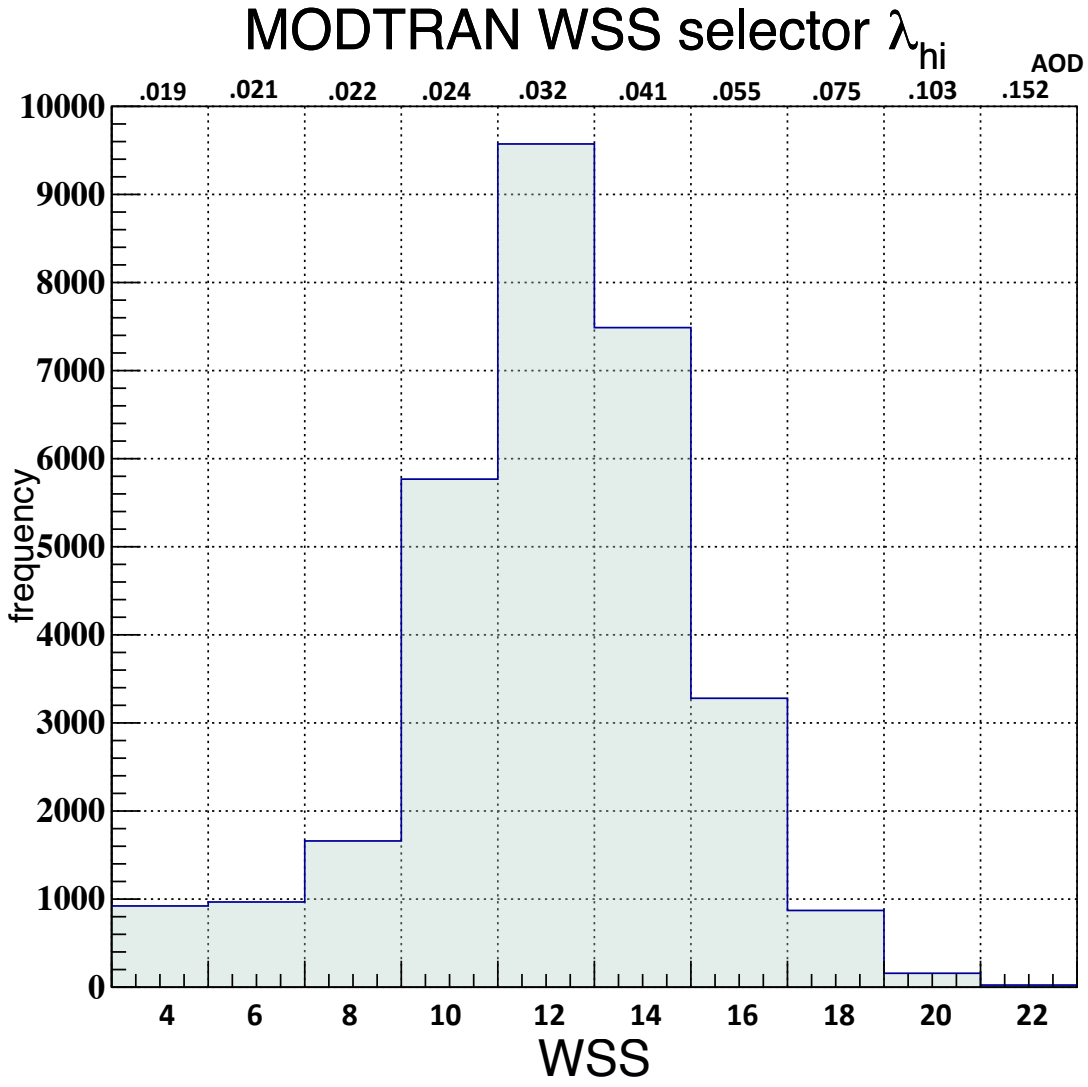

Fig. 4.21 A 1D histogram of the VERITAS site WSS aerosol estimation for $\approx$ 15,500 Hrs of cut ceilometer data (from $>$ 31,000 hrs of operational data, daylight excluded) over 5.5 years. The plot shows WSS without associated errors, with the average aerosol extinction WSS13.1. The AOD is included on the top axis; this may vary slightly for varying levels of water vapour.

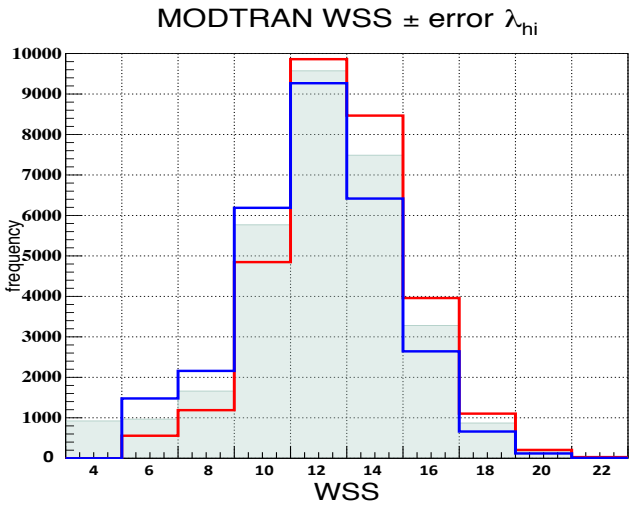

Fig. 4.22 The 1D histogram of Figure 4.21 with WSS+error (red) and WSS−error (blue) for the VERITAS site. The average aerosol extinction for WSS+error = WSS13.8, while for WSS−error = WSS12.9.

values, derived from $\beta^{corr}_{par(z,\lambda,H_2O)}$. The figure only shows the extinction estimate for λ_{hi} as this is closest to the true ceilometer wavelength (commented on in Section 4.3). Note that this plot also gives the binned values for AOD as derived by MODTRAN's Desert Dust model; slight variations occur for varying water vapour content where the shown values were derived from PWV bin 10 g cm^{-2}. For this period, the average aerosol extinction at VERITAS was WSS13.1, where for considerable time the working aerosol extinction was ∼WSS10-WSS12 (WSS10 and WSS12 are very close in aerosol extinction, as will be discussed in Chapter 5). The 5.5 years of data analysed have indicated that just ∼13% of data may be classified as elevated aerosols (≥WSS16), while only ∼3% is ≥WSS18. Setting upper limits on what constitutes normal and elevated aerosol loading is important for the Cherenkov imaging technique and is detailed in Chapter 5. The VERITAS collaboration operates with an aerosol extinction ∼WSS10, which is close in transmittance to the mean value estimated. Figure 4.22 shows the frequency of WSS being a particular extinction value when the + uncertainty in WSS (red lined plot) and the − uncertainty in WSS (blue lined plot) are added. These new histograms are plotted together with WSS from Figure 4.21. Adding (or subtracting) the PWV uncertainty and the Monte Carlo uncertainty shifts the

histogram to the right or left respectively (as would be expected). The ±WSS uncertainties are asymmetrical.

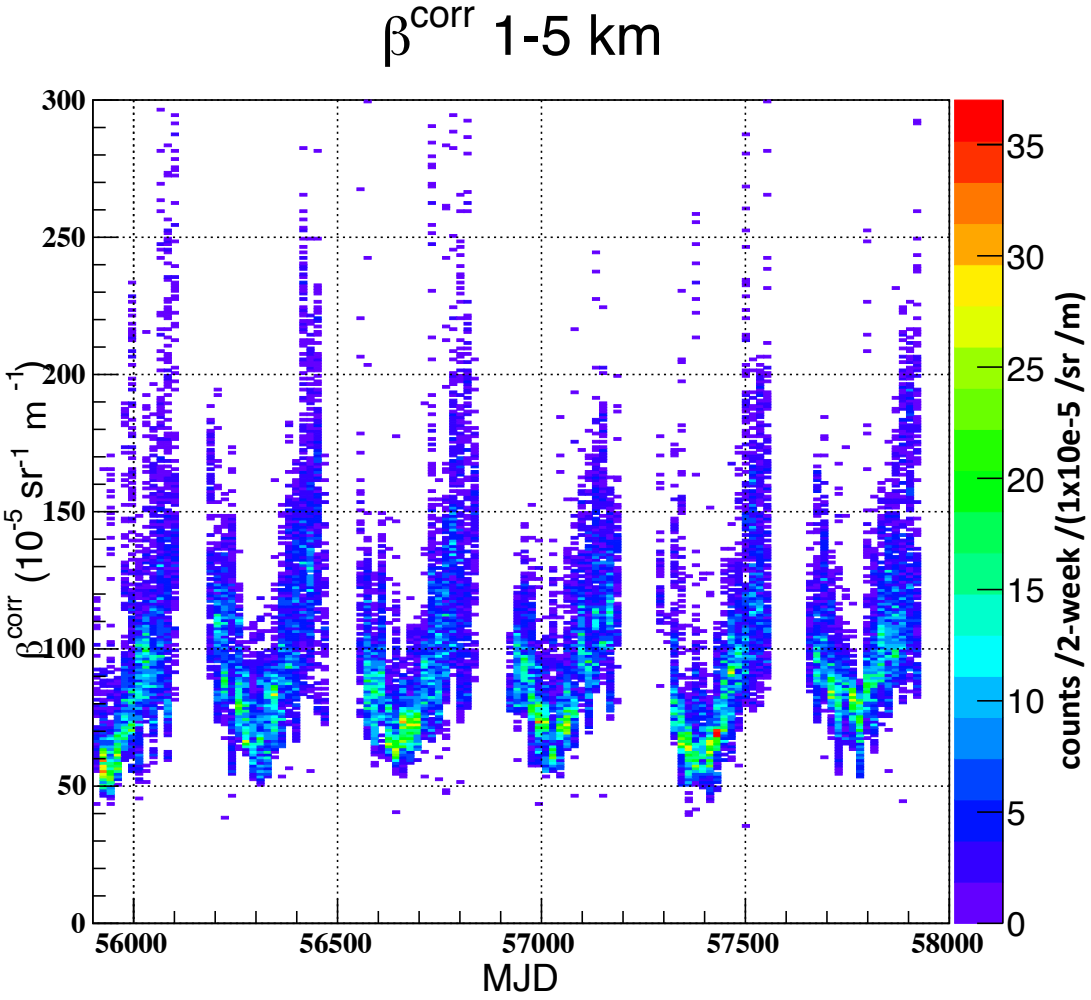

Fig. 4.23 A 2D histogram of the sum of corrected attenuated backscatter from 1-5 km a.g.l., $\sum_{i=1km}^{5km} \beta_i^{corr}$, vs MJD at the VERITAS site from the same data set as Figure 4.21. The time binning is two weeks, while backscattering is binned in 1x10^{-5} sr^{-1} m^{-1}. The backscattering is summed over the first 5 km to represent the aerosol optical depth through which the Cherenkov photons travel, which is also the comparison used in the least-squares selection of the WSS value that best represents the aerosol atmosphere.

The same data set from Figure 4.21 is now presented in 2D histogram format in Figure 4.23, with time binning of two weeks and backscatter binning of 1×10^{-5}sr^{-1}m^{-1}. It shows the now familiar seasonal trends. Attenuated backscattering shows more detail in aerosol profiles than the coarse binning of MODTRAN's WSS, thus its choice for highlighting year-

on-year aerosol trends.

Finally, a coarser binning is selected to show the increase of aerosol loading during longer time scales. Figure 4.24 displays the WSS selector (in bins of WSS02) plotted against the calendar month (in bins of 1 month). It shows a clear seasonal trends from December to June.

Towards the end of each observing year, seen just before the break in data taking due to summer-shutdown (detailed in Section 3.2.2), the total aerosol optical depth from 0-5 km a.g.l., τ_{0-5km}, (derivable from Equation 4.4) frequently exceeds 200-220 $\times 10^{-5}\text{sr}^{-1}\text{m}^{-1} \times S_{par}$ = 8.8×10^{-2} (where the lidar ratio $S = \frac{extinction}{backscatter}$). This equates to a > 4 fold increase compared to mid-VWinter observing season, with $\tau_{0-5km} = 2.0 \times 10^{-2}$.

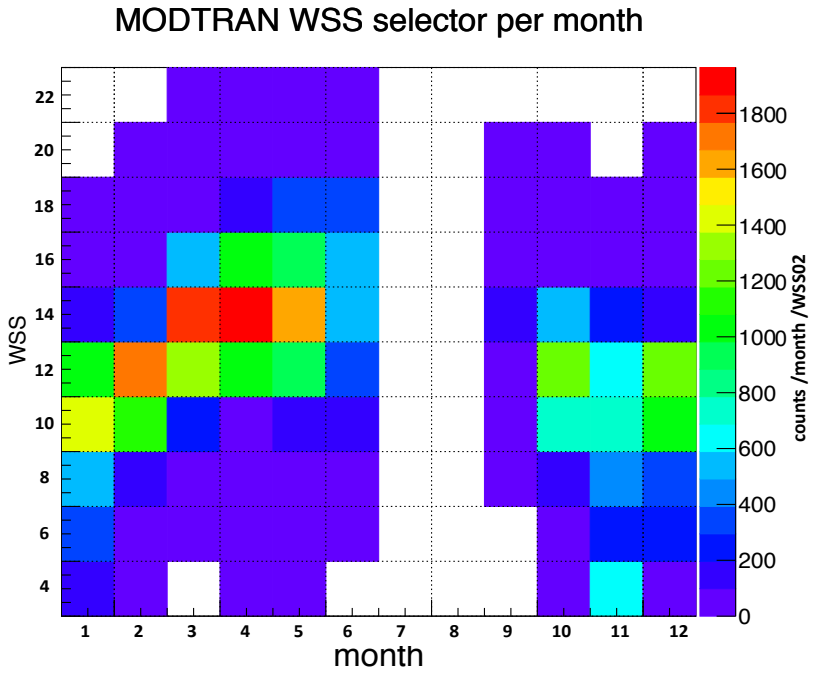

Fig. 4.24 A 2D histogram of WSS derived from corrected attenuated backscatter, $\beta^{corr}_{par_{hi}}$, binned per month (month 1 is January, Month 12 is December) from the same data set as Figure 4.21, displaying clear seasonal trends from December to June. Binning of 1 month and WSS02.

It is useful to calculate the expected drop in optical transmittance due to the increase in aerosols on site, mid-VWinter to end-VSummer. The Transmittance for mid-VWinter

season may be compared to Transmittance for end of observing year, through the bottom 5 km of atmosphere by the following approximation $T \approx 1 - total\ extinction$ (Equation 4.9)

$$change - Tr = \left(\frac{1 - \sum_{i=1}^{5} \left(\cancel{\alpha_{mol-ikm}^{VSummer}} + \alpha_{par-ikm} + \cancel{\alpha_{H_2O-ikm}^{VSummer}} \right)}{1 - \sum_{i=1}^{5} \left(\cancel{\alpha_{mol-ikm}^{VWinter}} + \alpha_{par-ikm} + \cancel{\alpha_{H_2O-ikm}^{VWinter}} \right)} \right) \tag{4.26}$$

where $change - Tr$ is the change (ratio) of transmittance from 0-5 km a.g.l. for VSummer over VWinter atmospheres and $\alpha_{par-ikm}$ is the particulate extinction for the i^{th} km a.g.l. It is noted that water vapour extinction is largely corrected (allowing cancellation of $\alpha_{H_2O-ikm}^{VSummer}$ and $\alpha_{H_2O-ikm}^{VWinter}$). The extinction profile for molecular VSummer and molecular VWinter atmospheres are near identical in the absence of water vapour, which is discussed in more detail in Appendix A (therefore the terms $\alpha_{mol-ikm}^{VSummer}$ and $\alpha_{mol-ikm}^{VWinter}$ cancel out). Substituting the cumulative corrected attenuated backscatter values from Figure 4.23 yields a value of $change - Tr$ $\sim$0.93, representing a drop of 7% in transmittance. This approximate calculation may be verified without utilising the simplifying approximation of $T = e^{-\tau_{0-5km}} \approx 1 - \tau_{0-5km}$. Here $change - Tr = \frac{e^{-\tau-HiAer}}{e^{-\tau-LoAer}}$. Substituting the values above yields $change - Tr$ $\sim$0.93. In rare circumstances, where τ_{0-5km} $\sim 400 \times 10^{-5} \mathrm{sr}^{-1}\mathrm{m}^{-1} \times S_{par}$, $change - Tr$ $\sim$0.85, representing a drop of 15% in transmittance.

Chapter 5

CORSIKA simulation studies

5.1 EAS simulations

This thesis relies heavily upon EAS simulations. CORSIKA (COsmic Ray SImulations for KAscade) is a detailed Monte Carlo program to study the evolution of EAS in the atmosphere. These showers are initiated by photons (VHE γ-rays), protons, and nuclei up to the atomic number of Fe. Originally CORSIKA was developed to perform simulations for the KASCADE experiment, [Doll et al., 1990, Klages et al., 1997], at Karlsruhe, Germany. It has been in continual development since it's first version released in 1989, being used by many high energy physics groups. Ongoing improvement is aided by updating particle cross-section and decay-time tables using data from the LHC experiment. Its applications range from Cherenkov telescope experiments such as VERITAS ($E_0 \sim 10^{12}$ eV) up to the UHE cosmic rays observed by groups such as AUGER ($E_0 > 10^{20}$ eV) [Abraham et al., 2009]. As all known factors which might alter the development of the shower are incorporated, a complex pilot input file has been developed. The principal variables for this thesis will be the progenitor type (γ-ray or proton), energy (100 GeV to 10 TeV), source elevation (00° or 30° from zenith), shower number for photon statistics and finally molecular atmo-

sphere profile (ATM31-ATM34, ATM61-ATM62, as discussed in Section 3.6.1).

Hadronic interactions and decay of unstable particles are simulated as follows. The distance covered by a hadron before it interacts or decays is determined by its interaction cross-section and probability of decay. The corresponding decay and interaction lengths are randomly determined within limits set by the tables mentioned. The shorter values are then taken as the actual path length by default. Most of the particles produced in high-energy interactions are unstable, and only those particles with sufficient interaction life-time are considered. For example, π^0 and other mesons have such a short lifetime that their interaction with the atmosphere before decay is negligible. Isolated neutrons are treated as stable particles because their mean lifetime of 14.7 mins is very large compared to the timescale of the showers. Muons are included in spite of their short decay times. This is because many may be produced close to the telescopes (within 500 m or less) and their Cherenkov emissions are detected readily with IACTs. VERITAS telescope multiplicity (using 2 or more telescopes) filters out these unwanted muonic additions to the Cherenkov imaging technique. All secondary particles are tracked explicitly along their trajectories through the atmosphere and CORSIKA calculates type, energy, location, direction and arrival times of all the particles of the shower that reach a selected observation level.

Electromagnetic interaction models are of much importance in this study. The interactions of electrons and photons are simulated using the Electron Gamma Shower System (EGS4) [Nelson et al., 1985]. For electrons or positrons, EGS4 treats bremsstrahlung, positron annihilation (in flight and at rest), Moliére multiple scattering (Coulomb scattering from nuclei), Bhabha (e^+e^-) and Møller (e^-e^-) scattering and annihilation. For γ-rays, Compton scattering, electron-positron production and photoelectric reactions are considered. EGS4 also reproduces the photo-production of muon pairs and the interactions with protons and neutrons of atmospheric nuclei.

The EAS simulation chain unfolds as follows. Firstly, the input card is set, with VERITAS site-specific parameters and Cherenkov options. Two of the main Cherenkov options are

shower reuse (how many times a simulated shower will be run through the detector simulation, set to 5 or 10 times) and scatter radius (the average light-pool scattering radius on the ground, currently set to 750 m for VERITAS, and 1000 m for the flat detector). Justification for shower reuse lies in the very small number of Cherenkov photons which reach the telescope mirrors, acknowledging that shower reuse will always be less preferential to extra shower production. The Cherenkov wavelength range is set from 200-700 nm. Secondly, an atmospheric height profile consisting of atmospheric density ($\mathrm{g\,cm^{-3}}$), atmospheric depth ($\mathrm{g\,cm^{-2}}$) and refractive index $(n-1)$ is provided. With this information particle interactions and decays at randomly selected heights are calculated along the path vector of the particle. This continues with the progenitor and resulting particles, until reaching the detector boundary. Here results are stored digitally as particle vectors or, if particle energies are below new interaction thresholds, decay ends the path vector and results are deleted. The work in this thesis uses the high-energy hadronic interaction model QGSJETII.3 [Ulrich et al., 2009] and low-energy hadronic interaction model URQMD 1.3cr [Djemil et al., 2005]. The switchover is set by the HILOW parameter in the input file at 80 GeV. The resulting CORSIKA output files with the various options selected according to the above will hereafter be referred to as CER files, that may be for a flat detector or volume detector.

5.2 Mono-energy simulations with ideal flat detector

Before examining EAS simulation sets for the VERITAS experiment, it is instructive to examine mono-energy simulations with an idealised flat detector. This approach allows one to sideline complex instrument response function (IRF) issues. This somewhat simplifies understanding of the complex particle interactions involving many variables. In particular, atmospheric parameters may be varied; knowing that both the detector response and the progenitor particle energy are a constant allows the atmospheric impact on EAS development to be more easily observed. Some specific questions with the Cherenkov imaging technique

currently requiring better understanding are:

- To what extent does the extinction due to aerosols depend on the shower zenith angle? Will large zenith angle data runs be adversely influenced by aerosols and water vapour? By simulating various EAS at fixed energies and at 00° and 30° from zenith, with various extinction values, this question may be examined.

- Is there an energy dependency involved in aerosol extinction? Keeping the progenitor γ-ray energy at a single value (mono-energy) offsets any energy reconstruction uncertainties. The following analysis varies energy, atmosphere model, aerosol extinction and detector photon integration window to test this question.

- Do differing water vapour profiles up to 25 km a.g.l. influence the results of VERITAS? Although MODTRAN does not point to Cherenkov wavelengths being affected by water vapour, there seems to be a loose correlation between lowering of L3 trigger rate and increased water vapour observed near summer-shutdown (briefly discussed in Section 3.4.7). For this analysis a new set of atmospheres has been developed, where normal, *1, and twice normal, *2, precipitable water values are used. Though *2 rarely occurs in VWinter months, and seldom in VSummer months (as seen in Section 3.2.1) before summer-shutdown, this scaling will accentuate the effects of water vapour, if any, on the results.

- What causes the drop in L3 rate observed seasonally, if not water vapour? VERITAS sporadically reports a large drop in L3 trigger rate in VSummer compared to VWinter. The cause may or may not be IRF independent, but is most likely a combination of both atmosphere and instrument. If the atmospheric component is real, it is important to ask are such atmospheric occurrences impacting the Cherenkov imaging technique, in calorimetry for example? A large set of proton EAS simulations have been produced along with γ-ray EAS for this analysis.

This work does not set out to definitively answer these important questions, but shed light on them and perhaps offer a direction for future research.

Progenitor	*energy* (GeV)	*ATM*	*Zenith* °	*WSS*	*Total no. showers*	*No. sets*
γ-ray	100	31-34, 61,62	00, 30	04-24	5000	92
γ-ray	300	31-34, 61,62	00, 30	04-24	3200	92
γ-ray	1000	31-34, 61,62	00, 30	04-24	1000	92
γ-ray	5000	31-34, 61,62	00, 30	04-24	140	92
proton	100	31-34	00	10,16	30000	8
proton	300	31-34	00	10,16	10000	8
proton	1000	31-34	00	04-24	2000	44
proton	3000	31-34	00	04-24	500	44
proton	5000	31-34	00	04-24	300	44
proton	10000	31-34	00	04-24	150	44

Table 5.1 A total of 460 sets of flat detector simulations were produced to examine the effects of aerosols and varying water vapour at VERITAS. γ-ray showers are simulated from 100 GeV to 5 TeV and proton showers from 100 GeV to 10 TeV. Atmospheres for VSummer *1 and *2 (WSS31 and WSS33) and VWinter *1 and *2 (ATM32 and ATM34) are produced for 00° and 30° from zenith. ATM61 and ATM62 atmospheres are produced for the γ-ray set alone. The full extinction set of WSS04 to WSS24 are produced for all simulations bar the low-energy proton showers.

5.2.1 Description of flat detector mono-energy analysis

Constructing a detector model of 1 km^2 with no detector / pixel spacing, no pixel saturation, a detector quantum efficiency = 1 and instantaneous detector response simplifies the simulations greatly. NSB$_{uv}$ is taken as negligible for further simplification. For efficient CPU usage the emission angle is set to wavelength independent (default setting), a good working approximation. All this reduces greatly the resources needed to produce usable photon statistics for filling histograms, in comparison to volume detectors with real IRFs. The parameter space for the flat detector study incorporates the progenitor type and energy along with the atmospheric parameters. A substantial set of 460 unique atmospheric simulations for the VERITAS site are tabulated in Table 5.1. The γ-ray energy range is from 100 GeV, the approximate VERITAS energy threshold, up to 5 TeV, a normal upper detection limit for

most sources observed. Higher energies are observed regularly at VERITAS, but their flux is quite low. Each shower is used 5 times in this flat detector analysis, with a scatter radius of 1 km from shower core. The atmosphere models are VWinter *1 = ATM31, VSummer *1 = ATM32, VWinter *2 = ATM33 and VSummer *2 = ATM34 (where *1 and *2 are normal and twice normal water vapour content). ATM31 and ATM32 correspond to the molecular atmospheres of ATM61 and ATM62 respectively, but with the Desert Dust extinction values of WSS04 to WSS24, in steps of WSS02. Note that ATM61 and ATM62 simulations have been added to all γ-ray showers, to compare differences between the current aerosol extinction profile and the proposed new aerosol extinction profiles. This is examined in detail below. Photon counting is initially integrated over the full 500 m from shower core available with the constructed detectors, but an additional photon count inside 100 m of shower core is also carried out. This is because the smaller integration area represents the collection area of VERITAS better, which is of the order of 10^5 m^2. Large zenith angle simulations ($\geq 60^\circ$ from zenith) are omitted as they comprise only a small subset of total data taken at VERITAS.

As an L3 array trigger rate study is to be carried out, proton EAS are also simulated. The proton showers $\geq$ 1 TeV are for 00° from zenith, ATM31-ATM34 and WSS04-WSS24. Lower energy proton showers are only examined with aerosol extinction for WSS10 and WSS16, the normal and elevated aerosol loading soon to be discussed. They represent normal and elevated aerosol loading at VERITAS. This decision to reduce extinction sets is because the number of photons from such low-energy proton showers produce far fewer Cherenkov photons than γ-ray showers of the same energy and shower number. As these proton showers will be only be used in L3 rate studies, 00° from zenith alone are examined.

5.2.2 Plotting and tabulating EAS simulations

For the flat detector simulations use has been made of ROSHA (ROot SHower Analysis), a histogram filling program derived from KASHA (KAscade SHower Analysis) of Karlsruhe

Institute of Technology. The 1D histograms, for lateral Cherenkov distributions of EAS, have distance from shower core binning of 2 m. 2D histograms, for Cherenkov height production, have distance from shower core binning of 2 m and height production binning of 100 m. Further, all 2D plots are derived with extinction profile WSS10 unless otherwise stated.

The uncertainties in binning are calculated as follows. The histogram represent weighted counts (where counts refers to the number of photons detected); assuming a Poisson distribution, the statistical uncertainty over a particular bin range may be computed as $\sqrt{SoW}$, where SoW (Sum of Weights) is the integral of the weighted entries in the bin range in question. The simulation data are presented in the following sections as ratios (comparisons with other simulations), where the uncertainty is calculated as follows. For a ratio $\frac{A}{B}$, the Poisson uncertainty is estimated from the A histogram for the bin range in question, called $A_{err} = \frac{\sqrt{SoW}}{SoW}$, while the same is done for B (B_{err}), derived from it's histogram in the bin range in question. The maximum uncertainty, err_{max}, for the ratio in question is

$$err_{max} = \left(\frac{A \times (1+A_{err})}{B \times (1-B_{err})} - \frac{A}{B}\right) \tag{5.1}$$

This will produce a slightly asymmetrical uncertainty estimation if for example $(1-A_{err})$ and $(1+B_{err})$ are used; here the largest uncertainty obtained by both estimations is chosen. It is noted that the uncertainties in mean Cherenkov height production are not estimated.

Due to the large amount of data produced by the simulation sets of Table 5.1, a condensed presentation form has been devised to convey the information, by tabulation. For this to be possible, certain abbreviations need to be used to represent how the data has been processed. The greek letter ν is is used for photon integration counts, where the standard integration window is 500 m from shower core. Sometimes a shorter integration window of 100 m from shower core is used; in this case a ratio of photon counts from shorter to longer photon integration windows, $\frac{100m}{500m}$, is denoted by ν'. Showers with shower axes of 00° from zenith are represented by $_{00}$, while showers from 30° from zenith are represented by $_{30}$. If a

comparison is to be made between showers from shower axes of 30° from zenith to showers from 00° from zenith, then $\frac{30}{00}$ is used. When one part alone of a simulation set is changed in comparison to another, for example the water vapour content, and the ratio of these sets is taken then "%" is used to denote the change. Therefore for a set progenitor type at a set energy, but with a change in water vapour, $\%\nu_{00}$ represents the change in photon counts over a 500 m integration window where the shower axes is from 00° from zenith.

5.2.3 Shower axis zenith angle and aerosol extinction

The simulation set for both 00° and 30° from zenith allows examination of the impact of shower axis zenith angle on extinction. As most γ-ray initiated Cherenkov photons derive from lower energy progenitor particles some plots for 100 GeV γ-ray EAS are produced. Figures 5.1 and 5.2 display lateral Cherenkov development, while Figure 5.3 displays Cherenkov production height. For these simulations a full extinction set of WSS04 to WSS24 is available. This comprehensive set of aerosol extinction profiles allows new, more precise, aerosol loadings to be incorporated into EAS simulations than was previously available. The total count of Cherenkov photons arriving at the flat detector (photon integration 0-500 m from shower core) for aerosol loading WSS04 to WSS24 (Figures 5.1 and 5.2) shows the impact of Desert Dust aerosols on VHE γ-ray Cherenkov photon arrival. Interestingly, there is little difference in overall Cherenkov transmission from WSS04 to WSS10. As the aerosol size distribution increases due to greater mixing force, the transmission decreases accordingly.

These same extinction values are applied to a longer shower axis path length (Table 5.2), where 30° from zenith simulations, produced in atmospheres ATM31 to ATM34, are examined. It is noted that the average production height of the Cherenkov photons is not altered by aerosols. The aerosol loadings found in our atmosphere are overwhelmingly in the boundary layer, typically below 5 km a.g.l. Even if this were not the case, the production of Cherenkov photons is influenced by the refractive index of air, n, which is not altered

by mineral aerosols. The average Cherenkov production heights for increased shower axis zenith angles do however increase, because of the additional increases in overall shower axis path length to detector. The atmosphere is modeled as planar by CORSIKA for zenith angles $\leq 70^{\circ}$, implying isobaric pressure (and hence constant n), with height. However as the progenitor and its secondaries spend longer time passing through a particular height bin, the probability of interaction increases. It is reasonable to assume a more lateral Cherenkov shower development, owing to increased interaction time per unit height. This is seen where on average there is an 8-10% increase in production height for 30° from zenith simulations over 00° from zenith, with a corresponding wider shower max region (as is seen in Figure 5.3). The increased production height is however not much greater than the corresponding uncertainty.

The increase in shower axis path length couples with the wider lateral shower development to greatly attenuate the number of Cherenkov photons arriving at detector by both Rayleigh and Mie scattering. Table 5.2 shows column $\nu_{\frac{30}{00}}$, the number of photons arriving from 30° from zenith against 00° from zenith, which shows that about $\frac{1}{3}$ of all Cherenkov photons are scattered before reaching the flat detector. Of interest are columns ν'_{00} and ν'_{30}, which roughly represents what proportion of photons that fall inside the VERITAS detector footprint (100 m) to the total flat detector integration (500 m). More photons from a 30° from zenith shower will fall outside the 100 m integration than the 00° from zenith counterpart, due to aforementioned extinction and lateral distribution increase. The fraction of photons arriving inside the VERITAS footprint from 00° and 30° from zenith, ν'_{00} and ν'_{30}, varies from $\frac{2}{3}$ to $\frac{3}{4}$ of the total photon count inside the 500 m integration radius for the same source elevation. When the extinction is increased from WSS10 to WSS16, these fractions remain very consistent, though the actual number of photons arriving inside the VERITAS footprint will decrease by another $\sim$10%.

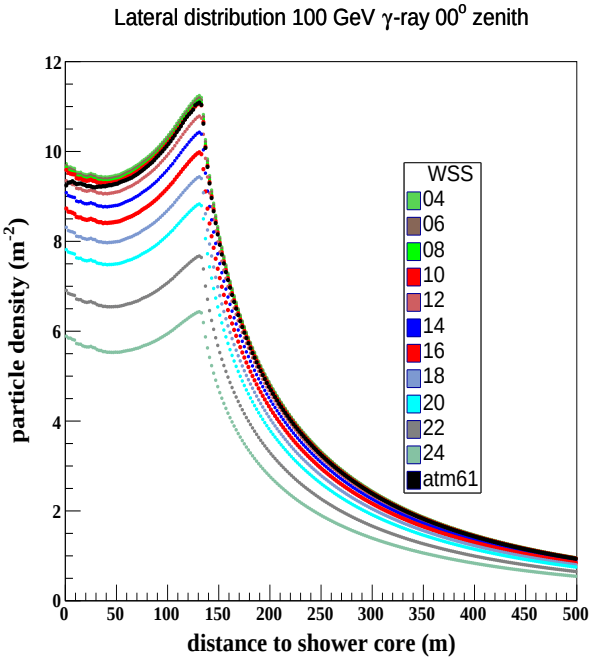

Fig. 5.1 1D histograms of the lateral distribution of Cherenkov photons which reach the detector from 5000×100 GeV γ-ray showers at 00° from zenith. A VWinter atmosphere with normal H_2O levels, *1, is used for production (ATM31). This simulation set is used eleven times for aerosol extinction WSS04-WSS24 (in steps of 2). The black plot represents ATM61, the original VWinter atmosphere with corresponding single extinction. This extinction is derived from a 50 km visibility rural aerosol model of MODTRAN (discussed in Section 3.6.2).

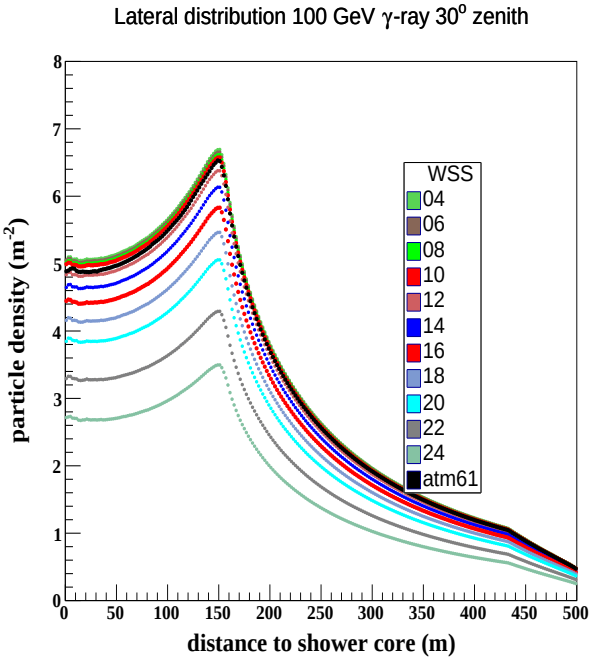

Fig. 5.2 1D histograms of the lateral distribution of Cherenkov photons which reach the detector from 5000×100 GeV γ-ray showers at 30° from zenith, identical atmosphere and extinction profiles used as for Figure 5.1.

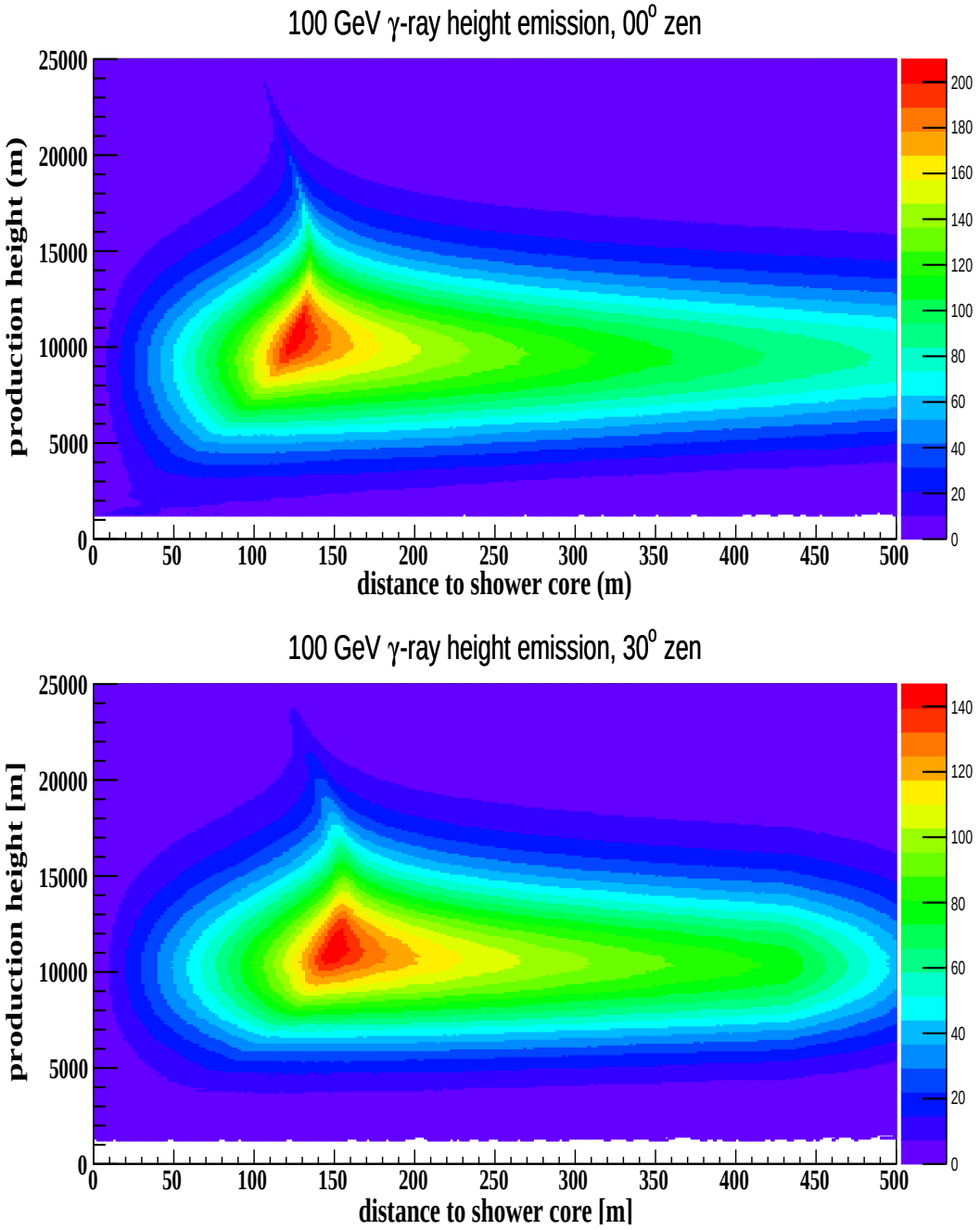

Fig. 5.3 A 2D histogram of the production height of Cherenkov photons which arrive at the detector from the same 5000 showers as Figures 5.1 and 5.2, with extinction WSS10. The average shower height for the 00° from zenith simulation is 10.0 km, while for the 30° zenith simulation it is 11.1 km (Table 5.2). Of interest is the lateral increase of Cherenkov emission for 30° zenith showers. Note that the faint blue areas on the peripheries in all 2D plots are due principally to Cherenkov light from $e^{\pm}$ with large transverse momenta.

γ-ray GeV	Ht_{00} (km) Ht_{30}	$\nu_{\frac{30}{00}}$	ν'_{00}	ν'_{30}	WSS16/WSS10
VWinter					
100	10.0 : 11.1	0.65±.04	0.72±.03	0.67±.03	0.90±.05
300	08.9 : 10.0	0.63±.02	0.75±.01	0.69±.02	0.91±.03
1000	08.0 : 09.0	0.63±.01	0.78±.01	0.72±.01	0.90±.01
5000	06.7 : 07.8	0.63±.008	0.83±.008	0.77±.008	0.92±.008
VSummer					
100	10.3 : 11.5	0.64±.04	0.72±.03	0.66±.03	0.90±.05
300	09.2 : 10.4	0.63±.02	0.76±.01	0.68±.01	0.90±.03
1000	08.3 : 09.3	0.61±.01	0.79±.01	0.71±.01	0.90±.01
5000	07.0 : 08.0	0.58±.008	0.84±.008	0.76±.008	0.91±.008

Table 5.2 Cherenkov arrival statistics from VHE γ-ray showers. Ht_{00} represents the mean production height (in km) of Cherenkov photons from 00° from zenith showers, Ht_{30} for 30° from zenith showers. The ratio $\nu_{\frac{30}{00}}$ represents the number of Cherenkov photons reaching the detector from 30° from zenith over 00° from zenith at WSS10. The columns ν'_{00} and ν'_{30} represents the ratio of photons arriving at detector integrated over 100 m to integrated over 500 m from shower core, for extinction WSS10 for both 00° from zenith and 30° from zenith respectively. This ratio also holds very well for WSS16, 00° from zenith and 30° from zenith. Column WSS16/WSS10 represents the ratio in photons from WSS16 over WSS10 from 00° zenith, in a *1 atmosphere. it is very consistent with WSS16/WSS10 from 30° from zenith. All photon counting, bar columns ν'_{00} and ν'_{30}, is carried out integrating over 500 m from shower core.

5.2.4 Progenitor particle energy and aerosol extinction

Higher energy γ-rays certainly produce many more Cherenkov photons than lower energy ones. For example, a 5 TeV γ-ray EAS produces $\sim$110 times the number of photons as a 100 GeV EAS. The lower mean emission height, 7 km a.g.l. for a 5 TeV γ-ray, produces a more tightly formed Cherenkov light pool around shower core than for a 100 GeV γ-ray shower, as seen in Figure 5.4, the lateral photon distribution, and Figure 5.5, the photon height production distribution.

It is useful to examine if Cherenkov production and transmission from γ-rays changes noticeably from 0.1 TeV $\leq E_\gamma \leq$ 5 TeV? This question is most computationally intensive, and only 140$\times$5 TeV γ-ray EAS have been produced. It would not be prudent to increase

the shower reuse to > 5 times; ideally for flat detectors lower shower reuse, if any, should occur. Availability of sufficient computational resources alone will improve on the data here presented.

Referring to column $\nu_{\frac{30}{00}}$ (Table 5.2), the fraction of photons arriving from 30° to 00° from zenith, there seems to be a decrease in this ratio in VSummer for increasing energies, though not as prevalant in VWinter months. This would seem counter-intuitive; it could be due to the small number of simulations produced for 5 TeV. Looking to columns ν'_{00} and ν'_{30}, the rough fraction of Cherenkov photons falling within the VERITAS footprint to total detector photon arrival, the energy dependency of photon arrival becomes clearer.

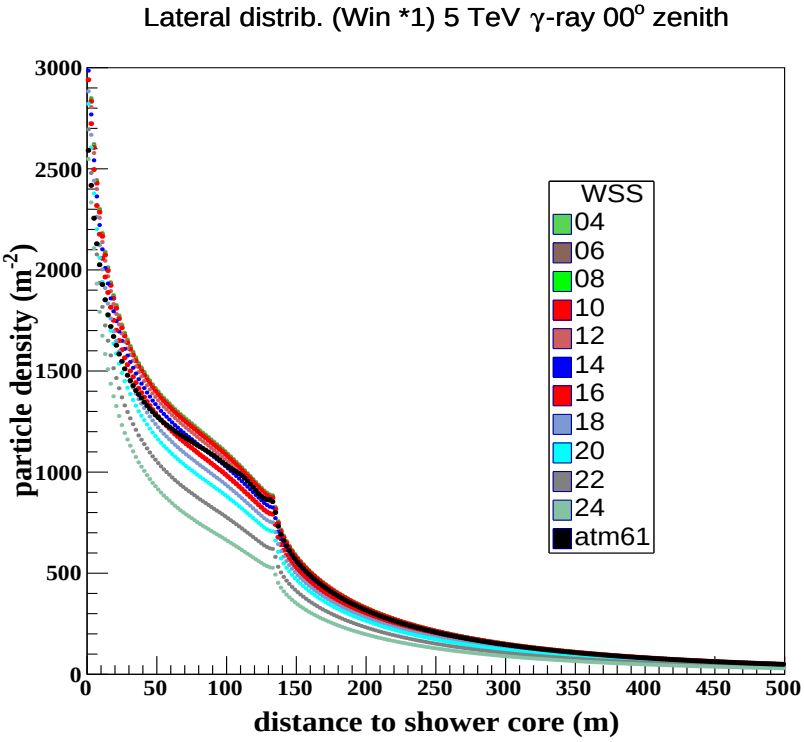

Fig. 5.4 1D histograms of the lateral distribution of Cherenkov photons from 140 5 TeV γ-ray showers with VWinter *1 and extinction WSS04-WSS24.

For 100 GeV showers at 00° from zenith, 72±3% of photons fall inside the VERITAS footprint compared to the 500 m integration. At 5 TeV this increases to 83-84%. As expected fewer Cherenkov photons arrive inside the VERITAS footprint for 30° zenith show-

ers. The ratio of ν'_{30} to ν'_{00}, not shown, is quite consistent over all energies quoted, being from 0.90-0.93. Also of interest is column WSS16/WSS10, which is consistent over the 0.1-5.0 TeV energy range, though the uncertainties are quite large for 100 GeV showers.

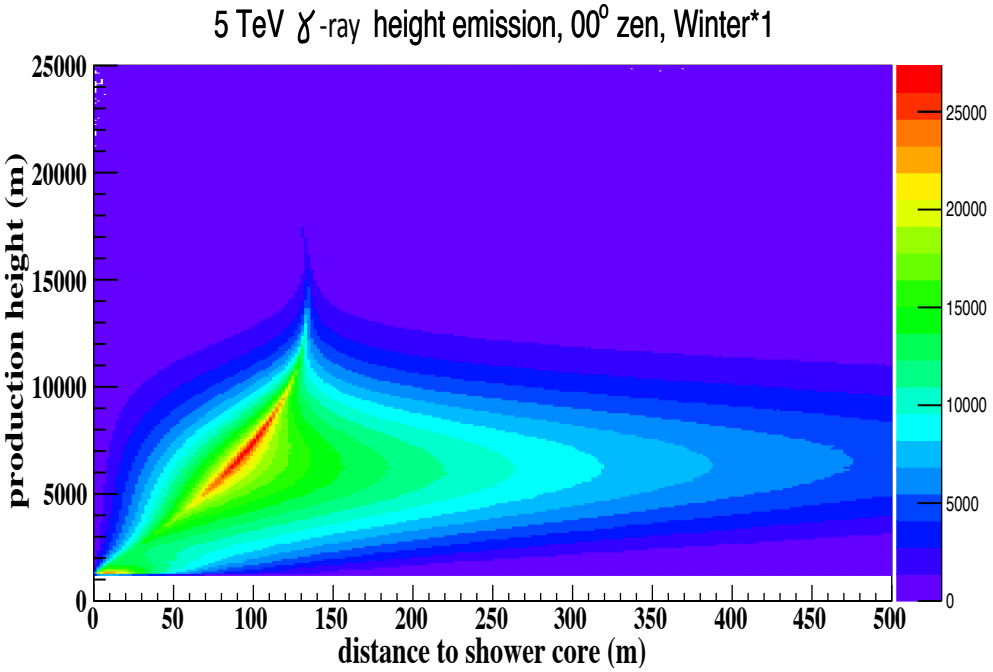

Fig. 5.5 2D histogram of the production height distribution of Cherenkov photons from 140 5 TeV γ-ray showers with VWinter *1 and extinction WSS10.

5.2.5 Water vapour and Cherenkov transmission

It has been noted for some time that the telescope L3 trigger rate lowered quite noticeably during VSummer observing months. These times corresponded to an increase in water vapour in the atmosphere as measured by radiosonde in Tucson, Arizona (detailed in Section 3.2.2). The question raised by this is, does the increased presence of water vapour in the atmosphere affect the production and transmission properties for Cherenkov photons from γ-ray progenitors? MODTRAN simulations would suggest not, as plots in Section 3.6.3 show a drop in photon transmittance for increased aerosol loading but not for increased water vapour. However, no known studies have been conducted previous to this thesis. For this important question a new set of simulations are devised and implemented. In addition

to VWinter *1 and VSummer *1, a further set of *2 or twice normal water vapour content atmospheres is produced, with corresponding unique WSS04 to WSS24 profiles, from 0-100 km a.g.l. Twice normal water vapour does not often occur during VERITAS operations. However this large difference in water vapour content between simulations will serve to highlight any associated impact on Cherenkov transmission. Refering to Table 5.3, columns

γ-ray GeV	$\%Ht_{00}$	$\%Ht_{30}$	$\%WSS10_{00}$	$\%WSS10_{30}$	$\%WSS16_{00}$	$\%WSS16_{30}$
VWinter						
100	1.00	1.00	1.00±.06	1.00±.06	1.00±.06	0.99±.08
300	1.00	1.00	1.00±.03	1.00±.04	1.00±.03	0.99±.04
1000	1.01	1.00	0.98±.01	0.99±.01	0.97±.01	0.99±.01
5000	0.98	0.98	1.05±.008	1.07±.01	1.05±.008	1.07±.008
VSummer						
100	1.00	1.00	1.00±.06	1.00±.06	1.00±.06	1.00±.08
300	1.00	1.00	1.00±.03	1.00±.04	1.00±.03	1.00±.04
1000	0.99	0.99	1.01±.01	1.01±.01	1.01±.01	1.01±.02
5000	0.99	0.98	1.04±.008	1.04±.01	1.04±.008	1.04±.008

Table 5.3 Cherenkov arrival statistics for varying water vapour. $\%Ht_{00}$ represents the ratio of mean production height for *1 over *2 atmospheres at 00° from zenith, $\%Ht_{30}$ for 30° from zenith showers. The aerosol extinction is WSS10 for both. $\%WSS10_{00}$ represents the ratio of WSS10 *1 photon arrival over WSS10 *2 photon arrival at 00° from zenith, $\%WSS10_{30}$ for 30° from zenith. The last two columns are the same, but for WSS16. All photon integration is over 500 m.

$\%WSS10_{00}$, $\%WSS16_{00}$ and $\%WSS10_{30}$, $\%WSS16_{30}$ represent the ratio of change in total photon count for *1 and *2 for the named aerosol extinction and zenith angle. For example, column $\%WSS10_{30}$ represents the difference in photon arrival within 500 m of shower core for a WSS10 atmosphere at 30° from zenith when the water vapour increases two-fold. Both VSummer and VWinter simulation sets seem consistent up to 1 TeV; however the uncertainties are quite large at lower energies. As energies increase to 5 TeV, there is a hint of a change in transmission above associates uncertainties; both VSummer and VWinter show a slight increase in photon count for *1. The increase is however borderline with the associated uncertainties involved. Additional analysis has shown that close to shower core

(within 25 m) an excess of photons is recorded between VSummer *2 and VSummer *1 at 5 TeV that is up to 10% the peak 5 TeV photon count for the same core distance. Integrating over the shorter 100 m radius the following values are found for 5 TeV showers. VSummer: $\%WSS10_{00}$ = 1.05±.007, $\%WSS16_{00}$ = 1.05±.008, $\%WSS10_{30}$ = 1.05±.007, $\%WSS16_{30}$ = 1.05±.008. VWinter: $\%WSS10_{00}$ = 1.06±.007, $\%WSS16_{00}$ = 1.06±.009, $\%WSS10_{30}$ = 1.09±.007, $\%WSS16_{30}$ = 1.09±.008. As the effect is close to shower core (≤25 m) it is unlikely to be detected with current generation PMTs, due to saturation effects.

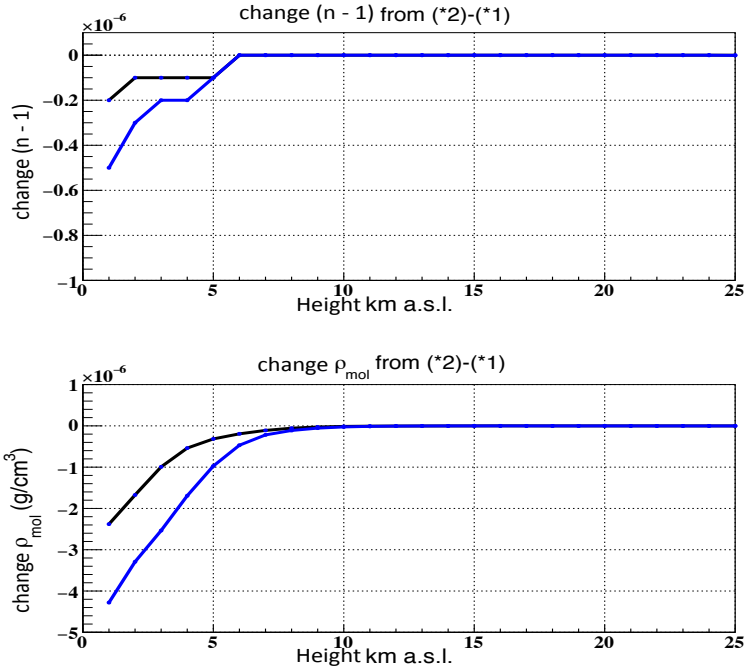

Fig. 5.6 A MODTRAN derived plot showing changes in refractive index and atmospheric density for VWinter (black) and VSummer (blue) atmospheres of *2 − *1, that is twice normal water vapour - normal water vapour. The change in refractive index caused by the increase in water vapour is only present up to 6 km a.s.l., while the change in atmospheric density is present up to 8 km a.s.l.

The change in refractive index, which is quoted as $(n - 1)$, and atmospheric depth, (ρ_{mol}), due to increased water vapour is plotted against the average height of the Tucson radiosonde readings (Figure 5.6). It is very small, and only present in the lower reaches of the atmosphere below shower max. It is unlikely that these decreases in refractive index and atmospheric depth will contribute to changes in Cherenkov photon production.

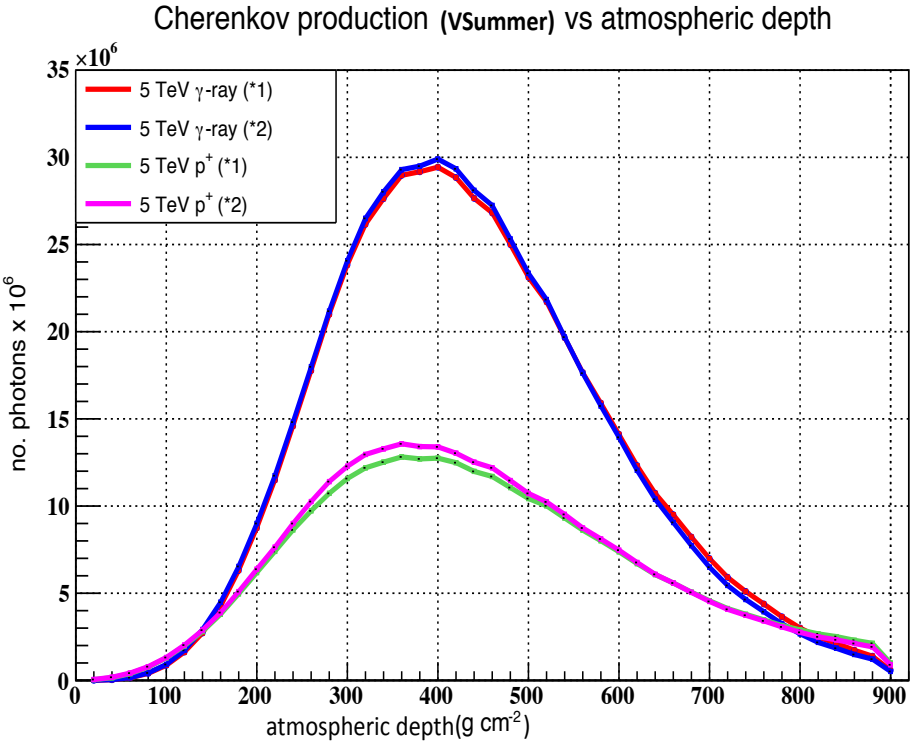

Fig. 5.7 A CORSIKA-derived plot of the production of Cherenkov photons against atmospheric depth for 140×5 TeV γ-ray showers and 300×5 TeV proton showers (discussed in Table 5.1). This data is pre-extinction. VSummer atmospheres, *1 and *2, at 00° from zenith are used. Uncertainty in photon counts are shown, but are too small to see (calculated as $\sqrt{N}$, where N = number of photons per atmospheric depth bin). Of interest is the slight increase of Cherenkov emission for *2; this can be understood by the longer path length the secondaries travel due to the slight increase in production height. However increased Rayleigh and Mie scattering scatters the Cherenkov photons so that more photons actually reach the flat detector in VWinter atmospheres, when extinction is lower.

Examining Cherenkov production vs atmospheric depth (pre-extinction), plotted in Figure 5.7, it can be seen that there is a slight excess of photons produced during the VSummer *2, 5 TeV, than VSummer *1, 5 TeV, for both γ-ray and proton progenitors. The uncertainties, determined by Poisson statistics, are plotted but are too small to see. The effect is slight and is probably caused by the slight increase in mean production height. The increase in photons detected in normal water vapour is likely due to the lower molecular extinction of these atmospheres. Closer to shower core, where the bulk of photons are emitted, we would expect to see the largest difference in photon arrival. Remembering the photon excess is

of the order of $\sim$5%, the flux of 5 TeV γ-rays is low and the occurrence of twice normal water content is rare, it is reasonable to assume the impact of water vapour on Cherenkov transmission is negligible. As the analysis of extragalactic VHE γ-ray sources in the next chapter is carried out below 1 TeV, no account of varying water vapour is taken.

5.2.6 ATM61-ATM62 and AMT31-AMT32 interchangeability

Finally, consideration is given to the interchangeability between the current MODTRAN aerosol model (50 km visibility tropospheric, ATM61-ATM62) and the proposed new MODTRAN aerosol model (Desert Dust, AMT31-AMT32). The analysis is presented in Table 5.4. Consideration is not given to should they be changed but to can they be interchanged. The currently employed extinction profile is likely a different aerosol mix than that found at VERITAS. The tropospheric model in use has a higher percentage of organics and some trace carbonaceous particles, a good match for the great plains of North America and Europe, but having slightly different optical properties than the Desert Dust mix. The statistical fluctuations from columns $\nu_{\frac{30}{00}}^{ATM6-}$ and $\nu_{\frac{30}{00}}^{WSS10}$ are consistent between both sets. Further, the shorter integration of 100 m from shower core, not reproduced in the table, yields very consistent results (differences of $\leq$1%) with the 500 m integration window presented for these columns.

Figure 5.8 shows a plot of the photon integration for ATM61 (black) and WSS04-WSS24, where WSS10 and WSS16 are highlighted in red. The transmission profile differences between the two aerosol models are visible but not of practical consequence, especially when the other systematic uncertainties are taken into account. WSS04-WSS10 produce a near identical transmission profile for Cherenkov photons; it is only from WSS12 onwards that differences in transmission clearly emerge.

γ-ray GeV	$\nu_{00}^{WSS10}/\nu_{00}^{ATM6-}$	$\nu_{30}^{WSS10}/\nu_{30}^{ATM6-}$	$\nu_{\frac{30}{00}}^{ATM6-}$	$\nu_{\frac{30}{00}}^{WSS10}$
VWinter				
100	1.01±.06	1.01±.07	0.65±.04	0.65±.04
300	1.06±.03	1.02±.04	0.66±.02	0.63±.02
1000	1.01±.01	1.04±.02	0.61±.01	0.63±.01
5000	0.99±.009	0.99±.01	0.58±.009	0.63±.008
VSummer				
100	1.04±.06	1.04±.07	0.65±.04	0.64±.04
300	1.00±.03	1.03±.04	0.61±.02	0.61±.02
1000	1.01±.01	1.00±.02	0.61±.01	0.63±.01
5000	1.07±.009	1.03±.01	0.61±.009	0.58±.008

Table 5.4 Cherenkov arrival comparison between the current atmospheric models, ATM61-ATM62, and the proposed new Desert Dust model, ATM31-ATM32 with WSS10. As ATM61-ATM62 are produced with *1 and one extinction profile, the comparison is limited to *1 atmospheres and extinction of WSS10. Column $\nu_{00}^{WSS10}/\nu_{00}^{ATM6-}$, upper part, displays the ratio of photons arriving from 00° from zenith for a ATM31-WSS10 atmosphere to the photons from an ATM61 atmosphere. The lower half is the same but for a VSummer atmosphere. Column $\nu_{30}^{WSS10}/\nu_{30}^{ATM6-}$ displays the same ratio again, but for 30° from zenith. Column $\nu_{\frac{30}{00}}^{ATM6-}$ displays the ratio of photons from a 30° from zenith simulation to a 00° from zenith, at ATM61 (upper part) and ATM62 (lower part). The same applies for the next column, but for ATM31 and ATM32 at WSS10.

Ceilometer studies of the aerosol loading of the atmosphere on site, presented in Section 4.9, have found that the average year on year aerosol loadings at VERITAS are best modeled by ∼WSS13. ATM61, ATM62 are slightly closer to this average aerosol extinction, but WSS10 is chosen at the *de facto* working aerosol loading for normal conditions, since it better accounts for the frequent times of low aerosol loading found especially in VWinter months.

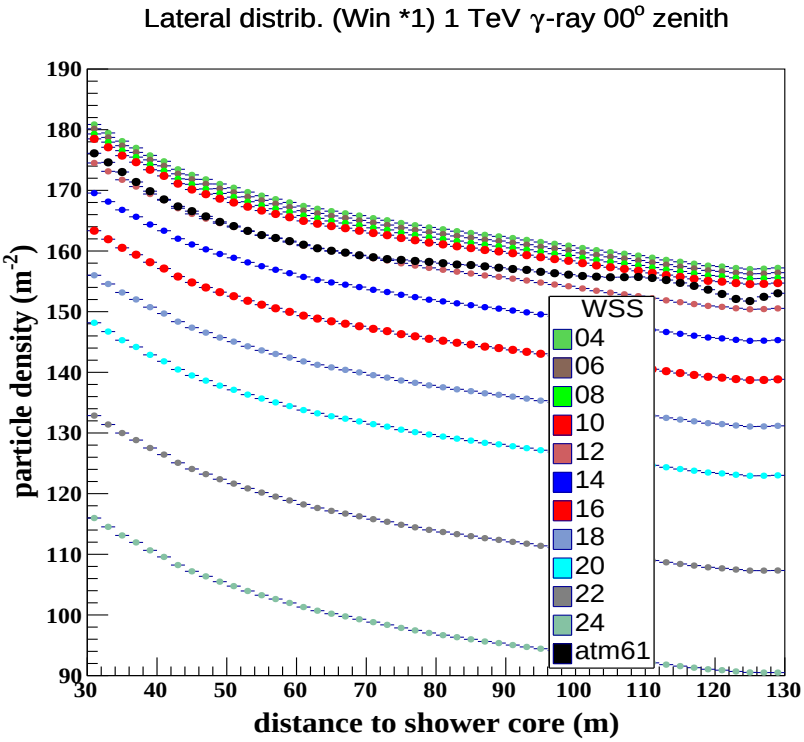

Fig. 5.8 Close-up of a section of a 1D histogram of the lateral distribution of Cherenkov photons from 1 TeV γ-ray showers in VWinter atmosphere, showing the photon integration for ATM61 (black) and WSS04-WSS24, where WSS10 and WSS16 are highlighted (red). The histograms show a visible difference in transmission profile between the rural 50 km visibility and Desert Dust models. However the values tabulated (Table 5.4) imply that this difference has little consequence when large photon statistics are available. Note how little difference in Cherenkov transmission exists between WSS04 and WSS10, due to small changes in aerosol size distribution and particle density.

5.3 Examining causes of L3 seasonal variability

The large set of simulated proton EAS and their Cherenkov photons (summarised in Table 5.1), are now subject to varying aerosol loading and water vapour. It is assumed that the overwhelming majority of cosmic rays are Hydrogen nuclei, whose arrival direction is largely isotropic (discussed in Section 3.4.7). For an examination of L3 variability, the hadronic simulation sets are given a similar analysis to γ-ray progenitors, from Sections 5.2.3 to 5.2.5, but without simulations with shower axis 30° from zenith.

5.3.1 Examining proton progenitor EAS and aerosols

The proton flux arriving at Earth is 3 to 4 orders of magnitude greater than the VHE γ-ray flux (when a VHE γ-ray emitter is present in the field of view). However, far fewer Cherenkov photons arrive at detector level from proton showers compared to the corresponding energy γ-rays showers. Indeed protons below 1 TeV may not feature large in the L3 trigger rate.

From Table 5.5, the column Ht^{*1}(km)Ht^{*2} indicates that the mean height production for proton showers. It may not be as representative of true shower max height as for γ-ray showers. By means of the frequency sidebar in Figure 5.10 it can be seen that the peak Cherenkov photon emission region is very close to ground level for hadronic showers; this is due to local muons. The proton shower max height is more difficult to discern, owing to its more diffuse nature compared to γ-ray EAS. The introduction of column $WSS16^{*2}/WSS10^{*1}$ is to compare normal VWinter transmissions with more extreme water vapour VSummer transmissions. WSS16/WSS10 again is very consistent over all energies. WSS16^{*2} / WSS10^{*1} displays more variability because two different EAS production sets were used in the comparison. Hadronic EAS, by their nature, offer many more possibilities for secondary particles to propagate, hence the larger variability in the simulation sets compared to γ-ray EAS. It is noted that the uncertainties for the 1^{st} km a.g.l. are very high. This is due to the majority of Cherenkov photons arriving at detector emanating from this height bin, which is not the case for γ-rays.

Of some interest is the lateral distribution of Cherenkov photons from a 5 TeV proton from 00° from zenith. The differences in photon counts arriving at detector through various aerosol extinction profiles (WSS04 to WSS24) is less distinct than from γ-ray progenitor showers (displayed in Figures 5.4 and 5.9), for counterintuitive reasons. The Cherenkov yield from γ-ray progenitors reaches maximum at shower max height ($\sim$7-8 km a.g.l.), meaning that the total aerosol extinction profile up to top of boundary layer impacts on the arriving photons. However, the shower max height for proton progenitors is most probably

closer to ground (due to VHE hadrons penetrating deeper into the atmosphere before interacting). This implies that only a fraction of the 5 km extinction profile impacts arriving Cherenkov photons. Thus the differences in cumulative aerosol extinction (from WSS04-WSS24) for γ-ray progenitors is greater than for proton progenitors. The greater lateral distribution in secondary particles from hadronic showers is the main underlying cause.

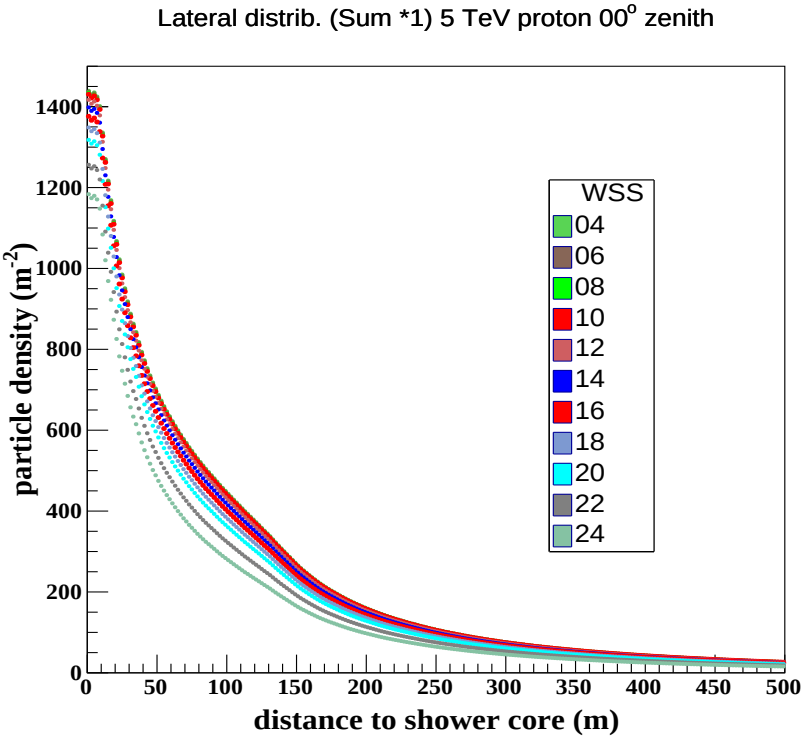

Fig. 5.9 1D histogram of the lateral distribution of Cherenkov photons from 300×5 TeV proton showers with VSummer *1 atmosphere and WSS04-WSS24 extinction at 00° zenith. Note how the varying extinction profiles are more closely bunched together compared to γ-ray EAS, due in large part to extra lateral dispersal of secondaries in the EAS, see text. Additionally, the lack of a light pool boundary (Figure 5.4) can be attributed to the same cause.

A clue as to what may cause L3 trigger rate variability may be elicited from column ν'_{00}, the number of photons from a 100 m integration over photons from a 500 m integration. It is seen that the Cherenkov photon arrival from proton showers $\leq$ 1 TeV can not compare with photon arrival for similar energy γ-ray shower within the VERITAS footprint. For 100 GeV γ-ray showers, $\nu'_{00} = 0.72 \pm .03$, for 300 GeV, $\nu'_{00} = 0.75 \pm .01$ (taken from Table 5.2, column

ν'_{00}). Proton showers $\leq$1TeV are less localised about the shower core. With greater energies proton showers become ever more localised and closer to shower axis ground impact than γ-rays. The Earth-hugging boundary layer of the atmosphere is highly turbulent in dusts and is where the largest aerosol particles reside. It is subject to high aerosol extinction, particularly during VSummer months. Such large aerosol extinctions are rarely present in VWinter season.

proton GeV	Ht^{*1}(km)Ht^{*2}	ν'_{00}	WSS16/WSS10	WSS16^{*2}/WSS10^{*1}	%WSS10$_{00}$	%WSS16$_{00}$
VWinter						
100	8.0 : 8.0	0.33±.08	0.91±.15	0.91±.15	1.00±.27	1.00±.28
300	7.3 : 7.4	0.54±.03	0.91±.06	0.91±.06	1.00±.07	1.00±.07
1000	6.9 : 7.0	0.75±.01	0.92±.02	0.89±.02	1.03±.02	1.03±.02
3000	6.7 : 6.5	0.81±.01	0.92±.02	1.00±.02	0.92±.02	0.92±.02
5000	6.4 : 6.3	0.83±.009	0.93±.01	1.00±.01	0.93±.01	0.93±.01
10000	6.0 : 6.0	0.87±.008	0.94±.008	0.87±.008	1.08±.008	1.08±.008
VSummer						
100	7.9 : 7.9	0.35±.08	0.91±.15	0.90±.15	1.00±.27	1.00±.28
300	7.6 : 7.5	0.59±.03	0.91±.06	0.93±.06	0.98±.07	0.98±.07
1000	7.2 : 7.3	0.75±.01	0.92±.02	0.93±.02	0.99±.02	0.99±.02
3000	6.8 : 6.9	0.81±.01	0.92±.02	0.95±.02	0.98±.02	0.98±.02
5000	6.5 : 6.7	0.84±.009	0.93±.01	0.90±.01	1.02±.01	1.03±.01
10000	6.2 : 6.2	0.86±.008	0.93±.008	0.92±.008	1.01±.008	1.01±.008

Table 5.5 Cherenkov arrival comparison table for proton initiated showers. Column Ht^{*1}(km)Ht^{*2} represents the mean Cherenkov height production for normal and twice normal water vapour. Column ν'_{00} is the approximate photon arrival fraction between the VERITAS footprint and the flat detector for WSS10 and *1 water vapour. Column $WSS16^{*2}/WSS10^{*1}$ is to compare normal VWinter transmissions with more extreme water vapour VSummer transmissions. Column WSS16/WSS10 is the change in photon arrival between normal and elevated aerosol loading for *1 water vapour. Columns %WSS10$_{00}$ and %WSS16$_{00}$ represent the change in photon arrival due to increased water vapour for the aerosol extinctions quoted. Of note is the greater differences is column ν'_{00} compared to the same column for γ-ray showers (Table 5.2), implying proton EAS do not contribute appreciable to L3 triggering if their energy is less that 1 TeV.

5.3.2 Relationship between aerosols and low L3 trigger rates

Four VERITAS data sets of L3 rate vs run duration were previously plotted, where a clear drop in triggering was observed (plotted in Figure 3.21). With new understanding gained

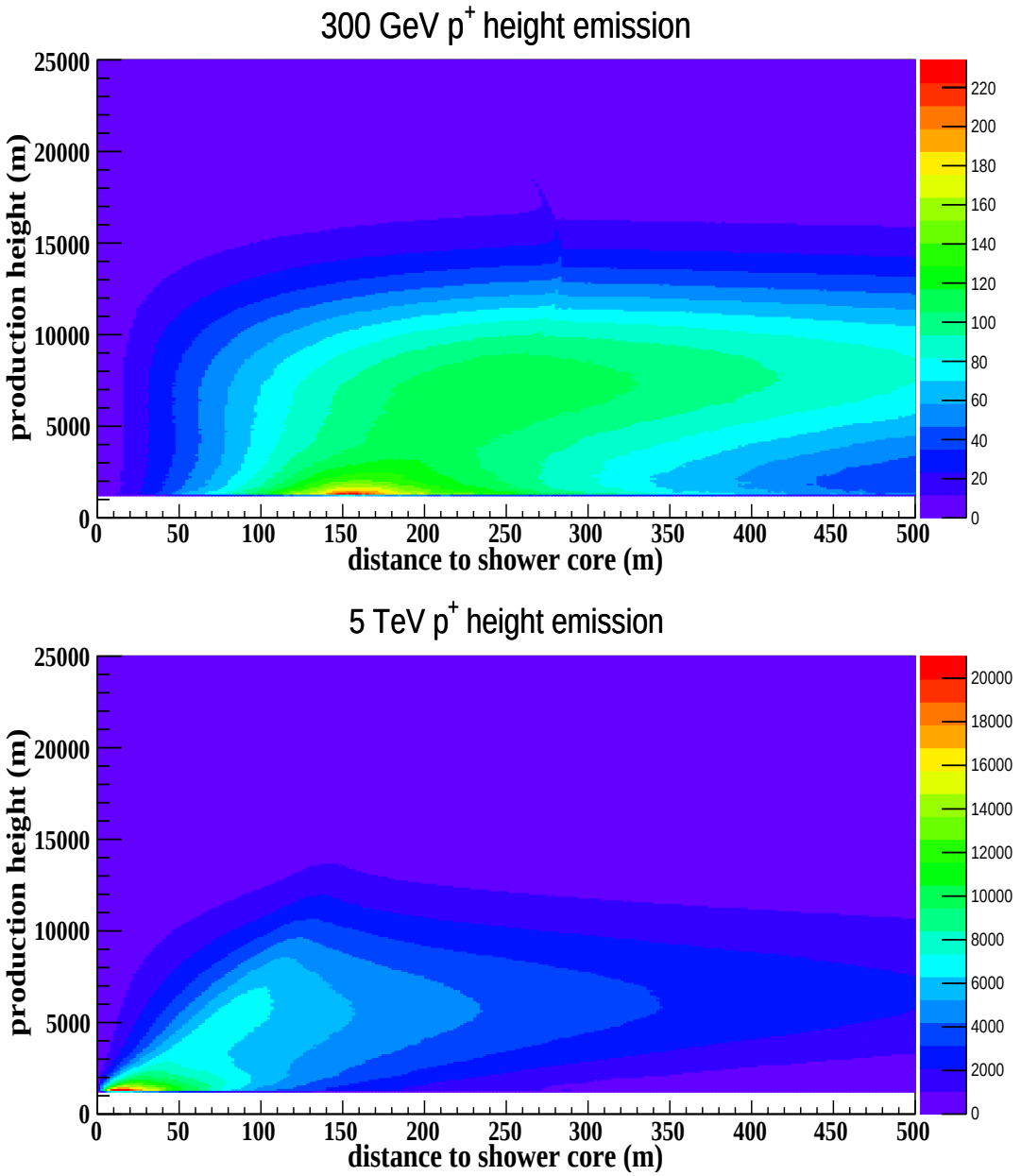

Fig. 5.10 2D histograms of the production height of Cherenkov photons which arrive at detector from 300 GeV and 5 TeV proton EASs, with VSummer *1 atmosphere and extinction WSS10. Note that the mean production height estimate for hadronic showers (Table 5.5) is less representative of the true shower max height than for γ-ray showers due to wider lateral distribution.

into aerosol loading on site, proton EAS and the lack of evidence for water vapour involvement, attention turns to examining the causes of L3 trigger rate drop, to ascertain if the atmosphere may be implicated or exonerated in the observed decline. Turning attention to Table 5.6 the four well controlled datasets show a clear drop in L3 rate with increased aerosol loading. It is the total aerosol loading from 1-5 km that shows better correlation than just the 1^{st} km alone, showing that the bulk of local muons have been excluded from the L3 trigger rate due to telescope multiplicity.

Refer to Figure 5.11 (whose dataset was previously plotted in Figure 3.19) where a large number of L3 trigger rates from low zenith angle runs, averaged over the run duration, shows the large difference in L3 trigger rate at VERITAS. The black crosses are two-week averaging of both L3 rate and corrected backscattering, β^{corr}. The binning for this scatterplot is 5 Hz and 5×10^{-5} sr^{-1} m^{-1} respectively. Referring to the maximum L3 rate,

MJD	*run no.*	*L3* (Hz)	$\bar{\beta}'$ 50-250 m	β^{corr} 1 km	β^{corr} 1-5 km	PWV (g cm^{-2})
56358.31458	67146	443	32	22	84	0.75
56394.22292	67959	418	33	26	100	0.85
56363.41319	67286	456	30	20	70	0.60
56414.28056	68251	403	72	55	145	0.70

Table 5.6 Four data sets (from Section 3.4.8) tabulated, where the backscattering is for 50 to 250 m, 1^{st} km and summed 1-5 km respectively, in arbitrary units. The water vapour content was very consistent for the datasets in question.

presumably indicative of optimal telescope performance, a downward trend is seen with increasing corrected attenuated backscattering, β^{corr}. The correlation factor is calculated as -0.46, which would at first seem to dissociate aerosol loading from L3 trigger rate change. However, this correlation estimation is given little credibility as the L3 trigger rate does not display a linear or stable operation over time.

In conclusion the following is summarised. A voluminous dataset of > 850 VERITAS data runs has shown that the maximum L3 triggering rate does not occur during periods of greatly increased aerosol loading. Proton EAS showers seem to have their shower max height very

close to ground, in the most turbulent aerosol loading part of the boundary layer. The measured aerosol loading profiles over 5.5 years at VERITAS have detected increased aerosol loading contemporaneous with most L3 trigger rate decrease. It therefore seems possible, though not definitive, that the drop in L3 trigger rate is due in part only to increased aerosol loading, which impacts on proton EAS Cherenkov transmittance arriving at detector more than for γ-ray EAS. There is still a large dataset at hand which shows that lowering L3 trigger rate occurs at times of nominal aerosol loading. The cause is unknown at the time of writing. This unexplained lowering of L3 triggering was the reason why the attempts to implement the Cherenkov Transparency Coefficient were abandoned (as mentioned in Section 3.4.7).

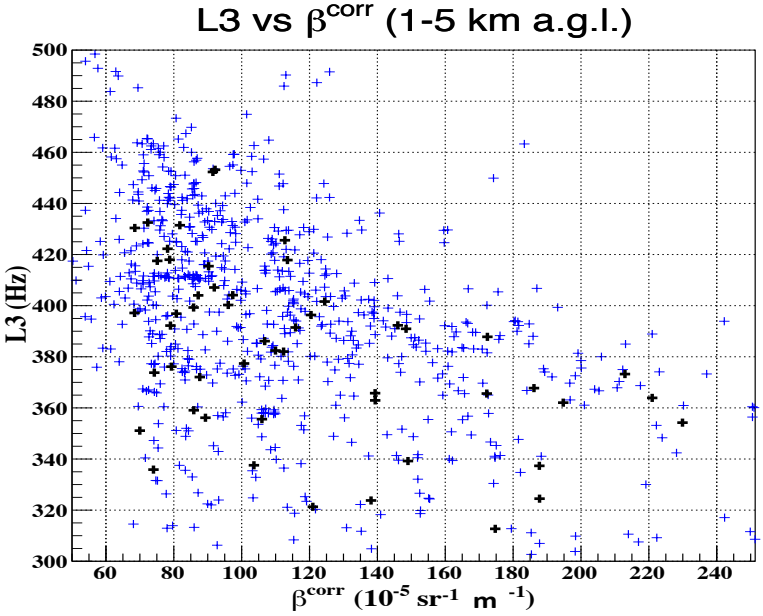

Fig. 5.11 A scatter plot of the L3 trigger rate, for 4-telescope operation at $\leq 10^{\circ}$ from zenith against the total corrected attenuated backscattering from 1-5 km a.g.l. at VERITAS. There is a great variation in triggering rate, as can be seen by the black crosses that represent the two week average for both L3 and β^{corr}. The correlation factor (Pearson) has been estimated at -0.46. However on examining the maximum rates (presumably representative of optimal operation), a decline in maximum L3 trigger rate can be seen with increasing backscatter. All data is from the V6 array.

It is now most important to ask if the presence of aerosols, which may impact on tele-

scope trigger rates to some degree, will impact on the Cherenkov imaging technique and in particular VHE γ-ray calorimetry.

5.4 The need for VERITAS detector simulations

Attention now turns to γ-ray EAS for an IACT experiment. What flat detector simulations are not able to do is determine the effects of aerosols on the shower image, whose moment fitting forms the basis of the Cherenkov imaging technique. The same atmospheres, ATM31 and ATM32, will be used while WSS10 serves as a good normal aerosol profile. The task now is to determine the aerosol extinction upper limit where this aerosol profile can effectively work, then select another extinction profile for elevated aerosol loadings. For this, use is made of new CORSIKA simulations produced for real volume detectors with a range of aerosol profiles from WSS10 to WSS18 in steps of WSS02. The detector simulation package for the VERITAS experiment, grisudet (part of GrISU [1]), and the data analysis package of the VERITAS experiment, *Eventdisplay*, are required to pass the CER (EAS Cherenkov photon) files through the telescope model and analyse the resulting output respectively. The new EAS simulations are held at fixed lower energies; energy resolution for the VERITAS experiment works best for 300 GeV $\leq$ E_{EAS} $\leq$ 3 TeV. 100 GeV progenitor γ-rays are incorporated in this study due to a soft γ-ray source that will be examined in the next chapter. Additionally, a fixed zenith angle will be used to simplify simulations. Fixed energy and fixed zenith angle simulation results can now be extrapolated to all energies up to 5 TeV and elevations as low as 30° from zenith as a result of work from the previous sections.

One further addition to simulations is added, varying night sky background in the UV (NSB_{uv}). For 100 GeV and 300 GeV EAS, three separate NSB_{uv} levels are simulated, 100 MHz, 425 MHz and 750 MHz, corresponding to dark skies, bright star field and moderate moonlight. The units for NSB_{uv} is more precisely photoelectrons ns^{-1} m^{-2} sr^{-1}, which may more practically be described by photoelectrons PMT^{-1} ns^{-1}. This is abbreviated to

[1] http://www.physics.utah.edu/gammaray/GrISU/

γ-ray GeV	*NSB noise* (MHz)	*no. CER files*	*total showers*
100	100, 425, 750	200	1.5×10^6
300	100, 425, 750	100	5.0×10^5
500	100	100	3.0×10^5
700	100	150	2.25×10^5

Table 5.7 Statistics table illustrating the far greater number of EAS showers that need to be generated for volume detectors than for flat detectors. The showers are reused 10 times, therefore column *total showers* is effectively one order of magnitude greater.

MHz in keeping with the VERITAS analysis. In a perfect world, NSB_{uv} fluctuations are caused by random pile up of single photoelectron pulses in the PMT. However afterpulses are spurious pulses that appear in the wake of true pulses, where every true pulse may be followed by one or more afterpulses. Afterpulses of PMTs thus increase the accidental trigger rates beyond the random pile up of individual NSB_{uv} photons by up to twofold. The current simulation set of GrISU does not include noise from the night sky background, this is added by *Eventdisplay* to the PMT traces on the fly from pre-generated noise library files. Current GrISU noise files range from 75-1000 MHz. VERITAS observations are carried out in NSB_{uv} = 750 MHz (moderate moonlight), but with reduced high voltage for the PMTs. This modification to simulations is not included in the analysis for this thesis. These upper limits chosen test the robustness of the telescope's energy reconstruction, represented in part by Figures 5.12 and 5.13, for various extinction profiles in 425 MHz NSB_{uv} levels.

5.4.1 Mono-energy EAS for aerosol extinction analysis with *Eventdisplay*

The simulation set to determine the upper working limits of WSS10 and the aerosol extinction profile best suited to represent elevated aerosol loading is now presented. All simulations were produced on the DV-Zeuthen cluster, Zeuthen, Germany using up to 200 nodes at a time, provided by Dell Dual Xeon E5-2660 and X5650 cores.

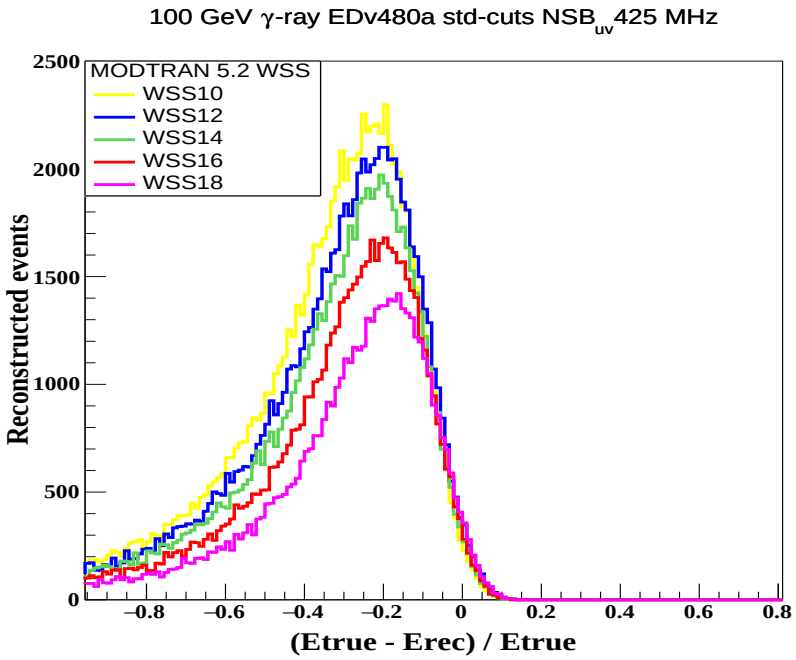

Fig. 5.12 1D histograms of the fractional change in reconstructed energy from 100 GeV γ-rays for various extinctions. The x-axis is derived from the true EAS energy (E_{true}) and the reconstructed or derived energy (E_{rec}). The simulations are produced with the 4-telescope V6 array, with ATM31 and 425 MHz noise. NSB_{uv} shifts the mean reconstructed energy, displayed in Table 5.8, to the left of 0 more than for higher energy showers. Increased extinction will shift the mean reconstructed energy to the right of 0, as the reconstructed energy reduces due to image size loss. Note also a narrowing of the distribution for increased extinction.

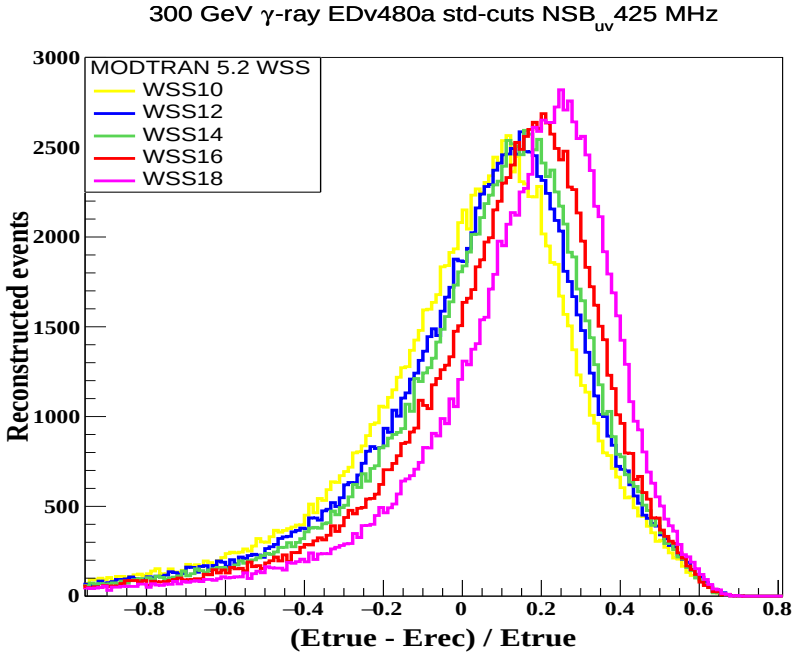

Fig. 5.13 Identical 1D histograms as per Figure 5.12 but with 300 GeV γ-ray showers. Energy reconstruction of γ-ray EAS of this energy and higher are progressively less affected by NSB_{uv}, hence the omission of extra sky noise simulations for 500 GeV and 700 GeV.

They are produced with fixed energies of 100 GeV, 300 GeV, 500 GeV and 700 GeV, having random, isotropic azimuth angles with a fixed zenith angle of 20°.

Each particular mono-energy simulation contains a set number of events, produced from a specific number of independent CORSIKA EAS showers (summarised in Table 5.7). Each shower is reused 10 times (explained in Section 5.1), while the showers are scattered over a circular area with a 750 m radius in the shower plane. These simulations are all for the V6 array configuration, with VWinter *1 atmosphere only. This simulation data is produced as follows. The Cherenkov photons are produced, then the CER files are passed through corsikaSimulationTools, an interface software between CORSIKA and the VERITAS experiment, providing utilities for both GrISU and *Eventdisplay*. It is here that extinction is applied to the photons and the file format converted for the telescope and array configuration simulations. GrISU simulates the ray tracing (photon vector interactions with the telescope) of the photons with global efficiencies and telescope shadowing. The output is then analysed by *Eventdisplay* standard analysis, for image cleaning and parameterisation, before analysis with *Eventdisplay* mscw-energy for energy reconstruction. The real and reconstructed energies are then pulled from the resulting ROOT file to fill the histograms and tables presented. As a new detector type is employed in these simulations, some new terms will have to be defined for the following data presented in Tables 5.8 and 5.9. $\overline{RecEn}$ is the average reconstruction energy of the shower images. This will vary from the true energy of the simulated shower (defined at production time). $N_{rec-WSS**}$ refers to the number of reconstructed showers at aerosol extinction WSS** (where ** is from 04-24). Some simulated showers may mot be reconstructed by the *Eventdisplay* package for various reasons. The ratio $N_{rec-WSS**}/N_{rec-WSS10}$ is thus the number of reconstructed showers at WSS** over the number of reconstructed showers at WSS10, which serves to highlight when the current aerosol extinction profile may need to be replaced. The associated uncertainties for the two tables are not calculated, which will be explained in the following section. It is noted that the same image parameter cuts, called standard cuts (whose parameters are given in Table

γ-ray GeV	WSS	$N_{rec-WSS**}/N_{rec-WSS10}$	$\%\overline{RecEn}$	*data loss %*
100	12	0.88	01.3	5.2
100	14	0.76	02.9	12
100	16	0.63	04.7	20
100	18	0.49	06.8	31
300	12	0.88	02.1	1.3
300	14	0.79	04.8	2.8
300	16	0.68	08.2	4.8
300	18	0.60	12.1	7.4
500	12	0.89	02.0	0.9
500	14	0.80	04.9	2.1
500	16	0.70	08.2	3.5
500	18	0.56	12.5	5.2
700	12	0.93	02.3	0.5
700	14	0.82	05.0	1.3
700	16	0.73	08.4	2.5
700	18	0.59	12.7	3.7

Table 5.8 The NSB_{uv} = 100 MHz, 20° from zenith, set of mono-energy simulations used for threshold determination of elevated aerosol profile in Desert Dust extinction. As WSS10 has been set as normal aerosol content all subsequent extinction profiles are measured with respect to it. Column $N_{rec-WSS**}/N_{rec-WSS10}$ represents the ratio of reconstructed events for a particular extinction with reconstructed events for WSS10 (between reconstruction difference of $\pm$ 100% or -1 to $+1$ on the plot). Column $\%\overline{RecEn}$ represents the change in mean reconstructed energy caused by a particular extinction profile. Finally, column *data loss %* indicates the events lost due to extinction, integrated over all events.

3.2), were used for all energies. This is because the comparative study presented here seeks to minimise differences between simulation sets. It would be more correct to use a soft cuts set for 100 GeV simulations; however the aim of the simulations is not accurate energy reconstruction but determining a global extinction level that may be set as elevated-aerosol loading.

Firstly, column $N_{rec-WSS**}/N_{rec-WSS10}$ of Table 5.8 displays the fractional loss of reconstructed events due to aerosol loading WSS12 to WSS18 integrated over a fractional difference of -1 to $+1$ (the x-axis of Figure 5.12). The limits of -1 to $+1$ were chosen as energy reconstruction outside these limits could be termed 'anomalous' and of little use for accurate

spectral studies. As expected, this difference in reconstructed events is largest for the lowest energy showers but stabilises from 300 GeV upwards for a given extinction. This would at first seem to imply that the VERITAS moment fitting algorithm, central to energy reconstruction, is robust to changes in aerosols above a threshold between 100 GeV and 300 GeV for standard cuts (recalling the bias towards moderate source energies due to the standard cuts used). However, examining column $\%\overline{RecEn}$, the change in reconstructed energy with regard to WSS10, it becomes evident that the reduced image size is being interpreted as a reduction in reconstructed energy. Thus, the histogram shifts to the right, by the percentage noted with respect to the WSS10 histogram. For WSS16, EAS with progenitors $\geq$ 300 GeV on average have their energy reconstruction shifted by 8%. Notably, this is very similar to the decrease in photon count for flat detector simulations for WSS16 over WSS10 aerosol extinction (Table 5.2, column $WSS16/WSS10$). The decrease in photon count was also of the order of $8-10\%$. Indeed this energy reconstruction shift of 8% holds for NSB_{uv} = 425 MHz and 750 MHz at 300 GeV (seen in Table 5.9). As energy reconstruction depends on image size, which is proportional to the number of Cherenkov photons arriving at telescope, it seems reasonable to relate a drop in photons with a corresponding drop in energy reconstruction.

Of note, but not tabulated, is the consistent RMS of the reconstructed energies in the simulation sets over a particular energy. For 100 GeV γ-rays RMS = $0.19-0.22$ GeV, for 300 GeV, RMS = $0.28-0.27$ GeV, while for higher energies RMS $\approx$ 0.29 GeV. These values only drop by $\leq 8\%$ over the range of extinction values. Having this stable dataset, acknowledging the bias towards moderate energy sources due to the standard cuts used, the following may be elicited;

- The reduction in mean reconstructed energy, $\%\overline{RecEn}$, from WSS10 to WSS16 in volume detectors at 20° from zenith is consistent with the reduction in photons arriving at a flat detector from 00° and 30° zenith. Remembering that the size parameter is proportional to PMT charge, which is proportional to number of photoelectrons, the

correlation seems probable.

- The reduction in number of reconstructed events for various extinction profiles measured against WSS10, $N_{rec-WSS**}/N_{rec-WSS10}$, is not impacted on by NSB_{uv} when the progenitor energy $\geq$300 GeV. This implies that $N_{rec-WSS**}/N_{rec-WSS10}$ may offer a reading where a threshold value for new aerosol extinction simulations are deemed necessary.

- Particular concern is given to column *data loss %*, which represents irretrievable information loss that can't be reconstructed with *Eventdisplay*. Low-energy and high-noise simulations may not be possible in high extinction scenarios (Table 5.9, column *data loss %*) where up to half of shower events may be lost to reconstruction for 100 GeV EAS simulations in a high sky noise measured at 750 MHz.

5.4.2 Summing up criteria and selection of elevated aerosol threshold

Having detailed the mono-energy simulation sets produced, the VERITAS standard cut selection and various sky noise levels, it is necessary to select the new extinction profile that will define elevated aerosol loading. There are two considerations; firstly, the loss in reconstructed events and secondly, the frequency of particular aerosol loadings that cause this loss. It is of little use to set an elevated aerosol threshold that is rarely ever encountered. WSS13 is determined to be the average year-on-year extinction profile for VERITAS. During episodic aerosol loading events this may rise to WSS18 ($\sim$3% of total observing time) or in rare cases WSS20 ($\sim$0.5% of total observing time) as displayed in Figure 4.21. However extinction $\geq$ WSS16 occurs for $\sim$15% for all data, and reduces the average reconstructed energies $\overline{RecEn}$ by $\sim$8% on average. This is not a large amount but it occurs frequently enough to warrant the work and resources required for production of IRF simulations. As the deciding factor on threshold for elevated aerosol IRF production is not based solely on

γ-ray GeV	NSB$_{uv}$ (MHz)	WSS	$N_{rec-WSS**}/N_{rec-WSS10}$	$\%\overline{RecEn}$	*data loss %*
100	425	12	0.86	01.8	8.0
100	425	14	0.74	02.0	18
100	425	16	0.60	03.8	30
100	425	18	0.44	05.6	43
300	425	12	0.89	03.0	1.4
300	425	14	0.80	04.8	3.0
300	425	16	0.70	08.1	5.3
300	425	18	0.59	13.0	8.0
100	750	12	0.86	00.6	11
100	750	14	–	–	–
100	750	16	0.54	02.4	39
100	750	18	0.38	03.4	53
300	750	12	0.89	02.1	1.6
300	750	14	0.81	04.8	3.8
300	750	16	0.69	08.0	6.4
300	750	18	0.57	12.0	9.6

Table 5.9 The NSB$_{uv}$ = 425 MHz and 750 MHz set of mono-energy simulations, for 100 GeV and 300 GeV. $N_{rec-WSS**}/N_{rec-WSS10}$ is the fractional loss of reconstructed events, while $\%\overline{RecEn}$ is the average reconstructed energy and *data loss %* indicated the % of events lost compared to the number of total simulated events. Note that simulation results for 100 GeV, 750 MHz WSS14 were overwritten by accident.

the data in Tables 5.8 and 5.9, the associated uncertainties have not been estimated.

Particular attention is made to WSS error estimation, which is essential in setting clear threshold values for aerosol analysis. In best working conditions, where the water vapour concentrations are low to medium and higher aerosol loadings increase SNR, the uncertainty in aerosol measurement is effectively 0 (due to WSS binning), but the uncertainty can be up to $\pm$WSS04 in rare circumstances. Recall that the increment in MODTRAN's WSS is in steps of WSS02. It is noted that the VERITAS telescope has an energy resolution of $\sim$15% at 1 TeV [Balokovic et al., 2016]. In light of the frequency of aerosol extinction profiles present at VERITAS more than the magnitude of aerosol extinction encountered, it seems wise to select WSS16 as the elevated aerosol loading threshold for IRF production for VERITAS V6 telescope array. It is noted that the 15% uncertainty in energy resolution may

hide the effects of elevated aerosols on energy reconstruction. Aerosol loading of ≥WSS18 are rare, but may possibly be catered for by WSS16 simulation sets. There is a difference of 4% in average reconstructed energy $\%\overline{RecEn}$ between WSS16 and WSS18 (seen from Tables 5.8 and 5.9). Aerosol loadings higher than WSS18 can have unique simulation sets produced with a parameter space limited to the source in question. Such aerosol loading of ≥WSS20 is exceptional; prudent judgement is needed in situations where the aerosol extinction is ≥WSS20, as the extinction may not be Desert Dust but carbonaceous aerosols with a very different optical response. Finally, it is noted that on average there is a 30% loss in constructed events from the ratio $N_{rec-WSS16}/N_{rec-WSS10}$, which is unavoidable due to the additional scatter of Cherenkov photons (which is nearly always single-scattering for aerosol particles).

5.5 Site specific IRFs for the VERITAS experiment

VERITAS experiment IRFs for data analysis are needed in great quantity. The Cherenkov photon files do not need to be produced for a full IRF production set, as existing CER (CORSIKA Cherenkov) files will be used that have previously been used for VERITAS IRFs. These CER files have been produced with an older atmospheric profile derived with an older radiative transfer code (MODTRAN 4.0), called atmosphere ATM21. A discussion about the interchangeability between ATM21 and ATM61 is found in Appendix A. This research of necessity uses CORSIKA simulations produced by the VERITAS calibration group, using atmospheric profiles ATM21 and ATM22, and CORSIKA simulations produced for this thesis, using atmospheric profiles ATM31-ATM34, in addition to ATM61 and ATM62. ATM21 is an older molecular profile derived from largely the same radiosonde readings as ATM31 / ATM61 but without an interpolating of density profile readings. ATM21 and ATM31 / ATM61 atmospheric profiles are very similar in EAS simulation application, with a differing Cherenkov yield of 3-5% close to shower core but dropping to ∼1% further

from shower core (ATM21 producing slightly more photons). The VERITAS collaboration now uses ATM31 / ATM61 atmospheric profiles for all new VWinter *1 CORSIKA simulations (flat detector, mono-energy and volume detector), likewise ATM32 / ATM62 for VSummer *1 simulations. They are importantly derived from a newer radiative transfer code, MODTRAN 5.2, which has an improvement in spectral resolution of almost an order of magnitude (as reported on in Section 3.6). The extinction profile for the corresponding ATM21 and ATM61 molecular profiles are almost identical, again see Appendix A. The extinction profile ext50km refers to the Tropospheric 50-km visibility aerosol extinction profile (reported on in Section 3.5.1) being used with the molecular extinction profile derived from ATM31 / ATM61 atmospheres (reported on in Section 3.6.1). Recall that the total atmospheric extinction profile for the new simulations is the sum of the molecular and particulate extinction profiles derived from MODTRAN 5.2; the total atmospheric extinction profile for the original MODTRAN 4.0 derived simulations (the official IRF set) is the molecular extinction of ATM21 and the Tropospheric 50 km visibility aerosol extinction profile.

The new ext50km IRFs produced need to be an accurate reproduction that yield consistent results with the official IRFs. When this is shown to be the case the ext50km and WSS16 IRFs, being identically produced in every way bar the aerosol extinction profile, are used as a comparison to examine the effects of aerosol-extinction correction.

These simulations (CER or Cherenkov photon files) were produced with random, isotropic azimuth angles, which are then binned for the production of lookup tables used in calorimetry. The zenith angles are binned at production stage as follows; 00, 20, 30, 35, 40, 45, 50, 55, 60, 65 degree zenith. A minimum γ-ray energy is set for particular zenith bin ranges; 30 GeV for zenith angle 00° and 20°, 100 GeV for Zenith angle 55° to 65°, and 50 GeV otherwise. A maximum energy of 200 TeV is set for all zenith angles, with a spectral index of -2. Each CER file produced by CORSIKA contains 10000 events, produced from 1000 independent CORSIKA showers each reused 10 times; these EAS are scattered over

a circular area with a 750 m radius in the shower plane. The atmospheric profile is chosen at Cherenkov production time, while the extinction profile is implemented later before IRF production time. A file reformatting is required for the CER files to be readable by the telescope simulation package, namely VERITAS bank format or .vbf file format. This operation is carried out along with molecular and aerosol extinction by the corsikaSimulationTools code.

Next, the telescope observing parameters are introduced. A range of observing offsets are produced for the full simulation set; they are 0.00, 0.25, 0.50, 0.75, 1.00, 1.25, 1.50, 1.75 and 2.00 $^{\circ}$ from the putative source position. These offsets may be used in wobble mode, where the ON and OFF regions are continually kept in field of view (described in Section 3.4.5), or extended source observing, where the OFF region may need further near contemporaneous runs at further distance from the ON region. Additionally, a range of 9 noise levels are introduced post CORSIKA production; these are 100, 150, 200, 250, 325, 425, 550, 750 and 1000 MHz. Just three of these NSB_{uv} levels were introduced previously (discussed in Section 5.8).

Finally the VERITAS telescope and array configurations are introduced to the simulation chain. The telescope array, V4 or V5, with various telescope combinations sets the light collecting structure available. Account is taken of shadowing effects of the camera box and supporting arms. Mirror reflectivities, PMT gain and quantum efficiencies are measured continually and updates to GrISU are done as needed. Each of the 2000 PMTs has a preamp; this output goes to the FADC where a hi-low gain switch reduces pixel saturation and increased low light gain. The hi-lo switch response function to the nano-second light pulses it detects have proven difficult to model. For this reason principally, the summation window used to estimate the integrated charge in each PMT is set to a lower value of 6 samples, representing 12 ns in length (described in Section 3.4.5). The current simulation sets being produced are for a spectrally soft and moderate extragalactic TeV emitter, and 6 samples is

found to give good energy reconstruction below 1 TeV.

One final amendment is needed, owing to the large processor time required to produce a full experiment simulation set. A smaller limited parameter space is chosen to test the thesis hypothesis of aerosol extinction and the Cherenkov technique. For this limited IRF set, elevation is $\leq 30^{\circ}$ from zenith, the wobble offset is 0.5° alone, the array configuration will be V6 (the current 4-telescope configuration with upgraded PMTs) with 4 operational telescope alone. Stipulating 4 operational telescopes means that should one telescope go offline due to malfunction for example, the data recorded by the 3 remaining operational telescopes will not be analysed. All nine noise levels will be included.

Eventdisplay standard analysis of the simulations is carried out, *i.e.* image cleaning, t_{zero} estimate, image parameterisation, pedvars, geometric angular reconstruction with stereoscopic array and event arrival time. Next, *Eventdisplay* mscw-energy analysis takes over, where the recorded events undergo calorimetry, followed by the development of lookup tables from the mscw-energy stage. The simulated air shower parameters are used to fill multi-parameter lookup tables, each being binned in pointing direction, impact parameter, wobble angle, noise, and all other required parameters. This is followed by the development of effective areas, accomplished by analysing the simulated showers a second time using mscw-energy, but using the previously generated lookup tables as a reference for the shower reconstruction. This yields a list of reconstructed showers with their corresponding reconstructed (derived by *Eventdisplay*) and true (given at time of production) properties which allows for systematic errors to be quantified. Next it is necessary to apply a set of γ/hadron separation cuts to the analysed simulations and produce the effective areas as follows

$$EA = A\left(\frac{N_{rec}}{N_{gen}}\right) \tag{5.2}$$

where A is the area over which the γ-rays were produced (shower axis scattered about a 750 m radius), N_{rec} is the number of γ-rays that were reconstructed and N_{gen} the number of γ-rays that were generated by simulation. Next, the radial acceptance tables are produced,

calculated from data in similar fields of view with no strong γ-ray source. This helps to determine relative camera trigger rate for images at distance from camera centre. Radial acceptances correct for the lowering in telescope pattern level (L2) triggering for images that are further from the camera centre.

Finally, the *Eventdisplay Anasum* analysis is run, where right ascension and declination bins for γ-ray counts and significance of detection are plotted to produce sky maps. Additionally spectral energy distributions are plotted, using the calorimetry results of *Eventdisplay* mscw-energy. *Eventdisplay Anasum* represents the last stage of the analysis chain.

Originally only a subset of the total number of CER files available were used, again to minimise the heavy computational demands of IRF production. From 00° to 30° from zenith a total of 6000 CER files were used in the first IRF production, representing 6×10^7 γ-ray events. This was found to offer insufficient statistics for spectral index and normalised flux studies. Hence, a full simulation set utilising 12000 CER files with a total of 1.2×10^8 γ-ray EAS or 1.2×10^9 events in total, was deployed in IRF production with the same limited parameter space.

5.5.1 Telescope IRFs for normal and elevated aerosols

It is necessary to produce a new IRF set to match as closely as possible the official collaboration IRF set for the limited parameter space in question. This is done using the 12000 CER files mentioned with a single extinction of ext50km. A sample of the resulting IRF production sets are now presented. A Lookup table for median Hillas fitted image length, $\hat{l}(S,D)$ from Section 3.4.5, is shown in Figure 5.14. It is produced using the ext50km IRF simulation set. To test the new simulation (ext50km) set against the official IRF set, Figure 5.15 shows the ratio of $\frac{official}{ext50km}$ for $\hat{l}(S,D)$. It is seen to be $\sim$1.0, where the bin-by-bin differences are at most $\pm$5% and average $\pm$2%. A Lookup table for median reconstructed energy (TeV) is shown in Figure 5.16. It is produced also using the ext50km IRF simulation set. To again test the new simulation set (ext50km) against the official IRF set, Figure 5.17 shows

the ratio of $\frac{official}{ext50km}$ for median reconstructed energy (TeV). It is also seen to be $\sim$1.0, again the bin-by-bin differences are at most $\pm$5% and average $\pm$2%. Note that Noise in measured in pedvar units (introduced in Section 3.4.5), related to NSB_{uv} MHz by lookup tables (not reproduced, but forming part of the *Eventdisplay* package). From these plots it can be assumed the the new ext50km IRF simulation set is a good replacement for the official IRF simulation set. More extensive analysis will be carried out in Chapter 6 that will further test this conclusion.

Next the elevated aerosol IRF set of WSS16 is produced. This is simply done by substituting the ext50km aerosol extinction file with the WSS16 aerosol extinction file and keeping all other parts of the IRF production set identical. This approach was adopted because the exact number of CER files used in the official IRF set is not known, and increased statistical uncertainties may unnecessarily be introduced by largely varying number of EAS simulations used to produce differing IRF sets. Further, there may be some slight differences in the GrISU simulation package over time. Refer first to Figure 5.18, the ratio of $\frac{WSS16}{ext50km}$ for $\hat{I}(S,D)$ derived from the lookup tables for the WSS16 and ext50km simulation sets. It is seen to be $\sim$1.0, where the bin-by-bin differences are at most $\pm$5% and again average $\pm$2%, as was the case for Figure 5.15. This is a surprising result, for it indicates that the increase in aerosol loading up to WSS16 does not impact on the imaging fitting algorithm. This is despite the loss of $\sim$8-10% of Cherenkov photons by extinction. The highly pixellated 499 PMT camera could explain this result. Next Figure 5.19 shows the ratio of $\frac{WSS16}{ext50km}$ for median reconstructed energy (TeV) again derived from the lookup tables for the WSS16 and ext50km simulation sets. Here a clear difference is observed between the simulation sets. It is seen that the reconstructed energy for WSS16 aerosol extinction IRF simulations are $\sim$8% lower than the corresponding ext50km IRF simulations. Again the extinction difference of $\sim$8% between WSS10/ext50km and WSS16 appears, as it has already in Section 5.4.1.

Finally, with a reliable method of measuring aerosol loading, and the required elevated

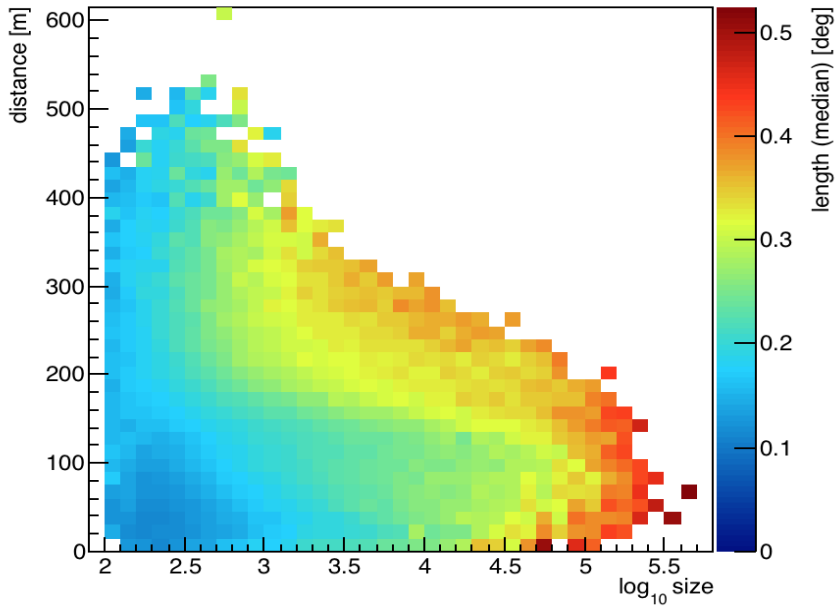

Fig. 5.14 A 2D plot of median Hillas fitted image length, $\hat{l}(S,D)$ for shower images produced by *Eventdisplay* from the ext50km collaboration IRF set. Noise is measured in pedvar units, related to NSB_{uv} MHz by lookup table. This simulation is for pedvar = 330, 20° from zenith, 0.5° wobble offset, azimuth bin 0 (the azimuth bin relates to the total of 360° being binned for simulation proposes. Bin 0 is due North). telescope 1 alone used.

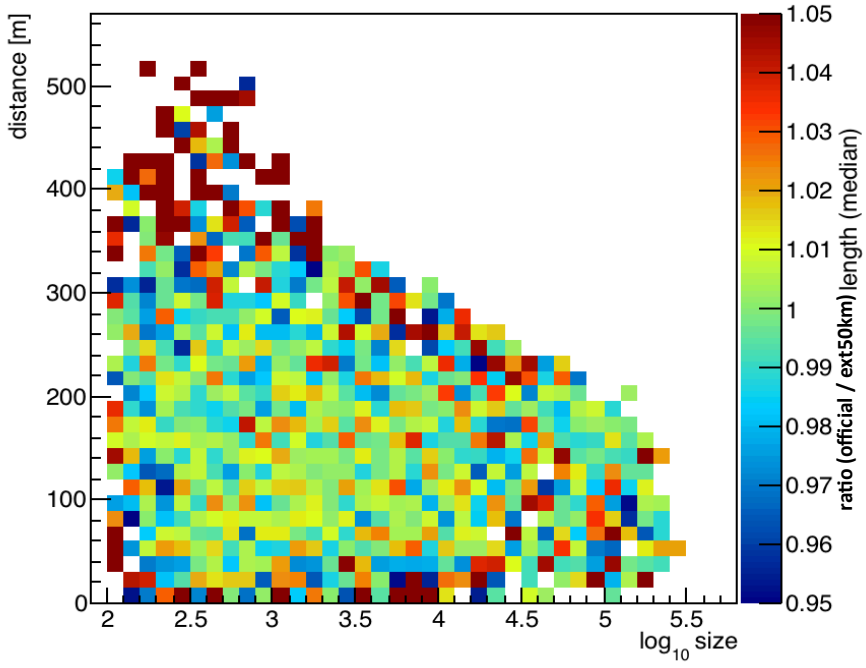

Fig. 5.15 A ratio, $\frac{official}{ext50km}$, of the 2D histograms of median Hillas fitted image length, $\hat{l}(S,D)$ for shower images produced with the official and ext50km IRFs. pedvar = 330, 20° from zenith, 0.5° wobble offset, azimuth bin 0 and telescope 1.

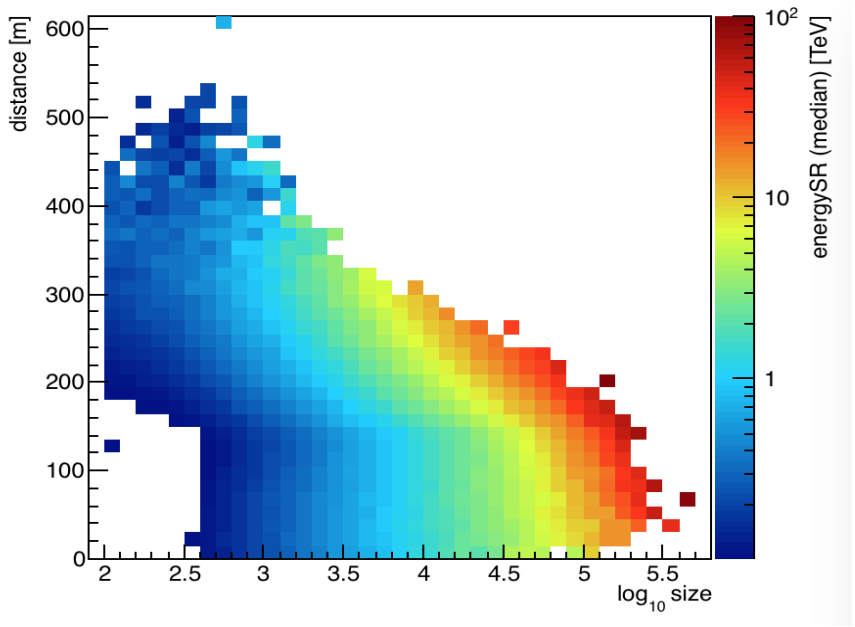

Fig. 5.16 A 2D plot of the median reconstructed energy (TeV) of shower images produced by *Eventdisplay* from the ext50km IRF set. This simulation is for pedvar = 330, 20° from zenith, 0.5° wobble offset, azimuth bin 0 and telescope 1. The blank area of the bottom left corner is due to data falling outside the plotting scales.

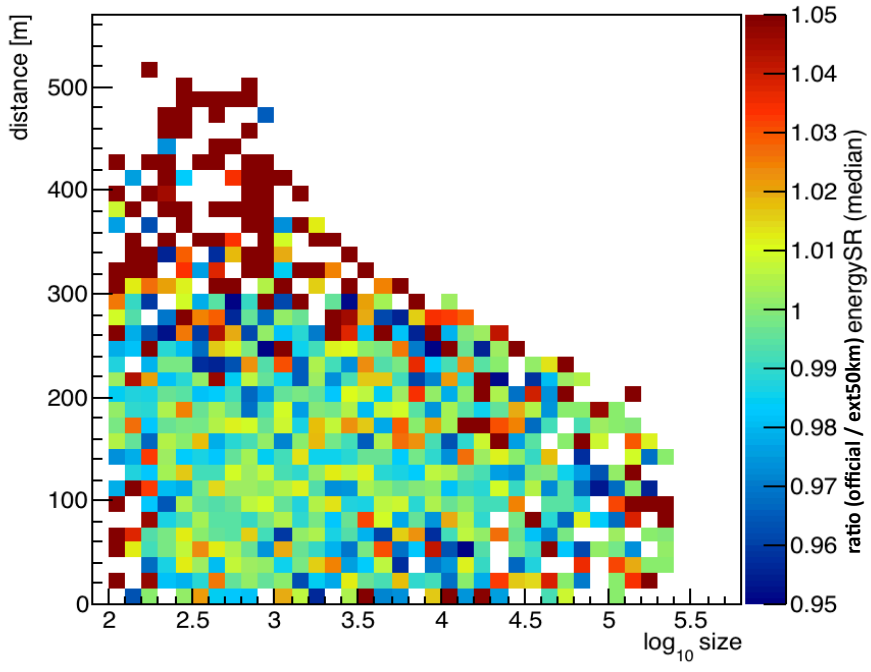

Fig. 5.17 A ratio, $\frac{official}{ext50km}$, of the 2D histograms of median reconstructed energy (TeV) of shower images produced with the official and ext50km IRFs. pedvar = 330, 20° from zenith, 0.5° wobble offset, azimuth bin 0 and telescope 1.

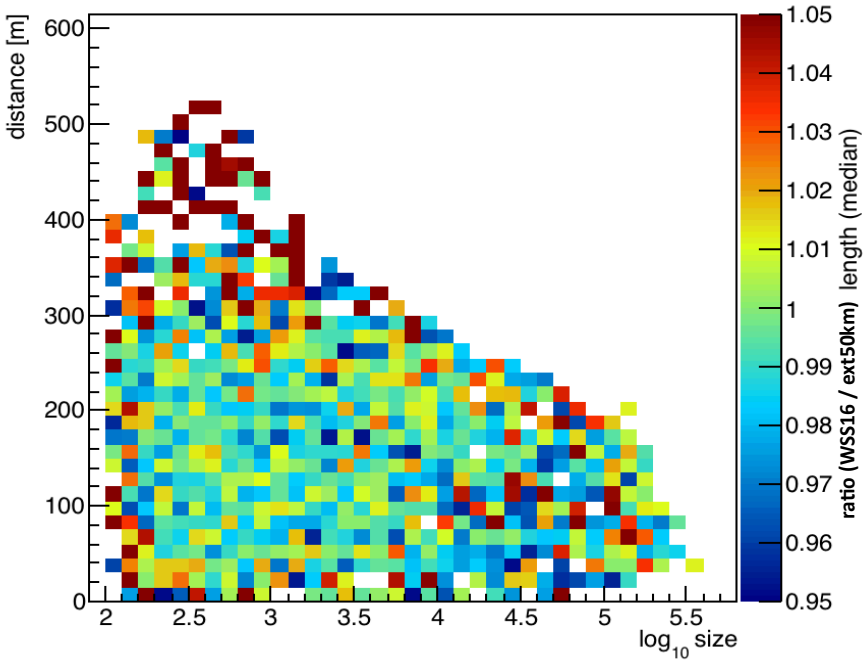

Fig. 5.18 A ratio, $\frac{WSS16}{ext50km}$, of the 2D histograms of energy of mean scale length (mscl) of shower images produced with the WSS16 and ext50km IRFs. pedvar = 330, 20° from zenith, 0.5° wobble offset, azimuth bin 0 and telescope 1.

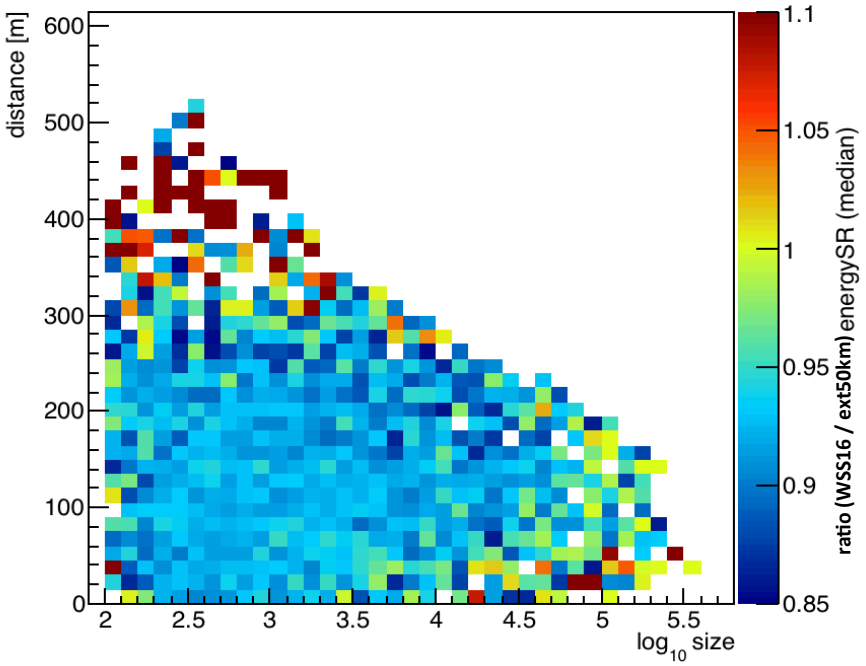

Fig. 5.19 A ratio, $\frac{WSS16}{ext50km}$, of the 2D histograms of energy of shower images produced with the WSS16 and ext50km IRFs. pedvar = 330, 20° from zenith, 0.5° wobble offset, azimuth bin 0 and telescope 1.

aerosol IRF simulation set tested, attention turns to real-world data. In April 2013 and April 2015 two blazars, a class of Active Galactic Nuclei that sporadically sends out relativistic charged particles along a narrow emission axis, were reported at distances of redshift $z = 0.031$ and $z = 0.94$. There was also elevated aerosols reported by the CL51 ceilometer on site during these VHE γ-ray episodes. The following methodology in analysis will be used. First, the official collaboration IRF set will be used to analyse a given source with the limited parameter set. This means that source data files that are not represented in the limited parameter set, such as source elevation below 30° zenith or with only 3 telescopes operational are rejected. Then the same limited parameter data set will be analysed with the ext50km and WSS16 IRF sets produced for this thesis.

Chapter 6

Studies of blazars with aerosol extinction correction

6.1 Sources of non-thermal radiation beyond our Galaxy

VHE γ-ray astronomy studies some of the most energetic events in the cosmos, at energies that largely can't be recreated on Earth. At maximum energy the LHC, Europe's main particle accelerator situated at CERN in Geneva, Switzerland, currently produces sub-atomic particles up to 14 TeV. The present VERITAS telescopes have a maximum energy response from 30-50 TeV, while water Cherenkov instruments can detect particles and photons over 100 TeV [DeYoung et al., 2012]. Extra-Galactic non-thermal events, from such sources as Active Galactic Nuclei (AGN), produce γ-rays at VERITAS sensitivity energies. Multi-wavelength campaigns, over many detection bands such as radio, infrared, visible, x-ray, High Energy (HE) (0.1 GeV $<$ E $<$ 100 GeV), Very High Energy (VHE) (100 GeV $<$ E $<$ 100 TeV) or Ultra High Energy (UHE) (E $>$ 100 TeV) (where flux permits) are of great value for fundamental research in high energy astrophysics. They are instrumental in constraining working models of these extreme environments, as for example the VERITAS paper on PKS 1441 +25 demonstrates [Abeysekara et al., 2015]. The following sections

will focus on Active Galactic Nuclei and their non-thermal emissions.

6.1.1 Active Galactic Nuclei

AGN produce some of the most energetic nuclei and photons in the known Universe. Their non-thermal emission mechanisms and (often highly) variable nature make detection and categorisation difficult. To date there are about 70 AGN catalogued by TeVCat [Wakely and Horan, 2008], the TeV source catalogue operated from the University of Chicago. About 1% of all galaxies have an active nucleus, a compact central region with increased luminosity which is home to a black hole of great mass. About 10% of these galaxies (AGN) have beamed relativistic jets emanating (often but not always) near-perpendicular to the galactic plane. These jets are powered by large regions of material orbiting the galaxy centre that accrete onto a Super Massive Black Hole (SMBH) of $\sim 10^7 - 10^{10}$ solar masses [Zel'dovich and Novikov, 1964]. For a detailed study of these extreme regions of particle acceleration to be feasible, an accurate categorisation system is required. See Figure 6.1 for one example of an AGN classification scheme [Beckmann and Shrader, 2013]. As two different extra-galactic non-thermal sources of VHE γ-rays, both AGN, will be examined in this thesis, a brief introduction into AGN classification will be of benefit.

AGN were originally discovered in the radio band and this classification type still persists. Around the SMBH orbits an accretion disk, which is made up of material from the local central environment (dusty torus) drawn in by intense tidal forces. This accretion disk is continually replenished by the dusty torus, a donut shaped region with gaseous and particulate matter orbiting the galactic centre. It is held in equilibrium by its rotational energy and the competing gravity of the outer star field and the inner black hole. The gravitational potential energy of the accreted material is turned into kinetic energy. In a bound steady state the virial theorem states that the kinetic energy $= -\frac{1}{2}$ potential energy; thus half of the potential energy is lost, principally by mass outflow and radiation. The accretion disk will thus heat up, due to a combination of material carried inward (gravitational) and outward

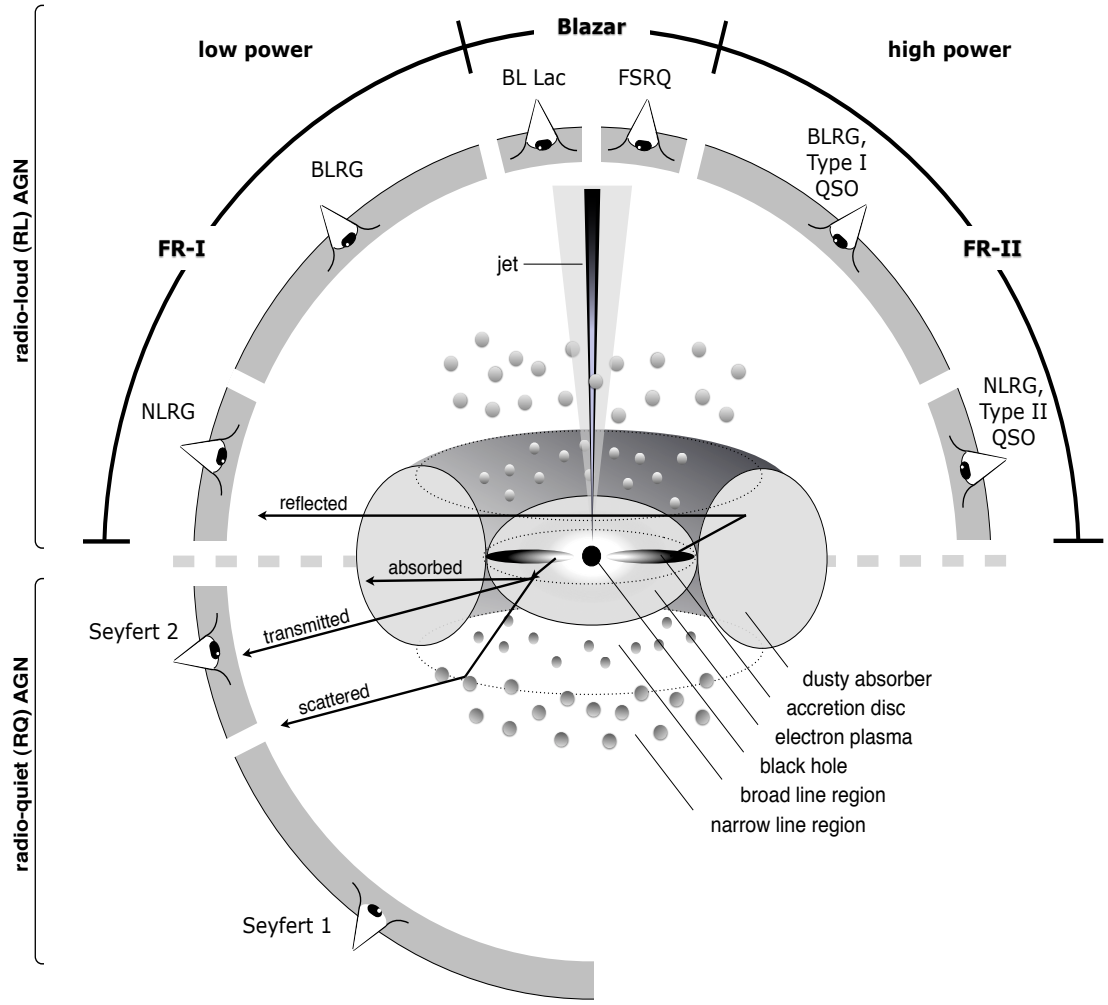

Fig. 6.1 Illustration of an AGN classification system that displays how viewing angle with respect to Earth has given rise to some of the observed properties of the source emission spectrum. This thesis only deals with the narrow emission region ascribed to blazars. Taken from Beckmann and Shrader [2013].

(angular momentum). The emmission from this region will be in the optical / UV. As the in-falling material has non-zero angular momentum, the system will come to equilibrium in a disk [Lynden-Bell, 1989]. Originally this disk was thought to be spatially thin, but simulations accounting for the convection and mass loss have shown it to be quite thick in spatial dimensions [Stone et al., 1999]. In addition, hot material, called an electron plasma in the diagram, forms above the accretion disk. This can inverse-Compton scatter photons up to x-ray energies. Above and below the plane of the accretion disk lie two absorption regions; the Broad Line Region and the Narrow Line Region. The division between these two regions arises from spatially extended areas of broad and narrow emission lines that seem to come from two distinct parts of the galactic nucleus. The constituent matter found in the Broad Line Region is not thought to be homogeneously dense, but higher density regions often termed 'clouds' are thought to freely move about. To date, the kinematic and morphological properties of these regions are open to question [Denney et al., 2009]. However, they remain of great interest as the mass of the black hole may be estimated from the radius of the Broad Line Region [Peterson et al., 2004]. A large fraction of the AGN's radiation may be obscured by interstellar gas and the dusty torus, but (in a steady-state situation) this will be re-radiated at some other waveband, most likely the infrared. Some accretion disks produce a pair of highly-collimated jets and fast outflows that emerge in opposite directions from close to the disk. The jet emission direction is determined either by the angular momentum axis of the accretion disk or the spin axis of the black hole.

6.1.2 Active Galactic Nuclei classification

There is a converging consensus on a system of unification for Radio Galaxies under the scheme outlined in Figure 6.1. This broad categorisation has lead to some attempts at redefinition and even broader classification [Landt et al., 2004]. AGN are broadly classified based on two criteria. Firstly, the prominence of their jets. If the jets are prominent the AGN is radio loud. Otherwise it is radio quiet. Secondly, the angle between the jet axis and the

viewing angle from Earth. The dusty torus obscures more jet emission as the viewing angle from Earth increases with respect to the jet axis.

When the angle of observation is acute, observing near perpendicular to the accretion disk rotational plane, the objects are classified Blazars. Blazars may be Flat Spectrum Radio Quasars (FSRQ) or BL Lac (named after its prototype, BL Lacertae [Schmitt, 1968]), based on the strength of their emission lines. They are ideal targets for multiwavelength studies as both have a broad continuum extending from the radio through to VHE γ-rays. BL Lacs are nearly devoid of emission lines. FSRQs are primarily characterized by their intense UV emission (from the accretion disk), strong broad emission lines in the optical spectrum (from the Broad Line Region), and infrared emission (re-emission from the dusty torus absorption, Section 6.1.1). Historically, optically-violent variable quasars were originally a subtype of blazar that consisted of a few rare, bright radio galaxies whose visible light output could change by up to 50% in a day. They have essentially become unified with FSRQs [Urry and Padovani, 1995].

Many of the Blazars detected at TeV energies exhibit extreme variability. The time-scales can range from years to minutes, and the observed flux can change by more than an order of magnitude. The mechanisms which drive the high-energy emission from blazars remains poorly understood. More detail is given in the next section.

The Fanaroff-Riley (FR) classification [Fanaroff and Riley, 1974] is used to distinguish Radio Loud Galaxies with active nuclei based on their radio luminosity and radio morphology. FR-I are sources whose luminosity decreases as the distance from the central galaxy or quasar increases while FR-II sources exhibit increasing luminosity at the extremities (lobes). The dividing line between FR-I (lower luminosity) and FR-II (higher luminosity) is broadly set at $L_\nu = 10^{32}$ ergs s^{-1} Hz^{-1}, where L_ν is the Luminosity per unit frequency at 1.4 GHz. However the dividing line is also governed by the host galaxie's properties [Ledlow and Owen, 1996].

Radio Loud quasistellar objects are not as tightly bound by galaxy mass and radio lumi-

nosity as are Radio Loud AGN [Donoso et al., 2010]. They were originally thought to be single stars of enormous brightness. Narrow Line Radio Galaxies are observed close to the accretion disk plane while Broad Line Radio Galaxies are observed closer to the perpendicular of the accretion disk. The Narrow Line Radio Galaxies spectrum derives from a greater percentage of the accretion disk emission being re-radiated and reflected by the molecular and particulate dusty torus than for the Broad Line Radio Galaxies spectrum.

For Radio Quiet Galaxies, a regular quasar or a Seyfert 1 galaxy is observed if the observation angle to the accretion plane is $\sim 30^{\circ}$, where the Narrow Line and Broad Line regions are visible. At smaller viewing angles to the accretion plane the Broad Line Region will be hidden by the torus, resulting in a Seyfert 2 galaxy classification. Perpendicular to the jet axis, the full extent of the jets may be seen, particularly at lower frequencies (for example Figure 6.2 from Marshall et al. [2002]). This figure shows a well known blazar, M87, from a viewing angle almost parallel with the accretion disk.

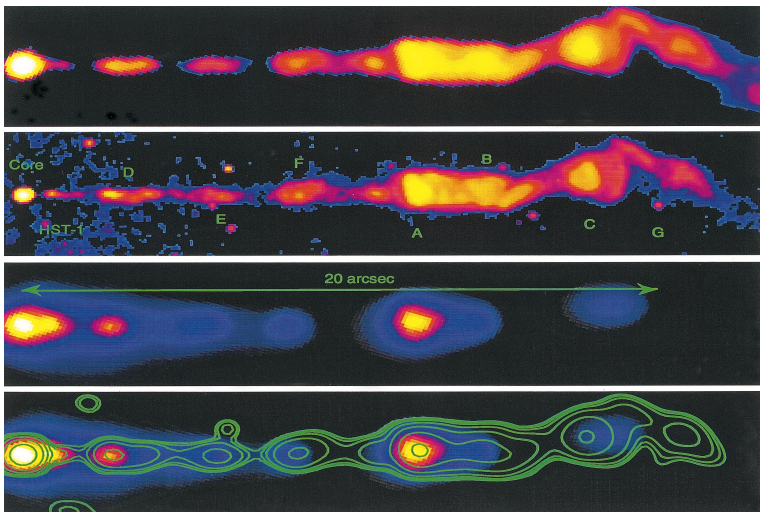

Fig. 6.2 M87 galaxy centre as a bright lobe, extreme left, with jet emission in three different bands; (top) 14.435 GHz using the Very Large Array, New Mexico, U.S.A., (second from top) The Hubble Space Telescope Planetary Camera image, (third from top) smoothed Chandra x-ray space telescope image in the x-ray band, (bottom) smoothed Chandra image overlaid with contours of a Gaussian-smoothed version of the Hubble image. Taken from Marshall et al. [2002].

6.2 Blazars

The most violent extragalactic emissions in the γ-ray sky, apart from γ-ray bursts, are dominated by blazars. Approximately 70 blazars have been detected at TeV energies with red shifts from $z = 0.031$ (Markarian 421, the first blazar detected) to $z = 0.954$ (S3 0218 +35) [Aliu et al., 2012d, Aliu et al., 2012b, Barnacka et al., 2016]. The spectra of blazars is double-peaked, and is most commonly plotted in a νF_ν representation of the Spectral Energy Distribution (SED). νF_ν is the energy density per unit frequency (measured in erg s^{-1} cm^{-2} Hz^{-1}) scaled by frequency (Hz). The lower-frequency spectral peak is due to synchrotron emission from energetic electrons, while the higher-frequency peak is believed to be from inverse Compton emission [Acciari et al., 2010].

6.2.1 Blazar sub-categorisation

BL Lac objects may be classified as low, intermediate or high-frequency peaked, determined by the position of the synchrotron peak on the SED. They exhibit rapid and large scale flux variability, with considerable optical polarization [Padovani and Giommi, 1995]. Finally, BL Lac objects have spectra that are overwhelmingly featureless (devoid of emission / absorption lines) in the non-thermal spectral regions [Falomo et al., 2014].

Only six blazars belong to the FSRQ class. In increasing redshift they are; PKS 0736 +017 ($z = 0.189$) [Ramirez et al., 2004], PKS 1510-089 ($z = 0.361$) [Marscher et al., 2010], PKS 1222+216 ($z = 0.432$) [Tavecchio, F. et al., 2011], 3C 279 ($z = 0.536$) [Stecker et al., 1992], PKS 1441+25 ($z = 0.939$), soon discussed in detail, and S3 0218+35 ($z = 0.954$) [Ahnen, M. L. et al., 2016]. FSRQs are thought to have accretion disks that efficiently enrich the environment of the supermassive black hole with UV to optical photons. The radiation from this photon-rich field, believed to emanate from the clouds (high-density regions) of the Broad Line Region and infrared radiation from the dusty torus, can interact with VHE γ-rays through pair production. This process prevents the escape of some VHE radiation from

the base of the jet [Donea and Protheroe, 2003].

6.2.2 Blazar non-thermal emission models

The emission models for blazars, comprising of the environment around the black hole, the production of the relativistic jets and the non-thermal particle interactions are next examined.

Accretion onto the black hole

Gas, dust and even whole stars may be captured gravitationally and spiral into a central SMBH [Park and Ricotti, 2012]. This central region generates enormous amounts of energy, most commonly as relativistic photons, electrons, positrons and other elementary particles. The large cloud of gas and material which extends well beyond the compact central region will, if it has net angular momentum, tend to flatten into a disk (accretion disk). This is because particle and molecular collisions in a direction parallel to the angular momentum vector will tend to sum to zero, whereas the collisions perpendicular to the angular momentum vector will tend to maintain their circular velocity. This accretion disk region is quite small, approximately 10^{-3} parsecs in size. An example of an accretion disk is illustrated in Figure 6.3, where a cut-away section of the dusty torus allows it to be seen in relation to the much larger torus.

As the disk becomes sufficiently dense, viscosity inside it both transfers angular momentum outwards and heats the disk. This is how the gravitational potential energy of the infalling material is radiated away. Eventually a reasonably stable state arises where matter spirals in through the disk, losing angular momentum via friction on its way inwards and becoming increasingly hotter until it falls off the inside edge (the last stable orbit) and crosses over the black hole horizon.

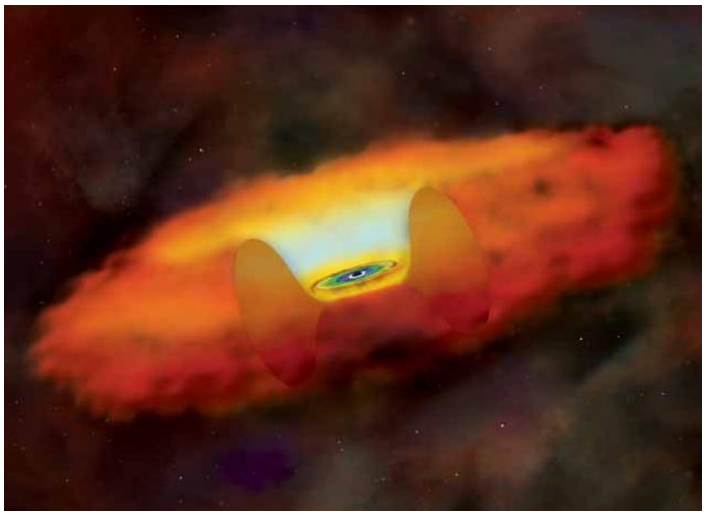

Fig. 6.3 An artists impression of a black hole surrounded by a disk of hot gas, and a large torus of cooler gas and dust [1].

Production of relativistic jets

The formation and subsequent propagation of relativistic jets is still an open question. However, there is good consensus as to the best method to investigate the dominant mechanisms in play. SMBHs with high rotational speed produce Poynting-dominated jets by accretion. These rapidly rotating SMBH systems are best studied by the general relativistic magneto-hydrodynamic equations of motion, which integrate the interactions between accretion disks and black holes, using the self-consistent field method [McKinney and Narayan, 2007]. These calculations and underlying theory lie outside the scope of this thesis. The main difficulties in understanding formation and propagation of relativistic jets are best summarised by the following questions: How are the observed jets so well collimated (with opening angles $\sim$3-5°)? Why are they so superluminally charged (with bulk Lorentz factors up to 10^3)? Why are the magnetized jets not disrupted by kink instabilities or other perturbations in jet formation?

The aforementioned simulations point to two types of jet production scenarios; one associated with an accretion disk that is heavily mass-loaded and another that is associated

[1] http://chandra.harvard.edu/resources/illustrations/quasar.html

directly with the black hole spin energy extraction [McKinney and Gammie, 2004]. The mass-loading model fails to produce bulk Lorentz factors $\geq$3. The second model, extraction of black hole spin energy by the Blandford–Znajek mechanism [Blandford and Znajek, 1977], shows that the Poynting-dominated jet has a Lorentz factor that is determined by the mass-loading of the jet, such that even low mass-loading can explain high bulk Lorentz factors [McKinney, 2005]. These relativistic jets can extend as far as many tens of kiloparsecs from the SMBH; a simulation of a jet (with associated helical magnetic fields that stabilise it) is seen in Figure 6.4.

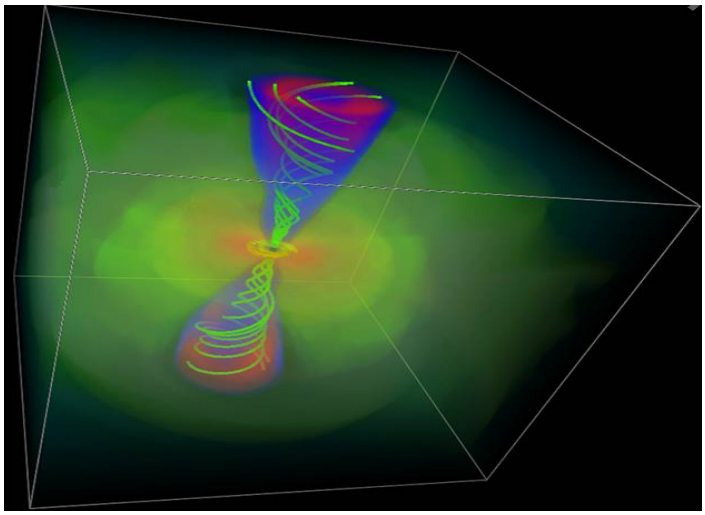

Fig. 6.4 Simulation [2]which shows a black hole pulling in nearby matter (yellow) and spraying energy back out in a jet (blue and red) that is held together by magnetic field lines (green).

Relativistic beaming

When the angle of the jet lines up sufficiently with Earth, the observed emission is boosted considerably by relativistic effects in the jet (relativistic beaming). The average velocity of the matter in the jet may be 0.95-0.99 c; this bulk velocity is not the speed of a particular particle, which may be higher again. The relationship between the emitted luminosity and the observed luminosity depends on characteristics of the jet, such as the magnetic fields

[2]http://kipac-web.stanford.edu/research/agn

and their interaction with superluminal particles. The particular factors involved are not important in this thesis [Maraschi and Rovetti, 1994]. Relativistic beaming has another property of interest; the relativistic jet pointing away from Earth will appear dimmer (due to the same relativistic effects). As a consequence, two intrinsically identical relativistic jets will have radically differing apparent luminosities depending on the angular distance between beam axis and Earth. This has the following unique consequence; a population of intrinsically identical blazars of equal distance from Earth but with random jet orientations will be observed as an inhomogeneous blazar population.

Doppler boosting

Relativistic beaming can be quantified and used to explore the observed spectra. A simple model can illustrate the effects of relativistic beaming on the luminosity observed. If Lum_e is the luminosity of the jet emitted in the rest frame of the jet and Lum_o the luminosity of the jet observed on Earth, then introducing the doppler factor, D [Kellermann et al., 2007], we have

$$Lum_o \propto Lum_e x D^S \tag{6.1}$$

where S depends on the geometry and spectral index and is typically in the range between 2 and 3.

Synchrotron emission in jets

Having described most briefly the astrophysical regions that produce and propagate relativistic particles, attention turns to the physical processes that produce the electromagnetic spectra observed. Synchrotron emission arises from relativistic electrons spiraling in magnetic fields. Synchrotron emission is responsible for the majority of extra-terrestrial radio sources detected. However for many relativistic jets, synchrotron emissions in the optical and x-ray bands are also observed, due to the extreme energy imparted to electrons and positrons in these environments [Blandford and Königl, 1979].

Inverse Compton scattering

Inverse Compton emission results when a very high energy electron or positron scatters off a lower-energy photon in an ambient photon field, transferring a large percentage of its energy in the process to the photon. This up scattering (transfer of energy to the collision object, removal of energy from the colliding object) produces a much higher-energy photon than the original.

Synchrotron Self-Compton

Electrons undergoing synchrotron radiation will create a photon population which, when sufficiently confined, allows other energetic spiraling electrons to interact with the generated photons via inverse Compton scattering. This can be considered a production-boost two step process. Photons produced by Synchrotron Self-Compton are very energetic, up to 50 TeV or more, and are found on the trailing edge of the second peak of νF_ν spectra.

External Compton

In order to explain the highly-variable nature of blazar flares, new emission models are explored. In one possible model, the photons that are energised in inverse Compton scattering are from regions external to the jet. In this hypothesis, the external Compton model [Sokolov and Marscher, 2005], the relativistic beaming of the inverse Compton radiation noticeably differs from the beaming produced by synchrotron and synchrotron Self-Compton components [Dermer, 1995]. The Broad Line Region or the wider torus, both poorly defined spatially, are the probable sources of the lower-energy photons. These hypothesised photons are often referred to as 'seed' photons.

Hadronic - pion decay

The narrow confines of the jet emanation region produces relativistic and highly-collimated electrons and protons that can interact with dense, compact clouds that are proposed to circulate in the Broad Line Region and perhaps the Narrow Line Region of a blazar [Beall and Bednarek, 1999]. γ-rays are produced from the decay of neutral pions, which are the result of hadronic collisions of the collimated beam with denser clouds. If these clouds are too dense or hot, the TeV γ-rays may be attenuated by the bremsstrahlung radiation in the cloud. The secondary pairs produced would not efficiently produce synchrotron flares because of the dominant role of inverse Compton scattering.

6.2.3 Measuring VHE γ-ray flux

Before discussing particular blazars, a common method of quantifying the VHE activity of a putative source is introduced, the crab unit (c.u.). The standard reference source for TeV astroparticle physics is the Crab nebula [Meyer et al., 2010]. Though there have been some detections of variability [Mayer et al., 2013] at HE, it has remained the reference against which all other VHE emitters are compared to. VHE source flux thus is in reference to crab units, which equates to a differential flux of 2.83×10^{-11} (E/TeV)$^{-2.62}$ cm^{-2} s^{-1} TeV^{-1} or an integral flux of 1.75×10^{-11} (E/TeV)$^{-1.62}$ cm^{-2} s^{-1} [Aharonian et al., 2004]. These figures were derived from $\sim$400 hours of quality-cut data from 1997 to 2002, with an energy range from 500 GeV to 80 TeV.

6.3 The relatively nearby blazar Mrk 421

Markarian 421 (Mrk 421 hereafter) is a nearby active galaxy (z = 0.031) with a featureless optical spectrum devoid of prominent emission or absorption lines. It has a strongly polarized variable optical and radio flux, and compact (milli arcsecond scale) radio emission. Mrk 421 is a high-synchrotron-peaked BL Lacertae object, which was first reported as a

VHE emitter in 1992 [Punch et al., 1992]. The typical VHE flux of this source is about 0.5 c.u., as reported in Abdo et al. [2011] and references therein. The highest level of VHE activity ever measured for this source was about 10 c.u. [Fortson et al., 2012]. The Mrk 421 SED is well described by a characteristic two-peak spectrum (as displayed in Figure 6.5) and discussed in the next section. In the more general context of blazars, Mrk 421 belongs to a subclass of HBL objects, relatively low luminosity sources with both peaks located at relatively high energies (∼1 keV and ∼100 GeV respectively).

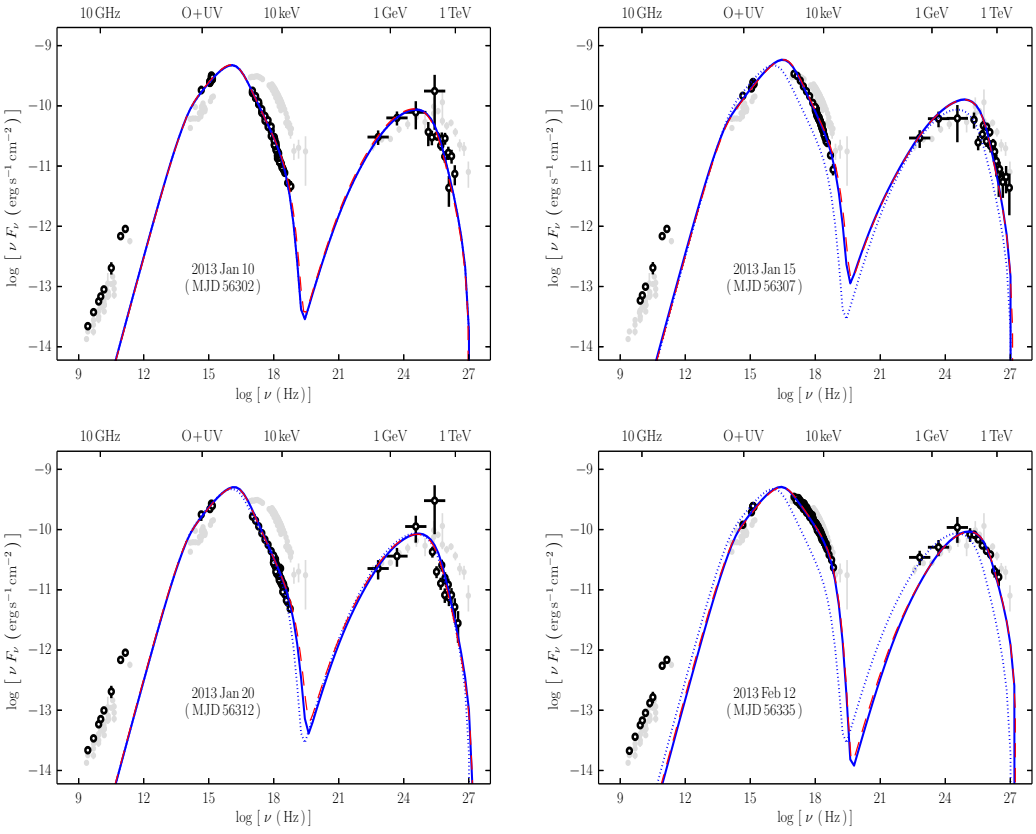

Fig. 6.5 The Spectral Energy Distribution of Mrk 421 from 2-3 months prior to the exceptional flaring episode of 2013, from simultaneous data from Swift-UVOT (170-650 nm), Swift-XRT (0.2-10 keV), NuSTAR (3-78.4 keV), Fermi-LAT (20 MeV-300 GeV), MAGIC (30 GeV-50 TeV), and VERITAS (30 GeV-50 TeV); refer to Balokovic et al. [2016] for a description of the instruments. The two left panels show low-state SEDs, while the two right show elevated-state SEDs. The solid blue lines show a simple one-zone SSC model, The grey background curves of each panel show the Mrk 421 SED from Abdo et al. [2011], which were averaged over a quiescent 4.5-month period. Taken from Balokovic et al. [2016].

6.3.1 The April 2013 flare episode

Three months prior to the April 2013 flaring episode, detailed observations of this HBL object were undertaken. The VERITAS multi-wavelength observations of Mrk 421 were carried out under good weather conditions during the period of the NuSTAR campaign [Balokovic et al., 2016]. NuSTAR is a space-based x-ray telescope that operates in the range of 3-79 keV. The resulting VERITAS data, with a quality-selected exposure time of 15.5 hr during the period MJD 56302 to MJD 56368, were almost all strictly simultaneous with NuSTAR exposures.

The VHE detection significance was found to vary between 18.7σ on MJD 56302 (2013/01/10, from 3 hr total data) and 40.4σ on MJD 56368 (2013/03/17, from 3 hr total data). No significant intranight variability was detected during this three month period. The multiwavelength effort intensified soon after due to rising activity; during three consecutive nights from MJD 56393-56395 (2013/04/11 to 2013/04/13) a persistently high flux of about 5 c.u. above 300 GeV was recorded. This emission was very variable with short-lived maxima reaching beyond 11 c.u. This implied an increase by a factor of more than 20 with respect to the typical (not lowest) VHE flux from this source above 300 GeV, and represents the highest VHE activity recorded for this object to date. Figure 6.6 shows the multiwavelength light curve from this period.

Besides MAGIC and VERITAS, the campaign also includes dedicated observations at radio and optical wavelengths with various instruments, and X-rays with Swift (another space-based x-ray telescope operating from 0.2-10 keV) and NuSTAR. The source had been found to be very high at optical and x-ray [Balokovic et al., 2013].

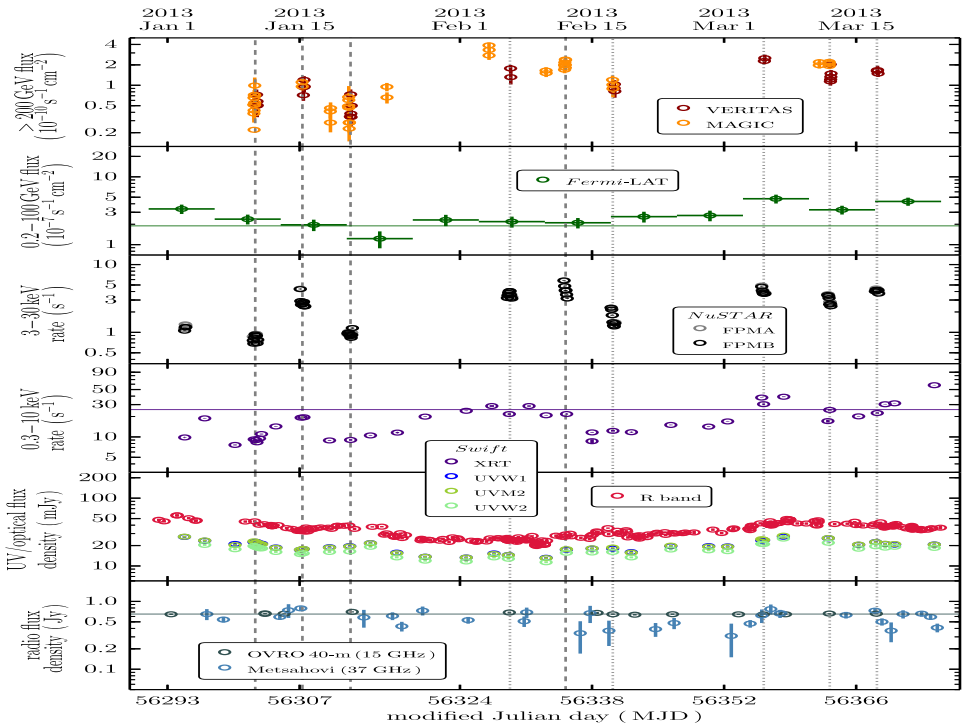

Fig. 6.6 Light curves for Mrk 421 from MAGIC, VERITAS (>200 GeV, ∼30 min binning), Fermi-LAT (binned weekly), NuSTAR (binned by orbit), Swift-XRT (complete observations), Swift-UVOT (complete observations), ground-based optical observatories (R band, intranight cadence (the host-galaxy contribution in the R band has been subtracted out)), OVRO and Metsahovi (15 and 37 GHz, both with 3-4-day cadence). The vertical lines mark midpoints of the coordinated NuSTAR and VHE observations. Taken from Balokovic et al. [2016].

6.3.2 Eventdisplay analysis of flaring Mrk 421

As this source was highly variable during the flaring period, with changes in spectral index from night to night, a single night alone was examined. The 13^{th} April showed the highest γ-ray output, with peak emissions reaching momentarily up to 11 c.u. as mentioned. This night's data were recorded under elevated aerosols, WSS16 (detailed in part in Section 4.8.4). Just four runs were selected for the analysis, due to a technical failure that caused VERITAS to operate with only three telescopes for part of the night. Additionally, passing cloud was present during the selected runs, necessitating cuts on data entering the analysis

chain.

In total ∼80 min of quality four-telescope data was examined with 3 separate extinction profiles with VWinter molecular profile; the official (introduced in Section 3.5.1), ext50km (detailed in Section 5.5), and WSS16 (defined in Section 5.4.2).

Referring to Table 6.1, is it noted that this is an exceptional VHE γ-ray event. The 80.10 min of select data recorded an excess of 122.8 σ after analysis with Eventdisplay anasum stage. VERITAS anasum refers to the final stage VERITAS analysis where individual runs are summed together to produce sky maps, spectral energy distributions and spectral fits, among others. The 122.8 σ detection allowed the spectral index to be calculated with unprecedented accuracy, ideal when small changes in reconstructed energy due to aerosol extinction are investigated. It is noticed that the number of ON/OFF events is altered little for the differing IRFs. This would seem to imply that aerosol extinction does not overly impact on γ-ray/hadron separation.

run no.	ON^{of}	ON^{50k}	ON^{w16}	OFF^{of}	OFF^{50k}	OFF^{w16}	σ^{of}	σ^{50k}	σ^{w16}
67977	808	778	770	5.33	5.00	4.83	53.7	52.7	52.2
67978	861	824	823	8.5	7.67	7.33	54.5	53.3	53.6
67979	1288	1247	1236	6.67	6.17	6.17	68.3	67.3	67.0
67986	1444	1380	1369	10.5	9.17	9.50	71.5	70.2	69.8

Table 6.1 The Eventdisplay anasum analysis results (discussed in Section 5.5) for Mrk 421 during 13^{th} April 2013. Run 67977 at 24° from zenith and duration 15.00 min. Run 67978, 18° and 15.00 min. Run 67979 at 11° and 20.05 min. Run 67986 at 28° and 30.05 min. All runs with WSS16 aerosol extinction. The final significance for the 80.10 min of data is 122.8 σ. Note that ^{of} refers to official collaboration IRFs, ^{50k} the ext50km IRFs and ^{w16} to WSS16 IRFs. The comparison between normal and elevated aerosols is made using the ext50km and WSS16 IRFs alone. OFF normalization = $\frac{1}{6}$ applied (explained in Section 3.4.5).

6.3.3 Sky map centered on Mrk 421

Sky map refers to a 2D histogram of excess γ-ray counts centered on the putative source with significance of detection and RA, DEC co-ordinates. Referring to Figure 6.7, the phenomenal γ-ray flare of the 13^{th} April 2013 becomes evident. This short-duration / high-γ-ray yield dataset was analysed with the three separate IRF simulation sets, two of which were specially produced for this analysis. Note that the comparison between differing aerosols is made using the ext50km and WSS16 IRFs alone. The official VERITAS IRF set differs from the ext50km set, by $\sim$3.5-4.0% for ON counts (detailed previously Section 5.5). Though

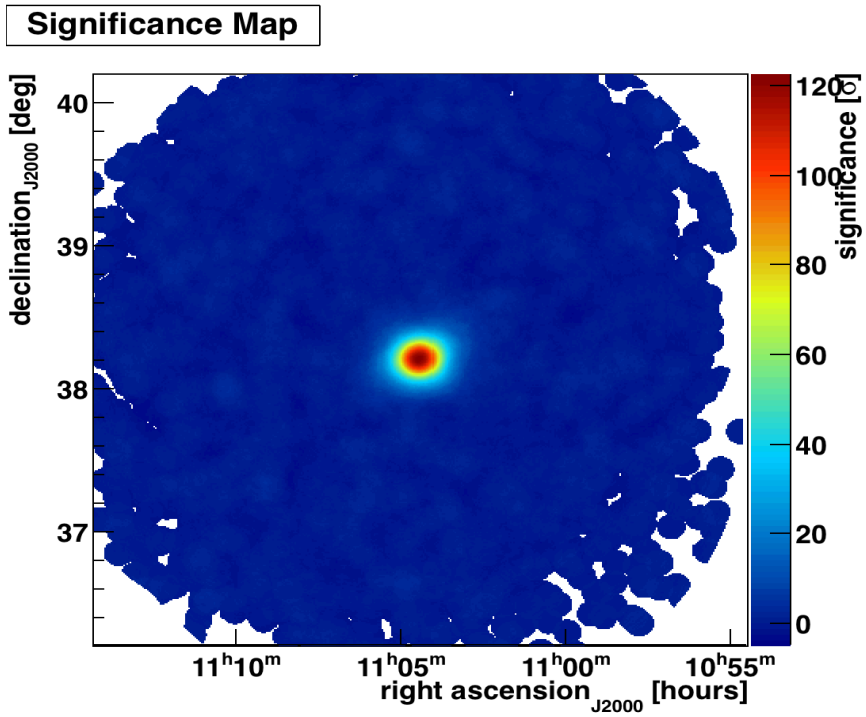

Fig. 6.7 The 2D histogram of significance centered on Mrk 421 from 13^{th} April. During just 80 min of data taking a peak significance > 120 σ was recorded. Note that the blank spaces are due to the background γ-ray counts not being detected in sufficient number during the limited exposure.

the WSS16 extinction set was shown to yield $\sim$8% fewer photons than for normal aerosol loading (quantified in Section 5.2.3), the overall ON and OFF counts are very similar (as seen in Table 6.1). This can be explained by the fact that γ/hadron seperation does not

depend primarily on image size alone (the summation of PMT charge in the moment-fitted ellipsoid, illustrated in Figure 3.16) but more on moment-fitted parameters that are derived from a highly pixellated PMT camera. A drop in Cherenkov photons arriving at the telescope of the order of $\sim$8% is not strongly detectable with a camera of just 499 PMTs. This can be better understood by reference to the IRF production sets for ext50km and WSS16; on being compared by lookup tables for median length, little difference in the simulations emerged. However the median reconstructed energies when compared differed by $\sim$8% (discused in Section 5.5.1). Due to a reduction in the VERITAS telescope's effective area from aerosol extinction, the corresponding loss of reconstructed events duw to the same extinction is approximately canceled out . From this analysis in can be said that γ/hadron seperation (for the current generation of IACT) is not impacted strongly by the introduction of elevated aerosol extinction up to WSS16.

6.3.4 Spectrum of Mrk 421

The primary motivation in producing new IRF simulations for elevated aerosols lies in calorimetry. An SED yields much important information that can be used to test, among other matters, VHE γ-ray production models.

The Mrk 421 analysis presented in Section 6.3.2 was energy binned to produce the spectra in Figure 6.8. Note the following caveats; energy reconstruction above 1 TeV is currently not supported with GrISU simulations; this not necessarily a hinderance for the work in this thesis which seeks to understand the impact of aerosol loading on the lower energy VHE γ-rays principally. Further, the spectrum is not linear, it is a power law with an exponential cut-off [Krennrich et al., 2001]

$$\frac{dN}{dE} \propto E^{-\Gamma \pm stat} e^{-\frac{E}{E_o \pm stat}} \mathrm{m}^{-2}\mathrm{s}^{-1}\mathrm{TeV}^{-1} \tag{6.2}$$

In the Krennrich et al. [2001] analysis from the Whipple 10 m experiment, the exponential cutoff was observed up to 17 TeV; therefore any exponential cutoff in the analysis presented herein will be largely truncated. This is unfortunate for an analysis of the cutoff region could yield a visible shift due to aerosol extinction correction. The power-law plot yields a negative slope, called the Spectral Index (Γ), which can often be approximated by a linear fit between E_{min} and E_{max}.

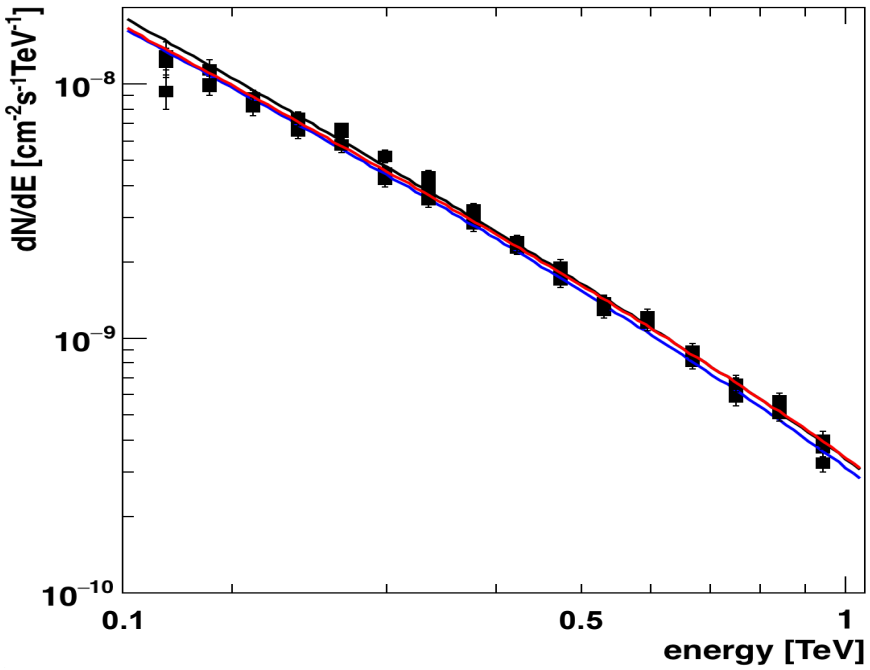

Fig. 6.8 A log-log plot of energy spectrum for Mrk 421 from 13^{th} April 2013 for an energy range of 140 GeV to 1 TeV. The fit is for a power law with exponential cutoff. Black represents the official IRF set, blue the ext50km IRFs and red is the WSS16 IRF set. Refer to upper half of Table 6.2.

The settings for the spectrum plots were as follows; energy bins = 0.05 TeV: The energy threshold was set to 10% of maximum effective area. Two separate energy ranges were chosen. (E_{min} to E_{max}) = 140 GeV to 1 TeV for the power law with exponential cutoff. (E_{min} to E_{max}) = 140 GeV to 400 GeV for the power law approximation alone. Two ranges were chosen to examine the impact of aerosol extinction on lower energy γ-ray EAS, as strong detections at higher energies will cause the spectral fit to ignore slight

changes at lower spectral ranges. The results from the three separate analyses are presented in Table 6.2, where the information is presented as $dN/dE = I \times (E/1TeV)^{-\Gamma} e^{E/E_o}$ and $dN/dE = I \times (E/1TeV)^{-\Gamma}$. Here I represents the flux normalisation in cm^{-2} s^{-1} TeV^{-1}, Γ represents the plot's slope between E_{min} and E_{max} (the spectral index) and E_o the exponential cutoff fit. Owing to the very large number of γ-rays detected, the errors in spectral index are very small. Referring to Figure 6.8, the energy spectrum from the three IRF sets

extinction	I (cm^{-2}s^{-1}TeV^{-1})	Γ	E_o TeV	χ^2/N
power law with exp cutoff (140 GeV - 1 TeV)				
official	$6.4 \pm 0.5\, x\, 10^{-10}$	-1.82 ± 0.05	1.56 ± 0.15	36.74/33 (1.1)
ext50km	$6.7 \pm 0.6\, x\, 10^{-10}$	-1.75 ± 0.06	1.30 ± 0.12	39.17/33 (1.2)
WSS16	$6.8 \pm 0.6\, x\, 10^{-10}$	-1.75 ± 0.06	1.45 ± 0.14	42.86/31 (1.4)
power law (140 GeV - 400 GeV)				
official	$5.5 \pm 0.7\, x\, 10^{-10}$	-1.81 ± 0.10	–	09.70/6 (1.6)
ext50km	$5.3 \pm 0.7\, x\, 10^{-10}$	-1.78 ± 0.10	–	10.56/6 (1.7)
WSS16	$6.5 \pm 0.9\, x\, 10^{-10}$	-1.63 ± 0.11	–	10.24/6 (1.7)

Table 6.2 The 13^{th} April 2013 spectral index for Mrk 421, for $dN/dE = I\, x\, (E/1TeV)^{-\Gamma}\, e^{E/E_o}$ (power law with exp cutoff) and $dN/dE = I\, x\, (E/1TeV)^{-\Gamma}$ (power law) for three IRF simulation sets. The values in brackets represent the χ^2/N fraction.

are plotted. Table 6.3 shows the number of γ-rays detected from Mrk 421 source location (N_{ON}), background non-normalised (N_{OFF}) and the excess (σ) in sixteen energy bins, for the three IRF sets. It is seen that from $E_\gamma \geq$0.237 TeV that the three IRFs produce largely consistent results, however below this limit WSS16 IRFs show a marked decline in significance σ. This is due to the power law assumption principally which assumes nominal atmospheric extinction with a constant effective area for a particular instrument parameter space. As the effective area decreases the flux of photons needs to increase correspondingly to register consistent significance estimations seen; this appears not to have happened below 0.237 TeV. The Eventdisplay analysis used was for the standard γ/hadron cut set (outlined in Section 3.4.5).

E_γ TeV	E_{min}-E_{max} TeV	N_{ON}^{of}	N_{ON}^{50k}	N_{ON}^{w16}	N_{OFF}^{of}	N_{OFF}^{50k}	N_{OFF}^{w16}	σ^{of}	σ^{50k}	σ^{w16}
0.168	0.158-0.178	063.0±08.	060.0±08.	041.0±06.	06.0±2.4	06.0±2.4	03.0±1.7	14.4	14.0	11.8
0.188	0.178-0.200	124.0±11.	146.0±12.	100.0±10.	21.0±4.6	22.0±4.7	16.0±4.0	19.2	21.1	17.4
0.211	0.200-0.224	242.0±16.	238.0±15.	150.0±12.	22.0±4.7	20.0±4.5	22.0±4.7	28.2	28.1	21.4
0.237	0.224-0.251	268.0±16.	253.0±16.	255.0±16.	22.0±4.7	20.0±4.5	16.0±4.0	29.9	29.1	29.6
0.266	0.251-0.282	319.0±18.	320.0±18.	270.0±16.	17.0±4.1	17.0±4.1	23.0±4.8	33.3	33.4	29.9
0.299	0.282-0.316	270.0±16.	264.0±16.	312.0±18.	13.0±3.6	10.0±3.2	14.0±3.7	30.8	30.7	33.2
0.335	0.316-0.355	327.0±18.	309.0±18.	267.0±16.	10.0±3.2	13.0±3.6	11.0±3.3	34.4	33.1	30.8
0.376	0.355-0.398	280.0±17.	273.0±17.	302.0±17.	11.0±3.3	12.0±3.5	11.0±3.3	31.6	31.1	32.9
0.422	0.398-0.447	273.0±17.	266.0±16.	267.0±16.	10.0±3.2	07.0±2.6	08.0±2.8	31.3	31.2	31.1
0.473	0.447-0.501	248.0±16.	242.0±16.	265.0±16.	04.0±2.0	02.0±1.4	06.0±2.4	30.4	30.3	31.2
0.531	0.501-0.562	232.0±15.	225.0±15.	229.0±15.	04.0±2.0	05.0±2.2	05.0±2.2	29.4	28.8	29.1
0.596	0.562-0.631	246.0±16.	244.0±16.	234.0±15.	08.0±2.8	05.0±2.2	05.0±2.2	29.8	30.0	29.4
0.668	0.631-0.708	208.0±14.	203.0±14.	217.0±15.	03.0±1.7	02.0±1.4	03.0±1.7	27.9	27.7	28.5
0.750	0.708-0.794	185.0±14.	174.0±13.	192.0±14.	05.0±2.2	04.0±2.0	03.0±1.7	26.0	25.3	26.8
0.841	0.794-0.891	187.0±14.	181.0±14.	173.0±13.	05.0±2.2	05.0±2.2	05.0±2.2	26.1	25.7	25.1
0.944	0.891-1.000	144.0±12.	130.0±11.	157.0±13.	01.0±1.0	00.0±0.0	03.0±1.7	23.4	22.5	24.1

Table 6.3 The anasum combined analysis for Mrk 421 during 13^{th} April 2013 for the official ^{of}, ext50km ^{50k} and WSS16 ^{w16} IRF production sets. Note that OFF region normalisation ($\frac{1}{6}$) is not applied. For $E_\gamma \leq$0.237 TeV the effects are most pronounced.

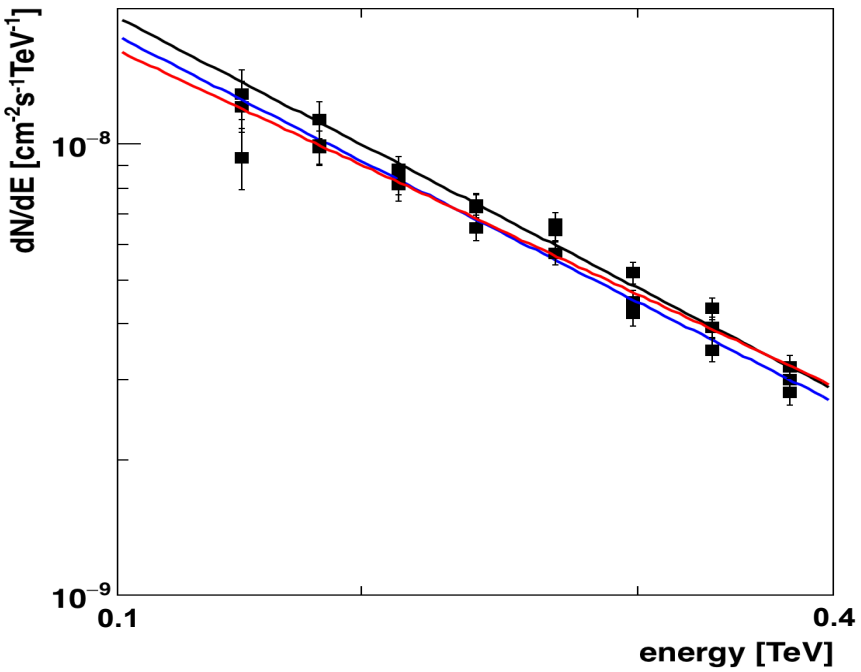

Fig. 6.9 A log-log plot of energy spectrum for Mrk 421 but with a shorter energy range of 140 GeV to 400 GeV, chosen to examine differences in spectral energy fit at lower energies. The fit is for a power law alone. Black represents the official IRF set, blue the ext50km IRFs and red is the WSS16 IRF set. Refer to lower half of Table 6.2.

Should the WSS16 IRF set have corrected the lowest energy EAS parameterised images for aerosol extinction loss, it would be reasonable to expect these corrected γ-rays shower images would be binned at a higher energy. This could have happened, but the large number of γ-rays already in the higher-energy bins would not permit a small jump in excess to be overly evident in a plot. The number of ON and OFF events tabulated gives finer detail. Table 6.1 shows a difference in ON counts between ext50km and WSS16 IRFs of just 31, or 0.7%. Table 6.3 shows a marked difference in energy bins below 0.3 TeV for the same ON events. The combination of a (slight) increase in energy threshold with a corresponding re-binning of ON events for WSS16 into higher energy bins can account for the tabulated data discussed. The differences do not lie outside of statistical and systematic uncertainties however. The power law plot of Figure 6.9, presented in the lower half of Table 6.2 does not show a hardening outside of statistical and systematic uncertainty. It must also be said that the χ^2/N fit for the power law approximation (Figure 6.9) was quite poor and may

render the spectrum unusable. In conclusion, the aerosol correction seen in spectral index, $\Delta\Gamma$, for the 13^{th} April 2013 data does not register as significant. This implies that VHE γ-ray sources with a moderate hardness ($\Gamma \sim 2$) that have been analysed with the VERITAS standard analysis are not in need of re-analysis if their data was obtained during episodes of elevated aerosols.

Finally, for a pure power law spectrum the data presented in Table 6.2 shows that the ext50km IRF set may be used in place of the official collaboration IRFs for the aerosol extinction analysis in this thesis. This is important for this study as the ext50km IRFs are known to be produced identically to WSS16 IRFs, with the exception of the a different extinction profile. It is outside the scope of this thesis to examine if the ext50km IRF set may be a replacement VERITAS IRF set for other analyses, such as light curves.

6.3.5 Systematic uncertainties and aerosol extinction correction

Apart from statistical uncertainties, observations of VHE γ-rays by IACTs are affected by rather large systematic uncertainties. A major drawback to their estimation is the lack of uniform test signals that would allow calibration of the entire instrument in combination with the showering process in the atmosphere.

The preferred option for systematic uncertainty estimation is the use of Monte Carlo simulations modelling both the atmospheric EAS production and propagation and the subsequent telescope IRF. Figure 6.10 tabulates all the contributing factors ($>2\%$) to the systematic uncertainty as determined by the MAGIC collaboration for observations of the Crab Nebula in 2008. The largest contributions to the systematic uncertainty come from the conversion of photons to measurable photoelectrons, item 7 in Figure 6.10. This can normally be measured with a light source uniformly illuminating the camera, as explained in Section 3.4.2. Item 2 relates to aerosol extinction, of more concern due to its variability and lack of robust estimation at VERITAS until this thesis.

Item	Source of Uncertainty	Class	Uncertainty (%)	Comments
1.....	Parametrization of Atmosphere in MC-simulation	A	3	Deviations due to yearly and daily pressure changes, deviations of real density distribution and standard atmosphere model
2.....	Atmospheric transmission losses due to Mie scattering	A, (C)	5	Lack of good measurements; short term unpredictable changes possible
3.....	Incorrect NSB simulation	A	3	MC assumes uniform NSB. Variations due to source location, air glow, variations due to manmade light. Stars in the FoV.
4.....	Reflectivity of main mirror	A	7	From measurements of reflected star images
5.....	Variation of the useful mirror area	A	3	Malfunctions of active mirror control resulting in focussing losses
6.....	Day to day reflectivity changes	A	2	Due to dust deposit variations and occasional dew deposit
7.....	Photon detection efficiency of the PMT/lightcatcher system	A, C	10-12	See text
8.....	Unusable camera channels	B	3	Dead PMTs (5-10 channels), problems in calibration (5-10 channels)
9.....	Trigger inefficiencies	B, C	4	Due to discriminator dead-time, baseline shifts/drifts, level differences trigger branch and FADC branch etc.
10.....	Signal drift in camera due to temperature drifts	A, C	2	Combination of PMT QE change (small), amplifier and optical transmitter drifts
11.....	Camera flatfielding	A,B	2	Calibration problem
12.....	Signal extractor	B	5	Complex effect due to trigger jitter (early pulses from PEs generated on 1st dynode) etc.; baseline jitter, shifts in FADCs
13.....	cuts and methods used in the analysis	B,C	5-30	Energy dependent, see discussion of differential energy spectrum
14.....	Losses of events during reconstruction	B(A)	8	Simplifications in MC simulation
15.....	Estimate of BG under source	B(A)	4	Camera nonuniformity not included in MC. Hadronic events not perfectly simulated in MC.
16.....	Small tracking instabilities	B	2	Source jitters around nominal camera position due to small tracking errors, small camera oscillations due to gusts etc, resulting in a wider signal spread than predicted by MC
17.....	Nonlinearities in the analog signal chain (PMT–FADC	C(A)	3-10	Saturation and nonlinearities of electronic and opto-electronic components

Fig. 6.10 A table of the principal systematic uncertainties that arise in the imaging atmospheric technique as determined by the MAGIC collaboration [Albert et al., 2008]. The parameters are classified according to their impact on various measurements. Class A are contributions to the uncertainty on the energy scale. Class B are contributions to the uncertainty in the event rate. Class C are contribution affecting the spectral slope.

Some of the systematic uncertainty has already been dealt with, these relate in part to the ceilometer laser's wide FWHM and the wavelength drift in peak emission. Additionally, the effective water vapour extinction estimation may be biased by the binned Precipitable Water Vapour estimate used in its calculation. These factors have already been addressed in Sections 4.5.1 and 4.5.3.

One further addition to systematic uncertainty in aerosol extinction that lies outside this thesis is estimation of the Angström coefficient, introduced in Section 3.6. The VERITAS collaboration lacks the instrumentation required for the estimation and monitoring of this intrinsic property of the aerosol species present on site at any moment. The intrinsic components relate to wavelength dependance and also particle shape asymmetry distribution. Sun photometers such as those provided by the AERONET programme (introduced in Section 4.1) would be capable of Angström coefficient monitoring during sunlight hours. A study on the impact of aerosol extinction on fluorescence radiation (of similar wavelength to Cherenkov radiation) at Pierre Auger observatory [Prouza et al., 2007], showed that the uncertainty in energy reconstruction due to unknown Angström coefficient was $\leq\sim 2\%$. This being the case, the systematic uncertainties estimated in this thesis relating to aerosol extinction are a partial but quite good approximation.

One common approach to determine a global systematic uncertainty for the imaging atmospheric technique is to estimate the systematic uncertainties of the various parameters separately and combine them. The general practice is to add them all in quadrature; this gives a slight underestimate of the total systematic uncertainty, but accounts reasonably for possible correlation between parameters. For work in this thesis, a global systematic uncertainty for a particular data set will not be estimated, but the change in such due to the introduction of better aerosol extinction profiling and subsequent introduction into VERITAS IRFs.

6.3.6 Aerosol derived systematic uncertainty estimation

As 5.5 years of ceilometer data have been analysed in Chapter 4, the results plotted in Figures 4.21 and 4.24 will be used to weigh the aerosol extinction at VERITAS for a typical April month. This may be called an average monthly aerosol climatology. This will have the effect of shifting the histogram of Figure 4.21 to the left by WSS02. The weights thus for each aerosol loading bin are $<$WSS12 $= 0.09$; WSS12 $= 0.29$; WSS14 $= 0.25$; WSS16 $= 0.24$; WSS18 $= 0.09$.

Tables 5.8 and 5.9 displayed comparative data of mono-energy VERITAS simulations which were produced with varying aerosol extinction. The VHE γ-ray energies produced were 100 GeV, 300 GeV, 500 GeV and 700 GeV, with shower axis 20° from zenith. These tables showed a change in reconstructed energy for varying aerosol loading that was largely energy independent above 300 GeV. The systematic uncertainty in reconstructed energy may be calculated by (aerosol bin weight) $\times$ (% change in reconstructed energy for aerosol bin) for the energy range in question (100 $-$ 700 GeV). This yields $0.29\times2\% + 0.25\times5\% + 0.24\times8\% + 0.09\times12\%$ which is $\sim$4.8%. This does not include an additional uncertainty introduced by the unknown Angström coefficient, which could bring the aerosol related systematic uncertainty in reconstructed energy to $\sim$6-7%. The average year-on-year aerosol loading yields a systematic uncertainty of $\sim$3% for reconstructed energies, which is comparable to the 5% quoted in the MAGIC paper [Albert et al., 2008] when Angström coefficient uncertainties are included. The maximum systematic uncertainty could be up to $12-15\%$ in severe aerosol loading approaching WSS20. These episodes are rare however as seen in Figure 4.21.

The above calculation does not account for the spectral energy distribution for a particular astrophysical source. This could be important for soft VHE emitters as the change in reconstructed energy is only energy independent above $\sim$300 GeV. This was seen in Table 5.9 where increases in night sky background noise had little difference in reconstructed energy. However for the Mrk 421 flare event analysed in this thesis, the adjustment is expected to

be small. This addition could easily be done by weighing the above calculation by the number of reconstructed events in the four energy bins above. The bins could be $<$ 200 GeV, 200-400 GeV, 400-600 GeV, 600-950 GeV. The binning will not be evenly distributed as the reconstructed events are already binned in the table. Referring to Table 6.3 the following weights apply; 0.12, 0.4, 0.28, 0.2 respectively. Only the lower energy bin need be adjusted, representing 12% of all reconstructed events. This adjustment is required for the combination of low energy γ-rays and variable NSB_{uv} lowers the difference in reconstructed energy for increased aerosol loading, as seen in Table 5.9. However, the highest NSB_{uv} levels tabulated only occur during periods of partial moonlight and are therefore not accounted for here. This further refinement in systematic uncertainty in reconstructed energy for the Mrk 421 April 2013 flare in the absence of elevated aerosol extinction correction is practically identical to the previous estimate, $\sim$6-7%.

6.4 Application to an extended data set

The aerosol extinction correction developed for the VERITAS experiment has shown to offer little improvement in calorimetry for a very powerful VHE γ-ray detection such as the April 2013 Mrk 421 flare if only a pure power law spectrum is assumed. However, there may be benefits for another data set if the putative source is a very soft ($\Gamma \geq \sim 4$) emitter. The new analysis is next used on such a very soft VHE γ-ray detection over the space of 5 days with varying aerosol loading, where the effects of correcting for increased aerosol extinction is investigated.

6.4.1 The distant blazar PKS 1441 +25

PKS 1441 +25 ($z = 0.9397 \pm 0.0003_{stat}$) is a known HE γ-ray FSRQ blazar. In January 2015 it was detected from HE γ-ray to the near infrared [Pacciani, 2015]. In April 2015 the Fermi Gamma-ray Space Large Area Telescope [Ahnen et al., 2015], detected the source with a

hard spectral index in the HE range. This, together with increased multiwavelength emissions, triggered VHE observations the MAGIC telescope and subsequent VHE detection [Ahnen et al., 2015]. A few days later, VERITAS reported the detection of VHE γ-rays from the putative FSRQ. Follow up observations of this source during April and May 2015 were carried out intensively in many bands.

6.4.2 The April 2015 flare episode

PKS 1441 +25 was detected at VHE energies from MJD 57133 (2015/04/21) to MJD 57140 (2015/04/28) with VERITAS [Abeysekara et al., 2015], which imaged γ-ray induced EAS from the source above 80 GeV. This enabled the centering of PKS 1441 +25 (VER J1443 +250) at a position consistent with its radio location and at a significance of 7.7 σ during the 15.0 hr exposure (2710 ON events, 13780 OFF events, OFF normalization $\frac{1}{6}$ not applied). With a standard Eventdisplay analysis, but with cuts optimized for soft VHE sources, an average flux of I ($>$ 80 GeV) = (5.0$\pm$0.7) x 10^{-11} cm^{-2} s^{-1} was obtained with a spectral index Γ = 5.3$\pm$0.5 up to 0.2 TeV. This corresponds to an intrinsic spectral index of Γ = 3.4$\pm$0.5 after EBL correction [Gilmore et al., 2012]. The continuous 5-day light curve revealed a constant emission during observations (χ^2/N = 7.4/6), with a fractional variability $F_{var} < 110\%$ at the 95% confidence level. The May 2015 observations, from MJD 57155-57166 (with a total of 3.8 hrs), did not reveal an excess, with 660 ON events to 3770 OFF events (Normalisation $\frac{1}{6}$ not applied). This resulted in an upper limit of I ($>$ 80 GeV) $<$ 4.3×10^{-11} cm^{-2} s^{-1} at the 99% confidence level. All results have been cross checked with an independent calibration and analysis package. Monte Carlo simulations calculated that the systematic uncertainties in calorimetry and photon index to be 20% and 0.2 respectively. The systematic uncertainty in the normalised flux for PKS 1441 +23 is $\sim$60%, which includes the energy scale uncertainty discussed in Archambault et al. [2014b].

An intensive multiwavelength analysis of the April 2015 dataset allowed some of the internal structure of PKS 1441 +25 to be determined [Abeysekara et al., 2015]. The source

of the γ-ray emission was within the relativistic jet but far from the SMHB. The emitting region was at least 0.3 parsec away, and most likely at 1.53 parsec distance. Moreover, the region emitting γ-rays was larger than typically seen in an active galaxy, measuring about 0.1 parsec across. This is deduced by radio waves observed contemporaneously, assuming they are emitted far from the black hole. Radio emissions produced in a very dense environments are immediately absorbed; only when the density lowers enough are they able to propagate outward. Of note too was the high radio emission frequency; normally quasars emit at low frequencies and not contemporaneous with the VHE emissions. However the radio fluctuations and γ-rays emission were synchronized. The most likely explanation for the synchronization is a common emission region. One mechanism that could explain this is shock regions; when the stream of particles moves away from the black hole, they collide into stationary regions, creating shock waves. The resulting energy imparted to the local environment from the shock waves may accelerate ionised particles sufficiently for non-thermal emission.

6.4.3 Eventdisplay analysis of April 2015 flaring episode

The April 2015 dataset alone is now subjected to the VERITAS analysis (detailed in Section 3.4.5). Some data was taken in May (officially in VSummer), but no VHE activity was found so this data are not included. Elevated aerosols were monitored during part of the April 2015 flare (as seen in Section 4.8.5), warrenting a re-analysis with WSS16 IRFs. The ext50km IRFs (utilised and verified in Sections 6.3.2 and 6.3.4), can now replace the collaboration official IRFs for comparison with WSS16 IRFs. Table 6.5 list the results of all data runs used and the corresponding aerosol extinction. Due to passing cloud or other telescope related problems, a number of data runs have been truncated to ensure data quality. The run durations are individually listed, resulting in a total of 817.9 min analysed data.

The PKS 1441 +25 dataset was extended over 5 days, with varying aerosol extinction. This offered an opportunity to test the threshold between normal and elevated aerosol loading

IRF	γ-ray ON	γ-ray OFF	σ	$\gamma\,\mathrm{min}^{-1}$	$\pm\gamma\,\mathrm{min}^{-1}$	CR min^{-1}
official	2514	2135.2	7.4	0.463	0.065	2.61
ext50km	2458	2076.3	7.5	0.467	0.065	2.54
WSS16^{str}	2444	2068.5	7.4	0.459	0.065	2.53
WSS16^{lse}	2435	2060.2	7.4	0.458	0.064	2.52

Table 6.4 PKS1441 +25 VERITAS anasum combined analysis. The above table compares the new IRF production sets by means of this soft γ-ray source. The column CR refers to cosmic rays. Refer to Table 6.5 for run by run statistics.

on VERITAS data. A two tier aerosol extinction selection has been used, *stringent* and *loose*. Stringent (stringent adherence to normal / elevated aerosol loading limits) refers to including runs whose aerosol extinction was $\geq$ WSS16 in the elevated aerosols analysis alone. All other runs whose aerosol extinction was $<$ WSS16 were analysed with the normal aerosol extinction IRFs. Loose (loose adherence to normal / elevated aerosol loading limits) refers to including runs whose aerosol extinction was $\geq$ WSS14 (with the error in aerosol extinction encompassing WSS16) in the elevated aerosols analysis. All other runs whose aerosol extinction was $<$ WSS14 were analysed with the normal aerosol extinction IRFs. In summary, data runs that do not qualify for elevated aerosol loading IRFs by either the stringent or loose criteria are analysed with ext50km IRFs. The justification for this test lies in the fact that WSS14 is closer in extinction to WSS16 than to ext50km. Of the 31 runs that entered the analysis, only five will not qualify for analysis with WSS16 IRF simulations under the loose selection criteria. Under stringent selection criteria, just 11 runs would qualify (Table 6.5).

From this data, with no energy binning, it is seen that there is no appreciable difference between the results obtained with the differing IRF sets. This is in keeping with what was found with the Mrk 421 analysis (in Section 6.3.2) where γ/hadron seperation did not seem to respond overly to elevated aerosol extinction correction. These IRFs were produced with optimised γ/hadron cuts for soft VHE γ-ray sources, unlike the analysis for Mrk 421 which used a standard cut set.

run no.	*Elev.*°	min	*WSS*	ON^{50k}	ON^{w16}	OFF^{50k}	OFF^{w16}	σ^{50k}	σ^{w16}	γ^{50k} min^{-1}	γ^{w16} min^{-1}
77384	62	30.12	16	78	80	71.8	71.2	0.7	0.9	0.205±0.32	0.293±0.32
77385	68	30.08	16	118	116	72.8	73.3	4.4	4.2	1.500±0.38	1.418±0.38
77386	74	30.05	16	103	104	82.7	81.0	2.0	2.3	0.667±0.36	0.765±0.36
77387	80	30.05	16	86	83	83.8	83.0	0.2	0.0	0.072±0.33	0.000±0.33
77389	83	30.05	14	127	123	84.2	86.2	4.0	3.4	1.425±0.40	1.226±0.39
77390	79	30.05	14	130	128	90.2	89.8	3.6	3.5	1.326±0.40	1.270±0.40
77391	74	30.03	14	87	86	76.5	75.5	1.1	1.1	0.350±0.33	0.350±0.33
77392	67	22.50	14	78	77	50.8	49.8	3.2	3.3	1.207±0.41	1.207±0.41
77393	61	30.05	14	72	72	66.3	67.0	0.6	0.6	0.189±0.30	0.166±0.30
77403	61	28.55	14	67	68	58.5	57.2	1.0	1.3	0.298±0.31	0.379±0.30
77404	67	30.07	16	87	86	69.8	68.0	1.8	1.9	0.571±0.33	0.599±0.33
77405	74	28.05	16	78	76	75.3	74.5	0.3	0.2	0.095±0.34	0.053±0.34
77406	80	28.55	14	98	100	83.2	82.8	1.5	1.7	0.520±0.37	0.601±0.37
77408	81	30.05	14	112	111	89.3	88.8	2.1	2.1	0.738±0.38	0.738±0.37
77409	77	30.05	14	100	100	82.2	82.0	1.8	1.8	0.593±0.36	0.599±0.36
77410	70	30.07	12	97	—	81.7	—-	1.5	—	0.510±0.36	————
77411	67	06.07	12	17	—	15.5	—-	0.3	—	0.247±0.73	————
77412	61	30.02	12	63	—	70.1	—-	−0.9	—	−0.255±0.29	————
77429	66	30.05	14	99	99	81.3	79.7	1.7	1.9	0.588±0.35	0.643±0.35
77430	60	30.03	14	65	61	69.5	69.2	−0.5	−0.9	−0.150±0.30	−0.272±0.28
77443	61	27.00	16	32	31	35.5	35.5	−0.6	−0.7	−0.130±0.21	−0.167±0.23
77444	65	07.00	16	17	16	11.3	11.3	1.4	1.2	0.810±0.62	0.667±0.60
77445	71	14.00	16	33	33	32.2	31.3	0.1	0.3	0.060±0.44	0.119±0.44
77453	73	15.00	16	53	49	42.2	41.3	1.5	1.1	0.722±0.52	0.511±0.50
77455	61	20.05	16	44	41	41.0	40.2	0.4	0.1	0.015±0.36	0.042±0.34
77467	76	30.05	14	96	94	67.5	66.7	3.0	2.9	0.948±0.35	0.910±0.34
77469	82	30.12	14	105	106	88.5	87.0	1.6	1.8	0.548±0.36	0.631±0.36
77470	79	30.02	14	120	121	91.5	91.0	2.6	2.7	0.949±0.39	0.999±0.39
77473	69	30.03	14	83	84	84.7	83.7	−0.2	0.0	−0.055±0.33	0.011±0.33
77474	63	30.03	12	45	—	50.5	—-	−0.7	—-	−0.275±0.37	————
77505	62	30.03	12	68	—	74.8	—-	−0.7	—-	−0.227±0.30	————

Table 6.5 Analysis table for PKS1441 +25, where ^{50k} is for ext50km IRFs, ^{w16} is for WSS16 IRFs.

IRF	I $(\mathrm{cm}^{-2}\mathrm{s}^{-1}0.1\mathrm{TeV}^{-1})$	Γ	χ^2/N
official	$7.64 \times 10^{-10} \pm 1.16 \times 10^{-10}$	-5.46 ± 0.57	$4.56/3$
ext50km	$8.87 \times 10^{-10} \pm 1.25 \times 10^{-10}$	-5.80 ± 0.53	$6.92/3$
WSS16^{str}	$8.88 \times 10^{-10} \pm 1.26 \times 10^{-10}$	-5.81 ± 0.57	$4.98/3$
WSS16^{lse}	$1.36 \times 10^{-9} \pm 3.31 \times 10^{-10}$	-6.68 ± 1.03	$1.18/2$

Table 6.6 The April 2015 photon flux and spectral index for PKS 1441 +25, presented as $dN/dE = I \times (E/0.1\mathrm{TeV})^{-\Gamma}$, for the three IRF simulation sets. Linear fitting from 0.078 TeV to 0.25 TeV, with 0.1 TeV energy binning and flux normalisation energy of 0.1 TeV.

Referring to Table 6.4, the results of the VERITAS anasum analysis is shown. Note that WSS16^{str} refers to stringent elevated aerosol limits, while WSS16^{lse} to loose. Again the only difference between ext50km and WSS16 IRFs is the aerosol extinction profile used in their production. In conclusion, the anasum combined analysis is dominated by statistics and therefore any possible improvement in spectrum reconstruction by aerosol extinction correction is lost.

6.4.4 SED of PKS 1441 +25 flare

For investigation into whether aerosol extinction correction will impact calorimetry of a soft VHE γ-ray emitter, a spectral analysis is required. Referring to Table 6.4 first, it is noted that there is little difference in excess significance between ext50km and WSS16 IRFs. This can be explained by the weakness of the detection which recorded an excess of just 380, 376 and 375 photons for the official, ext50km and WSS16 IRFs respectively. Referring to Table 6.6, there is little difference between ext50km and WSS16^{str} analysis as regards photon flux, however WSS16^{lse} shows an increase in flux of $\sim 1\sigma$. From Table 6.7 it is noticed that the lowest energy bin, 0.079-0.100 TeV, does not have a $N_{ON}^{w16l}/N_{OFF}^{w16l}/\sigma^{w16l}$ estimate for $WSS16^{lse}$, while the higher energy bins are noticeably higher in N_{ON}^{w16l} and associated columns than the other IRF sets. It could be possible that the γ-ray events from the missing lowest energy bin were raised or 'bumped up' to higher energy bins by excessive aerosol ex-

E_γ TeV	E_{min}-E_{max} TeV	N_{ON}^{of}	N_{ON}^{50k}	N_{OFF}^{of}	N_{OFF}^{50k}	σ^{of}	σ^{50k}
0.089	0.079-0.100	323.0±18.	320.0±18.	1501.0±39.	1472.0±38.	4.1	4.2
0.112	0.100-0.126	668.0±26.	681.0±26.	3097.0±56.	3045.0±55.	5.9	6.7
0.141	0.126-0.158	549.0±23.	537.0±23.	2987.0±55.	2949.0±54.	2.1	1.9
0.178	0.158-0.200	314.0±18.	297.0±17.	1566.0±40.	1492.0±39.	2.9	2.7
0.224	0.200-0.251	132.0±12.	123.0±11.	0790.0±28.	0749.0±27.	0.0	−0.2
E_γ TeV	E_{min}-E_{max} TeV	N_{ON}^{w16s}	N_{ON}^{w16l}	N_{OFF}^{w16s}	N_{OFF}^{w16l}	σ^{w16s}	σ^{w16l}
0.089	0.079-0.100	284.0±17.	–±–	1268.0±36.	–±–	4.4	–
0.112	0.100-0.126	677.0±26.	714.0±27.	3041.0±55.	3226.0±57.	6.6	6.7
0.141	0.126-0.158	561.0±24.	620.0±25.	3096.0±56.	3333.0±58.	1.8	2.5
0.178	0.158-0.200	315.0±18.	348.0±19.	1617.0±40.	1825.0±42.	2.5	2.3
0.224	0.200-0.251	138.0±12.	155.0±12.	0802.0±28.	0869.0±30.	0.3	0.8

Table 6.7 The anasum combined analysis for PKS1441 +25 during April 2015 for the official (top ^{of}), ext50km (top ^{50k}), WSS16stringent (bottom ^{w16s}) and WSS16loose (bottom ^{w16l}) IRF production sets. OFF normalisation has been applied.

tinction correction. Although 5 runs are observed with aerosol extinction WSS12, allowing normal aerosol IRF analysis for the loose criteria, only 1 has appreciable data taken at elevations less than 30° from zenith. Lower elevation dataruns have a higher energy threshold, which will hide changes in analysis results due to aerosol extinction correction. To examine elevated aerosol extinction more closely, a shorter runlist comprising data from WSS16 aerosol loading alone, 11 runs in total, were analysed with ext50km and WSS16 IRFs separately. However, there were insufficient γ-rays to produce a usable spectrum. The $WSS16^{lse}$ analysis set are therefore not to be a part of the PKS 1441 +25 analysis. Presented in Figure 6.11 are four separate SEDs from the official (black), ext50km (red), WSS16stringent (blue, obscured by red) and WSS16loose (green) IRF set analysis. Table 6.5 lists which runs qualify for either WSS16stringent or WSS16loose.

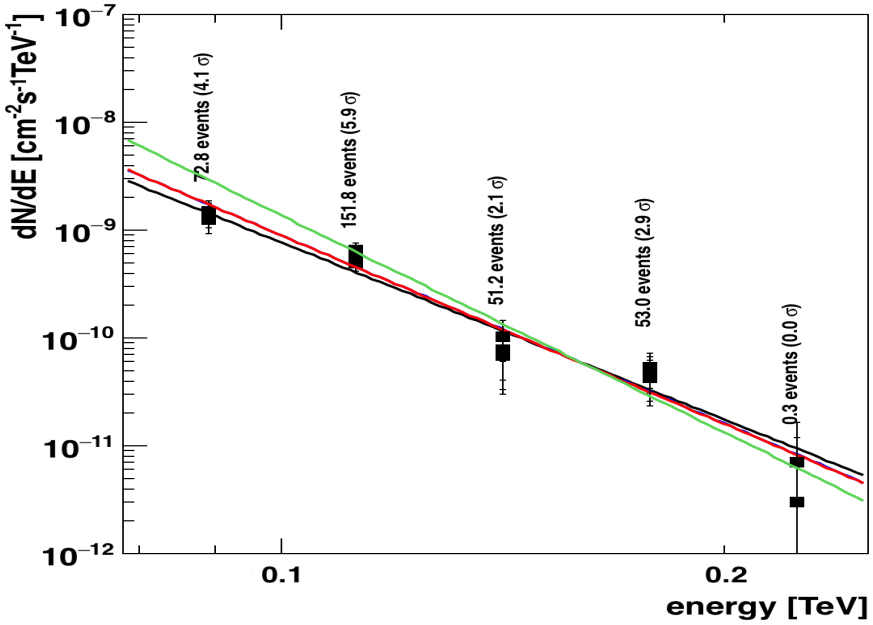

Fig. 6.11 Four power-law fits derived from anasum combined runs listed in Table 6.5 for official (black), ext50km (red), WSS16stringent (blue, obscured by red) and WSS16loose (green) analysis sets. The spectra are produced with the following settings, linear fitting from 0.078 TeV to 0.25 TeV, with 0.1 TeV energy binning and flux normalisation energy of 0.1 TeV.

The spectra are produced with the following settings, linear fitting from 0.078 TeV to 0.25 TeV, with 0.1 TeV energy binning and flux normalisation energy of 0.1 TeV. Referring to Table 6.7, columns (N_{ON}^{50k}) for ext50km ON source, and (N_{ON}^{w16s}) for $WSS16^{str}$ ON source, seem to show a migration of γ-rays events from lower to higher energy bins. In the N_{ON}^{w16s} column, from 0.079-0.100 TeV, the low number of events binned compared to the N_{ON}^{50k} column is offset by the larger number of events binned by N_{ON}^{w16s} from 0.126-0.251 TeV. However, this is not reflected in the overall significance σ, due to the large number of OFF source background γ-rays. The results are therefore inconclusive, owing probably to the

weakness of the detection, $\sim$380 γ-ray photons in $\sim$820 min of data. In conclusion, the aerosol extinction correction for the PKS 1441 +25 data set of April 2015 does not register any changes from the elevated aerosol correction developed in this thesis, due in part at least to low photon statistics. The 5.5 year aerosol loading analysis at VERITAS examined in Section 4.9 shows that periods of elevated aerosol loading are rare, and often do not coincide with times of excessive VHE γ-ray activity.

6.5 Conclusions to current analysis

Having undertaken analysis of two widely-differing extragalactic blazars with the aerosol extinction correction technique developed, the following may be noted. For a strong VHE γ-ray detection (Mrk 421), with minimal errors in spectral index estimation Γ, any hardening caused by lower energy γ-rays being corrected for elevated aerosol extinction is not outside of statistical uncertainties. There is good reason to believe that some low energy γ-rays have been re-binned into higher energy bins; yet above $\sim$250 GeV this correction is not visible due to the pure power law assumptions. It it therefore concluded that with the current generation of IACT a frequently encountered but not excessive aerosol extinction level (WSS16), set as the threshold for elevated aerosol loading (Section 5.4.2), does likely impact on calorimetry at VERITAS, but its effect on VERITAS effective area counter-balances the correction in the case of power law spectra. Should more excessive aerosol extinction (WSS18-WSS20) be present during a period of blazar flaring, the expected hardening in spectral index could be more pronounced. Such very elevated aerosol loadings seldom occur at VERITAS, particularly when VHE γ-ray activity approaching 2-5 c.u. is present. It must be noted that there may be justification for extending the Mrk 421 analysis into the multi-TeV region to examine if the exponential cutoff is impacted upon by aerosol extinction correction. Such an analysis would necessitate the use of other analysis packages of the VERITAS collaboration not introduced in this thesis. This level of VHE γ-ray activity

may be required to produce a spectral index with sufficiently low errors where the aerosol extinction correction would be pronounced. The aerosol extinction correction was expected to have a greater impact on softer spectral index sources than Mrk 421. This remains inconclusive, as the dataset chosen (PKS 1441 +25) was too weak (with fewer than 380 γ-rays detected over more than 820 min of quality-cut data) to allow a definitive conclusion on the validity of elevated aerosol loading correction for the current generation of IACT. Additionally, only $\frac{1}{3}$ of the dataset of PKS 1441 +25 was received during elevated aerosol loading. PKS 1441 +25 was chosen due to it being a soft VHE γ-ray source that afforded a rare opportunity to test aerosol extinction correction on the lower limits of VHE γ-ray energies.
In conclusion, the VHE γ-ray data recorded and analysed with VERITAS since first light in 2007 is not in need of re-analysis due to elevated aerosol loading being present on site at various times.

Chapter 7

Conclusion

7.1 Structuring the final conclusions

The research conclusions follow the thesis Chapters 3 to 6, with the intention of showing the unfolding understanding gained about the atmosphere at VERITAS over time, in particular the proposed impact of aerosol particles on the Cherenkov imaging technique. I have taken the lead in atmospheric monitoring developments and aerosol extinction correction techniques in the VERITAS Collaboration, working, in many instances, from the ground up without prior research to build upon.

7.1.1 Radiometer, Radiosonde and Radiative transfer innovation

A new measurement, the Clear Skies Ratio (CSR), was quantified for a fixed radiometer at VERITAS (Section 3.3) that confirmed (by use of contemporaneous ceilometer data) when no cloud base detections from ground to 13-15 km a.g.l were in the field of view of the radiometer (Section 3.3.1). Above this height, cloud would not impact strongly on Cherenkov light yields from EAS. An examination of 8 years of elevation correction and ambient-temperature correction of the radiometer data showed a seasonal trend of 'warmer skies' or increased infrared radiation in the absence of clouds during VSummer times. The most

probable culprit would be increased water vapour, however part of the increase in radiation could be due to aerosol loading. The radiometers were found to be unsuitable for aerosol optical depth estimation (Section 3.3.2).

Water vapour and its height profile at VERITAS became more prominent due to the work carried out in this thesis. An extensive archival radiosonde dataset from nearby Tucson, Arizona (Section 3.2) was used to make an interpolated Precipitable Water Volume (PWV) lookup table (Section 3.2.2). The Precipitable Water Volume interpolated values were deduced in 10 min bins and time stamped accordingly. Limits were set as to its applicability at VERITAS 60 km away, owing to the volatile nature of the hydrological cycle (Section 4.5.3). The interpolated PWV lookup table proved essential for effective water vapour extinction estimations. These complex extinction estimates are essential for corrections to ceilometer backscattering.

7.1.2 The Vaisala CL51 as aerosol monitor

The ceilometer instrument response and data analysis was undertaken from the ground up for the VERITAS Collaboration by me. Adopting an inter-disciplinary approach, supported by expertise in lidar and ceilometer application from the Centre for Climate and Pollution Studies (C-CAPS) of N.U.I. Galway, a methodology was devised that would allow the ceilometer end-user data to be used for aerosol profiling. The work now described would not have been possible without the support of Dr J. Preißler. As a Vaisala CL51 ceilometer was introduced on site in December 2011 for cloud base detection and ranging, it was chosen as prime candidate for aerosol loading profiling. This decision was made after careful examination of the other atmospheric monitoring instruments on site, the radiometers and the VERITAS telescope array. These instruments could only deliver a value for columnar aerosol optical depth, not a height-resolved aerosol-extinction profile required to examine accurately the nature of aerosol loading at VERITAS. Additionally the aerosol species on site was categoriesd and its lidar ratio deduced, with associated errors, by regional studies

(Sections 3.5.1, 3.7). MODTRAN 5.2 was chosen as the radiative transfer code for all atmospheric simulations. This thesis is the first reported research that uses MODTRAN for ceilometer analysis. The novel methodology required the production of almost 200 particular atmospheric simulations at ceilometer wavelengths, with the closest match to the measured molecular and particulate atmosphere being chosen as the *de facto* working atmosphere.

The attenuated backscatter data was first processed to remove poor data by quality cuts. Several novel quality cuts were developed, tested and implemented (Sections 4.4.1, 4.4.2 and 4.4.3). These included a cut on high infrared sky background noise as measured by an on-board photodiode, increased laser heatsink temperature, high water vapour variability from PWV tables as well as cloud-base height below 6 km a.g.l. In addition an algorithm was developed that removed data with faint passing cloud that did not trigger the on-board cloud-base-height algorithm. Finally a data-loss cut was introduced so that excessive quality cutting would not overly reduce the number of data samples in the 30 min analysis window. Next the attenuated backscattering was corrected for laser heatsink temperature before being averaged spatially and temporally.

The resulting quality cut data blocks, of 1 km and 30 min respectively, were corrected for water vapour extinction. This correction again featured several novelties. A binning for water-vapour profiles, which was used to produce molecular and particular extinction lookup tables, greatly reduced computation time. Also, MODTRAN allowed water vapour extinction, aerosol typologies and their hygroscopic nature to be incorporated with relative ease into a reasonable number of atmospheric simulations ($\sim$200), which dispensed of the need to run a MODTRAN simulation for each individual 30 min time bin ($\geq 3\times10^4$ in total). MODTRAN further easily estimated the molecular backscattering which could then be subtracted from the ceilometer backscattering. The error estimate for aerosol loading profiles was achieved by Monte Carlo methods, which were found to be $\sim$3-5% thanks to the quality cuts, while errors due to PWV estimation were incorporated into the total error

on top of these Monte Carlo errors. With a corrected attenuated-backscatter profile from 1-5 km a.g.l., comparisons could be made with a similar molecular atmosphere having differing aerosol profiles, until a best match was found between the estimated aerosol extinction and the simulated aerosol extinction by least squares.

Close to five years of ceilometer data, from 2011 to 2016, comprising $>1.8 \times 10^7$ unique attenuated backscattering readings, were analysed with the use of ROOT, the data analysis framework of the high energy physics community. It showed that the average desert aerosol content at VERITAS equated to $\sim$WSS13, quite close in extinction to the 50 km visibility tropospheric extinction model in use by the VERITAS Collaboration (Section 4.9). The seasonal aerosol trends, reported in regional studies, were clearly visible and quantifiable over the five years of data (Figure 4.23). An approximate estimation of the upper limit on transmission loss due to elevated aerosol loading was calculated by means of the Beers-Lambert approximation. It was found to be $\leq$0.07 compared to optimal observing during VWinter months. This estimate is assuming a constant Angstrom exponent derived from the Desert Dust aerosol model of MODTRAN, as no means of Angstrom exponent measurement was available on site. The resulting aerosol profiles next need to be binned into 'normal' or 'elevated' aerosol loading for the purpose of detailed VERITAS data analysis. This follows below.

7.1.3 EAS simulation analysis

Previous work in the VERITAS Collaboration brought an improvement to modelling the molecular profiles at VERITAS. These new profiles, named ATM61 and ATM62 (Appendix A.2), were used by me to produce new VERITAS atmospheric extinction profiles (named ATM31 and ATM32) incorporating MODTRAN's Desert Dust extinction profiles (Section 3.6.2). The official collaboration extinction profile, the Tropospheric model with 50 km visibility, was found to be substitutable with Desert Dust WSS10 (Section 5.2.6). WSS04-WSS24 were chosen as a range of new aerosol extinction profiles to best match the con-

ditions at VERITAS, as they offer distinct extinction profiles for progenitor VHE γ-rays EAS Cherenkov light yields (Section 5.2.3). This was found not to be the case with proton progenitor EAS (Section 5.3.1). This research was aided greatly by Dr Gernot Maier, DESY Zeuthen, Germany, and Dr Henrike Fleischhack, Michigan Technological University, U.S.A. My original contribution was the introduction of ATM31 to ATM34 profiles, molecular profiles identical to ATM61 and ATM62 but with Desert Dust aerosol extinction. As times of decreased L3 trigger rate occurred often during times of high water vapour content in the atmosphere, new molecular profiles with twice normal (*2) water vapour content were produced. These profiles were called ATM33, for VWinter *2, and ATM34, for VSummer *2 (Appendix A.2). Corresponding molecular and aerosol extinction profiles were produced, again with Desert Dust WSS04-WSS24. These new atmospheric profiles, with subsequent testing, were my contribution.

Having made accurate estimates of aerosol extinction at VERITAS, the impact of this extinction on EAS propagation was examined. Firstly, for simplicity, mono-energy EAS at fixed zenith angles and idealised flat detectors were utilised; 460 custom EAS simulations were produced with the following variables: progenitor particle (γ-ray or proton), energy (100 GeV to 5 TeV (γ-ray), 100 GeV to 10 TeV (proton)), angle from zenith (00° or 30°) and atmosphere (VSummer and VWinter, normal and twice normal PWV). The following properties of aerosol extinction on EAS Cherenkov photon arrival were observed. Decreasing source elevation from 00° to 30° from zenith reduces the total number of Cherenkov photons arriving by $\frac{1}{3}$ while increasing the mean production height by $\sim$10%, for a given atmosphere and extinction. The reduction in atmospheric transmittance for elevated aerosol loading compared to optimal conditions is $\sim$0.08-0.10, which is consistent for 00° or 30° from zenith. The number of Cherenkov photons arriving within the VERITAS footprint (radius = 100 m from shower core) is energy dependent. It ranges from 72% to 83% of photons arriving within 500 m of shower core for 100 GeV to 5 TeV γ-ray EAS 00° from zenith . Finally, there is little difference in Cherenkov propagation for aerosol extinctions WSS04 to

WSS10, but a non-linear increase thereafter. This results of these simulations are presented in tabular form, being laid out according to progenitor energy, angle from zenith, integration distance, aerosol extinction *etc*. for a comparative study.

High water vapour is often present during VERITAS observing, yet no known study of its impact on the Cherenkov technique had been conducted prior to this thesis. Using ATM31 to ATM34 profiles, for lower energy γ-rays there is no appreciable difference in photon arrival between *1 and *2 equivalent atmospheres. For 5 TeV progenitors there are hints of an excess of photons arriving at the flat detector for both VSummer *1 and VWinter *1 simulations over corresponding *2 simulations. As the increase in Cherenkov photon arrival is close to shower core ($\leq$ 25 m) it is unlikely to be detected strongly in current generation PMTs, due to saturation effects. The photon excess is of the order of 5-6%, but inside the VERITAS footprint the difference rises to 7-9%. The results are inconclusive due to the small number of 5 TeV EAS produced.

The seasonal drop in L3 trigger rate warranted the production of extensive proton EAS. These simulations showed that the mean production height for Cherenkov photons arriving at detector is very close to ground, perhaps $\sim$250-300 m, while protons with energies $<$ 1 TeV will not arrive within the approximate VERITAS footprint (of 100 m radius from shower core) from zenith. As flat detector simulations are not capable of rejecting local muons, as VERITAS stereoscopicity can, it is reasonable to assume that the bulk of the Cherenkov photons arriving at the flat detector from so close to ground may be muons, and hence not impact on the L3 array level triggering of VERITAS. Additionally, there is little difference between extinction profiles WSS04-WSS24, due to the showers lateral development causing most Cherenkov photons produced at heights $\geq$3 km a.s.l. to be lost to detection by Rayleigh scattering principally. Plotting L3 trigger rate quality cut data against the averaged corrected attenuated backscattering from 50-250 m, 0-1 km, and the sum of backscattering from 0-5 km yields a plot where the L3 maximum rate (indicative of optimal VERITAS telescope array performance) and corrected attenuated backscatter appears

to show an anti-correlation. That is, during periods of high aerosol loading the maximum L3 trigger rate is lower that times of lower aerosol loading. However, there are many instances of L3 trigger rates that are lower than this maximum rate for unknown reasons. Thus observed, aerosol extinction likely contributes to lowering L3 trigger rate but other factors, probably instrument related, are also involved.

Volume detector simulations for VERITAS, again for mono-energies and fixed zenith angle, were produced to determine an upper working limit for normal aerosol loading and to determine where new IRFs for elevated aerosol loading may be needed. As aerosol extinction increases, the reduced image size causes the mean reconstruction energy to shift accordingly by a percentage noted with respect to normal aerosol loading, represented by MODTRAN's WSS10. For WSS16, EAS with progenitors $\geq$ 300 GeV on average have their energy reconstruction shifted by $\sim$8%. Notably, this is very similar to the change in atmospheric transmittance for elevated aerosol loading compared to optimal conditions, where a decrease in photon count was of the order of 8-10%. This energy reconstruction shift of $\sim$8% holds for NSB_{uv} = 425 MHz and 750 MHz at 300 GeV. As energy reconstruction depends on image size, which is proportional to the number of Cherenkov photons arriving at telescope, it seems reasonable to relate a drop in photons with a corresponding drop in energy reconstruction. There is a large drop in the number of reconstructed events due to increased aerosol extinction. Though the shift in mean reconstructed energy is of the order of $\sim$8% for a change in aerosol loading from WSS10 to WSS16, the number of reconstructed events (counted within $\pm$100% of the true energy) drops by $\sim$30%. This is due to the increased Cherenkov scatter radius, which also increases the impact parameter. Finally, it was deemed unwise to choose an elevated aerosol threshold of WSS18 or greater, owing to the rarity of such aerosol loading episodes at VERITAS.

7.1.4 Extragalactic source analysis

The exceptional VHE γ-ray flare of Mrk421 in April 2013 was analysed with the standard and new elevated aerosol extinctions. Just one day of optimal data was selected where aerosol extinction levels were elevated at WSS16. This occurred on the day when Mrk 421 episodically reached a record 11 crab units. For the official extinction set, ext50km, the following results was obtained; $I = 6.7\pm0.6\times10^{-10}$ cm^{-2}s^{-1}TeV^{-1}, $\Gamma = -1.75\pm0.06$, $E_o = 1.30\pm0.12$, $\chi^2/NDF = 39.17/33$. For the elevated aerosol extinction set, WSS16, the following results was obtained; $I = 6.8\pm0.6\times10^{-10}$ cm^{-2}s^{-1}TeV^{-1}, $\Gamma = -1.75\pm0.06$, $E_o = 1.45\pm0.14$, $\chi^2/NDF = 42.86/31$. The shift in exponential cutoff, though within systematic uncertainty, is of interest as shifts in spectral features may become visible with aerosol extinction correction, as power law assumptions do not apply. It is noted that from $E_\gamma \geq 237$ GeV the three IRFs produce largely consistent significances in the respective energy bins. However below 237 GeV the WSS16 IRFs show a marked decline in significance σ, which is to be expected as the VHE γ-rays are being rebinned due to the correction applied. The spectral plot deviates slightly from a power-law with exponential cutoff below 237 GeV, but the differences are small. In conclusion, for the powerful VHE γ-ray detection observed no improvement in spectral index estimation was achieved when elevated aerosols IRFs were used.

Finally, a soft VHE γ-ray source was chosen to be analysed in light of discrepancies seen in low energy binning; PKS 1441 +25 data from April 2015 was found suitable. For the official extinction set, ext50km, the following results was obtained; $I = 8.87\times10^{-12}\pm1.25\times10^{-12}$ cm^{-2}s^{-1}TeV^{-1}, $\Gamma = -5.80\pm0.53$, $\chi^2/NDF = 6.92/3$. For the elevated extinction set, WSS16, the following results was obtained; $I = 8.88\times10^{-12}\pm1.26\times10^{-12}$ cm^{-2}s^{-1}TeV^{-1}, $\Gamma = -5.81\pm0.57$, $\chi^2/NDF = 4.98/3$. In conclusion, the aerosol extinction correction for the PKS 1441 +25 data set of April 2015 does not benefit noticeably from the novel elevated aerosol correction developed in this thesis.

7.1.5 Aerosol related systematic uncertainty analysis

Due to the very large amount of atmospheric data produced in this thesis, coupled with detailed VERITAS instrument response functions, an accurate estimate for the systematic uncertainty arising from aerosol extinction has been determined. Analysis of year-on-year aerosol loading shows that, when a systematic uncertainty of $\sim$2% is included for the Angström coefficient (underivable in this thesis) the the overall systematic uncertainty in energy reconstruction arising from not knowing of the presence of elevated aerosol loading is $\sim$5%. This is comparable to the findings of the MAGIC collaboration [Albert et al., 2008]. For the Mrk 421 April 2013 flaring episode, where elevated aerosol loading of WSS16 was measured, the systematic uncertainty in reconstructed energy is of the order of 6-7%. In excessive but rare instances of aerosol loading the systematic uncertainty in reconstructed energy may be of the order of 12-15%.

References

Aab, A. et al. (2016). Evidence for a mixed mass composition at the 'ankle' in the cosmic-ray spectrum. *Physics Letters B*, 762:288 – 295.

Abdalla, H., Abramowski, A., Aharonian, F., Ait Benkhali, F., et al. (2017). The population of TeV pulsar wind nebulae in the H.E.S.S. galactic plane survey. *arXiv preprint arXiv:1702.08280*.

Abdo, A. A. et al. (2011). Fermi Large Area Telescope observations of Mrk 421: The missing piece of its spectral energy distribution. *The Astrophysical Journal*, 736(2):131.

Abeysekara, A., Archambault, S., Archer, A., Benbow, W., et al. (2016). VERITAS and multiwavelength observations of the BL Lacertae object 1ES 1741+ 196. *Monthly Notices of the Royal Astronomical Society*, 459(3):2550–2557.

Abeysekara, A. U., Archambault, S., Archer, A., Aune, T., et al. (2015). γ-rays from the Quasar PKS 1441+25: Story of an escape. *The Astrophysical Journal Letters*, 815(2):L22.

Abeysekara, A. U., Archambault, S., Archer, A., Benbow, W., et al. (2017a). Discovery of VHE emission from RGB J2243+203 and derivation of its redshift upper limit. *The Astrophysical Journal Supplement Series*, 233(1):7.

Abeysekara, A. U., Archambault, S., Archer, A., Benbow, W., et al. (2017b). A luminous and isolated γ-ray flare from the blazar B2 1215+30. *The Astrophysical Journal*, 836(2):205.

Abeysekara, A. U., Archambault, S., Archer, A., Benbow, W., et al. (2017c). A search for spectral hysteresis and energy-dependent time lags from X-ray and TeV γ-ray observations of Mrk 421. *The Astrophysical Journal*, 834(1):2.

Abraham, J., Abreu, P., Aglietta, M., Aguirre, C., et al. (2009). Upper limit on the cosmic-ray photon fraction at EeV energies from the Pierre Auger observatory. *Astroparticle Physics*, 31(6):399–406.

Abreu, P., Aglietta, M., Ahlers, M., Ahn, E., et al. (2012). Description of atmospheric conditions at the Pierre Auger observatory using the global data assimilation system (GDAS). *Astroparticle Physics*, 35(9):591–607.

Acciari, V., Aliu, E., Arlen, T., Aune, T., et al. (2010). The discovery of γ-ray emission from the blazar RGB J0710+ 591. *The Astrophysical Journal Letters*, 715(1):L49.

Acciari, V., Aliu, E., Arlen, T., Aune, T., et al. (2011a). VERITAS observations of γ-ray bursts detected by Swift. *The Astrophysical Journal*, 743(1):62.

Acciari, V., Aliu, E., Arlen, T., Aune, T., et al. (2011b). VERITAS observations of the TeV binary LS i+ 61{*circ* 303 during 2008-2010. *The Astrophysical Journal*, 738(1):3.

Acciari, V., Arlen, T., Aune, T., Benbow, W., et al. (2014). Observation of Mrk 421 in TeV γ-rays over a 14-year time span. *Astroparticle Physics*, 54:1–10.

Ackerman, S. (1997). Remote sensing aerosols using satellite infrared observations. *Journal of Geophysical Research: Atmospheres*, 102(D14):17069–17079.

Aharonian, F., Akhperjanian, A., Beilicke, M., Bernlöhr, K., et al. (2004). The Crab Nebula and pulsar between 500 GeV and 80 TeV: observations with the HEGRA stereoscopic air Cerenkov telescopes. *The Astrophysical Journal*, 614(2):897.

Aharonian, F., Buckley, J., Kifune, T., and Sinnis, G. (2008). High energy astrophysics with ground-based γ-ray detectors. *Reports on Progress in Physics*, 71(9):096901.

Ahnen, M., Ansoldi, S., Antonelli, L., Antoranz, P., et al. (2015). Very high energy γ-rays from the universe's middle age: Detection of the z = 0.940 blazar PKS 1441+25 with MAGIC. *Astrophysical Journal, Letters*, 815:L23.

Ahnen, M. L., Ansoldi, S., Antonelli, L. A., et al. (2016). Detection of VHE γ-ray emission from the gravitationally lensed blazar QSO B0218+357 with the MAGIC telescopes. *Astronomy & Astrophysics*, 595:A98.

Albert, J., Aliu, E., Anderhub, H., Antoranz, P., et al. (2008). Vhe γ-ray observation of the Crab Nebula and its Pulsar with the MAGIC telescope. *The Astrophysical Journal*, 674(2):1037.

Aleksić, J., Ansoldi, S., Antonelli, L., Antoranz, P., et al. (2016). The major upgrade of the MAGIC telescopes, part ii: A performance study using observations of the Crab Nebula. *Astroparticle Physics*, 72:76–94.

Aliu, E., Archambault, S., Archer, A., Aune, et al. (2015a). A search for pulsations from Geminga above 100 GeV with VERITAS. *The Astrophysical Journal*, 800(1):61.

Aliu, E., Archambault, S., Archer, A., Benbow, W., et al. (2016). A search for VHE γ-rays from the missing link binary pulsar J1023+0038 with VERITAS. *The Astrophysical Journal*, 831(2):193.

Aliu, E., Archambault, S., Arlen, T., Aune, T., et al. (2012a). Discovery of HE and VHE γ-ray emission from the blazar RBS 0413. *The Astrophysical Journal*, 750(2):94.

Aliu, E., Archambault, S., Arlen, T., Aune, T., et al. (2012b). Multiwavelength observations of the AGN 1ES 0414+ 009 with VERITAS, Fermi-LAT, SWIFT-XRT, and MDM. *The Astrophysical Journal*, 755(2):118.

Aliu, E., Archambault, S., Arlen, T., Aune, T., et al. (2012c). Search for a correlation between VHE γ-rays and giant radio pulses in the Crab pulsar. *The Astrophysical Journal*, 760(2):136.

Aliu, E., Archambault, S., Arlen, T., Aune, T., et al. (2012d). VERITAS observations of six bright, hard-spectrum Fermi-LAT blazars. *The Astrophysical Journal*, 759(2):102.

Aliu, E., Archambault, S., Arlen, T., Aune, T., et al. (2012e). VERITAS observations of the Nova in V407 Cygni. *The Astrophysical Journal*, 754(1):77.

Aliu, E., Archambault, S., Arlen, T., Aune, T., et al. (2013a). Discovery of TeV γ-ray emission toward SNR G78. 2+ 2.1. *The Astrophysical Journal*, 770(2):93.

Aliu, E., Archambault, S., Arlen, T., Aune, T., et al. (2013b). Discovery of TeV γ-ray emissions from CTA 1 by VERITAS. *The Astrophysical Journal*, 764(1):38.

Aliu, E., Archambault, S., Arlen, T., Aune, T., et al. (2013c). Multiwavelength observations and modeling of 1ES 1959+ 650 in a low flux state. *The Astrophysical Journal*, 775(1):3.

Aliu, E., Archambault, S., Arlen, T., Aune, T., et al. (2014a). A three-year multi-wavelength study of the VHE γ-ray blazar 1ES 0229+ 200. *The Astrophysical Journal*, 782(1):13.

Aliu, E., Archambault, S., Aune, T., Behera, B., et al. (2013d). Long-term TeV and x-ray observations of the γ-ray binary H.E.S.S. J0632+ 057. *The Astrophysical Journal*, 780(2):168.

Aliu, E., Archambault, S., Aune, T., Behera, B., et al. (2014b). Investigating the TeV morphology of MGRO J1908+ 06 with VERITAS. *The Astrophysical Journal*, 787(2):166.

Aliu, E., Archambault, S., Aune, T., Benbow, W., et al. (2013e). A search for enhanced VHE γ-ray emission from the march 2013 Crab Nebula flare. *The Astrophysical Journal Letters*, 781(1):L11.

Aliu, E., Archambault, S., Behera, B., Berger, K., et al. (2013f). Multiwavelength observations of the TeV binary LS I+ 61° 303 with VERITAS, Fermi-LAT, and swift-XRT during a TeV outburst. *The Astrophysical Journal*, 779(1):88.

Aliu, E., Archer, A., Aune, T., Barnacka, A., et al. (2015b). VERITAS observations of the BL Lac object PG 1553+ 113. *The Astrophysical Journal*, 799(1):7.

Aliu, E., Arlen, T., Aune, T., Beilicke, M., et al. (2011a). Detection of pulsed γ-rays above 100 GeV from the Crab pulsar. *Science*, 334(6052):69–72.

Aliu, E., Arlen, T., Aune, T., Beilicke, M., et al. (2011b). VERITAS observations of the unusual extragalactic transient swift J164449. 3+ 573451. *The Astrophysical Journal Letters*, 738(2):L30.

Aliu, E., Arlen, T., Aune, T., Beilicke, M., et al. (2012f). VERITAS observations of day-scale flaring of M 87 in 2010 april. *The Astrophysical Journal*, 746(2):141.

Aliu, E., Aune, T., Behera, B., Beilicke, M., Benbow, W., et al. (2014c). Spatially resolving the VHE emission from MGRO J2019+37 with VERITAS. *The Astrophysical Journal*, 788(1):78.

Aliu, E., Aune, T., Behera, B., Beilicke, M., et al. (2014d). Observations of the unidentified γ-ray source TeV J2032+ 4130 by VERITAS. *The Astrophysical Journal*, 783(1):16.

Aliu, E., Aune, T., Beilicke, M., Benbow, W., et al. (2011c). Multiwavelength observations of the previously unidentified blazar RX J0648. 7+ 1516. *The Astrophysical Journal*, 742(2):127.

Allen, C., Archambault, S., Archer, A., Benbow, W., et al. (2017). VHE γ-ray observations of the blazar 1ES 2344+514 with VERITAS. *Monthly Notices of the Royal Astronomical Society*, 471(2):2117–2123.

Andreae, M. and Gelencsér, A. (2006). Black carbon or brown carbon? the nature of light-absorbing carbonaceous aerosols. *Atmospheric Chemistry and Physics*, 6(10):3131–3148.

Ångström, A. (1961). Techniques of determinig the turbidity of the atmosphere. *Tellus*, 13(2):214–223.

Ansmann, A., Riebesell, M., and Weitkamp, C. (1990). Measurement of atmospheric aerosol extinction profiles with a Raman lidar. *Optics letters*, 15(13):746–748.

Archambault, S., Archer, A., Aune, T., Barnacka, A., et al. (2016a). Exceptionally bright TeV flares from the binary LS I+ 61° 303. *The Astrophysical Journal Letters*, 817(1):L7.

Archambault, S., Archer, A., Barnacka, A., Behera, B., et al. (2016b). Discovery of very high energy gamma rays from 1es 1440+ 122. *Monthly Notices of the Royal Astronomical Society*, 461(1):202–208.

Archambault, S., Archer, A., Beilicke, M., Benbow, W., et al. (2015). VERITAS detection of γ-ray flaring activity from the BL Lac object 1ES 1727+ 502 during bright moonlight observations. *The Astrophysical Journal*, 808(2):110.

Archambault, S., Archer, A., Benbow, W., Bird, R., et al. (2016c). Upper limits from five years of blazar observations with the veritas cherenkov telescopes. *The Astronomical Journal*, 151(6):142.

Archambault, S., Archer, A., Benbow, W., Bird, R., et al. (2017a). Dark matter constraints from a joint analysis of dwarf Spheroidal galaxy observations with VERITAS. *Physical Review D*, 95(8):082001.

Archambault, S., Archer, A., Benbow, W., Bird, R., et al. (2017b). Gamma-ray observations of tycho's supernova remnant with veritas and fermi. *The Astrophysical Journal*, 836(1):23.

Archambault, S., Archer, A., Benbow, W., Bird, R., et al. (2017c). γ-ray observations under bright moonlight with VERITAS. *Astroparticle Physics*, 91:34–43.

Archambault, S., Archer, A., Benbow, W., Buchovecky, M., et al. (2017d). Search for magnetically broadened cascade emission from blazars with VERITAS. *The Astrophysical Journal*, 835(2):288.

Archambault, S., Arlen, T., Aune, T., Behera, B., et al. (2013a). Discovery of a new TeV gamma-ray source: Ver J0521+ 211. *The Astrophysical Journal*, 776(2):69.

Archambault, S., Aune, T., Behera, B., Beilicke, M., et al. (2014a). Deep broadband observations of the distant γ-ray blazar PKS 1424+ 240. *The Astrophysical Journal Letters*, 785(1):L16.

Archambault, S., Beilicke, M., Benbow, W., Berger, K., et al. (2013b). VERITAS observations of the microquasar Cygnus X-3. *The Astrophysical Journal*, 779(2):150.

Archambault, S. et al. (2014b). Deep broadband observations of the distant γ-ray blazar PKS 1424+ 240. *The Astrophysical Journal Letters*, 785(1):L16.

Archambault, S., Hanna, D., and Griffin, S. (2013). In-situ measurements of whole-dish reflectivity for VERITAS. *ArXiv e-prints*.

Archer, A., Barnacka, A., Beilicke, M., Benbow, W., et al. (2014). VHE observations of the Galactic Center Region by VERITAS in 2010-2012. *The Astrophysical Journal*, 790(2):149.

Archer, A., Benbow, W., Bird, R., Bourbeau, E., et al. (2016a). VHE observations of the binaries V 404 Cyg and 4U 0115+ 634 during giant x-ray outbursts. *The Astrophysical Journal*, 831(1):113.

Archer, A., Benbow, W., Bird, R., Buchovecky, M., et al. (2016b). Tev gamma-ray observations of the galactic center ridge by veritas. *The Astrophysical Journal*, 821(2):129.

Arlen, T., Aune, T., Beilicke, M., Benbow, W., et al. (2012). Rapid TeV γ-ray flaring of BL Lacertae. *The Astrophysical Journal*, 762(2):92.

Axford, W. (1962). The interaction between the solar wind and the earth's magnetosphere. *Journal of Geophysical Research*, 67(10):3791–3796.

Aye, K., Chadwick, P., Daniel, M., McComb, T., et al. (2001). Atmospheric sensing for ground-based γ-ray telescopes. In *Proceedings of ICRC*, volume 2001.

Balokovic, M. et al. (2016). Multiwavelength study of quiescent states of Mrk 421 with unprecedented hard x-ray coverage provided by NuSTAR in 2013. *The Astrophysical Journal*, 819(2):156.

Balokovic, M., Furniss, A., Madejski, G., and Harrison, F. (2013). NuSTAR detects extreme X-ray flaring of Mrk 421. *The Astronomer's Telegram*, 4974.

Baloković, M., Paneque, D., Madejski, G., Furniss, A., et al. (2016). Multiwavelength study of quiescent states of Mrk 421 with unprecedented hard x-ray coverage provided by NuSTAR in 2013. *The Astrophysical Journal*, 819(2):156.

Barducci, A., Guzzi, D., Marcoionni, P., and Pippi, I. (2004). Algorithm for the retrieval of columnar water vapor from hyperspectral remotely sensed data. *Applied Optics*, 43(29):5552–5563.

Barnacka, A., Geller, M. J., Dell'Antonio, I. P., and Zitrin, A. (2016). The structure of the strongly lensed γ-ray source B2 0218+35. *The Astrophysical Journal*, 821(1):58.

Beall, J. H. and Bednarek, W. (1999). On the hadronic beam model for γ-ray production in blazars. *The Astrophysical Journal*, 510(1):188.

Beckmann, V. and Shrader, C. R. (2013). The AGN phenomenon: open issues. *arXiv preprint*, ARXIV:1302.1397;.

Berhlohr, K. (2008). Simulation of imaging atmospheric cherenkov telescopes with CORSIKA and sim-telarray. *Astroparticle Physics*, 30(3):149–158.

Beringer, J., Arguin, J.-F., Barnett, R., Copic, K., et al. (2012). Review of particle physics particle data group. *Physical Review D (Particles, Fields, Gravitation and Cosmology)*, 86(1).

Berk, A., Bernstein, L. S., Anderson, G. P., Acharya, P. K., et al. (1998). MODTRAN: A moderate resolution model for LOWTRAN7. *Remote Sensing Environment*, 65(1):367–375.

Berk, A., Bernstein, L. S., and Robertson, D. C. (1989). MODTRAN: A moderate resolution model for LOWTRAN7. *Air Force Geophysical Laboratory*, Rep. GL-TR-89-0122(1).

Bernath, P. F. (2002). The spectroscopy of water vapour: Experiment, theory and applications. *Phys. Chem. Chem. Phys.*, 4:1501–1509.

Bernlöhr, K. (2000). Impact of atmospheric parameters on the atmospheric Cherenkov technique. *Astroparticle Physics*, 12(4):255–268.

Bird, R. (2015). *Probing Cosmic Rays with VERITAS: Observations of M 31 and the Positron Fraction*. UCD theses. UCD University Library.

Blandford, R. and Königl, A. (1979). Relativistic jets as compact radio sources. *The Astrophysical Journal*, 232:34–48.

Blandford, R. D. and Znajek, R. L. (1977). Electromagnetic extraction of energy from Kerr black holes. *Monthly Notices of the Royal Astronomical Society*, 179(3):433–456.

Bouguer, P. (1729). *Essai d'optique sur la gradation de la lumière*. Jombert.

Bucholtz, A. (1995). Rayleigh-scattering calculations for the terrestrial atmosphere. *Applied Optics*, 34(15):2765–2773.

Burton, S. P., Ferrare, R. A., Hostetler, C. A., Hair, J. W., et al. (2012). Aerosol classification using airborne High Spectral Resolution lidar measurements, a methodology and examples. *Atmospheric Measurement Techniques*, 5(1):73–98.

Capdevielle, J. and Gawin, J. (1982). The radial electron distribution in extensive air showers. *Journal of Physics G: Nuclear Physics*, 8(9):1317.

Chandrasekhar, S. (1960). Radiative transfer. *Dover Publications Inc.*, 1(1):393.

Chen, B., Huang, J., Minnis, P., Hu, Y., et al. (2010). Detection of dust aerosol by combining CALIPSO active lidar and passive IR measurements. *Atmospheric Chemistry and Physics*, 10(9):4241–4251.

Chin, M., Diehl, T., Ginoux, P., and Malm, W. (2007). Intercontinental transport of pollution and dust aerosols: implications for regional air quality. *Atmospheric Chemistry and Physics*, 7(21):5501–5517.

Cocconi, G. (1959). *Proc. 6th ICRC, Moscow*, 1(2):309–.

Cotton, E. S. and Davies, J. M. (1961). Solar furnace. US Patent 2,987,961.

Csavina, J., Landázuri, A., Wonaschütz, A., Rine, K., et al. (2011). Metal and Metalloid contaminants in atmospheric aerosols from mining operations. *Water, Air, & Soil Pollution*, 221(1):145–157.

Daniel, M. (2007). The VERITAS standard data analysis. *arXiv preprint arXiv:0709.4006*.

Daniel, M. (2008). Application of radiosonde data to VERITAS simulations. In *Proc. 30th International Cosmic Ray Conference, Mérida*, volume 3, pages 1329–1332. Citeseer.

Daniel, M., Consortium, C., et al. (2015). The atmospheric monitoring strategy for the Cherenkov Telescope Array. In *Journal of Physics: Conference Series*, volume 595, page 012009. IOP Publishing.

Davies, J. M. and Cotton, E. S. (1957). Design of the quartermaster solar furnace. *Solar Energy*, 1(2–3):16 – 22. The Proceedings of the Solar Furnace Symposium.

De Angelis, A., Galanti, G., and Roncadelli, M. (2013). Transparency of the Universe to γ-rays. *Monthly Notices of the Royal Astronomical Society*, 432:3245–3249.

De Tomasi, F., Tafuro, A., and Perrone, M. (2006). Height and seasonal dependence of aerosol optical properties over southeast Italy. *Journal of Geophysical Research: Atmospheres*, 111(D10).

Denney, K., Peterson, B. M., Pogge, R., Adair, A., et al. (2009). Diverse kinematic signatures from reverberation mapping of the broad-line region in AGNs. *The Astrophysical Journal Letters*, 704(2):L80.

Dermer, C. D. (1995). On the Beaming Statistics of γ-Ray Sources. *Astrophysical Journal*, 446:L63.

DeYoung, T., collaboration, H., et al. (2012). The HAWC observatory. *Nuclear Instruments and Methods in Physics Research Section A: Accelerators, Spectrometers, Detectors and Associated Equipment*, 692:72–76.

Di Biagio, C., Boucher, H., Caquineau, S., Chevaillier, S., et al. (2014). Variability of the infrared complex refractive index of African mineral dust: experimental estimation and implications for radiative transfer and satellite remote sensing. *Atmospheric Chemistry and Physics*, 14(20):11093–11116.

Djemil, T., Attallah, R., and Capdevielle, J. (2005). Simulation of the atmospheric muon flux with CORSIKA. *International Journal of Modern Physics A*, 20(29):6950–6952.

Doll, P., Engler, J., Gils, H., Heck, D., et al. (1990). The Karlsruhe cosmic ray project KASCADE. *Verh. Dtsch. Phys. Ges.*, 25(5):1388.

Donea, A.-C. and Protheroe, R. J. (2003). γ-rays from the quasar PKS 1441+25: Story of an escape. *Astroparticle Physics*, 18(4):377–393.

Donoso, E., Li, C., Kauffmann, G., Best, P. N., and Heckman, T. M. (2010). Clustering of radio galaxies and quasars. *Monthly Notices of the Royal Astronomical Society*, 407(2):1078–1089.

Dorner, D., Nilsson, K., and Bretz, T. (2009). A method to correct IACT data for atmospheric absorption due to the Saharan air layer. *Astronomy & Astrophysics*, 493(2):721–725.

Dubovik, O., Holben, B., Eck, T. F., Smirnov, A., et al. (2002). Variability of absorption and optical properties of key aerosol types observed in worldwide locations. *Journal of the atmospheric sciences*, 59(3):590–608.

Durre, I., Vose, R. S., and Wuertz, D. B. (2006). Overview of the Integrated Global Radiosonde Archive. *Journal of Climate*, 19(1):53–68.

Dwek, E. and Krennrich, F. (2013). The extragalactic background light and the γ-ray opacity of the universe. *Astroparticle Physics*, 43:112–133.

Eck, T., Holben, B., Reid, J., Dubovik, O., et al. (1999). Wavelength dependence of the optical depth of biomass burning, urban, and desert dust aerosols. *Journal of Geophysical Research: Atmospheres*, 104(D24):31333–31349.

Elterman, L. (1968). UV, visible and IR attenuation for altitudes to 50 km, 1968. *Environmental research papers no. 285*, page 56.

Falomo, R., Pian, E., and Treves, A. (2014). An optical view of BL Lacertae objects. *The Astronomy and Astrophysics Review*, 22(1):1–38.

Fanaroff, B. and Riley, J. (1974). The morphology of extragalactic radio sources of high and low luminosity. *Monthly notice of Royal Astronomical society*, 167:31–36.

Fazio, G., Helmken, H., O'Mongain, E., and Weekes, T. (1972). Detection of HE γ-rays from the Crab Nebula. *The Astrophysical Journal*, 175:L117.

Fernald, F. G., Herman, B. M., and Reagan, J. A. (1972). Determination of aerosol height distributions by lidar. *Journal of Applied meteorology*, 11(3):482–489.

Feynman, R. P., Leighton, R. B., and Sands, M. (1965). The Feynman lectures on physics; vol. i. *American Journal of Physics*, 33(9):750–752.

Flentje, H., Claude, H., Elste, T., Gilge, S., et al. (2010). The Eyjafjallajökull eruption in April 2010-detection of volcanic plume using in-situ measurements, ozone sondes and lidar-ceilometer profiles. *Atmospheric Chemistry and Physics*, 10(20):10085–10092.

Fortson, L., Collaboration, V., and Collaborators, F. (2012). Results from VERITAS observations on the giant flare from Mrk 421 in February 2010. *AIP Conference Proceedings*, 1505(1):514–517.

Frank, I. and Tamm, I. (1937). Coherent visible radiation from fast electrons passing through matter. *CR Acad. Sci. USSR*, 14:109–114.

Friedlander, S. and Wang, C. (1966). The self-preserving particle size distribution for coagulation by Brownian motion. *Journal of Colloid and interface Science*, 22(2):126–132.

Fruck, C. and Gaug, M. (2015). Atmospheric monitoring in MAGIC and data corrections. In *EPJ Web of Conferences*, volume 89, page 02003. EDP Sciences.

Fruck, C., Gaug, M., Zanin, R., Dorner, D., et al. (2014). A novel lidar-based atmospheric calibration method for improving the data analysis of MAGIC. *arXiv preprint arXiv:1403.3591*.

Furniss, A., Noda, K., Boggs, S., Chiang, J., et al. (2015). First NuSTAR observations of Mrk 501 within a radio to TeV multi-instrument campaign. *The Astrophysical Journal*, 812(1):65.

Galbraith, W. and Jelley, J. (1953). Light pulses from the night sky associated with cosmic rays. *Nature*, 171:349–350.

Gilmore, R. C., Somerville, R. S., Primack, J. R., and Domínguez, A. (2012). Semi-analytic modelling of the extragalactic background light and consequences for extragalactic γ-ray spectra. *Monthly Notices of the Royal Astronomical Society*, 422:3189–3207.

Goyer, G.G., W. R. (1963). The laser and its application to Meteorology. *Bulletin of the American Meteorological Society*, 44(9):564–575.

Grieder, P. K. (2010). *Extensive Air Showers*, volume 1. Springer.

Griffin, S. (2011). *VERy TRenDy: The VERITAS Transient Detector*. McGill theses. McGill University Library.

Guenette, R. (2010). *VERITAS Observations of Galactic Compact Objects*. McGill theses. McGill University Library.

Hahn, D. W. (2006). Light scattering theory. *Department of Mechanical and Aerospace Engineering, Florida*.

Hahn, J. and De los Reyes, R. (2015). Atmospheric monitoring in H.E.S.S. In *EPJ Web of Conferences*, volume 89, page 02002. EDP Sciences.

Hahn, J., De los Reyes, R., Bernlöhr, K., Krüger, P., et al. (2014). Impact of aerosols and adverse atmospheric conditions on the data quality for spectral analysis of the H.E.S.S. telescopes. *Astroparticle Physics*, 54:25–32.

Hanna, D., McCann, A., McCutcheon, M., and Nikkinen, L. (2010). An LED-based flasher system for VERITAS. *Nuclear Instruments and Methods in Physics Research Section A: Accelerators, Spectrometers, Detectors and Associated Equipment*, 612(2):278–287.

Heck, D. (2005). Introduction to CORSIKA and historical review. *VIHKOS CORSIKA School, Lauterbad, Germany*.

Heck, D., Schatz, G., Knapp, J., Thouw, T., and Capdevielle, J. (1998). CORSIKA: A Monte Carlo code to simulate extensive air showers. Technical report.

Heese, B., Flentje, H., Althausen, D., Ansmann, A., and Frey, S. (2010). Ceilometer lidar comparison: backscatter coefficient retrieval and signal-to-noise ratio determination. *Atmospheric Measurement Techniques*, 3(6):1763–1770.

Henyey, L. G. and Greenstein, J. L. (1941). Diffuse radiation in the Galaxy. *Astrophysical Journal*, 93:70–83.

Hess, V. (1936). The nobel prize in physics 1936. *The Nobel Foundation*.

Hess, V. F. (1912). Observations of the penetrating radiation on seven balloon flights. *Physik. Zeitschr*, 13:1084–1091.

Hillas, A. M. (1985). Cerenkov light images of EAS produced by primary γ-rays. In *International Cosmic Ray Conference*, volume 3.

Holben, B., Tanre, D., Smirnov, A., Eck, T., et al. (2001). An emerging ground-based aerosol climatology: Aerosol optical depth from AERONET. *Journal of Geophysical Research: Atmospheres*, 106(D11):12067–12097.

Holben, B. N., Eck, T., Slutsker, I., et al. (1998). AERONET—a federated instrument network and data archive for aerosol characterization. *Remote sensing of environment*, 66(1):1–16.

Holder, J. (2005). Exploiting VERITAS Timing Information. *International Cosmic Ray Conference*, 5:383.

Holder, J. (2015). Atmospheric Cherenkov γ-ray Telescopes. *ArXiv e-prints*.

Holder, J., Atkins, R., Badran, H., Blaylock, G., et al. (2006a). The first VERITAS telescope. *Astroparticle Physics*, 25(6):391–401.

Holder, J. et al. (2006b). The first {VERITAS} telescope. *Astroparticle Physics*, 25(6):391 – 401.

Holder, J. et al. (2015). VERITAS: HAWC's Neighbour to the North. *ArXiv e-prints*.

Huang, J. and McElroy, M. B. (2014). Contributions of the Hadley and Ferrel Circulations to the energetics of the atmosphere over the past 32 years. *Journal of Climate*, 27(7):2656–2666.

Humensky, T. B. f. (2005). Calibration of VERITAS Telescope 1 via Muons. *Proc.29th International Cosmic Ray Conference, Pune*.

IceCube, Aartsen, M. G., Ackermann, M., Adams, J., Aguilar, J. A., et al. (2017). Multi-wavelength follow-up of a rare IceCube neutrino multiplet. *Astronomy & Astrophysics*, 607:A115.

Kellermann, K. I., Kovalev, Y. Y., Lister, M. L., Homan, D. C., et al. (2007). Doppler boosting, superluminal motion, and the kinematics of AGN jets. *Astrophysics and Space Science*, 311(1):231–239.

Kieda, D. et al. (2013). The γ-ray detection sensitivity of the upgraded VERITAS observatory. *Proceedings of the 33rd International Cosmic Ray Conference (ICRC2013),Rio de Janiero, Brazil*.

Kildea, J., Atkins, R., Badran, H., Blaylock, G., et al. (2007). The Whipple observatory 10m γ-ray telescope, 1997-2006. *Astroparticle Physics*, 28(2):182–195.

Klages, H., Apel, W., Bekk, K., Bollmann, E., et al. (1997). The KASCADE experiment. *Nuclear Physics B-Proceedings Supplements*, 52(3):92–102.

Klett, Witwe, E., Detleffsen, Peter, C., et al. (1760). *IH Lambert... Photometria sive de mensura et gradibus luminis, colorum et umbrae*. sumptibus viduae Eberhardi Klett.

Klett, J. D. (1981). Stable analytical inversion solution for processing lidar returns. *Applied Optics*, 20(2):211–220.

Kotthaus, S., O'Connor, E., Münkel, C., Charlton-Perez, C., et al. (2016). Recommendations for processing atmospheric attenuated backscatter profiles from Vaisala CL31 ceilometers. *Atmospheric Measurement Techniques*, 9(8):3769–3791.

Kovalev, V. A. and Eichinger, W. E. (2004). *Elastic lidar: theory, practice, and analysis methods*. John Wiley & Sons.

Krawczynski, H., Carter-Lewis, D., Duke, C., Holder, J., et al. (2006). γ-hadron separation methods for the VERITAS array of four imaging atmospheric cherenkov telescopes. *Astroparticle Physics*, 25(6):380–390.

Krennrich, F. (2009). γ-ray astronomy with atmospheric Cherenkov telescopes: the future. *New Journal of Physics*, 11(11):115008.

Krennrich, F., Badran, H., Bond, I., Bradbury, S., et al. (2001). Cutoff in the TeV energy spectrum of Mrk 421 during strong flares in 2001. *The Astrophysical Journal Letters*, 560(1):L45.

Krennrich, F., Bond, I., Boyle, P., et al. (2004). VERITAS: the Very Energetic Radiation Imaging Telescope Array System. *New Astronomy Reviews*, 48(5):345 – 349. 2nd VERITAS Symposium on the Astrophysics of Extragalactic Sources.

Landt, H., Padovani, P., Perlman, E., and Giommi, P. (2004). A physical classification scheme for blazars. *Monthly Notices of the Royal Astronomical Society*, 351(1):83–100.

Laven, P. (2003). Simulation of rainbows, coronas, and glories by use of Mie theory. *Applied Optics*, 42(3):436–444.

LeBohec, S., Atkins, R., Badran, H., Blaylock, G., et al. (2006). Deployment of the VERITAS observatory. In *Journal of Physics: Conference Series*, volume 47, page 232. IOP Publishing.

Ledlow, M. J. and Owen, F. N. (1996). A 20cm VLA survey of Abell clusters of galaxies vi. radio/optical luminosity functions. *arXiv preprint astro-ph/9607014*.

Li, J., Carlson, B. E., Dubovik, O., and Lacis, A. A. (2014). Recent trends in aerosol optical properties derived from AERONET measurements. *Atmospheric Chemistry and Physics*, 14(22):12271–12289.

Li, J., Torres, D. F., Rea, N., de Oña Wilhelmi, E., et al. (2016). Search for γ-ray emission from AE Aquarii with seven years of Fermi-LAT observations. *Astrophysical Journal*, 832:35.

Li, T.-P. and Ma, Y.-Q. (1983). Analysis methods for results in γ-ray astronomy. *The Astrophysical Journal*, 272:317–324.

Lockwood, M. (2002). An evaluation of the correlation between open solar flux and total solar irradiance. *Astronomy & Astrophysics*, 382(2):678–687.

Longair, M. S. (2011). *High energy astrophysics*. cambridge university Press.

Lorenz, E. and Wagner, R. (2012). VHE γ-ray astronomy. *The European Physical Journal H*, 37(3):459–513.

Lynden-Bell, D. (1989). Galactic nuclei as collapsed old quasars. *Accretion: A Collection of Influential Papers*, 223:98.

Maier, G. (2008). Monte Carlo studies of the VERITAS array of Cherenkov telescopes. *International Cosmic Ray Conference*, 3:1413–1416.

Maraschi, L. and Rovetti, F. (1994). A unified relativistic beaming model for BL Lacertae objects and flat spectrum radio quasars. *The Astrophysical Journal*, 436:79–88.

Marscher, A. P., Jorstad, S. G., Larionov, V. M., Aller, M. F., et al. (2010). Probing the inner jet of the quasar PKS 1510-089 with multi-waveband monitoring during strong γ-ray activity. *The Astrophysical Journal Letters*, 710(2):L126.

Marshall, H., Miller, B., Davis, D., Perlman, E., Wise, M., Canizares, C., and Harris, D. (2002). A high-resolution x-ray image of the jet in M87. *The Astrophysical Journal*, 564(2):683.

Matthews, J. (2005). A Heitler model of extensive air showers. *Astroparticle Physics*, 22(5):387–397.

Mayer, M., Buehler, R., Hays, E., Cheung, C. C., et al. (2013). Rapid γ-ray flux variability during the 2013 march Crab Nebula flare. *The Astrophysical Journal Letters*, 775(2):L37.

McCann, A., Hanna, D., Kildea, J., and McCutcheon, M. (2010). A new mirror alignment system for the VERITAS telescopes. *Astroparticle Physics*, 32(6):325–329.

McClatchey, R. A., Fenn, R., Selby, J. A., Volz, F., and Garing, J. (1972). Optical properties of the atmosphere.

McCormick, M. P. (2005). Airborne and spaceborne lidar. In *Lidar*, pages 355–397. Springer.

McKinney, J. C. (2005). Total and jet Blandford-Znajek power in the presence of an accretion disk. *The Astrophysical Journal Letters*, 630(1):L5.

McKinney, J. C. and Gammie, C. F. (2004). A measurement of the electromagnetic luminosity of a Kerr black hole. *The Astrophysical Journal*, 611(2):977.

McKinney, J. C. and Narayan, R. (2007). Disc–jet coupling in black hole accretion systems–i. general relativistic magnetohydrodynamical models. *Monthly Notices of the Royal Astronomical Society*, 375(2):513–530.

Meyer, M., Horns, D., and Zechlin, H.-S. (2010). The Crab nebula as a standard candle in very high-energy astrophysics. *Astronomy & Astrophysics*, 523:A2.

Michel, L. (1950). Interaction between four half-spin particles and the decay of the μ-meson. *Proceedings of the Physical Society. Section A*, 63(5):514.

Mie, G. (1908). Beiträge zur optik trüber medien, speziell kolloidaler metallösungen. *Annalen der physik*, 330(3):377–445.

Milroy, C., Martucci, G., Lolli, S., Loaec, S., et al. (2011). On the ability of pseudo-operational ground-based light detection and ranging (lidar) sensors to determine boundary-layer structure: intercomparison and comparison with in-situ radiosounding. *Atmospheric Measurement Techniques Discussions*, 4:563–597.

Mishchenko, M. I. and Travis, L. D. (2008). Gustav Mie and the evolving discipline of electromagnetic scattering by particles. *Bulletin of the American Meteorological Society*, 89(12):1853–1861.

Mona, L., Liu, Z., Müller, D., Omar, A., Papayannis, A., et al. (2012). Lidar measurements for desert dust characterization: an overview. *Advances in Meteorology*, 2012.

Morrison, P. (1958). On γ-ray astronomy. *Nuovo Cimento*, 1(7):858–864.

Muller, D., Ansmann, A., Mattis, I., Tesche, M., et al. (2007). Aerosol-type-dependent lidar ratios observed with Raman lidar. *Journal of Geophysical Research: Atmospheres*, 112(D16):n/a–n/a. D16202.

Münkel, C., Eresmaa, N., Räsänen, J., and Karppinen, A. (2007). Retrieval of mixing height and dust concentration with lidar ceilometer. *Boundary-Layer Meteorology*, 124(1):117–128.

Münkel, C. and Roininen, R. (2010). Automatic monitoring of boundary layer structures with ceilometer. *Vaisala News*, 184.

Nee, P. F. (1964). Hourly variability of density at radiosonde height. *Journal of Applied Meteorology*, 3(1):175–178.

Nelson, W. R., Hirayama, H., and Rogers, D. W. (1985). The EGS4 code system, SLAC. *Report Slac-265*.

Nolan, S., Puehlhofer, G., and Rulten, C. (2010). Detailed studies of atmospheric calibration in imaging Cherenkov astronomy. *Astroparticle Physics*, 34(5):304–313.

Okayasu, M. and Fukuda, M. (1992). Estimation of the reliability of 0.98 μm InGaAs/GaAs strained quantum well lasers. *Journal of applied physics*, 72(6):2119–2124.

Omar, A. H., Winker, D. M., Vaughan, M. A., Hu, Y., et al. (2009). The CALIPSO automated aerosol classification and lidar ratio selection algorithm. *Journal of Atmospheric and Oceanic Technology*, 26(10):1994–2014.

Pacciani, L. (2015). Optical, X-ray, γ-ray flare of the FSRQ PKS 1441+25. *The Astronomer's Telegram*, 7402.

Padovani, P. and Giommi, P. (1995). A sample-oriented catalogue of BL Lacertae objects. *Monthly Notices of the Royal Astronomical Society*, 277(4):1477–1490.

Park, K. and Ricotti, M. (2012). Accretion onto black holes from large scales regulated by radiative feedback. ii. growth rate and duty cycle. *The Astrophysical Journal*, 747(1):9.

Park, N. et al. (2016). Performance of the VERITAS experiment. *Proceedings of Science (ICRC2015) 771*, 236.

Penndorf, R. (1957). Tables of the refractive index for standard air and the Rayleigh scattering coefficient for the spectral region between 0.2 and 20.0 μ and their application to atmospheric optics. *Josa*, 47(2):176–182.

Peterson, B. M., Ferrarese, L., Gilbert, K., Kaspi, S., et al. (2004). Central masses and broad-line region sizes of active galactic nuclei. ii. a homogeneous analysis of a large reverberation-mapping database. *The Astrophysical Journal*, 613(2):682.

Pornsawad, P., D'Amico, G., Böckmann, C., Amodeo, A., and Pappalardo, G. (2012). Retrieval of aerosol extinction coefficient profiles from Raman lidar data by inversion method. *Applied Optics*, 51(12):2035–2044.

Prouza, M. et al. (2007). Systematic study of atmosphere-induced influences and uncertainties on shower reconstruction at the pierre auger observatory. *arXiv preprint arXiv:0706.1719*.

Punch, M., Akerlof, C. W., Cawley, M., Chantell, M., et al. (1992). Detection of TeV photons from the active galaxy Mrk 421. *Nature*, 358(6386):477–478.

Quinn, J., Akerlof, C., Biller, S., Buckley, J., et al. (1996). Detection of γ-rays with e > 300 GeV from Mrk 501. *The Astrophysical Journal Letters*, 456(2):L83.

Ramanathan, V., Crutzen, P., Kiehl, J., and Rosenfeld, D. (2001). Aerosols, climate, and the hydrological cycle. *science*, 294(5549):2119–2124.

Ramirez, A., De Diego, J., Dultzin-Hacyan, D., and González-Pérez, J. (2004). Optical variability of PKS 0736+ 017. *Astronomy & Astrophysics*, 421(1):83–89.

Rao, M. and Sreekantan, B. V. (1998). *Extensive air showers*. World scientific.

Rayleigh, L. (1871). On the light from the sky, its polarisation and colour. *Philosophical Magazine*, 1(41):107–120, 274–279.

Rayleigh, L. (1881). X. on the electromagnetic theory of light. *The London, Edinburgh, and Dublin Philosophical Magazine and Journal of Science*, 12(73):81–101.

Rayleigh, L. (1899). XXXIV. on the transmission of light through an atmosphere containing small particles in suspension, and on the origin of the blue of the sky. *The London, Edinburgh, and Dublin Philosophical Magazine and Journal of Science*, 47(287):375–384.

Rebillot, P., Buckley, J., Dowkontt, P., and Kosack, K. (2003). The VERITAS flash ADC electronics system. In *International Cosmic Ray Conference*, volume 5, page 2827.

Roache, E., Irvin, R., Perkins, J., Harris, K., Falcone, A., Finley, J., and WEEKES, T. (2008). Mirror facets for the VERITAS telescopes. In *Proceedings of the 30th International Cosmic Ray Conference*, volume 3, page 1397.

Rodell, M., Houser, P., Jambor, U., Gottschalck, J., et al. (2004). The global land data assimilation system. *Bulletin of the American Meteorological Society*, 85(3):381–394.

Rogers, R. R., Hostetler, C. A., Hair, J. W., Ferrare, R. A., et al. (2011). Assessment of the CALIPSO lidar 532 nm attenuated backscatter calibration using the NASA LaRC airborne High Spectral Resolution Lidar. *Atmospheric Chemistry and Physics*, 11(3):1295–1311.

Rossi, B. and Greisen, K. (1941). Cosmic-ray theory. *Reviews of Modern Physics*, 13(4):240.

Rothman, L. S., GAMACHE, R. R., TIPPING, R. H., RINSLAND, C. P., et al. (1992). MODTRAN: A moderate resolution model for LOWTRAN7. *Journal of Quantitative Spectroscopy and Radiative Transfer*, 48(516):469–507.

Russell, C. (2000). The solar wind interaction with the earth's magnetosphere: a tutorial. *IEEE transactions on plasma science*, 28(6):1818–1830.

Schmitt, J. L. (1968). BL Lac identified as a radio source. *Nature*, 218(5142):663–663.

Shettle, E. P. (1984). Optical and radiative properties of a desert aerosol model. *Proceedings of the Symposiumon Radiation in the Atmosphere*, pages 74–77.

Shettle, E. P. and Fenn, R. W. (1979). Models for the Aerosols of the Lower Atmosphere and the Effects of Humidity Variations on Their Optical Properties. *AFGL-TR-79-0214*.

Singh, A., Siingh, D., and Singh, R. (2011). Impact of galactic cosmic rays on Earth's atmosphere and human health. *Atmospheric Environment*, 45(23):3806 – 3818.

Sobczyńska, D. and Bednarek, W. (2014). Influence of clouds on the parameters of images measured by IACT at very high energies. *Journal of Physics G: Nuclear and Particle Physics*, 41(12):125201.

Sokolov, A. and Marscher, A. P. (2005). External Compton radiation from rapid nonthermal flares in blazars. *The Astrophysical Journal*, 629(1):52.

Sorek-Hamer, M., Cohen, A., Levy, R., Ziv, B., and Broday, D. (2013). Classification of dust days by satellite remotely sensed aerosol products. *International Journal of Remote Sensing*, 34(8):2672–2688.

Sorooshian, A., Wonaschütz, A., Jarjour, E. G., Hashimoto, B. I., et al. (2011). An aerosol climatology for a rapidly growing arid region (southern arizona): Major aerosol species and remotely sensed aerosol properties. *Journal of Geophysical Research: Atmospheres*, 116(D19):n/a–n/a. D19205.

Stecker, F., De Jager, O., and Salamon, M. (1992). TeV γ-rays from 3C 279-a possible probe of origin and intergalactic infrared radiation fields. *The Astrophysical Journal*, 390:L49–L52.

Stein, A., Draxler, R. R., Rolph, G. D., Stunder, B. J., Cohen, M., and Ngan, F. (2015). NOAAs HYSPLIT atmospheric transport and dispersion modeling system. *Bulletin of the American Meteorological Society*, 96(12):2059–2077.

Stone, J. M., Pringle, J. E., and Begelman, M. C. (1999). Hydrodynamical non-radiative accretion flows in two dimensions. *Monthly Notices of the Royal Astronomical Society*, 310(4):1002–1016.

Swordy, S., Fortson, L., Hinton, J., Hörandel, J., et al. (2002). The composition of cosmic rays at the knee. 18(2):129–150.

Tavecchio, F., Becerra-Gonzalez, J., Ghisellini, G., Stamerra, A., et al. (2011). On the origin of the γ-ray emission from the flaring blazar PKS1222+216. *Astronomy & Astrophysics*, 534:A86.

Teillet, P. M. (1990). Rayleigh optical depth comparisons from various sources. *Applied Optics*, 29(13):1897–1900.

Thomson, W. (1888). XLVI. on the reflexion and refraction of light. *The London, Edinburgh, and Dublin Philosophical Magazine and Journal of Science*, 26(162):414–425.

Tsaknakis, G., Papayannis, A., Kokkalis, P., Amiridis, V., et al. (2011). Inter-comparison of lidar and ceilometer retrievals for aerosol and planetary boundary layer profiling over Athens, Greece. *Atmospheric Measurement Techniques*, 4(6):1261–1273.

Ulrich, R., Engel, R., Müller, S., Schüssler, F., and Unger, M. (2009). Proton-air cross section and extensive air showers. *Nuclear Physics B-Proceedings Supplements*, 196:335–340.

Urry, C. and Padovani, P. (1995). Unified Schemes for Radio-Loud Active Galactic Nuclei. *Publications of the Astronomical Society of the Pacific*, 107:803.

Völk, H. J. and Bernlöhr, K. (2009). Imaging very high energy γ-ray telescopes. *Experimental Astronomy*, 25(1-3):173–191.

Wakely, S. and Horan, D. (2008). TeVCat: An online catalog for very high energy γ-ray astronomy. In *International Cosmic Ray Conference*, volume 3, pages 1341–1344.

Weekes, T. C., Cawley, M., Fegan, D., Gibbs, K., et al. (1989). Observation of TeV γ-rays from the Crab Nebula using the atmospheric Cerenkov imaging technique. *The Astrophysical Journal*, 342:379–395.

Weekes, T. C. and Turver, K. (1977). γ-ray astronomy from 10-100 GeV: A new approach. In *Recent Advances in γ-Ray Astronomy*, volume 124.

Weinstein, A. (2008). The VERITAS Trigger System. *International Cosmic Ray Conference*, 3:1539–1542.

Weitkamp, C. (2006). *Lidar: range-resolved optical remote sensing of the atmosphere*, volume 102. Springer Science & Business.

Welton, E. J., Campbell, J. R., Spinhirne, J. D., and Scott III, V. S. (2001). Global monitoring of clouds and aerosols using a network of micropulse lidar systems. In *Second International Asia-Pacific Symposium on Remote Sensing of the Atmosphere, Environment, and Space*, pages 151–158. International Society for Optics and Photonics.

Wenny, B., Schafer, J., DeLuisi, J., Saxena, V., et al. (1998). A study of regional aerosol radiative properties and effects on ultraviolet-B radiation. *Journal of Geophysical Research: Atmospheres*, 103(D14):17083–17097.

Wiegner, M. and Gasteiger, J. (2015). Correction of water vapor absorption for aerosol remote sensing with ceilometers. *Atmospheric Measurement Techniques*, 8(9):3971–3984.

Wiegner, M., Madonna, F., Binietoglou, I., Forkel, R., et al. (2014). What is the benefit of ceilometers for aerosol remote sensing, an answer from EARLINET. *Atmospheric Measurement Techniques*, 7(7):1979–1997.

Winker, D. M., Pelon, J. R., and McCormick, M. P. (2003). The CALIPSO mission: Spaceborne lidar for observation of aerosols and clouds. pages 1–11.

Xie, S.-P. (1998). Ocean–atmosphere interaction in the making of the Walker circulation and equatorial cold tongue. *Journal of climate*, 11(2):189–201.

Yang, P., Feng, Q., Hong, G., Kattawar, G. W., et al. (2007). Modeling of the scattering and radiative properties of nonspherical dust-like aerosols. *Journal of Aerosol Science*, 38(10):995–1014.

Zel'dovich, Y. B. and Novikov, I. (1964). The radiation of gravity waves by bodies moving in the field of a collapsing star. In *Soviet Physics Doklady*, volume 9, page 246.

Zitzer, B. and Collaboration, V. (2012). Upgrade plans for VERITAS. *Physics Procedia*, 37:1365–1372.

Appendix A

MODTRAN Atmospheric Simulations

A.1 Main questions regarding atmospheric simulations

As this work relies heavily on atmospheric simulations, Section A.2 deals with some preliminaries such as radiosonde data analysis, MODTRAN input card generation and atmospheric density / refractive index profile production with MODTRAN. Next, the atmosphere profiles with corresponding extinction profiles used need to be explained, with justifications given for their use. In Section A.3 consideration is given to the many smaller atmospheric profiles produced by MODTRAN for the ceilometer analysis. Questions such as season transition, extinction profile comparison and water vapour content are examined.

It is noted at the outset that the work in Section A.2 is largely due to the efforts of Dr. Henrike Fleischhack, Michigan Technological University, whose support in this thesis is gratefully acknowledged.

A.2 Preparatory work for EAS simulations

Radiosonde data was downloaded from http://badc.nerc.ac.uk/home/index.html. The atmospheric sounding data allows the following atmospheric constituent profiles for the VERITAS site to be determined for the day and time in question.

University of Wyoming – Radiosonde Data

72274 TUS Tucson Observations at 00Z 01 Jun 2016

PRES hPa	HGHT m	TEMP C	DWPT C	RELH %	MIXR g/kg	DRCT deg	SKNT knot	THTA K	THTE K	THTV K
1000.0	23									
925.0	716									
921.0	751	33.0	-6.0	8	2.66	175	5	313.4	322.3	313.9
914.0	820	30.8	-6.2	9	2.64	192	5	311.9	320.6	312.4
904.4	914	29.8	-6.3	9	2.65	215	6	311.8	320.6	312.3
892.0	1037	28.6	-6.4	10	2.67	217	6	311.8	320.6	312.3
873.8	1219	26.9	-7.2	10	2.55	220	6	311.8	320.3	312.3
850.0	1463	24.6	-8.4	11	2.40	310	2	311.9	319.9	312.4
814.3	1829	21.0	-8.6	13	2.47	340	1	312.0	320.2	312.4
785.7	2134	18.1	-8.7	15	2.54	170	4	312.0	320.4	312.4
758.2	2438	15.1	-8.8	18	2.60	330	7	311.9	320.6	312.4
731.6	2743	12.1	-8.9	22	2.67	190	2	311.9	320.7	312.4
722.0	2855	11.0	-9.0	24	2.69	136	2	311.9	320.8	312.4
700.0	3112	8.6	-9.4	27	2.69	10	2	312.0	320.9	312.5
654.5	3658	3.3	-10.2	36	2.69	100	2	312.1	320.9	312.6
630.4	3962	0.4	-10.7	43	2.69	135	1	312.1	320.9	312.6
611.0	4216	-2.1	-11.1	50	2.69	85	11	312.0	320.9	312.5
607.0	4267	-2.6	-11.3	51	2.68	75	13	312.1	320.9	312.6
584.0	4572	-5.3	-12.3	58	2.56	60	12	312.3	320.8	312.8
571.0	4750	-6.9	-12.9	62	2.49	77	11	312.5	320.8	312.9
561.7	4877	-7.9	-14.4	60	2.25	90	11	312.8	320.3	313.2
551.0	5027	-9.1	-16.1	57	1.99	97	11	313.1	319.8	313.4
540.0	5182	-10.6	-16.9	59	1.89	105	12	313.1	319.5	313.5
533.0	5283	-11.5	-17.5	61	1.83	107	12	313.2	319.4	313.5
524.0	5414	-12.7	-19.7	56	1.54	109	13	313.3	318.5	313.6
517.0	5516	-13.5	-23.5	43	1.12	111	13	313.5	317.4	313.7
500.0	5770	-15.5	-29.5	29	0.67	115	14	314.1	316.5	314.2
499.0	5785	-15.7	-29.7	29	0.66	111	13	314.0	316.4	314.1
498.6	5791	-15.7	-30.1	28	0.63	110	12	314.1	316.3	314.2
493.0	5876	-16.1	-36.1	16	0.36	118	11	314.6	315.9	314.7
478.6	6096	-18.0	-37.4	17	0.32	140	10	314.9	316.1	314.9
471.0	6216	-19.1	-38.1	17	0.31	128	15	315.0	316.2	315.1
462.0	6359	-18.7	-42.7	10	0.19	114	20	317.3	318.0	317.3
459.4	6401	-19.0	-42.4	11	0.20	110	22	317.4	318.2	317.4
448.0	6586	-20.3	-41.3	14	0.23	111	21	318.1	318.9	318.1
434.0	6819	-22.3	-38.3	22	0.32	112	20	318.4	319.6	318.5
422.0	7024	-23.9	-30.9	52	0.69	113	20	318.9	321.5	319.1
400.0	7410	-27.5	-33.5	57	0.57	115	18	319.2	321.3	319.3
394.0	7519	-28.5	-34.5	56	0.52	115	17	319.2	321.2	319.3
388.4	7620	-29.2	-36.8	48	0.42	115	17	319.7	321.3	319.8
384.0	7702	-29.7	-38.7	41	0.35	111	17	320.0	321.4	320.1
360.0	8159	-33.3	-43.3	36	0.23	92	17	321.1	322.1	321.2
341.0	8534	-36.6	-44.5	44	0.21	75	17	321.7	322.5	321.7
324.0	8889	-39.7	-45.7	53	0.20	75	18	322.1	322.9	322.2
312.0	9144	-41.9	-47.9	52	0.16	75	18	322.6	323.3	322.7
301.0	9388	-43.9	-49.9	51	0.13	93	16	323.1	323.6	323.1
300.0	9410	-43.9	-49.9	51	0.13	95	16	323.4	323.9	323.4
298.3	9449	-44.2	-50.5	50	0.13	95	14	323.5	324.0	323.5
287.0	9706	-46.1	-54.1	40	0.09	122	12	324.4	324.7	324.4
280.0	9871	-46.7	-63.7	13	0.03	140	12	325.8	325.9	325.8
268.0	10161	-47.9	-66.9	9	0.02	171	10	328.1	328.2	328.1
255.0	10489	-47.5	-70.5	5	0.01	206	8	333.4	333.5	333.4
251.0	10594	-48.3	-71.3	5	0.01	217	7	333.7	333.8	333.8
250.0	10620	-48.1	-71.1	5	0.01	220	7	334.4	334.5	334.4
245.0	10754	-47.7	-71.7	5	0.01	231	6	337.0	337.0	337.0
236.0	11000	-49.5	-72.5	5	0.01	252	4	337.9	337.9	337.9
226.2	11278	-50.3	-73.8	5	0.01	275	1	340.8	340.9	340.8
216.0	11579	-51.1	-75.1	4	0.01	253	9	344.0	344.1	344.0
206.0	11887	-51.4	-77.2	3	0.01	230	17	348.3	348.4	348.3
200.0	12080	-51.5	-78.5	3	0.00	235	15	351.1	351.1	351.1
187.5	12497	-53.7	-80.7	2	0.00	235	16	354.1	354.1	354.1
184.0	12618	-54.3	-81.3	2	0.00	245	19	355.0	355.0	355.0
180.0	12759	-53.1	-81.1	2	0.00	254	20	359.2	359.2	359.2
172.0	13052	-52.1	-83.1	1	0.00	272	21	365.5	365.5	365.5
170.6	13106	-52.5	-83.3	1	0.00	275	21	365.6	365.6	365.6
167.0	13243	-53.7	-83.7	1	0.00	271	21	365.9	366.0	365.9
159.0	13558	-54.1	-85.1	1	0.00	260	20	370.4	370.4	370.4
155.1	13716	-54.8	-85.4	1	0.00	255	19	371.9	371.9	371.9
150.0	13930	-55.7	-85.7	1	0.00	265	23	373.9	373.9	373.9
148.0	14015	-56.1	-86.1	1	0.00	267	23	374.6	374.7	374.6
140.9	14326	-56.4	-86.4	1	0.00	275	22	379.4	379.4	379.4
138.0	14460	-56.5	-86.5	1	0.00	262	22	381.5	381.5	381.5
134.3	14630	-57.7	-86.9	1	0.00	245	22	382.4	382.4	382.4
133.0	14693	-58.1	-87.1	1	0.00	245	23	382.7	382.7	382.7
128.0	14935	-58.3	-87.3	1	0.00	270	27	386.6	386.6	386.6
123.0	15185	-58.5	-87.5	1	0.00	262	28	390.6	390.6	390.6
121.9	15240	-58.6	-87.6	1	0.00	260	28	391.3	391.3	391.3
116.1	15545	-59.5	-88.0	1	0.00	265	30	395.2	395.2	395.2
111.0	15828	-60.3	-88.3	1	0.00	268	25	398.9	398.9	398.9
107.0	16058	-59.3	-88.3	1	0.00	270	22	405.0	405.0	405.0
100.0	16480	-60.9	-88.9	1	0.00	275	15	409.8	409.8	409.8
87.5	17309	-61.1	-89.1	1	0.00	232	12	425.3	425.3	425.3
74.6	18288	-64.0	-91.3	1	0.00	180	8	439.0	439.0	439.0
70.3	18654	-65.1	-92.1	1	0.00	222	6	444.2	444.2	444.2

Table A.1 Radiosonde data from 1st June 2016-1st part.

```
   70.0  18680  -64.9  -91.9      1   0.00    225      6  445.2  445.2  445.2
   67.5  18898  -63.9  -91.3      1   0.00      0      0  451.9  451.9  451.9
   63.9  19239  -62.3  -90.3      1   0.00    354      4  462.7  462.7  462.7
   59.8  19646  -64.1  -91.1      1   0.00    348      9  467.5  467.5  467.5
   58.2  19812  -63.1  -90.9      1   0.00    345     11  473.3  473.3  473.3
   56.0  20050  -61.7  -90.7      1   0.00     12      9  481.8  481.8  481.8
   52.5  20447  -62.9  -90.9      1   0.00     56      7  488.0  488.0  488.0
   51.2  20603  -60.3  -89.3      1   0.00     74      6  497.6  497.6  497.6
   50.0  20750  -60.9  -89.9      1   0.00     90      5  499.5  499.6  499.5
   49.1  20863  -59.7  -88.7      1   0.00     84      7  505.0  505.0  505.0
   45.5  21336  -60.4  -89.4      1   0.00     60     14  514.3  514.3  514.3
   43.3  21641  -60.9  -89.9      1   0.00     80     16  520.4  520.5  520.4
   43.2  21662  -60.9  -89.9      1   0.00     80     16  520.9  520.9  520.9
   41.3  21946  -59.0  -88.9      1   0.00     80     16  532.4  532.4  532.4
   39.1  22288  -56.7  -87.7      1   0.00     55     15  546.5  546.5  546.5
   37.5  22555  -56.9  -87.9      1   0.00     35     14  552.5  552.6  552.5
   35.7  22860  -57.2  -88.2      1   0.00     85     25  559.5  559.5  559.5
   34.0  23172  -57.5  -88.5      1   0.00     85     12  566.7  566.7  566.7
   34.0  23165  -57.5  -88.5      1   0.00     85     12  566.5  566.5  566.5
   32.5  23470  -56.1  -87.5      1   0.01     75     17  578.1  578.1  578.1
   30.9  23774  -54.6  -86.4      1   0.01     65     12  589.9  590.0  589.9
   30.0  23970  -53.7  -85.7      1   0.01     75     15  597.6  597.7  597.6
   29.5  24079  -53.6  -85.6      1   0.01     90     18  600.8  600.9  600.8
   28.1  24384  -53.4  -85.4      1   0.01     85     18  609.7  609.8  609.7
   26.8  24689  -53.1  -85.1      1   0.01     90     23  618.7  618.8  618.7
   25.6  24994  -52.9  -84.9      1   0.01    115     14  627.8  628.0  627.8
   23.8  25458  -52.5  -84.5      1   0.01     92     12  642.0  642.1  642.0
   23.3  25603  -51.8  -84.2      1   0.01     85     11  648.3  648.4  648.3
   22.2  25908  -50.2  -83.6      1   0.02     90      6  661.6  661.8  661.6
   21.6  26087  -49.3  -83.3      1   0.02     66     12  669.6  669.8  669.6
   21.2  26213  -49.4  -83.2      1   0.02     50     17  673.0  673.2  673.0
   20.0  26590  -49.7  -82.7      1   0.02     70     16  683.3  683.5  683.3
   17.6  27432  -48.9  -82.4      1   0.03     80     20  711.4  711.6  711.4
   16.8  27737  -48.6  -82.3      1   0.03     90     24  721.8  722.1  721.8
   15.6  28223  -48.1  -82.1      1   0.03    126     18  738.8  739.1  738.8
   15.3  28352  -46.3  -81.3      1   0.04    134     16  748.9  749.3  748.9
   15.3  28346  -46.4  -81.3      1   0.04    135     16  748.4  748.8  748.4
   14.6  28651  -45.7  -80.8      1   0.04    105     10  760.6  761.0  760.6
   12.8  29566  -43.7  -79.4      1   0.06     85     19  797.5  798.2  797.5
   11.7  30175  -42.4  -78.4      1   0.07     95     22  823.4  824.3  823.4
   11.7  30151  -42.5  -78.5      1   0.07     95     22  822.0  822.9  822.1
   11.2  30480  -40.5  -77.4      1   0.09     95     13  840.8  841.9  840.9
   11.1  30509  -40.3  -77.3      1   0.09     95     13  842.5  843.6  842.5
   10.7  30785  -41.2  -77.5      1   0.09     95     15  849.1  850.3  849.1
   10.5  30887  -41.5  -77.5      1   0.09     90     13  851.5  852.7  851.6
   10.2  31090  -39.9  -76.9      1   0.11     80     10  864.6  866.0  864.7
   10.2  31085  -39.9  -76.9      1   0.11     80     10  864.6  865.9  864.6
   10.0  31220  -40.7  -77.7      1   0.10     80     18  866.5  867.7  866.5
    9.8  31394  -41.2  -77.8      1   0.10     85     24  871.0  872.2  871.0
    9.4  31640  -41.9  -77.9      1   0.10    101     25  877.4  878.7  877.4
    8.9  32014  -38.1  -76.1      1   0.14    126     27  905.8  907.7  905.9
    8.5  32309  -37.5  -75.5      1   0.16    145     29  919.4  921.5  919.5
    8.2  32614  -36.6  -74.7      1   0.19    140     12  934.5  937.0  934.6
    8.2  32580  -36.9  -74.9      1   0.18    141     14  932.0  934.5  932.1
    7.7  33019  -33.1  -72.1      1   0.29    107     12  964.2  968.2  964.4
    7.4  33298  -33.3  -72.3      1   0.30     84     13  974.4  978.5  974.6
    7.2  33528  -32.5  -72.1      1   0.32     65     13  986.9  991.3  987.1
    7.0  33690  -31.9  -71.9      1   0.33     80     12  995.8 1000.5  996.0
    6.9  33833  -31.4  -71.3      1   0.37     50     16 1003.8 1009.0 1004.0
    6.7  34000  -30.7  -70.7      1   0.41              1013.3 1019.2 1013.6
Station information and sounding indices
                        Station identifier: TUS
                            Station number: 72274
                          Observation time: 160601/0000
                          Station latitude: 32.23
                         Station longitude: -110.96
                         Station elevation: 751.0
                           Showalter index: 1.04
                              Lifted index: 0.63
    LIFT computed using virtual temperature: 0.39
                                SWEAT index: 18.01
                                    K index: 13.70
                          Cross totals index: 7.10
                       Vertical totals index: 40.10
                         Totals totals index: 47.20
      Convective Available Potential Energy: 0.00
             CAPE using virtual temperature: 0.00
                       Convective Inhibition: 0.00
             CINS using virtual temperature: 0.00
                      Bulk Richardson Number: 0.00
          Bulk Richardson Number using CAPV: 0.00
  Temp [K] of the Lifted Condensation Level: 259.89
Pres [hPa] of the Lifted Condensation Level: 527.97
     Mean mixed layer potential temperature: 311.93
              Mean mixed layer mixing ratio: 2.63
              1000 hPa to 500 hPa thickness: 5747.00
Precipitable water [mm] for entire sounding: 11.22
```

Table A.2 Radiosonde data from 1^{st} June 2016-2^{nd} part.

Height	Pressure	Temperature	Rel Humidity	null	null
1.000	901.636	287.144	32.404	0.000	0.000AAH
2.000	799.975	280.326	35.172	0.000	0.000AAH
3.000	707.468	274.057	31.703	0.000	0.000AAH
4.000	623.599	268.167	25.974	0.000	0.000AAH
5.000	548.173	261.626	24.821	0.000	0.000AAH
6.000	480.323	254.611	26.331	0.000	0.000AAH
7.000	419.179	247.314	27.719	0.000	0.000AAH
8.000	364.211	239.876	27.496	0.000	0.000AAH
9.000	315.222	232.446	27.330	0.000	0.000AAH
10.000	271.536	225.421	27.222	0.000	0.000AAH
11.000	232.919	219.682	26.187	0.000	0.000AAH
12.000	199.175	216.595	22.771	0.000	0.000AAH
13.000	170.005	215.476	18.217	0.000	0.000AAH
14.000	144.997	213.698	14.869	0.000	0.000AAH
15.000	123.391	211.018	13.580	0.000	0.000AAH
16.000	104.874	208.258	13.016	0.000	0.000AAH
17.000	88.959	206.593	12.849	0.000	0.000AAH
18.000	75.388	206.171	12.680	0.000	0.000AAH
19.000	63.896	206.791	12.347	0.000	0.000AAH
20.000	54.194	208.032	11.871	0.000	0.000AAH
21.000	46.014	209.474	11.283	0.000	0.000AAH
22.000	39.119	211.049	10.596	0.000	0.000AAH
23.000	33.292	212.682	9.951	0.000	0.000AAH
24.000	28.363	214.078	9.219	0.000	0.000AAH
25.000	24.197	215.565	8.407	0.000	0.000AAH
27.500					
30.000					
32.500					
35.000					
37.500					
40.000					
42.500					
45.000					
47.500					
50.000					
55.000					
60.000					
65.000					
70.000					
75.000					
80.000					
85.000					
90.000					
95.000					
100.000					
105.000					
110.000					
115.000					
120.000					

Table A.3 Radiosonde derived pressure, temperature and relative humidity, prepared for Card 2C1 inclusion.

Some of the measurements of most interest are pressure, temperature, relative humidity / dewpoint. Tables A.1 and A.2 form one completed sounding from the 1^{st} June 2016 at Tucson, Az. Eventdisplay has proprietary code to change these individual soundings

over many years into averaged seasonal soundings, using VAtmosphereSoundings.cpp. This gives an output that can be added to MODTRAN (via Card 2C1 [1]) to allow a user-defined atmosphere to be produced, named VWinter and VSummer.

Table A.3 shows the VWinter profile with height, pressure, temperature and relative humidity. Unknown gas concentrations and relavant profiles above 25 km a.s.l. are taken from MODTRAN default models. With all other (card) inputs completed the final run file for MODTRAN (.tp5 file) may be generated, whose output is set to give the required atmosphere profiles to run CORSIKA simulations. CORSIKA requires height profiles of refractive index and atmospheric depth principally to produce ita EAS simulations.

Table A.4 shows ATM31 molecular profile which is identical to ATM61 but having a different aerosol extinction profile associated with it. Table A.5 shows ATM33, differing from ATM31 in water vapour content alone.

The original collaboration-wide atmospheric simulations were ATM21 and ATM22. Interpolated profiles from January, February and March 1995-2013 and December 1995-2012 were averaged to obtain the new winter atmosphere molecular profile, ATM61 in addition to the new summer atmosphere molecular profile ATM62. The scaled density profile (see Figure 3.1 and subsequent explanation) of this new model, together with the scaled density profile of ATM21 / ATM22, the radiosonde data soundings averaged (year on year) and the midlatitude winter model of MODTRAN, can be seen in Figures A.1 and A.2. Though the soundings that produces ATM21 / ATM61 and ATM22 / ATM62 appear very similar, for this work they must be compared by EAS simulation production. Figure A.3 shows three mono-energy VERITAS site specific EAS simulations for a flat detector for ATM21 / ATM61. There is a typical flattening of the lateral photon distribution up to about 140 m from shower axis (apart for an outer rim of increased Cherenkov photon arrival corresponding to the air shower boundary), beyond which the photon count falls of sharply. Outside of this $\sim$140 m radius, Cherenkov photon counts for ATM21 and ATM61 profiles agree to

[1] The inputs to run MODTRAN are organised in a series of 'cards', refer to the MODTRAN user manual for more information

```
# Atmospheric Model 31 (Improved VWinter,Desert Dust ext, normal H2O)
#Col. #1          #2           #3           #4
# Alt [km]     rho [g/cm^3] thick [g/cm^2]    n-1
     1.000    1.09154e-03  9.20914e+02  2.56800e-04
     2.000    9.92469e-04  8.17080e+02  2.33400e-04
     3.000    8.98303e-04  7.22595e+02  2.11200e-04
     4.000    8.09558e-04  6.36932e+02  1.90300e-04
     5.000    7.29596e-04  5.59894e+02  1.71500e-04
     6.000    6.57009e-04  4.90593e+02  1.54400e-04
     7.000    5.90362e-04  4.28142e+02  1.38700e-04
     8.000    5.28877e-04  3.71998e+02  1.24300e-04
     9.000    4.72393e-04  3.21962e+02  1.11000e-04
    10.000    4.19627e-04  2.77342e+02  9.85900e-05
    11.000    3.69359e-04  2.37899e+02  8.67800e-05
    12.000    3.20341e-04  2.03434e+02  7.52700e-05
    13.000    2.74848e-04  1.73640e+02  6.45800e-05
    14.000    2.36371e-04  1.48097e+02  5.55400e-05
    15.000    2.03704e-04  1.26029e+02  4.78600e-05
    16.000    1.75429e-04  1.07116e+02  4.12200e-05
    17.000    1.50010e-04  9.08611e+01  3.52500e-05
    18.000    1.27385e-04  7.69999e+01  2.99300e-05
    19.000    1.07643e-04  6.52622e+01  2.52900e-05
    20.000    9.07536e-05  5.53527e+01  2.13200e-05
    21.000    7.65254e-05  4.69978e+01  1.79800e-05
    22.000    6.45711e-05  3.99554e+01  1.51700e-05
    23.000    5.45314e-05  3.40038e+01  1.28100e-05
    24.000    4.61537e-05  2.89694e+01  1.08400e-05
    25.000    3.91021e-05  2.47144e+01  9.18800e-06
    27.500    2.66087e-05  1.68119e+01  6.25200e-06
    30.000    1.77871e-05  1.13373e+01  4.17900e-06
    32.500    1.19495e-05  7.72163e+00  2.80800e-06
    35.000    7.91825e-06  5.29078e+00  1.86000e-06
    37.500    5.32540e-06  3.67696e+00  1.25100e-06
    40.000    3.62410e-06  2.58410e+00  8.51500e-07
    42.500    2.50028e-06  1.83849e+00  5.87500e-07
    45.000    1.73848e-06  1.31758e+00  4.08500e-07
    47.500    1.23526e-06  9.60094e-01  2.90200e-07
    50.000    8.95512e-07  6.97604e-01  2.10400e-07
    55.000    4.83923e-07  3.69740e-01  1.13700e-07
    60.000    2.61141e-07  1.92021e-01  6.13600e-08
    65.000    1.37382e-07  9.70312e-02  3.22800e-08
    70.000    7.09729e-08  4.80049e-02  1.66800e-08
    75.000    3.50900e-08  2.26747e-02  8.24500e-09
    80.000    1.70787e-08  1.05202e-02  4.01300e-09
    85.000    7.95082e-09  4.65750e-03  1.86800e-09
    90.000    3.45752e-09  2.02234e-03  8.12300e-10
    95.000    1.46674e-09  8.95752e-04  3.44600e-10
   100.000    6.48615e-10  4.15702e-04  1.52500e-10
   105.000    2.93860e-10  2.04276e-04  6.90299e-11
   110.000    1.42302e-10  1.08266e-04  3.33300e-11
   115.000    7.13388e-11  6.12829e-05  1.67000e-11
   120.000    3.76618e-11  3.67697e-05  8.84692e-12
```

Table A.4 ATM31 atmospheric profiles, showing the atmospheric density, atmospheric depth and refractive index as $(n - 1)$. Derived using MODTRAN 5.2 and 18 years of radiosonde data.

```
# Atmospheric Model 33 (Improved VWinter, Desert Dust ext, 2X normal H2O)
#Col. #1          #2           #3            #4
# Alt [km]    rho [g/cm^3] thick [g/cm^2]    n-1
     1.000    1.08916e-03  9.20914e+02  2.56600e-04
     2.000    9.90795e-04  8.17080e+02  2.33300e-04
     3.000    8.97310e-04  7.22595e+02  2.11100e-04
     3.500    8.52032e-04  6.78413e+02  2.00400e-04
     4.000    8.09020e-04  6.36932e+02  1.90200e-04
     5.000    7.29280e-04  5.59894e+02  1.71400e-04
     6.000    6.56816e-04  4.90593e+02  1.54400e-04
     7.000    5.90252e-04  4.28142e+02  1.38700e-04
     8.000    5.28821e-04  3.71998e+02  1.24300e-04
     9.000    4.72366e-04  3.21962e+02  1.11000e-04
    10.000    4.19614e-04  2.77342e+02  9.85900e-05
    11.000    3.69352e-04  2.37899e+02  8.67800e-05
    12.000    3.20337e-04  2.03434e+02  7.52700e-05
    13.000    2.74845e-04  1.73640e+02  6.45800e-05
    14.000    2.36369e-04  1.48097e+02  5.55400e-05
    15.000    2.03703e-04  1.26029e+02  4.78600e-05
    16.000    1.75429e-04  1.07116e+02  4.12200e-05
    17.000    1.50010e-04  9.08611e+01  3.52500e-05
    18.000    1.27384e-04  7.69999e+01  2.99300e-05
    19.000    1.07642e-04  6.52622e+01  2.52900e-05
    20.000    9.07529e-05  5.53527e+01  2.13200e-05
    21.000    7.65245e-05  4.69978e+01  1.79800e-05
    22.000    6.45701e-05  3.99554e+01  1.51700e-05
    23.000    5.45302e-05  3.40038e+01  1.28100e-05
    24.000    4.61525e-05  2.89694e+01  1.08400e-05
    25.000    3.91008e-05  2.47144e+01  9.18800e-06
    27.500    2.66087e-05  1.68119e+01  6.25200e-06
    30.000    1.77871e-05  1.13373e+01  4.17900e-06
    32.500    1.19495e-05  7.72163e+00  2.80800e-06
    35.000    7.91823e-06  5.29078e+00  1.86000e-06
    37.500    5.32537e-06  3.67696e+00  1.25100e-06
    40.000    3.62410e-06  2.58410e+00  8.51500e-07
    42.500    2.50028e-06  1.83849e+00  5.87400e-07
    45.000    1.73848e-06  1.31758e+00  4.08500e-07
    47.500    1.23526e-06  9.60094e-01  2.90200e-07
    50.000    8.95512e-07  6.97604e-01  2.10400e-07
    55.000    4.83923e-07  3.69740e-01  1.13700e-07
    60.000    2.61141e-07  1.92021e-01  6.13600e-08
    65.000    1.37382e-07  9.70312e-02  3.22800e-08
    70.000    7.09729e-08  4.80049e-02  1.66800e-08
    75.000    3.50900e-08  2.26747e-02  8.24500e-09
    80.000    1.70787e-08  1.05202e-02  4.01300e-09
    85.000    7.95082e-09  4.65750e-03  1.86800e-09
    90.000    3.45752e-09  2.02234e-03  8.12300e-10
    95.000    1.46674e-09  8.95752e-04  3.44600e-10
   100.000    6.48615e-10  4.15702e-04  1.52500e-10
   105.000    2.93860e-10  2.04276e-04  6.90299e-11
   110.000    1.42302e-10  1.08266e-04  3.33300e-11
   115.000    7.13388e-11  6.12829e-05  1.67000e-11
   120.000    3.76618e-11  3.67697e-05  8.84692e-12
```

Table A.5 ATM33 atmospheric profiles, showing the atmospheric density, atmospheric depth and refractive index as $(n - 1)$. Derived as ATM31 but with twice normal water vapour content.

within $\pm 2\%$. Inside this $\sim$140 m radius, there are differences on the order of $\sim 3\%$ between ATM21 and ATM61 profiles. The differences are energy dependent, however there does not seem to be a correlation between γ-ray energies and atmospheric profile photon yields. It must be remembered that ATM21 molecular profiles were derived with MODTRAN 4.0, with spectral resolution of 1.0 cm^{-1}, compared to spectral resolution of 0.1 cm^{-1} for MODTRAN 5.2. As the differences between ATM21 and ATM61 are $\leq 3\%$ (shown in part Figure A.5) the VERITAS Collaboration has adopted ATM61 for all new CORSIKA simulations, as have I.

As well as the atmospheric profiles that define atmospheric depth and refractive index, the extinction profiles (molecular and particulate) must be compared. When the ATM21 extinction profile, from molecular and particulate extinction combined, and the extinction profile derived from the US76 standard atmosphere are compared to the new ATM61 extinction profiles, the relative differences are small, $\sim 1\%$, for most wavelengths.

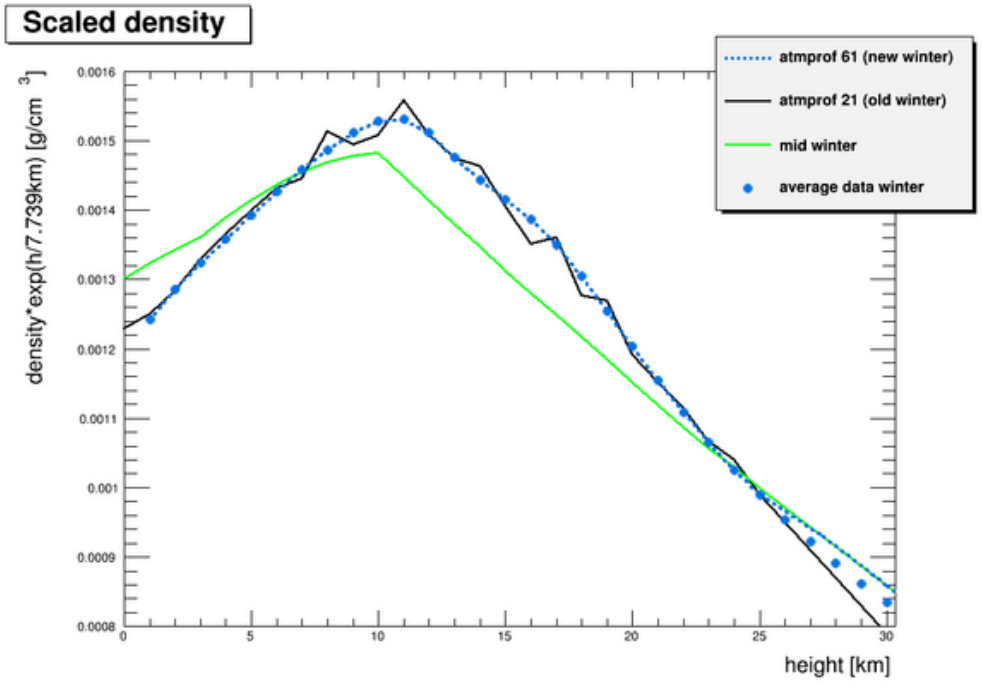

Fig. A.1 ATM21 to ATM61 scaled atmospheric density comparison. The applied interpolation smooths out the density profile to more realistically represent the true profile at VERITAS. (Plot: H. Fleischhack).

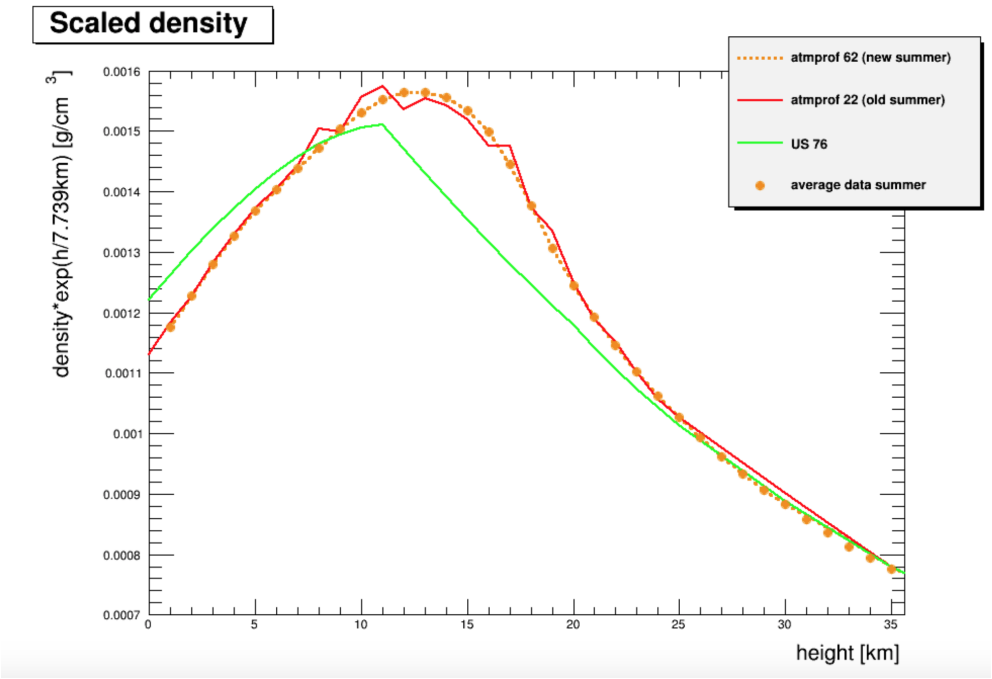

Fig. A.2 ATM22 to ATM62 scaled atmospheric density comparison. The applied interpolation smooths out the density profile to more realistically represent the true profile at VERITAS. (Plot: H. Fleischhack).

In conclusion, going from the ATM21 profiles to smoother ATM61 atmospheric profiles, with an associated change in MODTRAN version from MODTRAN 4.0 to MODTRAN 5.2, has led to slightly lower transmittance than found in the older simulations. However, the effect on the Cherenkov light yield is of the order of a few percent and negligible compared to the effect of the yearly variations of density profile, and the variations in aerosol loading. There remains the change in overall extinction profile resulting from the change in molecular profiles. For this, a similar comparative study will be carried out, shown in Figures A.3 and A.4. These plots display the overall extinction from ∼200-700 nm from 12 km a.s.l. to VERITAS ground level for ATM21 / ATM61 and ATM22 / ATM62, using the same MODTRAN derived aerosol model. It is seen that the overall difference in atmospheric extinction at Cherenkov wavelengths os ∼1-1.5%.

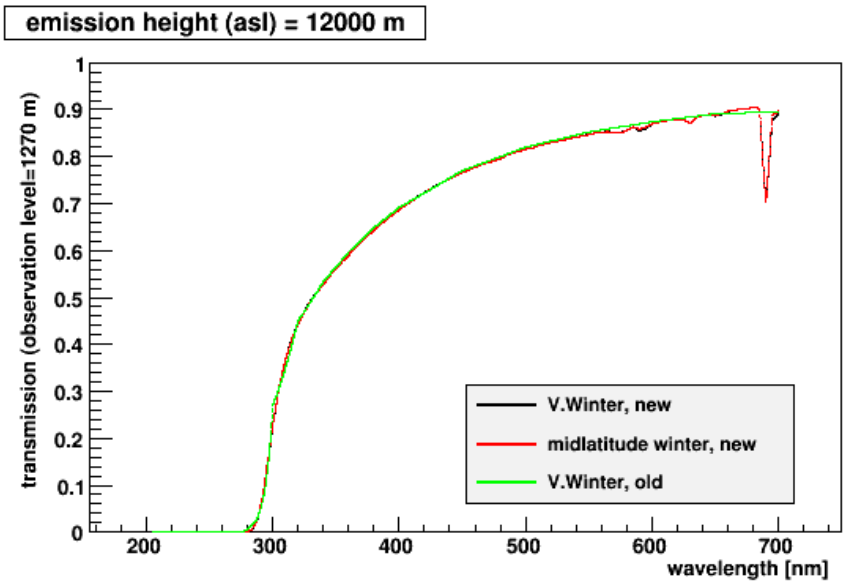

Fig. A.3 A plot showing the transmission probability (transmittance) from 12 km a.s.l. to VERITAS ground level using the ATM21 and ATM61 extinction profiles. The differences in extinction are $\sim$1%, therefore the extinction profile of ATM61 may be adopted as the working molecular extinction profile. (Plot: H.Fleischhack).

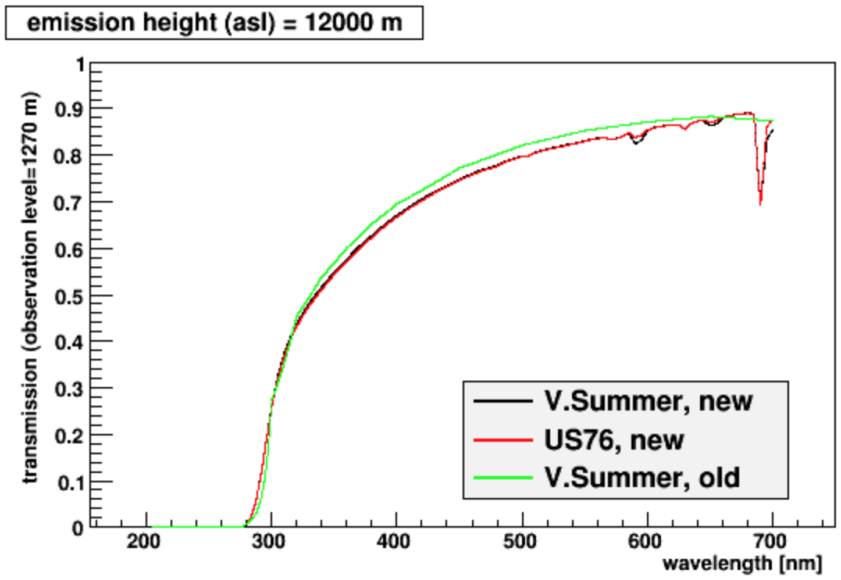

Fig. A.4 A plot showing the transmission probability (transmittance) from 12 km a.s.l. to VERITAS ground level using the ATM22 and ATM62 extinction profiles. The differences in extinction are $\sim$1.5%, therefore the extinction profile of ATM62 may be adopted as the working molecular extinction profile. (Plot: H.Fleischhack).

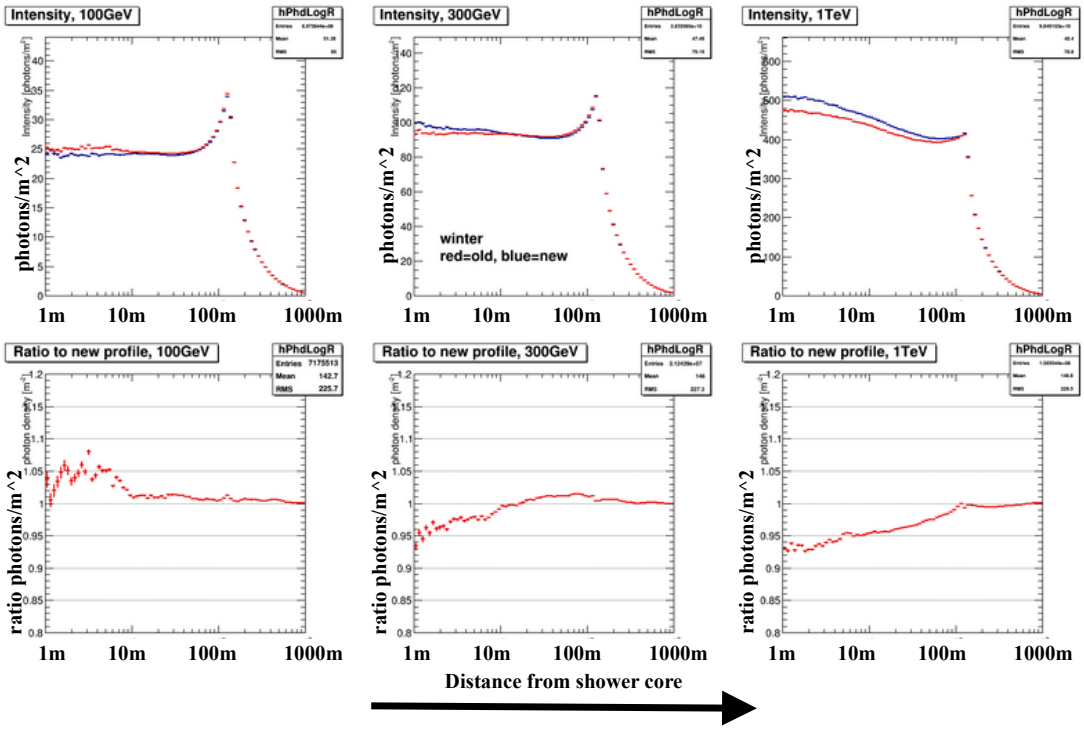

Fig. A.5 100, 300 and 1000 GeV γ-rays from zenith have their Cherenkov photons collected by an ideal flat detector, as per Chapter 5. The greatest differences in photon yield is close to shower axis. (Plot: H.Fleischhack).

From this analysis ATM31, identical to ATM61 except for the associated aerosol extinction profiles, is to be taken as the *de facto* atmospheric profiles for VERITAS EAS simulations during VWinter, with the Desert Dust aerosol model to replace the Tropospheric 50 km model, as described in Section 5.2.6. The same is true for ATM32 replacing ATM62 and associated aerosol profiles during VSummer.

Finally, there remains the ceilometer extinction profile analysis. It is essential to determine the impact of changing molecular and water vapour profiles on the extinction of Cherenkov photons, for the first 5 km a.g.l. at VERITAS. This will help determine if VSummer / VWinter changeover will impact noticeably on the extinction profiles from 900-920 nm.

Wavelength	Tr 0-1 km	Tr 1-2 km	Tr 2-3 km	Tr 3-4 km	Tr 4-5 km	Tr 5-6 km
900.000	0.90845042	0.92953068	0.95180672	0.97201514	0.98325980	0.98921621
901.000	0.90917879	0.93077350	0.95330060	0.97330415	0.98421991	0.98985696
902.000	0.91714519	0.93613094	0.95651257	0.97519100	0.98536414	0.99051929
903.000	0.93260998	0.94703335	0.96328849	0.97927547	0.98791707	0.99207765
904.000	0.94944757	0.95967901	0.97172636	0.98466659	0.99143732	0.99431753
905.000	0.95557582	0.96452022	0.97512007	0.98691565	0.99294037	0.99529529
906.000	0.94193584	0.95480955	0.96905798	0.98324937	0.99063146	0.99387687
907.000	0.92331547	0.94140238	0.96056861	0.97805077	0.98733658	0.99183995
908.000	0.91845530	0.93804288	0.95852989	0.97685426	0.98662090	0.99142820
909.000	0.91677678	0.93714386	0.95817697	0.97677004	0.98665404	0.99151057
910.000	0.91417533	0.93547618	0.95725262	0.97627860	0.98638803	0.99137491
911.000	0.92091316	0.94006693	0.95992953	0.97777879	0.98726588	0.99187237
912.000	0.92498827	0.94294614	0.96167940	0.97878367	0.98785895	0.99221069
913.000	0.91924953	0.93943453	0.95990336	0.97790754	0.98739702	0.99197233
914.000	0.91795653	0.93883085	0.95977974	0.97796750	0.98750126	0.99207920
915.000	0.91497874	0.93681449	0.95861137	0.97731417	0.98712498	0.99187434
916.000	0.91577923	0.93767852	0.95933890	0.97783375	0.98749441	0.99212229
917.000	0.92383361	0.94355947	0.96309632	0.98013085	0.98895252	0.99302655
918.000	0.92253649	0.94262171	0.96252680	0.97980648	0.98877102	0.99293572
919.000	0.93030012	0.94800812	0.96580118	0.98175824	0.98998958	0.99368382
920.000	0.95101118	0.96238506	0.97451842	0.98689318	0.99313897	0.99556905

Table A.6 The transmittance profiles for ceilometer wavelengths for VWinter atmosphere, where aerosol extinction = WSS10 and PWV = 7.5 mm.

A.3 Preparatory work for ceilometer analysis

Turning attention to atmospheric transition windows, the question of transmittance profiles during this period is examined. For the ceilometer analysis as a whole, many simulations from 900-920 nm, 0-6 km a.s.l, WSS04-WSS24 and PWV 0.0-2.0 g cm^{-2} (0-20 mm) were produced for VSummer and VWinter. In addition, the following boundary layers were set; 0-2, 0-3 and 0-5 km a.g.l. The highest boundary layer, 0-5 km, was chosen for use in this thesis, due to sporadic increases in aerosol loading at heights up to 4 km a.g.l. witnessed at VERITAS from time to time. The choice is not critical as the total optical depth is of more importance for γ-ray EAS Cherenkov light yields reaching ground. Examples of the transmittance files produced are shown in Tables A.6 to A.9. It is noted that the differences in overall transmittance through the 6 km of atmosphere simulated for a particular wavelength, aerosol extinction and PWV bin in VSummer and VWinter is $<1\%$, and often around 0.5%. This is irrespective of how heavily laden the atmosphere is with water vapour and the increase of aerosol loading.

Wavelength	Tr 0-1 km	Tr 1-2 km	Tr 2-3 km	Tr 3-4 km	Tr 4-5 km	Tr 5-6 km
900.000	0.84347814	0.87968373	0.91649377	0.94755220	0.96614897	0.97767597
901.000	0.83958912	0.87730038	0.91587937	0.94804919	0.96700156	0.97851169
902.000	0.85664845	0.88920921	0.92310417	0.95229483	0.96959639	0.98004627
903.000	0.88661426	0.91146576	0.93783730	0.96166784	0.97568506	0.98387969
904.000	0.91404825	0.93330061	0.95377833	0.97279412	0.98344529	0.98909050
905.000	0.92219371	0.94034749	0.95946741	0.97708189	0.98658276	0.99128401
906.000	0.89637262	0.92067397	0.94614369	0.96848959	0.98095459	0.98772067
907.000	0.86289591	0.89491522	0.92833322	0.95675790	0.97315621	0.98271769
908.000	0.85458201	0.88878286	0.92421532	0.95413059	0.97148585	0.98171127
909.000	0.85113192	0.88671261	0.92324662	0.95380640	0.97148836	0.98187202
910.000	0.84578079	0.88305122	0.92108434	0.95259792	0.97081989	0.98152727
911.000	0.85936368	0.89317977	0.92763352	0.95653868	0.97321290	0.98291147
912.000	0.86574429	0.89833385	0.93130285	0.95890290	0.97469932	0.98379183
913.000	0.85006863	0.88774514	0.92537832	0.95582163	0.97304404	0.98294258
914.000	0.84605300	0.88515639	0.92412829	0.95538557	0.97297913	0.98304427
915.000	0.84035653	0.88087785	0.92135972	0.95372224	0.97197974	0.98248136
916.000	0.83894032	0.88079959	0.92206204	0.95454776	0.97268152	0.98301136
917.000	0.85248506	0.89171046	0.92985344	0.95974153	0.97614223	0.98522770
918.000	0.85170764	0.89054853	0.92882222	0.95904016	0.97571409	0.98498958
919.000	0.86892962	0.90288448	0.93664306	0.96385264	0.97878861	0.98691028
920.000	0.91010004	0.93348098	0.95660573	0.97624183	0.98663640	0.99172771

Table A.7 The transmittance profiles for ceilometer wavelengths for VSummer atmosphere, where aerosol extinction = WSS10 and PWV = 7.5 mm. $\frac{ext0-6kmVWinter}{ext0-6kmVSummer}$ at 908 nm = $\frac{0.78909}{0.78425} = 1.0062$.

Wavelength	Tr 0-1 km	Tr 1-2 km	Tr 2-3 km	Tr 3-4 km	Tr 4-5 km	Tr 5-6 km
900.000	0.91886079	0.93081707	0.94493312	0.96419036	0.97888070	0.98759758
901.000	0.92065907	0.93249202	0.94653171	0.96566087	0.98002845	0.98830277
902.000	0.92791533	0.93808490	0.95060980	0.96828103	0.98149168	0.98902446
903.000	0.94103599	0.94862694	0.95861441	0.97362626	0.98452371	0.99053931
904.000	0.95527464	0.96053958	0.96808612	0.98033005	0.98855340	0.99264914
905.000	0.96052885	0.96506214	0.97178936	0.98304743	0.99024767	0.99356073
906.000	0.94916093	0.95582271	0.96470213	0.97828245	0.98754317	0.99221152
907.000	0.93343210	0.94300580	0.95483112	0.97157788	0.98369092	0.99027145
908.000	0.92895877	0.93954164	0.95229632	0.96993321	0.98279083	0.98984432
909.000	0.92687660	0.93817139	0.95149732	0.96957886	0.98269355	0.98984903
910.000	0.92418987	0.93620145	0.95015115	0.96878552	0.98229778	0.98967797
911.000	0.92986816	0.94068903	0.95346344	0.97087729	0.98339343	0.99018621
912.000	0.93359810	0.94364691	0.95566547	0.97229278	0.98415256	0.99054497
913.000	0.92897534	0.94020522	0.95331502	0.97096193	0.98355043	0.99030507
914.000	0.92781788	0.93947148	0.95293891	0.97087580	0.98361242	0.99038410
915.000	0.92509848	0.93736351	0.95141047	0.96992135	0.98311758	0.99016291
916.000	0.92574769	0.93807572	0.95211017	0.97050196	0.98351169	0.99039006
917.000	0.93257165	0.94369483	0.95647687	0.97347343	0.98522139	0.99125910
918.000	0.93118840	0.94260943	0.95568180	0.97297454	0.98495901	0.99114704
919.000	0.93745565	0.94766313	0.95951223	0.97551244	0.98638380	0.99185520
920.000	0.95513654	0.96174246	0.97005844	0.98240215	0.99019545	0.99371058

Table A.8 The extinction files for ceilometer wavelengths for VWinter atmosphere, where extinction = WSS10 and PWV = 20 mm.

Wavelength	Tr 0-1 km	Tr 1-2 km	Tr 2-3 km	Tr 3-4 km	Tr 4-5 km	Tr 5-6 km
900.000	0.86095625	0.88228220	0.90572929	0.93501937	0.95959604	0.97634745
901.000	0.85907328	0.88076931	0.90483892	0.93507075	0.96046722	0.97735941
902.000	0.87459034	0.89299136	0.91389292	0.94093430	0.96374357	0.97902048
903.000	0.90068364	0.91452986	0.93080324	0.95277590	0.97084701	0.98274779
904.000	0.92457908	0.93515849	0.94795316	0.96583021	0.97947609	0.98767793
905.000	0.93190074	0.94177777	0.95377308	0.97060168	0.98287421	0.98973435
906.000	0.90960103	0.92300379	0.93873888	0.95987487	0.97638112	0.98633397
907.000	0.88022977	0.89824688	0.91879362	0.94542390	0.96743751	0.98154587
908.000	0.87228006	0.89189231	0.91391212	0.94201732	0.96539754	0.98049462
909.000	0.86815315	0.88900232	0.91207886	0.94109100	0.96508408	0.98046851
910.000	0.86255825	0.88472790	0.90902627	0.93919706	0.96409672	0.98002791
911.000	0.87434971	0.89451075	0.91668749	0.94441539	0.96701735	0.98141301
912.000	0.88059616	0.89980459	0.92097712	0.94750398	0.96886200	0.98233360
913.000	0.86740220	0.88947165	0.91349715	0.94298708	0.96672344	0.98149699
914.000	0.86364788	0.88667047	0.91160727	0.94202417	0.96646172	0.98153967
915.000	0.85824811	0.88224030	0.90818030	0.93971580	0.96517837	0.98093510
916.000	0.85722846	0.88194549	0.90846956	0.94038665	0.96586955	0.98141533
917.000	0.86938012	0.89244097	0.91711336	0.94675982	0.96984881	0.98354495
918.000	0.86808020	0.89108473	0.91585410	0.94577932	0.96924829	0.98325056
919.000	0.88233972	0.90273803	0.92486590	0.95191944	0.97280216	0.98506528
920.000	0.91849828	0.93262041	0.94822001	0.96800417	0.98215902	0.98980242

Table A.9 The extinction files for ceilometer wavelengths for VSummer atmosphere, where extinction = WSS10 and PWV = 20 mm. $\frac{ext0-6kmVWinter}{ext0-6kmVSummer}$ at 908 nm $= \frac{0.63878}{0.63399} = 1.0076$.

From Tables A.6 and A.7 for example (both simulation sets having the same PWV and same aerosol extinction), the total extinction from 0-6 km is calculated for both VSummer and VWinter for the expected peak emission wavelength of the ceilometer, 908 nm. This is repeated for VSummer and VWinter with aerosol extinction WSS10 and PWV 20 mm (Tables A.8 , A.9). Again the difference in transmittance profiles at 908 nm $<1\%$. Another VSummer and VWinter comparison with aerosol extinction WSS16 and PWV 7.5 mm yielded the following result; $\frac{ext0-6kmVWinter}{ext0-6kmVSummer}$ at 908 nm $= \frac{0.72692}{0.72057} = 1.0088$. In conclusion, for the ceilometer analysis during VSummer and VWinter atmospheres, the difference in transmittance at the atmosphere transition window is $< 1\%$. For future ceilometer analysis, it would be permissable to use just one VERITAS season for all ceilometer transmittance analysis, VWinter, to reduce the complexity of the analysis.

Appendix B

Co-authored publications

B.1 A list of co-authored publications

This final addition to my thesis gives a most brief introduction to the published work undertaken while I was a graduate student with the VERITAS collaboration. The main contributions I made are referred to in Section 1.1.2. The list starts from the most recent publication, ending when I became a co-signing author with VERITAS in *circa* 2010.

B.1.1 The co-authored publications

1. *Multiwavelength follow-up of a rare IceCube neutrino multiplet* [IceCube et al., 2017]

2. *Dark matter constraints from a joint analysis of dwarf Spheroidal galaxy observations with VERITAS* [Archambault et al., 2017a]

3. *Gamma-ray observations under bright moonlight with VERITAS* [Archambault et al., 2017c]

4. *Search for Magnetically Broadened Cascade Emission from Blazars with VERITAS* [Archambault et al., 2017d]

5. *Discovery of Very-high-energy Emission from RGB J2243+203 and Derivation of Its Redshift Upper Limit* [Abeysekara et al., 2017a]

6. *Gamma-Ray Observations of Tycho's Supernova Remnant with VERITAS and Fermi* [Archambault et al., 2017b]

7. *Very High Energy observations of the binaries V 404 CYG and 4U 0115+634 during giant X-ray outbursts* [Archer et al., 2016a]

8. *Very-High-Energy γ-Ray Observations of the Blazar 1ES 2344+514 with VERITAS* [Allen et al., 2017]

9. *A search for spectral hysteresis and energy-dependent time lags from X-ray and TeV γ-ray observations of Mrk 421* [Abeysekara et al., 2017c]

10. *A Luminous and Isolated Gamma-Ray Flare from the Blazar B2 1215+30* [Abeysekara et al., 2017b]

11. *A search for VHE γ-rays from the missing link binary pulsar J1023+0038 with VERITAS* [Aliu et al., 2016]

12. *Upper limits from five years of blazar observations with the VERITAS Cherenkov telescopes* [Archambault et al., 2016c]

13. *VERITAS and multiwavelength observations of the BL Lacertae object 1ES 1741+196* [Abeysekara et al., 2016]

14. *TeV Gamma-ray Observations of The Galactic Center Ridge By VERITAS* [Archer et al., 2016b]

15. *Gamma-Rays from the Quasar PKS 1441+ 25: Story of an Escape* [Abeysekara et al., 2015]

16. *Exceptionally Bright TeV Flares from the Binary LS I+ 61° 303* Archambault et al. [2016a]

17. *Multiwavelength study of quiescent states of MRK 421 with unprecedented hard x-ray coverage provided by NuSTAR in 2013* [Baloković et al., 2016]

18. *First NuSTAR observations of Mrk 501 within a radio to TeV multi-instrument campaign* [Furniss et al., 2015]

19. *VERITAS detection of γ-ray flaring activity from the BL Lac object 1ES 1727+ 502 during bright moonlight observations* [Archambault et al., 2015]

20. *A Search for Pulsations from Geminga above 100 GeV with VERITAS* [Aliu et al., 2015a]

21. *Discovery of very high energy gamma rays from 1ES 1440+ 122* [Archambault et al., 2016b].

22. *Very-high Energy Observations of the Galactic Center Region by VERITAS in 2010-2012* [Archer et al., 2014]

23. *VERITAS observations of the BL Lac object PG 1553+ 113* [Aliu et al., 2015b].

24. *Deep broadband observations of the distant gamma-ray blazar PKS 1424+ 240* [Archambault et al., 2014a].

25. *Spatially Resolving the Very High Energy Emission from MGRO J2019+37 with VERITAS* [Aliu et al., 2014c]

26. *Investigating the TeV Morphology of MGRO J1908+ 06 with VERITAS* [Aliu et al., 2014b]

27. *A search for enhanced VHE γ-ray emission from the March 2013 Crab Nebula flare* [Aliu et al., 2013e]

28. *Deep broadband observations of the distant γ-ray blazar PKS 1424+ 240* [Archambault et al., 2014a]

29. *Observations of the unidentified γ-ray source TeV J2032+ 4130 by VERITAS* [Aliu et al., 2014d]

30. *A Three-year Multi-wavelength Study of the VHE γ-Ray Blazar 1ES 0229+ 200* [Aliu et al., 2014a]

31. *Long-term TeV and X-ray Observations of the γ-ray Binary H.E.S.S. J0632+ 057* [Aliu et al., 2013d]

32. *VERITAS observations of the microquasar Cygnus X-3* [Archambault et al., 2013b]

33. *Observation of Mrk 421 in TeV γ-rays over a 14-year time span* [Acciari et al., 2014]

34. *Multiwavelength observations of the TeV binary LS I+ 61° 303 with VERITAS, Fermi-LAT, and swift/XRT during a TeV outburst* [Aliu et al., 2013f]

35. *Long term observations of B2 1215+ 30 with VERITAS* [Aliu et al., 2013d]

36. *A search for enhanced VHE γ-ray emission from the March 2013 Crab Nebula flare* [Aliu et al., 2013e]

37. *Discovery of a new TeV gamma-ray source: Ver J0521+ 211* [Archambault et al., 2013a]

38. *Multiwavelength observations and modeling of 1ES 1959+ 650 in a low flux state* [Aliu et al., 2013c]

39. *Discovery of TeV γ-ray emission toward SNR G78. 2+ 2.1* [Aliu et al., 2013a]

40. *Discovery of TeV γ-ray emissions from CTA 1 by VERITAS* [Aliu et al., 2013b]

41. *Rapid TeV γ-ray flaring of BL Lacertae* [Arlen et al., 2012]

42. *VERITAS observations of six bright, hard-spectrum Fermi-LAT blazars* [Aliu et al., 2012d]

43. *Search for a correlation between VHE γ-rays and giant radio pulses in the Crab pulsar* [Aliu et al., 2012c]

44. *Multiwavelength Observations of the AGN 1ES 0414+ 009 with VERITAS, Fermi-LAT, SWIFT-XRT, and MDM* [Aliu et al., 2012b]

45. *VERITAS Observations of the Nova in V407 Cygni* [Aliu et al., 2012e]

46. *Discovery of HE and VHE γ-ray emission from the blazar RBS 0413* [Aliu et al., 2012a]

47. *VERITAS deep observations of the dwarf spheroidal galaxy Segue 1* [Aliu et al., 2012e]

48. *VERITAS Observations of Day-scale Flaring of M 87 in 2010 April* [Aliu et al., 2012f]

49. *Multiwavelength Observations of the Previously Unidentified Blazar RX J0648. 7+ 1516* [Aliu et al., 2011c]

50. *VERITAS observations of γ-ray bursts detected by Swift* [Acciari et al., 2011a]

51. *Detection of pulsed γ-rays above 100 GeV from the Crab pulsar* [Aliu et al., 2011a]

52. *VERITAS observations of the unusual extragalactic transient Swift J164449. 3+ 573451* [Aliu et al., 2011b]

53. *VERITAS observations of the TeV binary LS I+ 61° 303 during 2008-2010* [Acciari et al., 2011b]